UCSB-HEP-96-01
HUTP-96/A023
To be published in Reviews of Modern Physics

The discovery of the top quark

Claudio Campagnari

University of California, Santa Barbara, California 93106

Melissa Franklin

Harvard University, Cambridge, Massachussets 02138

arXiv:hep-ex/9608003v1 2 Aug 1996

Abstract

Evidence for pair production of a new particle consistent with the Standard Model top quark has been reported recently by groups studying proton anti-proton collisions at 1.8 TeV center of mass energy at the Fermi National Accelerator Laboratory. In this paper we review the history of the search for the top quark in electron positron and proton anti-proton collisions. We report on a number of precise electro-weak measurements and the value of the top quark mass which can be extracted from these measurements within the context of the Standard Model. We review the theoretical predictions for top quark production and the dominant backgrounds. We describe the collider and the detectors that were used to measure the pair production process and follow on to describe the data from which the existence of the top quark is evinced. Finally, we present possible measurements that could be made in the future with more data, measurements of quantities that would confirm the nature of this particle, the details of its production in hadron collisions, and its decay properties.

CONTENTS

I. Introduction 3
II. The role of the top quark in the Standard Model 4
III. Top mass and precision electro-weak measurements 7
A. Neutral current experiment measurments 8
1. Asymmetries at the Z 9
2. R_b 12
B. W mass 12

C. Global fits for M_{top} and M_{Higgs} 15
IV. Top quark production 19
A. Production mechanisms and cross sections 19
B. Top quark hadronization 26
C. Underlying event 28
D. Modelling of top quark production 29
V. Top quark signatures 32
A. Standard Model top quark decay modes 32
B. Detection of the top decay products 33
1. Detection of electrons and muons 35
2. Detection of quarks 36
3. Detection of neutrinos 42
4. Detection of tau leptons 43
C. All hadronic mode 44
D. Dilepton mode 44
E. Lepton + jets mode 47
1. $W+$ jets background 47
2. Separation of $W+$ jets and $t\bar{t}$ for $M_{top} < M_W + M_b$ 50
3. Kinematic differences between $t\bar{t}$ and $W+$ jets 52
4. b-quark tagging 57
VI. Early searches for the top quark 62
A. Searches in e^+e^- collisions 62
B. Early searches in $p\bar{p}$ collisions assuming Standard Model top-quark decay 63
C. Searches for non-Standard Model top quark decay modes 69
VII. The Fermilab proton anti-proton collider 72
A. Linear accelerators and synchrotrons 72
B. Anti-proton source 73
C. Collider 73
VIII. Discovery of the top quark 74
A. Dilepton analysis results from CDF and D0 76
1. $Z \to ee/\mu\mu$ background 77
2. $Z \to \tau\tau$ background 78
3. Drell-Yan Background 82
4. WW background 82
5. $b\bar{b}$ and fake lepton backgrounds 83
6. Results 86
B. Lepton + jets + b-tag 88
1. Selection of lepton + jets data before b-tagging 88
2. Lepton tagging in CDF and D0 89
3. Displaced-vertex tagging in CDF 95
4. Summary and cross checks of the tagging background calculation on $Z+$ jets 100
C. Lepton + jets 102
1. D0 lepton + jet kinematic analysis 102
2. CDF lepton + jets kinematic analysis 107
3. Summary of lepton + jets kinematic analyses 110
D. Significance of the top signal 112
E. Measurement of the $p\bar{p} \to t\bar{t}$ cross-section 113
IX. Measurement of the top quark mass 114
A. Direct measurements of the top quark mass from lepton + jets events 115
1. Constrained fits, combinatorics, and top mass resolution 116
2. CDF and D0 top mass measurements 119
3. Jet energy corrections and systematics on the M_{top} measurement 123
4. Updated CDF and D0 top mass measurements 126
B. Top mass from dilepton events and kinematic distributions 130
C. Reconstruction of the W mass from hadronic decays in lepton + jets events 133
X. Future prospects 136
A. Accelerator and detector upgrades 136
B. Improving the top mass measurement 137
C. Probing the Wtb vertex 139
D. Further tests of the Standard Model and searches for new physics in the top quark sector 143
XI. Conclusion 146

ACKNOWLEDGMENTS 146
References 148

I. INTRODUCTION

The intensive experimental efforts in the search for the heaviest fundamental fermion culminated in 1995 with the discovery of the top quark in proton-antiproton annhilations at the Fermilab Tevatron Collider. Observation of the top quark is the latest in a long series of triumphs for the Standard Model of particles and fields. The top quark is the last fundamental fermion and the next-to-last fundamental particle predicted by the Standard Model. Only the Higgs boson remains unobserved.

The search for the top quark started in the late seventies, soon after discovery of the companion bottom-quark. It has been a long and arduous process because the top quark turned out to be much more massive than was originally expected. The mass of the top quark is remarkably large, approximately 200 times larger than the mass of the proton and 40 times higher than the mass of the next lightest quark. Whether this property of the top quark is a mere accident or a manifestation of a deeper physical process is an unanswered question in particle physics.

The discovery of the top quark has been made possible by the technological progresses in high energy physics in the past fifteen years. In particular, the development of proton-antiproton colliders, pioneered first at CERN and then at Fermilab has been a crucial ingredient in the discovery of the top.

In this article we review the discovery of the top quark as well as the developments that led to it. In Section II we discuss the top quark within the framework of the Standard Model. While the top quark mass is a free parameter in the Standard Model, its value enters in calculations of a number of electroweak observables. The top-mass dependence of the theoretical predictions is in general rather weak. However, the accuracy of many of these measurements is now such that meaningful constraints on the top quark mass can be obtained by comparing them with theoretical predictions. These constraints constitute a test of the predictive power of the Standard Model, and are reviewed in Section III. The top production mechanisms in proton-antiproton collisions, and the experimental signatures of top events that are crucial to the understanding of the experimental results are discussed in Section IV and V. Early searches for the top quark are described in Section VI. The Tevatron Collider, whose remarkable performance played a very important role in the discovery of the top quark, will be described briefly in Section VII. The data that finally led to the discovery of the top quark are reviewed in Section VIII. The value of the top mass is of fundamental importance, and it is needed to complete precise tests of the Standard Model. Furthermore, from an experimental point of view, the techniques developed to measure the top mass are new and particularly interesting. The top mass measurement is described in Section IX. Historically, discoveries of new leptons or quarks have opened up new fields of inquiry which have enhanced our understanding of elementary particles and their interactions. Consequently, this article concludes in Section X with a discussion of the experimental prospects for top physics.

II. THE ROLE OF THE TOP QUARK IN THE STANDARD MODEL

Quarks and leptons constitute the basic building blocks of matter in the Standard Model (SM). There are three *generations* of quarks and leptons in the model, with identical quantum numbers, but different masses. Within each generation, quarks and leptons appear in pairs, (see Fig. 1). The left-handed quarks form weak isospin doublets, with the Q= +2/3 and Q= −1/3 quarks having weak isospin $I_3 = +1/2$ and $-1/2$ respectively.

Quarks

			I_3	Y	$Q = I_3 + Y/2$
$\begin{bmatrix} u \\ d \end{bmatrix}_L$	$\begin{bmatrix} c \\ s \end{bmatrix}_L$	$\begin{bmatrix} t \\ b \end{bmatrix}_L$	+1/2	+1/3	+2/3
			−1/2	+1/3	−1/3
u_R	c_R	t_R	0	+4/3	+2/3
d_R	s_R	b_R	0	−2/3	−1/3

Leptons

$\begin{bmatrix} \nu_e \\ e \end{bmatrix}_L$	$\begin{bmatrix} \nu_\mu \\ \mu \end{bmatrix}_L$	$\begin{bmatrix} \nu_\tau \\ \tau \end{bmatrix}_L$	+1/2	−1	0
			−1/2	−1	−1
e_R	μ_R	τ_R	0	−2	−1

FIG. 1. Leptons and quarks in SU(2)xU(1) (Standard Model). Also shown are the values for the SU(2) weak isospin (I_3), U(1) weak hypercharge (Y), and electric charge (Q, in units of the electron charge). The subscripts L and R refer to the left and right-handed components respectively.

The tau-lepton (τ) was the first particle of the third generation to be discovered (Perl *et al.*, 1975). A short time later, in 1977, the Υ was discovered at Fermilab (Herb *et al.*, 1977) as a resonance in the $\mu^+\mu^-$ invariant mass spectrum in the reaction p + nucleon $\rightarrow \mu^+\mu^-+$ X. This resonance was interpreted as a $b\bar{b}$ bound state (the Υ), which subsequently decays into muon pairs. As will become abundantly clear in the remainder of this paper, the top signature in hadron collisions is much more complicated.

In the past fifteen years, a tremendous amount of experimental data on the properties of the b-quark and of b-flavored hadrons have become available, mostly from experiments at e^+e^- colliders. Both the charge and the weak isospin of the bottom-quark are by now well established ($Q_b = -1/3$, and $I_3 = -1/2$).

The value of the charge was first inferred from measurements of the Υ leptonic width (Berger *et al.*, 1978; Darden *et al.*, 1978; Bienlein *et al.*, 1978) at the DORIS e^+e^- storage

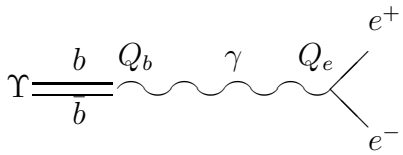

FIG. 2. Feynman diagram for $\Upsilon \to e^+e^-$.

Model 1	Model 2	Model 3	Experimental value
1.05 keV	1.07 keV	1.15 ± 0.20 keV	1.22 ± 0.03 keV

TABLE I. The experimental value of $\Gamma(\Upsilon \to e^+e^-)$ compared with theoretical expectations from quark-antiquark potential models assuming $Q_b = -1/3$. Model 1 : Krasemann and Ono, 1979. Model 2 : Büchmuller, Grunberg and Tye, 1980. Model 3 : Voloshin and Zakharov, 1980. The quoted experimental value is from the compilation of the Particle Data Group, corrected by 7 % for consistency in comparison with potential model calculations, which only include the lowest order Born term (Montanet *et al.*, 1994).

ring. This width is proportional to the square of the charge of the b-quark, (see Fig. 2), and can be quantitatively estimated from heavy quark-antiquark potential models, see Table I (Quigg and Rosner, 1977; Eichten and Gottfried, 1977; Rosner, Quigg, and Thacker, 1978; Krasemann and Ono, 1979; Büchmuller, Grunberg and Tye, 1980; Voloshin and Zakharov, 1980). The charge assignment was subsequently confirmed by measurements of R $= \sigma(e^+e^- \to \text{hadrons}) / \sigma(e^+e^- \to \mu^+\mu^-)$. At lowest order, and ignoring resonance effects, R $= \sum_{quarks} 3Q_q^2$, where the factor of three arises from the fact that quarks come in three colors. The sum is over all quarks that can be produced, i.e. all quarks with mass below one-half the center of mass energy of the e^+e^- system. Above threshold for $b\bar{b}$ production, the value of R was found to increase by $0.36 \pm 0.09 \pm 0.03$ (Rice *et al.*, 1982), in agreement with the expectations of $3Q_b^2$=1/3. The pole mass of the b-quark is estimated to be in the range 4.5 - 4.9 GeV/c^2 from knowledge of the Υ and b-meson masses (Montanet *et al.*, 1994).

The weak isospin of the b-quark was first extracted from the forward-backward asymmetry (A_{FB}) in $e^+e^- \to b\bar{b}$. This asymmetry is defined in terms of the b-quark production cross section $\sigma(b)$ as

$$A_{FB} = \frac{\sigma(b, \theta > 90^o) - \sigma(b, \theta < 90^o)}{\sigma(b, \theta > 90^o) + \sigma(b, \theta < 90^o)}$$

where θ is the polar angle of the b-quark in the e^+e^- center of mass as measured from the direction of flight of the e^-. The asymmetry originates from the coupling of the Z to fermions, which in the Standard Model depends on the weak isospin through a term in the lagrangian of the form $\bar{f}\gamma_\mu(g_V - g_A\gamma_5)Z^\mu f$, where the vector and axial couplings g_V and g_a are given by

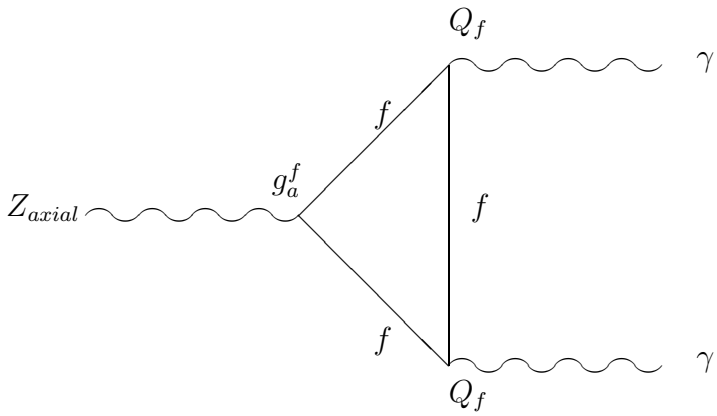

FIG. 3. An example of a fermion triangle diagram which could cause an anomaly; g_a^f is the fermion axial coupling to the Z, and Q_f is the fermion charge.

$$g_V = \frac{I_3 - 2Q\sin^2\theta_W}{2\sin\theta_W\cos\theta_W}$$
$$g_A = \frac{I_3}{2\sin\theta_W\cos\theta_W}$$

and θ_W is the Weinberg angle. The first measurement of A_{FB} was performed in the mid-eighties ($A_{FB} = -22.8 \pm 6.0 \pm 2.5\%$ at $\sqrt{s} = 34.6$ GeV; Bartel *et al.*, 1984), and was found to be consistent with the Standard Model prediction ($A_{FB} = -25\%$) assuming $I_3 = -1/2$ for the weak isospin of the b-quark. Alternative isospin assignments (e.g. I=0) for the bottom-quark were also found to be inconsistent with the observed suppression of flavor-changing neutral current decays of b-mesons. If the b-quark formed a weak-isospin singlet, and if there were only five quarks (u, d, c, s, b), then it can be shown that $BR(B \to Xl^+l^-) \geq 0.12$ $BR(B \to Xl\nu) \approx 0.026$ (Kane and Peskin, 1982). This was soon found to be inconsistent with the first upper limits placed on flavor changing neutral currents in b-decays, $BR(B \to Xl^+l^-) < 0.008$ at 90% C.L. (Matteuzzi *et al.*, 1983).

The $I_3 = -1/2$ isospin of the bottom quark implies the existence of an additional quark, the top quark, as the third-generation weak isospin partner of the bottom quark. Furthermore, the existence of such a third generation quark doublet, in conjunction with the presence of three lepton generations, ensures the necessary cancellations in diagrams contributing to triangle anomalies. For the electro-weak theory to be renormalizable, the sum over fermions for diagrams such as the one displayed in Fig. 3 should vanish (see for example Leader and Pedrazzi, 1982). The contributions to this diagram for each fermion in the theory is proportional to $N_c g_a^f Q_f^2$, where the factor $N_c = 3$ is the number of colors and applies to quarks only. Hence, the contribution from a lepton isodoublet exactly cancels that of a quark isodoublet. With three lepton generations, the existence of a third quark isodoublet, whose members are the top and bottom quarks, results in the desired cancellation of triangle anomalies.

Measurements of the Z width at the LEP and SLC colliders rule out the existence of a 4th generation neutrino with mass $M_\nu \lesssim M_Z/2$ (Montanet *et al.*, 1994). Unless the 4th generation neutrino is very massive, no additional generations are allowed in the context of the Standard Model. The top quark is therefore the last fermion expected in the Standard Model. Only the Higgs boson is left to be discovered in order to complete the particle and

field content of the minimal Standard Model.

While the Standard Model predicts the charge and weak isospin of the top quark ($Q = 2/3$, and $I_3 = 1/2$), its mass remains a free parameter. As we will discuss in Section IX, the recent top mass measurements yield $M_{top} = 175 \pm 8$ GeV/c^2, a factor of 40 higher than the mass of the second heaviest fundamental fermion (the b-quark). The reason for such a high mass for the top quark is a mystery of the Standard Model. It does however occur quite naturally in local supersymmetric theories where the electro-weak symmetry is broken through radiative corrections (Ibanez and Lopez, 1983; J. Ellis *et al.*, 1983; Alvarez-Gaume, Polchinski, and Wise, 1983).

The value of the top mass enters in the calculation of radiative corrections to a large number of electro-weak observables. As we will discuss in Section III, the level of precision achieved in these measurements is good enough that a comparison between the measured top mass and the calculation of electro-weak radiative corrections provides a stringent test of electro-weak theory and is sensitive to physics beyond the Standard Model.

III. TOP MASS AND PRECISION ELECTRO-WEAK MEASUREMENTS

Over the past few years, a number of very precise measurements at e^+e^- colliders have been performed using large samples of Z events. At CERN the four LEP experiments (Aleph, Delphi, L3, and Opal) have collected of order two million Z events each, and at the SLC collider at SLAC the SLD experiment has collected a data sample of order one hundred thousand events. Although the SLAC data sample is considerably smaller than the LEP data sample, it was possible to polarize the beams at the SLC and this lead to a competitive measurement of the Weinberg angle. The level of accuracy of the LEP and SLC measurements, as well as of measurements of the W-boson mass at the Tevatron, is now such that the data are not well described by tree-level theoretical calculations and radiative corrections must be included.

If we assume that the Standard Model can be used to correctly calculate higher order electro-weak processes, we can infer the top quark mass by comparing these calculations to precise measurements (Altarelli, Kleiss, and Verzegnassi, 1989). We can then check whether this value is consistent with the directly measured top quark mass. The free parameters in the model are the weak coupling constant G_{Fermi}, the electromagnetic coupling constant α, the Weinberg angle, θ_W, the mass of the Higgs boson, M_{Higgs}, the strong coupling constant α_s, the masses of the six quarks, the masses of the six leptons, and the four quark mixing parameters which determine the CKM matrix.

At lowest order the masses of the weak intermediate vector bosons can be determined completely from the first three of these parameters, G_{Fermi}, α, and θ_W. The best measured Standard Model parameters are α, G_{Fermi} and M_Z. Using these three parameters we can, at lowest order predict several measurable quantites. However, when higher order corrections are considered, the fermions and Higgs masses enter into the calculations. The top mass plays a particularly large role in these radiative corrections due to the large mass difference beween the top quark and its weak isospin partner, the bottom quark. The dependence of these radiative corrections on the top quark mass contains terms quadratic in M_{top} of the form M_{top}^2/M_Z^2, whereas the Higgs mass dependence is logarithmic ($\ln(M_{Higgs}/M_Z)$). Fig. 4

shows two higher order diagrams involving top quark and Higgs radiative corrections which modify observables at the Z resonance.

A. Neutral current experiment measurments

At LEP and SLC, the line shape and asymmetries at the Z have been precisely measured and can be compared with theoretical prediction. The uncertainties on most of these quantities are smaller from the LEP measurements due to the size of the LEP data samples. These quantities are:

- The total width of the Z, Γ_Z.
- The value of the hadronic cross section at the Z peak, $\sigma^0_{had} \equiv \frac{12\pi}{m_Z^2}\frac{\Gamma_{ee}\Gamma_{had}}{\Gamma_Z^2}$.
- The ratio of the hadronic to leptonic widths, $R_l \equiv \Gamma_{had}/\Gamma_{ll}$.
- The forward-backward asymmetry in $Z \to ll$ decays, $A^{0,l}_{FB} \equiv \frac{3}{4}A_e A_f$ where $A_f \equiv \frac{2g_{Vf}g_{Af}}{g^2_{Vf}+g^2_{Af}}$, and the leptons ($l$) include e, μ and τ.
- A_τ as defined above. This is obtained from measurements of the τ polarization defined as $P_\tau \equiv \frac{\sigma_R-\sigma_L}{\sigma_R+\sigma_L}$ where σ_R and σ_L are the τ pair cross sections for the production of right and left-handed τ's respectively.
- A_e, as defined above, i.e. $A_e \equiv \frac{2g_{Ve}g_{Ae}}{g^2_{Ve}+g^2_{Ae}}$.
- The forward-backward asymmetry for decays, $Z \to b\overline{b}$ and $Z \to c\overline{c}$, at the Z pole mass, $A^{0,b}_{FB}$ and $A^{0,c}_{FB}$.
- The value of $\sin^2\theta^{lept}_{eff} \equiv \frac{1}{4}(1-\frac{g_{Vl}}{g_{Al}})$ from the hadronic charge asymmetry, $< Q_{FB} >$ which is the forward-backward asymmetry measured from $Z \to q\overline{q}$ decays. The charge of the outgoing quark is determined using a statistical weighting method.
- The ratios $R_b \equiv \frac{\Gamma_Z^{b\overline{b}}}{\Gamma_Z^{hadrons}}$ and $R_c \equiv \frac{\Gamma_Z^{c\overline{c}}}{\Gamma_Z^{hadrons}}$.
- The left-right asymmetry, $\mathrm{A}_{LR} \equiv (\sigma_L - \sigma_R)/(\sigma_L + \sigma_R)$, where σ_L and σ_R are the production cross sections for Z bosons at the Z pole energy with left-handed and right-handed electrons respectively. This measurement has been performed only at the SLC, since the beams are unpolarized at LEP.

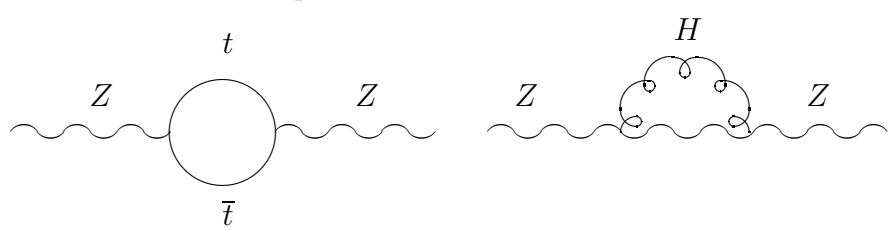

FIG. 4. Examples of radiative corrections to the Z mass involving top quarks or Higgs boson loops.

In Fig. 5 and Fig. 6 we show the measurements of the variables listed above at LEP (The LEP Collaborations, 1995), compared with Standard Model expectations as a function of the top quark mass. The vertical bands are the measurements, where the width of the bands include one standard deviation uncertainties. The cross-hatched bands show the theoretical predictions taking into account the uncertainty on the Higgs mass (the inner bands) and the uncertainty on the value of the strong coupling constant α_s (the outer bands). In calculating the theoretical uncertainties, the Higgs mass is varied from 60 to 1000 GeV/c^2 and α_s is varied within the interval $\alpha_s(M_z^2) = 0.123 \pm 0.006$ (Bethke, 1995). The dependence of the Z width measurements on α_s enters through radiative diagrams involving gluons, an example of which is shown in Fig. 7. The LEP measurements are consistent with theoretical predictions, except for the ratios R_b and R_c, which will be discussed in Section III.A.2.

1. Asymmetries at the Z

The asymmetries measured at LEP, $A_{FB}^{0,l}$, A_τ, A_e, $A_{FB}^{0,b}$, $A_{FB}^{0,c}$ and $< Q_{FB} >$ are effectively measurements of $\sin^2\theta_{eff}^{lept}$. Despite the lower statistics SLC Z sample, the A_{LR} measurement from SLD provides a competitive measurement of $\sin^2\theta_{eff}^{lept}$. $\sin^2\theta_{eff}^{lept}$ has also been measured in νN experiments at lower center of mass energies (Abramowicz *et al.*, 1986; Blondel *et al.*, 1990; Allaby *et al.*, 1986 and 1987; Arroyo *et al.*, 1994). All of these measurements of $\sin^2\theta_{eff}^{lept}$ are found to be consistent within their respective uncertainties and are combined. The combined result from LEP is $\sin^2\theta_{eff}^{lept} = 0.23186 \pm 0.00034$, while the corresponding result from the SLD A_{LR} measurement is $\sin^2\theta_{eff}^{lept} = 0.23049 \pm 0.00050$ (Woods, 1996). Figure 8 summarizes all the measurements of $\sin^2\theta_{eff}^{lept}$.

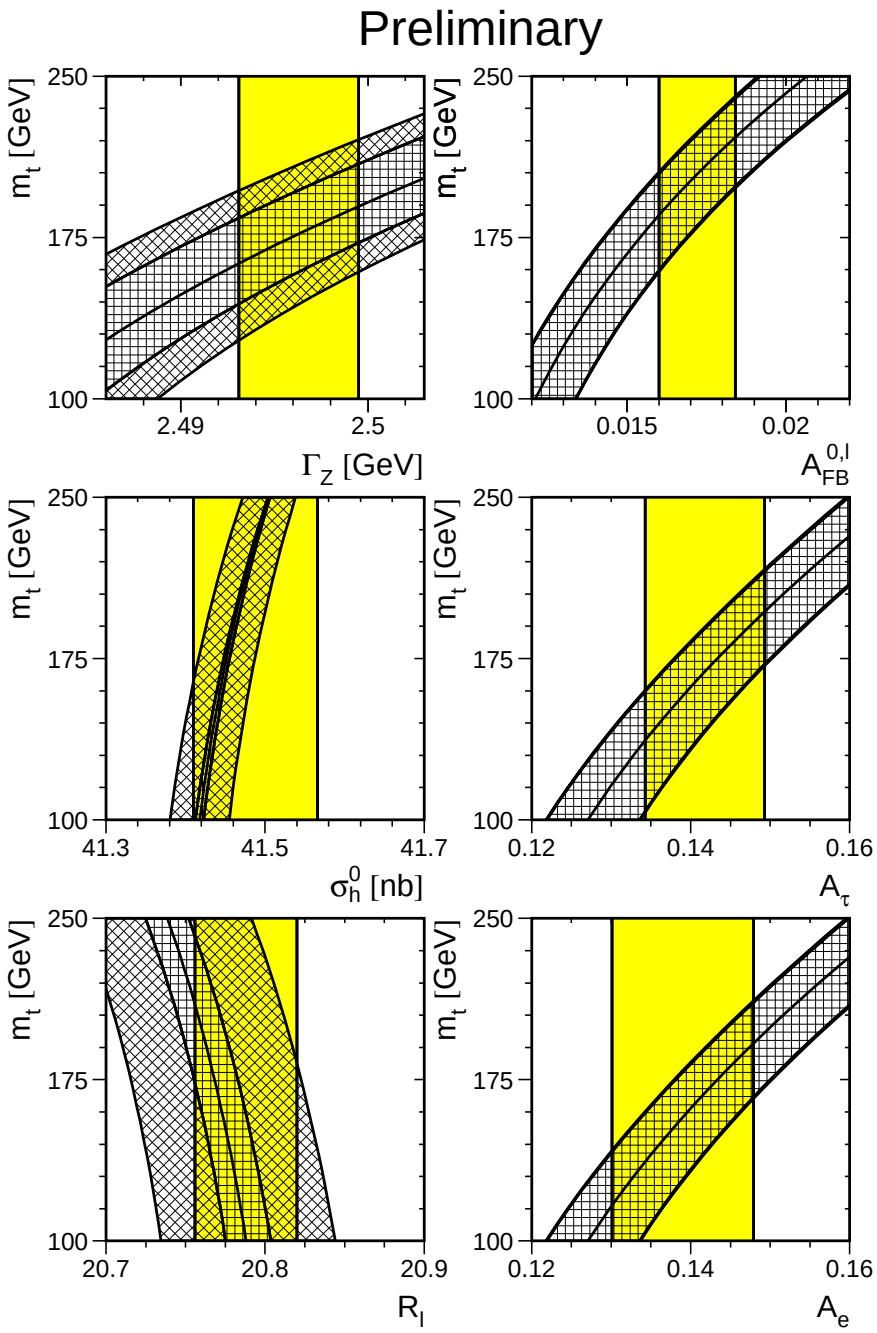

FIG. 5. Comparison of LEP measurements with Standard Model predictions as a function of M_{top}. The experimental errors on the parameters are indicated as vertical bands. The cross-hatch pattern parallel to the axes indicates the variation of the Standard Model prediction with M_{Higgs} spanning the interval $60 \leq M_{Higgs} \leq 1000$ GeV/c^2, and the diagonal cross-hatch pattern corresponds to a variation of $\alpha_s(M_Z^2)$ within the interval $\alpha_s(M_Z^2) = 0.123 \pm 0.006$. The total width of the band corresponds to the linear sum of both uncertainties (The LEP Collaborations, 1995).

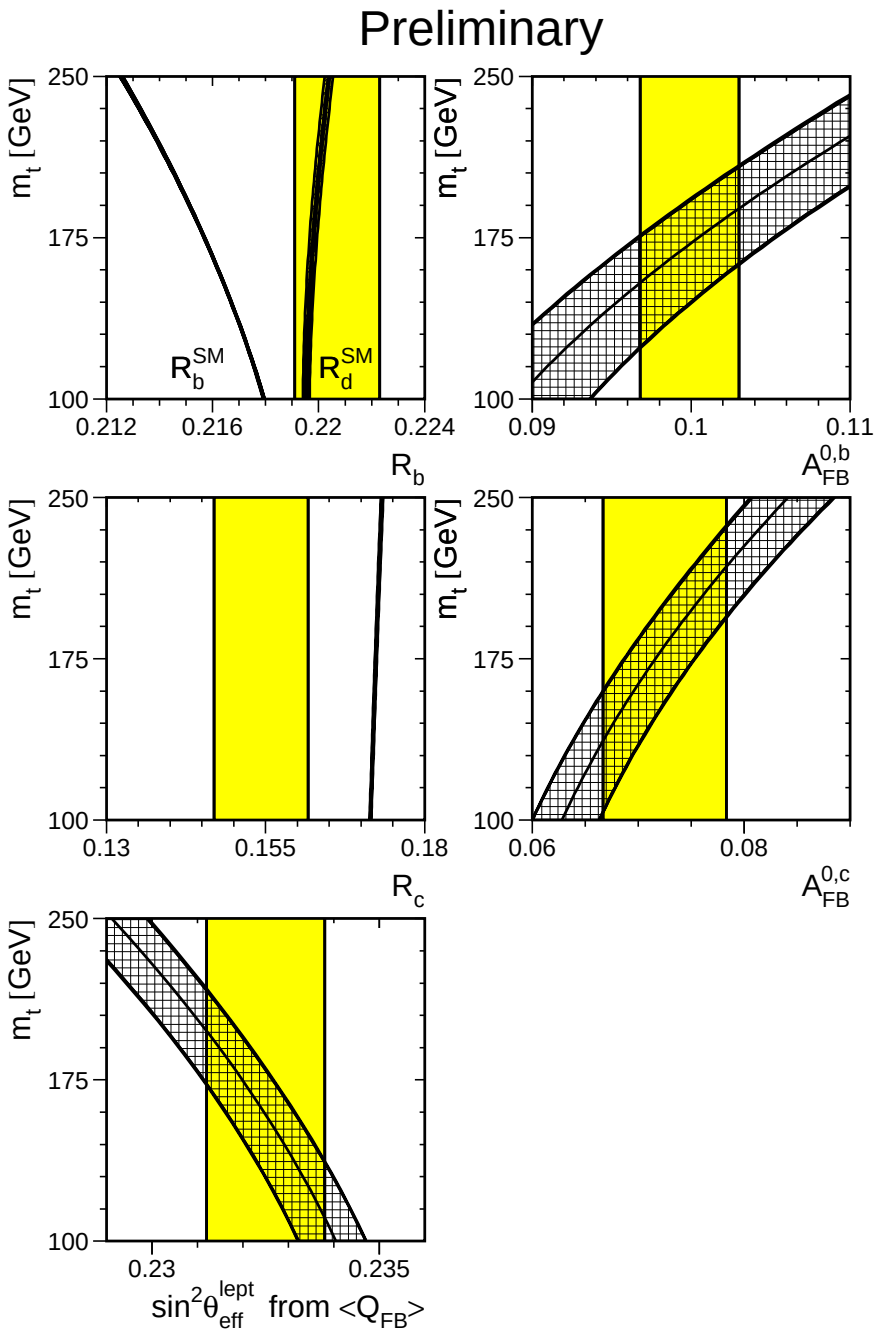

FIG. 6. Comparison of LEP measurements with Standard Model predictions as a function of M_{top} as in the previous figure. For the ratios of the partial widths the variations with M_{Higgs} and $\alpha_s(M_Z^2)$ nearly cancel. For the comparison of R_b with the Standard Model the value R_c has been fixed to its Standard Model prediction. To illustrate the impact of special vertex corrections to R_b, the Standard Model prediction for R_d is also shown (The LEP Collaborations, 1995).

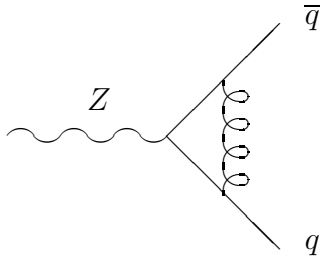

FIG. 7. One Feyman diagram illustrating a QCD correction to the Z width.

2. R_b

The decay of the Z into $b\overline{b}$ is of particular interest, because it is sensitive through weak vertex corrections to the top quark mass, (see Fig. 9). The dependence of all the Z partial widths on the Higgs mass is due mostly to corrections to the Z propagator. Therefore, in R_b, the ratio of $\Gamma_Z^{b\overline{b}}$ to $\Gamma_Z^{hadrons}$, most of the Higgs and α_s dependence cancels. This ratio then gives the only indirect measurement of the top mass independent of the Higgs mass. A comparison between the experimental measurement and the theoretical prediction is a particularly good test of the Standard Model and possibly the first place to look for new (non-Standard Model) physics.

The value of R_b from the combinations of many measurements at LEP and SLC is higher than expected, whereas the value of R_c is lower than expected. The measurement of R_b depends on what is assumed for R_c because charm quarks are a background to the bottom quark signal in the data. Because the two are correlated, R_b is quoted either assuming a Standard Model value for R_c, or the measured value. In Fig. 10 we show the LEP measurements of R_c vs. R_b, together with the Standard Model theoretical prediction based on the direct measurement of the top quark mass performed at the Tevatron (see Section IX). The disagreement between data and theory may be an indication of new physics beyond the Standard Model (see for example Altarelli *et al.* 1996; Wells and Kane, 1995).

B. W mass

The W vector boson mass (M_W) also depends on the top quark and Higgs masses through loop diagrams like those shown in Fig. 11, in which $W \to t\overline{b} \to$W, or $W \to WH \to W$. A precise measurement of M_W constrains the top mass for a fixed Higgs mass. When combined with a precise measurement of the top mass, such a measurement can provide information on the Higgs mass, or, in the case of disagreement with theory, can signal the presence of new physics. Even with precise direct measurements of M_{top} and M_W, however, the constraints on M_{Higgs} are weak, because the Higgs mass dependence is only logarithmic. The present status of the W and top mass measurements, and their comparison with theory, is summarized in Fig. 12.

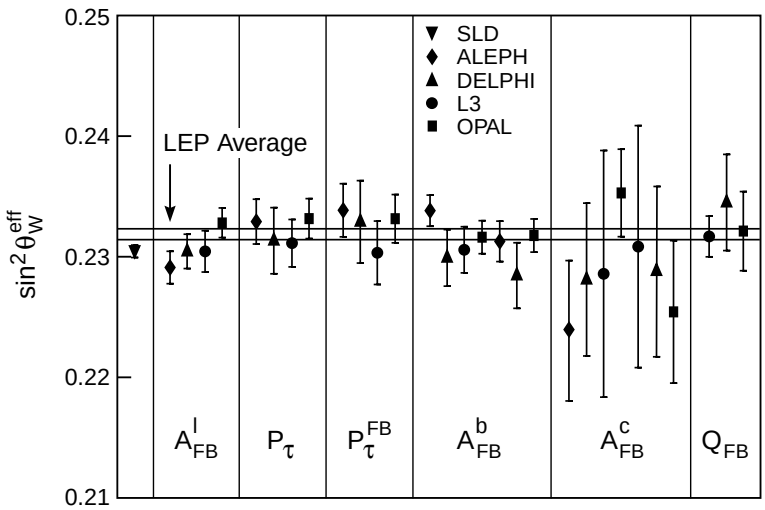

FIG. 8. A summary of the measurements of $\sin^2\theta_{eff}^{lept}$ from LEP and SLC. The leftmost point is the value from A_{LR} at SLD; $\sin^2\theta_{eff}^{lept} = 0.2305 \pm 0.0005$. The LEP average is $\sin^2\theta_{eff}^{lept} = 0.2319 \pm 0.0004$. (Woods, 1996).

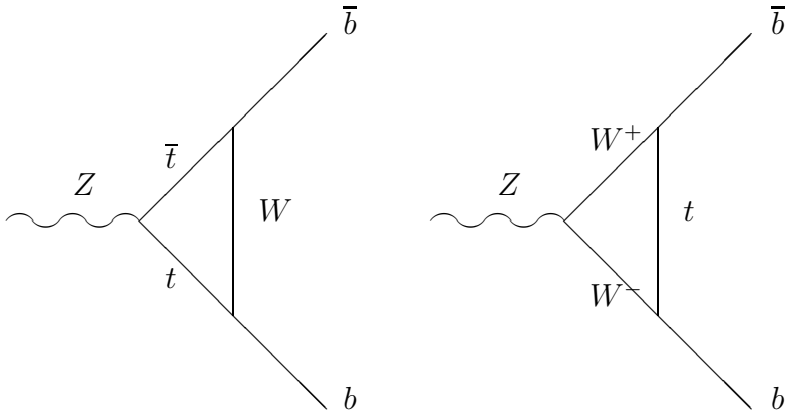

FIG. 9. Diagrams showing t-quark corrections to $Z \to b\overline{b}$.

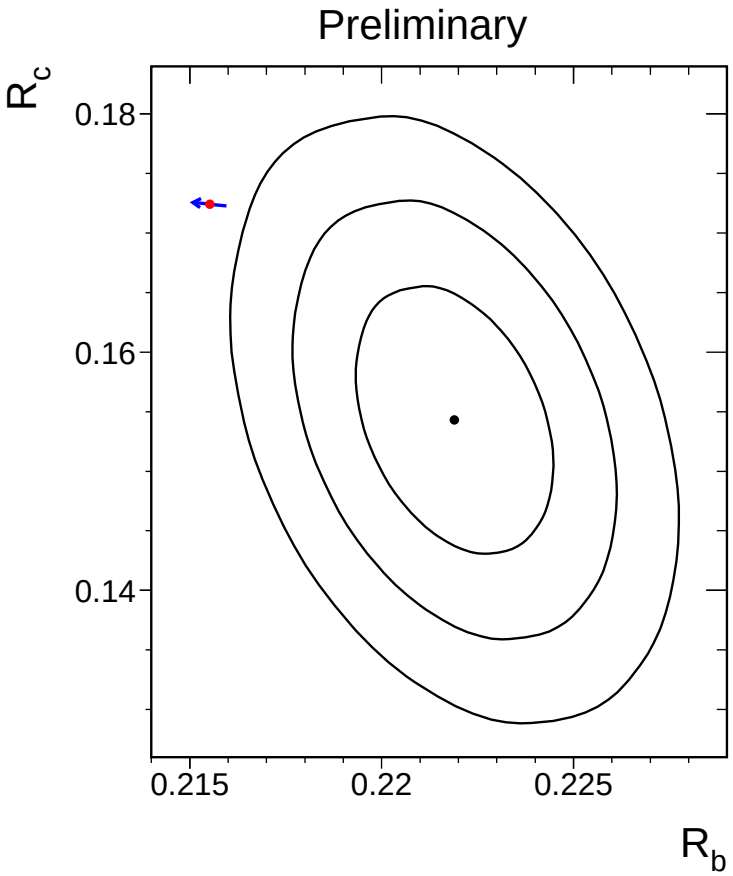

FIG. 10. Contours in the R_b - R_c plane derived from LEP data, corresponding to 68%, 95% and 99.7% confidence levels assuming Gaussian systematic errors. The Standard Model prediction for $M_{top} = 180 \pm 12$ GeV/c^2 is also shown as a dot with an arrow through it. (This is the average of the 1995 CDF and D0 top mass measurements; the current average is 175 ± 8 GeV/c^2). The arrow points in the direction of increasing values of M_{top} (The LEP Collaborations, 1995).

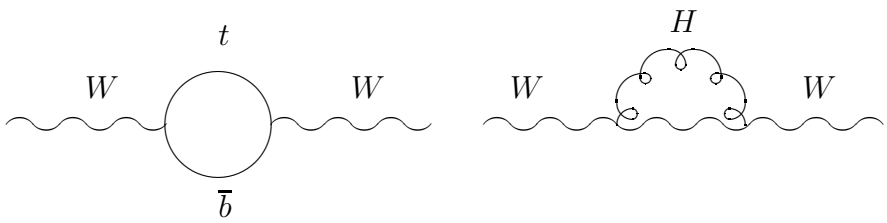

FIG. 11. Lowest order radiative corrections to the W mass involving top and bottom quarks and the Higgs.

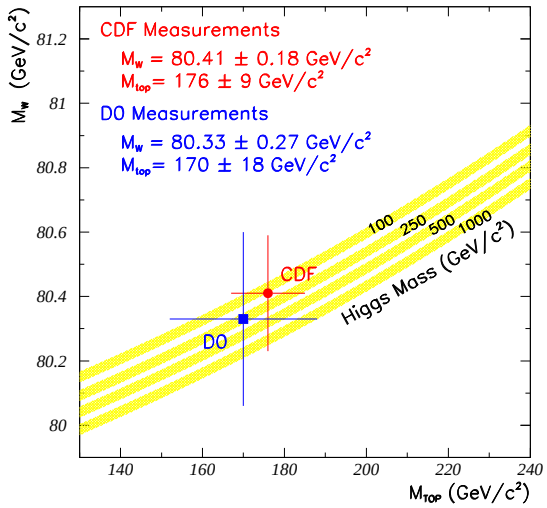

FIG. 12. W mass and top quark mass measurements from the Fermilab collider experiments (CDF and D0). The top mass values are from the full Tevatron data sets, with an integrated luminosity of $\approx$ 100 pb^{-1}. The W mass values are derived from analyses of the first 15-20 pb^{-1} only. The lines are Standard Model predictions for four different Higgs masses (Flattum,1996).

C. Global fits for M_{top} and M_{Higgs}

Combining the indirect information from the neutral current experiments and the W mass measurement, a global fit for M_{top} has been made by the LEP Electro-Weak Working Group (The LEP Collaborations, 1995). The fits are made with α_s and M_{top} as free parameters, since α_s at the Z mass has a large uncertainty. The best predicted value for M_{top} using data from LEP, SLC, the Fermilab collider W mass measurements and ν N scattering data, is $M_{top} = 178 \pm 8^{+17}_{-20}$ GeV/c^2, with $\alpha_s = 0.123 \pm 0.004 \pm 0.002$ and with $\chi^2/d.o.f. = 28/14$ (where we have chosen $M_{Higgs} = 300$ GeV/c^2 to quote the goodness of fit). The second uncertainty in this fit to the top mass comes from varying M_{Higgs} from 60 GeV/c^2 to 1 TeV/c^2. The fit results are in good agreement with the directly measured values of α_s and M_{top}, $\alpha_s(M_Z) = 0.123 \pm 0.006$ (Bethke, 1995) and $M_{top} = 175 \pm 8$ GeV/c^2, see Section IX. The variation of the fit-χ^2 as a function of M_{top} for three different choices of M_{Higgs} is displayed in Fig. 13.

In conclusion, all the neutral current data, as well as the W and top mass measurements are in agreement with each other, with the exception of the measurement of R_b. The situation is nicely summarized in Fig. 14. In this figure, the correlation between R_l and R_b is due

to the fact that R_l depends on the total hadronic width, and hence on $\Gamma(Z \to b\bar{b})$. Given the measured value of R_l and α_s, and assuming Standard Model dependence of the partial widths on $\sin^2\theta_{eff}^{lept}$ for all but the b-quarks, R_l constrains R_b and $\sin^2\theta_{eff}^{lept}$. These three measurements are compared with the Standard Model prediction given the measured top mass. The measured values of R_b and R_c are somewhat inconsistent with the combination of $\sin^2\theta_{eff}^{lept}$, R_l and M_{top} within the context of the Standard Model.

Despite the large number of very precise measurements, there is still little information on the mass of the Higgs boson, although the data seems to prefer a low value for M_{Higgs}, (see Fig. 13). An estimate for the Higgs mass can be made using all the neutral current and hadron collider data as shown in Fig. 15. The best estimate of the Higgs mass is shown with and without the R_b and R_c measurements included. In all cases a Higgs mass less than 300 GeV/c^2 is favored with large uncertainty.

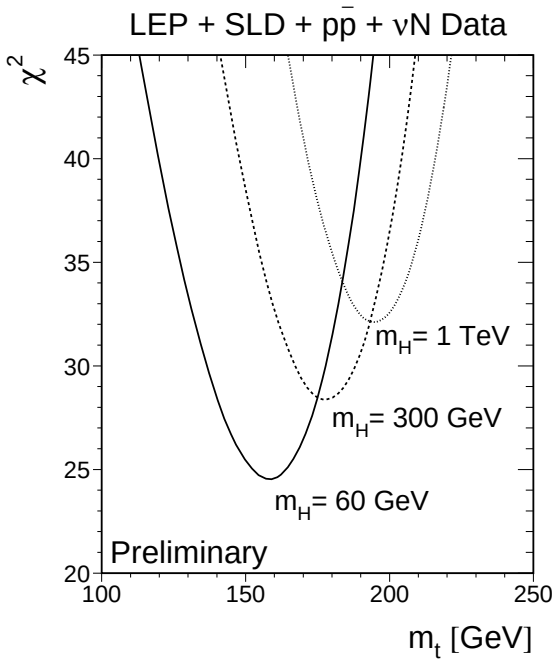

FIG. 13. The χ^2 curves for the Standard Model fit to the electro-weak precision measurements from LEP, SLD, CDF and D0 (W mass only) and neutrino scattering experiments as a function of M_{top} for three different Higgs mass values spanning the interval 60 GeV/c^2 $\leq M_{Higgs} \leq$ 1000 GeV/c^2. The number of degrees of freedom is 14 (The LEP Collaborations, 1995).

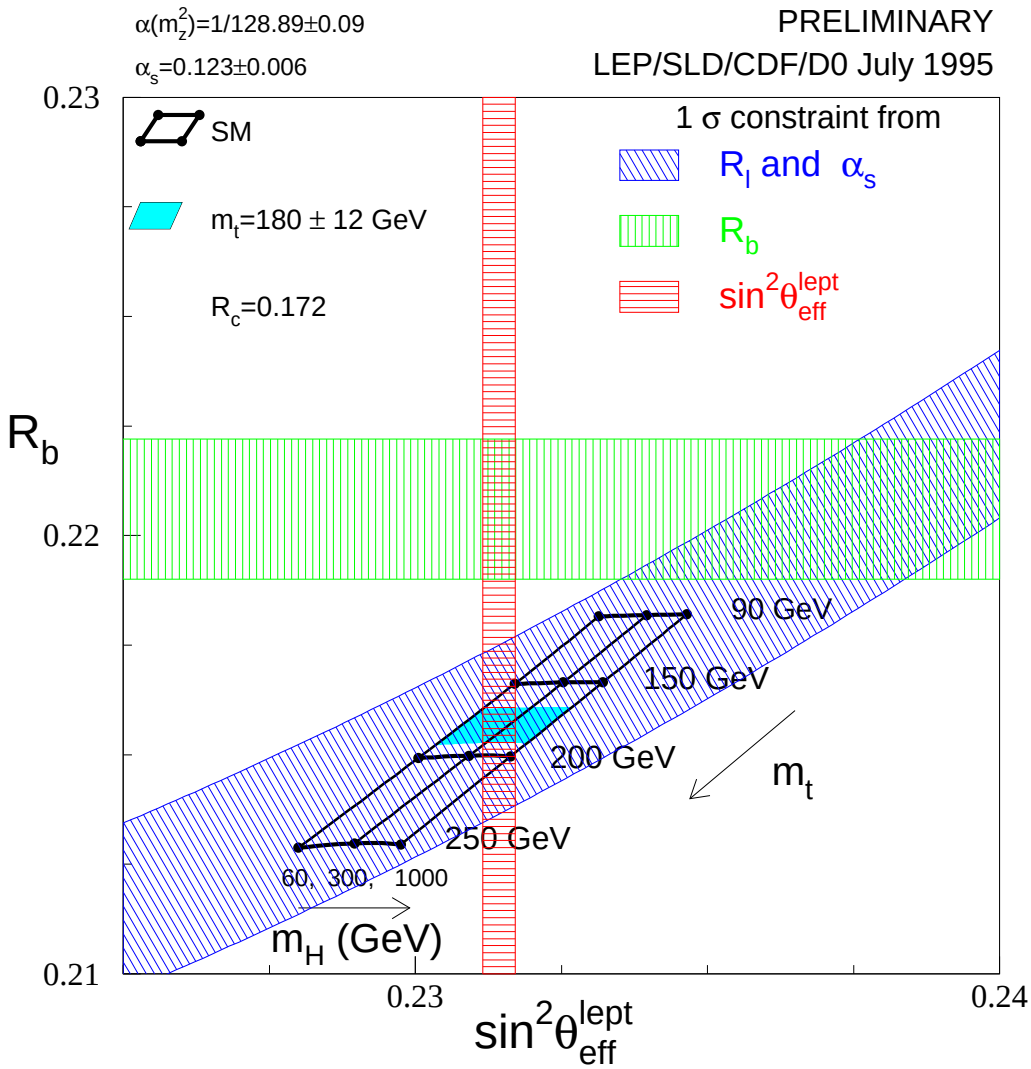

FIG. 14. The combined LEP/SLD measurements of $\sin^2\theta_{eff}^{lept}$ and R_b assuming the Standard Model value of $R_c = 0.172$ and the Standard Model prediction. Also shown is the constraint resulting from the measurement of R_l on these variables, assuming $\alpha_s(M_Z^2) = 0.123 \pm 0.006$, as well as the Standard Model dependence of light-quark partial widths on $\sin^2\theta_{eff}^{lept}$ (The LEP Collaborations, 1995).

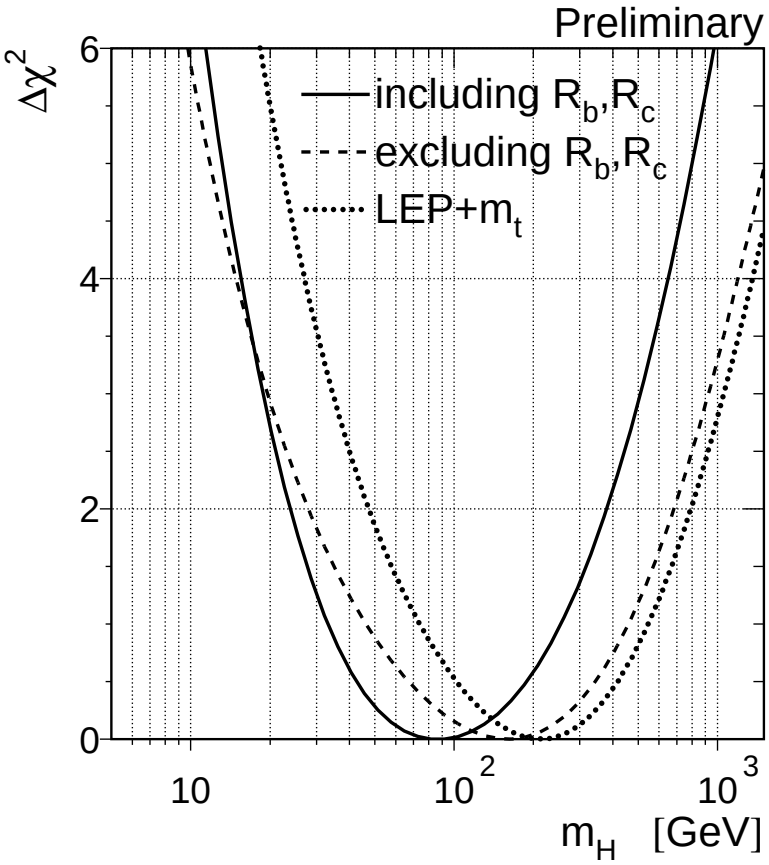

FIG. 15. $\Delta\chi^2 = \chi^2 - \chi^2_{min}$ vs M_{Higgs} curves. The continuous line uses all the data from neutral currents and $p\overline{p}$. The dashed line excludes the LEP and SLD R_b and R_c measurements. The dotted line excludes the SLD data (The LEP Collaborations, 1995).

IV. TOP QUARK PRODUCTION

Because of its large mass, the top quark can only be observed directly in collider experiments, where sufficiently high center-of-mass energies ($\sqrt{s}$) have been achieved. In electron-positron collisions, top quarks are produced in pairs via a photon or a Z. Since at lowest order this is a purely electro-weak process, the cross section and production kinematics can be precisely predicted. Today's highest energies e^+e^- accelerators, LEP at CERN and SLC at SLAC, operate at $\sqrt{s} \approx \mathrm{M}_z \approx 91$ GeV, and therefore the mass region $\mathrm{M}_{top} > 46$ GeV/c^2 cannot be explored. Searches for top in e^+e^- collisions will be briefly reviewed in Section VI. The HERA electron-proton collider at DESY has achieved a center-of-mass energy of ≈ 310 GeV. However the top production cross section at HERA is too small for observation and study of the top quark.

Significantly higher center-of-mass energies have been achieved at hadron colliders. The $p\bar{p}$ collider at CERN (the S$p\bar{p}$S), which operated between 1981 and 1989, reached $\sqrt{s} =$ 630 GeV; the $p\bar{p}$ collider at Fermilab (the Tevatron) came on line in 1987 with $\sqrt{s} = 1800$ GeV = 1.8 TeV; a new pp collider (LHC, $\sqrt{s} = 14$ TeV) is under development at CERN, and is expected to begin operation in 2003. Until a very high energy e^+e^- machine is built, top quark physics can be directly pursued only at hadron colliders. In this Section we will concentrate on the production of top quarks in $p\bar{p}$ collisions. Top quarks are produced by colliding partons (quarks, gluons, and antiquarks) from the proton and anti-proton. Therefore many aspects of our discussion also apply to other (e.g. pp) hadron-hadron collisions. Because the partons carry only a fraction of the momentum of the hadron, the center-of-mass energies of parton-parton collisions span a wide range of energies, see the discussion of parton luminosities in Section IV.A.

A. Production mechanisms and cross sections

There are three mechanisms for top production in $p\bar{p}$ collisions :

- Pair production of top quarks, $p\bar{p} \to t\bar{t}$ + X. The leading order Feynman diagrams for this process are shown in Fig. 16. At higher order, gluon-quark scattering also contributes. $t\bar{t}$ pairs can also be produced through a Z or a photon, however the cross section is much smaller and we will not consider this possibility further.

- Drell-Yan production of a W boson, with subsequent decay into $t\bar{b}$, i.e. $p\bar{p} \to$W + X; $W \to t\bar{b}$, (see Fig. 17). Except for small contributions from off mass-shell W boson production, this mechanism only contributes for top masses smaller than $\mathrm{M}_W - \mathrm{M}_b$.

- Single top-quark production via W-gluon fusion, see Fig 18. Photon-gluon and Z-gluon fusion are also allowed, with a much lower cross section.

As will be illustrated in this Section, at Fermilab's Tevatron the strong-interaction pair production process ($p\bar{p} \to t\bar{t}$) is dominant over a wide range of top masses. For $\mathrm{M}_{top} \approx 60$ GeV/c^2, the top production rate from $W \to t\bar{b}$ is comparable to that of $t\bar{t}$. For very high top mass, above $\mathrm{M}_{top} \approx 220$ GeV/c^2, the expected cross section for single top production

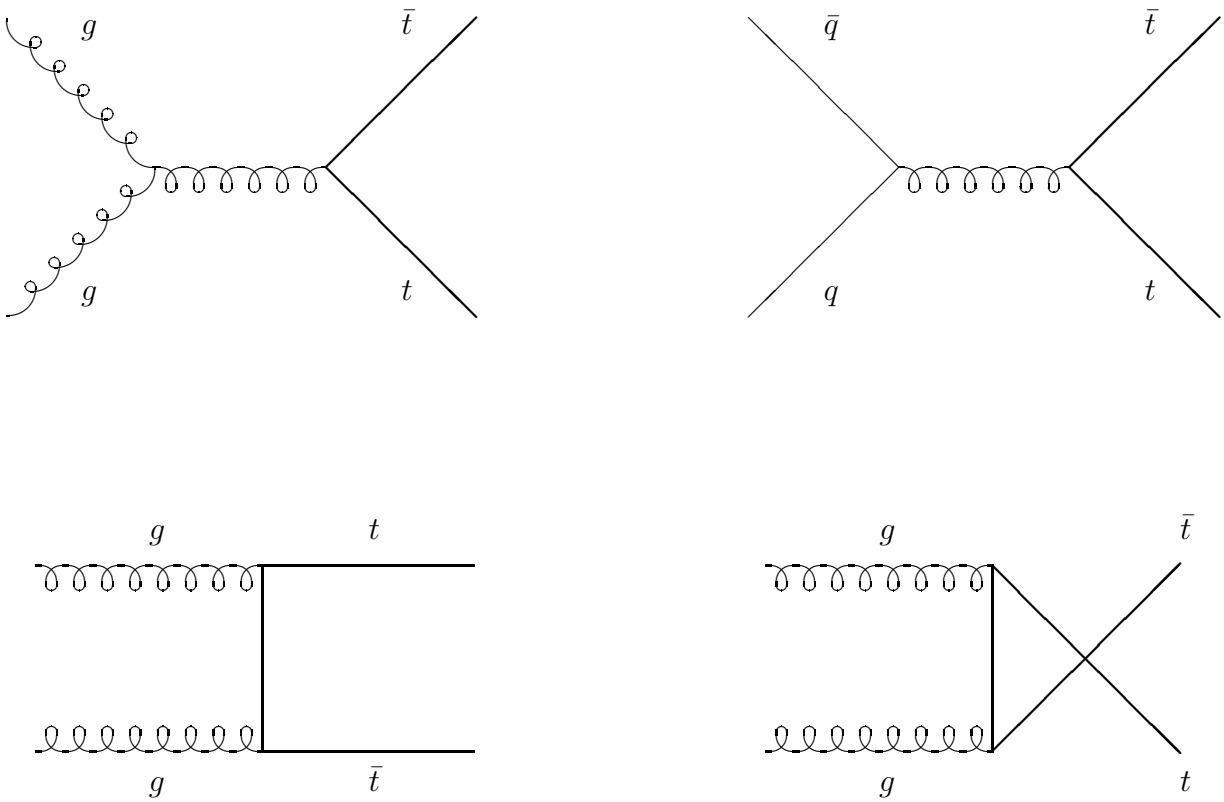

FIG. 16. Lowest order Feynman diagrams for production of $t\bar{t}$ pairs in $p\bar{p}$ collisions.

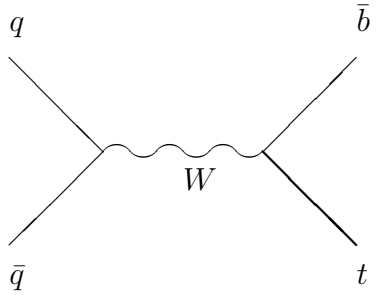

FIG. 17. Lowest order Feynman diagram for Drell-Yan production of $t\bar{b}$ pairs, $p\bar{p} \to W \to t\bar{b}$.

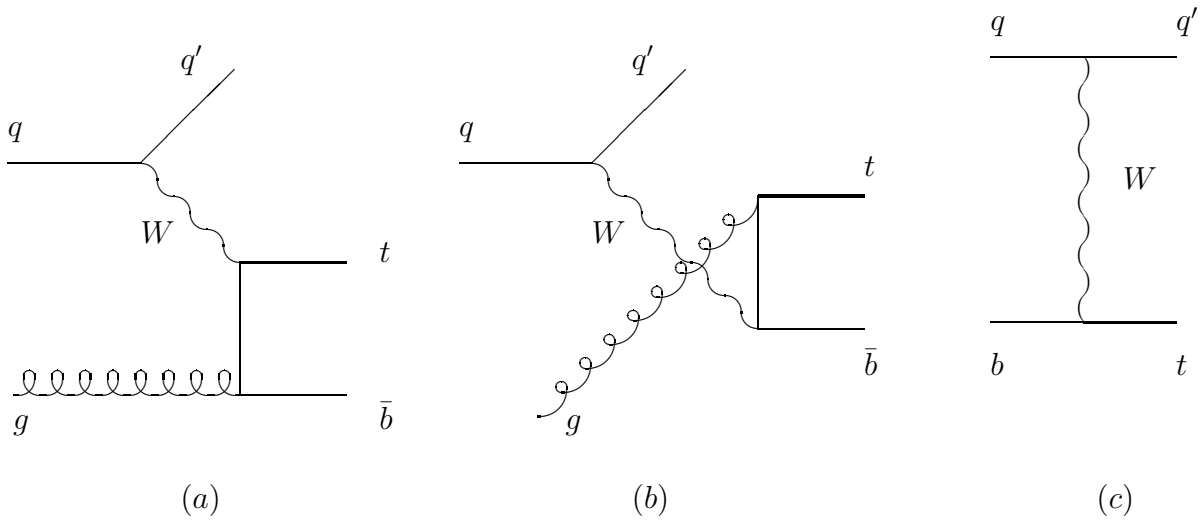

FIG. 18. Lowest order Feynman diagrams for production of a single top quark via W-gluon fusion in $p\bar{p}$ collisions. When combining diagrams (a) and (c), care must be exercised to avoid double counting and to define the b-quark distribution inside the proton in a consistent fashion (Heinson, Belyaev, and Boos, 1995; Carlson and Yuan, 1995).

through W-gluon fusion becomes larger than the pair production cross section due to the very high parton center-of-mass energy required to produce a $t\bar{t}$ pair (see discussion below).

The pair production cross section for heavy quarks such as the top can be calculated in perturbative QCD. It factorizes as a product of the parton distribution functions inside the protons and the parton-parton point cross section, and is written as a sum over contributions from partons inside the proton and anti-proton (Collins, Soper, and Sterman, 1986) :

$$\sigma(p\bar{p} \to t\bar{t}) = \sum_{i,j} \int dx_i F_i(x_i, \mu^2) \int dx_j F_j(x_j, \mu^2) \hat{\sigma}_{ij}(\hat{s}, \mu^2, M_{top}).$$

The functions F_i and F_j are the number densities of light partons (quarks, antiquarks, and gluons) evaluated at a scale μ in the proton and anti-proton; x_i and x_j are the momentum fractions of the incoming partons, i.e. parton i (j) has momentum $x_i P$ ($-x_j P$), where P is the magnitude of the proton momentum in the center of mass frame (which in colliding beam experiments coincides with the lab frame); $\hat{\sigma}_{ij}$ is the point cross section for $i + j \to t\bar{t}$ and $\hat{s} = 4x_i x_j P^2 = x_i x_j s$ is the square of the center of mass energy of the parton-parton collision. The factorization and renormalization scale μ is an arbitrary parameter with dimensions of energy, which is introduced in the renormalization procedure. The exact result for the cross section should be independent of the value of μ. However, since calculations are performed to finite order in perturbative QCD, cross-section predictions are in general dependent on the choice of scale, which is usually taken to be of the order of M_{top}. The sensitivity of perturbative calculations to reasonable variations in μ is used to estimate the accuracy of the prediction. Parametrizations of the parton number densities (F_i and F_j) are extracted from fits to a large number of experimental results, mostly from deep inelastic scattering, see for example Fig. 19.

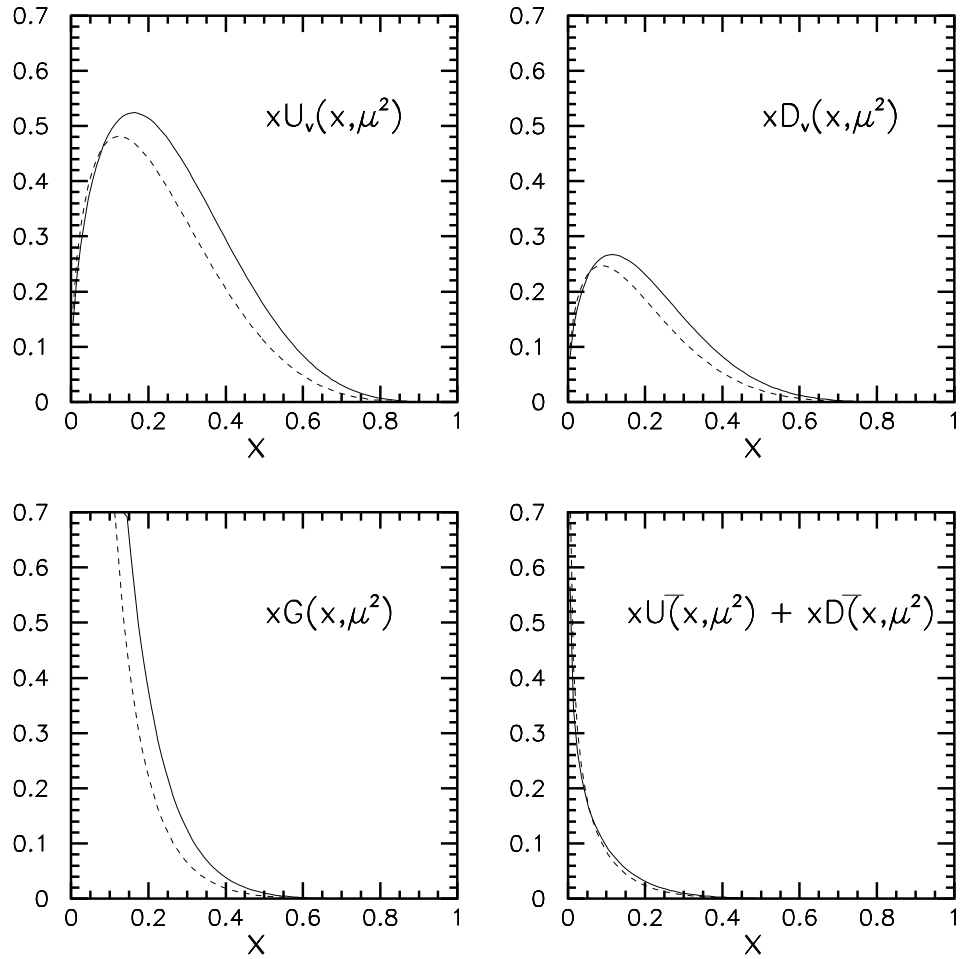

FIG. 19. MT-B2 parametrization (Morfin and Tung, 1991) of xF_i for valence u-quarks, $xU_v(x,\mu^2)$, valence d-quarks, $xD_v(x,\mu^2)$, gluons, $xG(x,\mu^2)$, and sea u- and d-quarks, $x\bar{U}(x,\mu^2) + x\bar{D}(x,\mu^2)$. These are calculated at $\mu^2 = (20\ \mathrm{GeV})^2$ (solid line) and $\mu^2 = (400\ \mathrm{GeV})^2$ (dashed line). The $t\bar{t}$ cross section is usually calculated with $\mu^2 = \mathrm{M}^2_{top}$.

The cross section for $p\bar{p} \to t\bar{t}$ can also be written as (Eichten *et al.*, 1984) :

$$\frac{d\sigma}{d\tau} = \sum_{ij} \frac{dL_{ij}}{d\tau} \hat{\sigma}_{ij}(\hat{s}, \mu^2, M_{top})$$

where $\tau = \hat{s}/s$ and $dL_{ij}/d\tau$ are the differential parton luminosities defined as :

$$\frac{dL_{ij}}{d\tau} = \frac{1}{1+\delta_{ij}} \int_{\tau}^{1} \frac{dx}{x} \; [F_i(x,\mu^2)F_j(\tau/x,\mu^2) + F_j(x,\mu^2)F_i(\tau/x,\mu^2)].$$

The parton luminosities for quark-antiquark and gluon-gluon processes at Tevatron energies are displayed in Fig. 20. The sharp fall-off of these luminosities with increasing $\hat{s}$, as well as the asymptotic $1/\hat{s}$ dependence of $\hat{\sigma}$, result in predictions for the $t\bar{t}$ cross-sections which fall steeply as a function of M_{top}. At $\sqrt{s} = 1.8$ TeV the gg luminosity is larger than the $q\bar{q}$ luminosity up to $\hat{s} \approx (220\ \mathrm{GeV})^2$. As a result, top pair production is dominated by

the $gg \to t\bar{t}$ process up to $M_{top} \approx 90$ GeV/c^2. For higher top quark mass, $q\bar{q}$ initial states are the most important source of $t\bar{t}$ pairs.

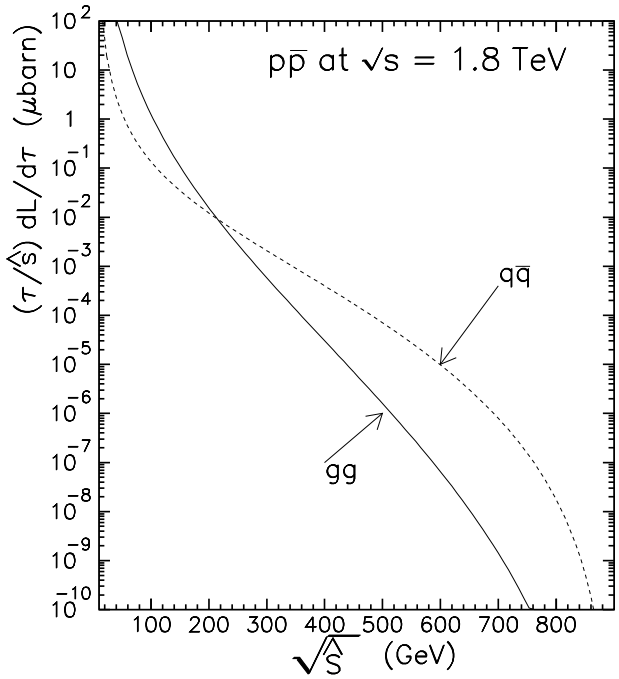

FIG. 20. Gluon-gluon (gg) and quark-antiquark ($q\bar{q} = u\bar{u} + d\bar{d} + s\bar{s}$) parton luminosities in $p\bar{p}$ collisions at $\sqrt{s} = 1.8$ TeV. These are calculated using the MT-B2 parametrization of the parton distribution functions (Morfin and Tung, 1991) evaluated at a scale $\mu^2 = \hat{s}$.

The leading order (LO) cross section for producing a pair of heavy quarks in parton-parton collisions was calculated in the late 1970's (Gluck, Owens, and Reya, 1978; Combridge, 1979; Babcock, Sivers, and Wolfram, 1978; Hagiwara and Yoshino, 1979; Jones and Wyld, 1978; Georgi *et al.*, 1978). The full next-to-leading order (NLO) calculation was performed by Nason, Dawson, and Ellis in 1988, and shortly afterwards by Beenaker *et al.*, 1991. On the basis of their result, cross-section predictions were then made (Altarelli *et al.*, 1988; Ellis, 1991) by convoluting the partonic cross-section with parametrizations of the parton distribution functions.

There are two sources of uncertainty in such a calculation of the $p\bar{p} \to t\bar{t}$ cross-section as a function of M_{top}. As mentioned above, the first uncertainty is due to the nature of the perturbative QCD calculation for the partonic cross-section ($\hat{\sigma}$). The size of the uncertainty is customarily quantified by varying the arbitrary value of the scale μ by a factor of two around the top mass. Note that this is not a rigorous procedure, and it merely results in a *reasonable* estimate of the systematic uncertainty due to the missing higher order terms in the calculation. An additional uncertainty arises from the limited knowledge of the input parton distribution functions, and the assumed value of the QCD parameter Λ_{QCD}. The Λ_{QCD}-dependence arises from the fact that the assumed value of Λ_{QCD} affects the μ^2 evolution of both α_s and the quark and gluon distributions. In particular, the extraction of the gluon distribution from deep inelastic data also depends on Λ_{QCD}. The uncertainty on the cross-section calculation due to the parton distribution uncertainties are

Calculation	Order	$\sigma(t\bar{t})$
(1) Ellis, 1991	NLO	$4.20^{+0.28}_{-0.54}$ pb
(2) Laenen, Smith and van Neerven, 1994	NLO + gluon resummation	$4.94^{+0.71}_{-0.45}$ pb
(3) Berger and Contopanagos, 1995	NLO + gluon resummation	$5.52^{+0.07}_{-0.45}$ pb
(4) Catani *et al.*, 1996	NLO + gluon resummation	$4.75^{+0.63}_{-0.68}$ pb

TABLE II. Calculations of the $p\bar{p} \rightarrow t\bar{t}$ cross-sections at Tevatron energies for $M_{top} = 175$ GeV/c^2. Note that these cross-section calculations use different sets of parton distribution functions (PDFs). The systematic uncertainties in (2) and (3) do not include the effects of varying the input PDFs.

very hard to quantify. This uncertainty is usually estimated by studying the variations of the calculated cross-section using different parametrizations for the parton distribution functions and different values of Λ_{QCD}. As a result of these studies, the total theoretical uncertainty on the $t\bar{t}$ production cross-section at $\sqrt{s} = 1.8$ TeV is estimated to be of order $\pm$ 20%. The uncertainties due to the choice of scale and to the parton distribution assumptions are found to contribute approximately the same amount to the total uncertainty.

The next-to-leading-order, $O(\alpha_s^3)$, predictions for the pair production cross-section have been subsequently refined by Laenen, Smith, and van Neerven (1992 and 1994). In their calculation the corrections due to initial state gluon brehmstrahlung, which are large near $t\bar{t}$ threshold, have been resummed to all orders in perturbative QCD, and have been included in the computation. This procedure introduces a new scale $\mu_0 >> \Lambda_{QCD}$, where the resummation is terminated since the calculation diverges as $\mu_0 \rightarrow 0$, where nonperturbative effects are expected to dominate. Given that the corrections due to soft gluons have been shown to be positive at all orders in perturbative QCD for $\mu = M_{top}$, they estimate the lower limit on the $t\bar{t}$ cross-section as the sum of the full $O(\alpha_s^3)$ prediction and the $O(\alpha_s^4)$ soft gluon correction, using the conservative value of $\Lambda_{QCD} = 105$ MeV. Their best estimate of the cross section includes the full gluon resummation contributions, and the uncertainty arises mostly from the choice of μ_0, which is allowed to become as small as $0.05M_{top}$ and $0.2M_{top}$ for the $q\bar{q} \rightarrow t\bar{t}$ and $gg \rightarrow t\bar{t}$ channels respectively.

A separate calculation of the $t\bar{t}$ cross-section including the perturbative resummation of gluon radiative corrections has become available in the past year (Berger and Contopanagos, 1995). This calculation is based on Principal Value Resummation (PVR) techniques (Contopanagos and Sterman, 1993 and 1994), and is independent of the arbitrary infrared cutoff μ_0. Theoretical uncertainties are estimated by varying the renormalization and factorization scale μ by a factor of two around the top mass. A more recent evaluation of the effects of gluon resummation suggests that its contribution is much smaller than previously thought (Catani *et al.*, 1996). In Table II we summarize the results of the various calculations of the $p\bar{p} \rightarrow t\bar{t}$ cross-section at Tevatron energies for a top mass of 175 GeV/c^2 which, as we will discuss in Section IX, corresponds to the directly measured value of the top mass.

The expected top production cross-sections at Tevatron and S$p\bar{p}$S energies, for the three production mechanisms, are displayed in Fig. 21 and Fig. 22. The Drell-Yan cross section, $\sigma(p\bar{p} \rightarrow W \rightarrow t\bar{b})$, is calculated from the diagram shown in Fig. 17. The value of this cross

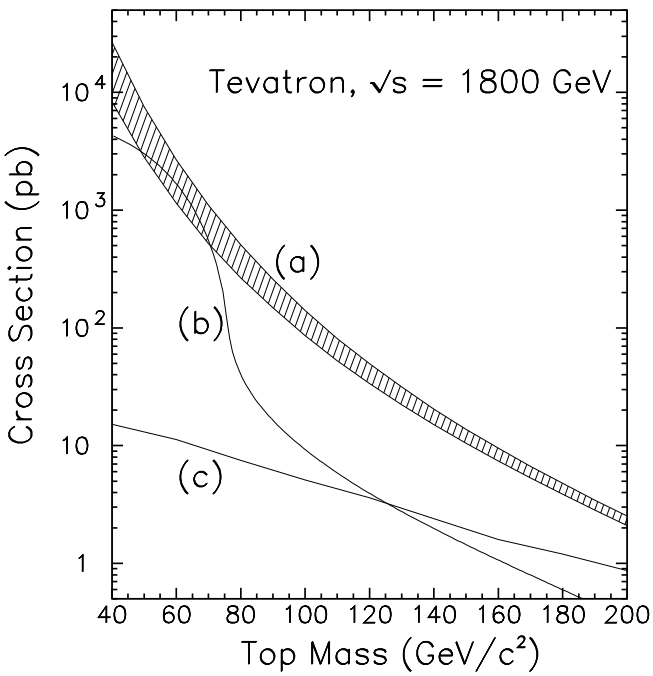

FIG. 21. Top production cross-sections in $p\bar{p}$ collisions at $\sqrt{s} = 1.8$ TeV. (a) $p\bar{p} \to t\bar{t}$ from Laenen, Smith and van Neerveen, 1994. The band represents the estimated theoretical uncertainty; (b) sum of $t\bar{b}$ and $\bar{t}b$ from W decay (Drell-Yan); (c) sum of $t\bar{b}$ and $\bar{t}b$ from W-gluon fusion. See text for details.

section is normalized to the rate of W production through measurements of $p\bar{p} \to W \to e\nu$ (F. Abe *et al.*, 1991b; Alitti, *et al.*, 1990a; Albajar *et al.*, 1991a), including corrections for the phase-space suppression of a $t\bar{b}$ pair and the finite W width. The tree-level W-gluon fusion cross-section has been calculated by several authors (Willenbrock and Dicus, 1986; Yuan, 1990; Anselmo, van Eijk, and Bordes, 1992; Ellis and Parke, 1992; Bordes and van Eijk, 1993); the cross sections shown in Figs. 21 and 22 are obtained using the PYTHIA Monte Carlo event generator (Sjöstrand and Bengtsson, 1987). Since the W-gluon fusion matrix element is calculated at tree level, the systematic uncertainties on the absolute rate prediction can be large, see for example Ellis and Parke, 1992. Here we have used the default PYTHIA scale $\mu^2 = 0.5$ ($\mathrm{M}_{t1}^2 + \mathrm{M}_{t2}^2$), where M_{t1} and M_{t2} are the transverse masses of the outgoing partons. Recently, a calculation of the next-to-leading order QCD corrections for the W-gluon fusion process has been performed (Bordes and van Eijk, 1995), and the enhancement of the cross section over the Born-level result has been found to be of order 30%. It is worth mentioning that, despite their apparent similarities, the Drell Yan and W-gluon mechanisms are quite distinct. The higher order Drell-Yan diagram, $qg \to qW^*$, $W^* \to t\bar{b}$ (see Fig. 23) and the W-gluon fusion diagrams (see Fig. 18) have the same initial and final state partons. However, in one case the W is space-like, and in the other case it is time-like. Furthermore, the $t\bar{b}$ pairs in the two processes are in different color states.

As anticipated, the pair production cross-section at the Tevatron (see Fig. 21) is dominant up to very high mass, except for the top mass region around 60 GeV/c^2, where the cross sections for the $t\bar{t}$ and $W \to t\bar{b}$ processes are approximately equal. On the other hand, at

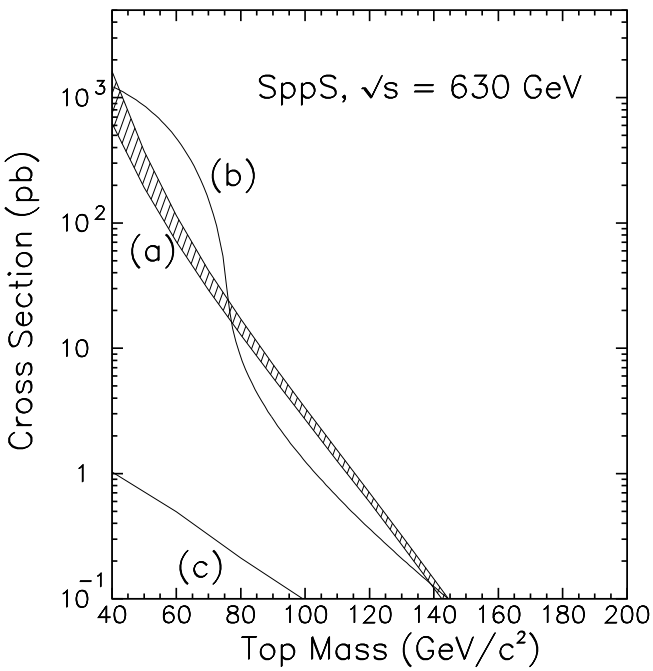

FIG. 22. Top production cross-sections in $p\bar{p}$ collisions at $\sqrt{s} = 0.63$ TeV. (a) $p\bar{p} \to t\bar{t}$ from Laenen, Smith and van Neerveen, 1994. The band represents the estimated theoretical uncertainty; (b) sum of $t\bar{b}$ and $\bar{t}b$ from W decay (Drell-Yan); (c) sum of $t\bar{b}$ and $\bar{t}b$ from W-gluon fusion. See text for details.

the lower energy of the S$\bar{p}p$S collider, top production through W decay dominates in the mass region 40-80 GeV/c^2, (see Fig. 22). Once the experimental evidence started pointing towards higher top masses (see Section VI), it became clear that top searches at the S$\bar{p}p$S were not competitive with those at the Tevatron, due to the lower $t\bar{t}$ cross-section at $\sqrt{s} =$ 630 GeV.

It should be emphasized that top production is a very rare process in $p\bar{p}$ collisions. The total inelastic cross-section at the Tevatron is approximately 60 mb (F. Abe *et al.*, 1994b), ten orders of magnitude higher than $\sigma(t\bar{t})$ for $\mathrm{M}_{top} = 175$ GeV/c^2. Therefore, in trying to isolate a top signal, both excellent background rejection and high luminosities are critical.

In the remainder of this Section and in most of this review we will concentrate on the $p\bar{p} \to t\bar{t}$ reaction. We will however revisit the W-gluon fusion process in Section X, since it is interesting in its own right and its study will become accessible in the not too distant future.

B. Top quark hadronization

Quarks are not observed as free particles but are confined to form hadronic bound states. The top quark however is unique in that its mass is high enough that it can decay before hadronization. According to the Standard Model, top quarks undergo the weak decay $t \to Wb$, where the W boson is real if $\mathrm{M}_{top} > \mathrm{M}_W + \mathrm{M}_b$, and virtual otherwise. Decay modes such as $t \to Ws$ and $t \to Wd$ are also allowed. They are suppressed by factors of $|V_{ts}|^2/|V_{tb}|^2 \approx$

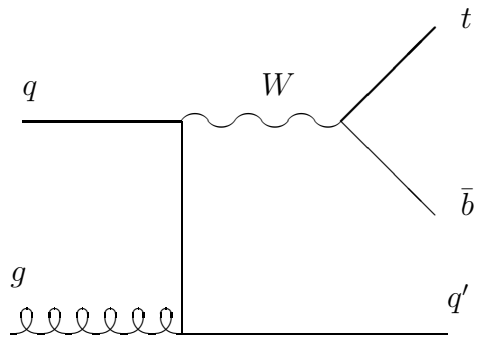

FIG. 23. Diagram contributing to the O(α_s) corrections to the Drell-Yan process $p\bar{p} \rightarrow W \rightarrow t\bar{b}$.

10^{-3} and $|V_{td}|^2/|V_{tb}|^2 \approx 5$ x 10^{-4} respectively, where V_{ij} is a Cabibbo-Kobayashi-Maskawa (CKM) mixing-matrix element (Montanet *et al.*, 1994). The expected width of the top quark, and hence the lifetime, as a function of its mass, is shown in Fig. 24.

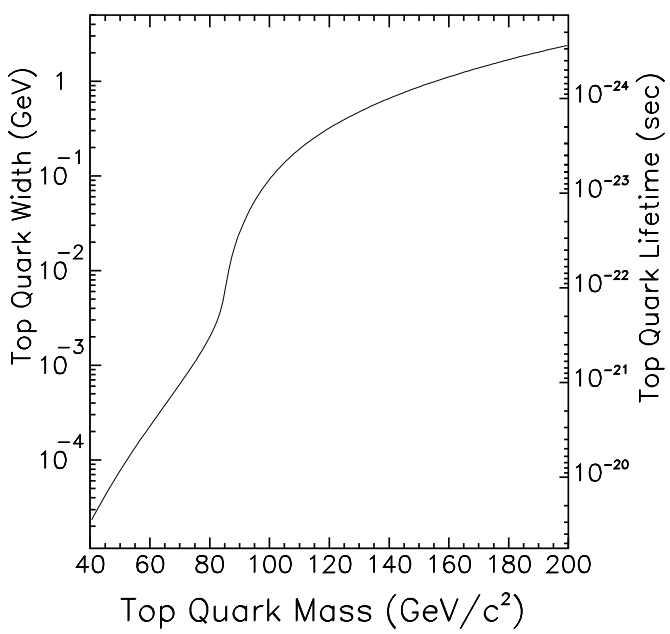

FIG. 24. The Standard Model width of the top quark as a function of its mass (Bigi, 1986). Note the transition between the region of virtual and real W decays which occurs at $M_{top} \approx M_W + M_b$.

The hadronization process, which is non-perturbative in nature, is not well understood. However, the formation of hadrons is estimated to take place in a time of order $\Lambda_{QCD}^{-1} \approx$ O(100 MeV)$^{-1} \approx$ O(10^{-23}) seconds (Bigi, 1986). As can be seen in Fig. 24, the top lifetime becomes shorter than this characteristic time if the top mass is higher than approximately 100 GeV/c^2. A more quantitative treatment is given by Orr (1991), and is briefly summarized here. In this model, the t and the $\bar{t}$ emerging from the hard scatter are linked by color strings to the remnants of the proton and anti-proton. When the separation between the outgoing quarks and the color-connected remnants exceeds a distance of order 1 fm, the stretched color string is expected to break, resulting in the creation of fragmentation particles from

the vacuum, and possibly the formation of a bound state top hadron. For $M_{top} > 165$ GeV/c^2, the top production kinematics at the Tevatron are such that essentially all top quarks are expected to decay before having travelled that minimum distance. Conversely, for top masses below 120 GeV/c^2, the overwhelming majority of top quarks will survive to a distance of 1 fm, and hadronization effects are expected to occur. Varying the assumption on the hadronization distance by a factor of two results in a mass-shift of order 20 GeV/c^2 for the transition region between hadronization and free-quark decay.

The exceedingly short top-quark lifetime is due not only to the very high mass, but also to the fact that $M_{top} > M_b$, so that the the top can decay into Wb, and this decay mode is not CKM suppressed. A heavy $I_3 = -1/2$ fourth generation quark (b') would decay into Wu', where u' here stands for an $I_3 = +1/2$ up-type quark. The decay rate would be proportional to the square of the CKM mixing-matrix element that connects b' and u'. If the b' were lighter than the fourth-generation up-type quark, then only generation-changing, CKM suppressed, decays would be allowed. As a result, the lifetime of such a fourth generation quark could be considerably longer than that of a top-quark of the same mass. Fourth generation heavy hadrons, as well as new quarkonia states, could then still be allowed to form.

Even if hadronization effects do occur in $t\bar{t}$ production, their effects, although potentially interesting, are not expected to be experimentally observable, at least in the forseeable future. The reason is that the fragmentation of heavy quarks is *hard*, i.e. the fractional energy loss of the top quark as it hadronizes is small (Peterson *et al.*, 1983). Distortions to the kinematics of the top quark from the perturbative partonic calculation are minimal. Additional particles produced in the hadronization process have little effect on the overall event topology. If a top hadron is indeed produced, the kinematics of the top decay will not be very different from that of a free quark decay since the companion quark is so much lighter. The fragmentation of the b-quark produced in top decay could potentially be more seriously affected. This is because the color string would link the b-quark to the light quark produced in the top fragmentation rather than the proton or anti-proton remnant (Orr, 1991). However, all top-quark experimental studies to date have not been precise enough to be sensitive to fragmentation assumptions.

C. Underlying event

After the hard collision, the remnants of the proton and anti-proton also hadronize. This process cannot be described within the framework of perturbative QCD, and is therefore poorly understood. The particles from the remnant hadronization form what is usually referred to as the *underlying event*. The structure of the underlying event is similar to that of the bulk of soft $p\bar{p}$ collisions (the so-called minimum bias events).

Minimum bias events are events collected with a simple interaction trigger. This trigger usually consists of a coincidence between large banks of scintillator counters in the very forward and backward regions, and is highly efficient for all types of inelastic $p\bar{p}$ collisions, except for singly diffractive events. In minimum bias events, the average transverse momentum of the hadrons is $P_T \approx 500$ MeV/c (Para, 1988). (Transverse momentum is the component of momentum perpendicular to the direction of the beams). Most of the energy is carried away by particles which remain inside the beam pipe and are not seen in the

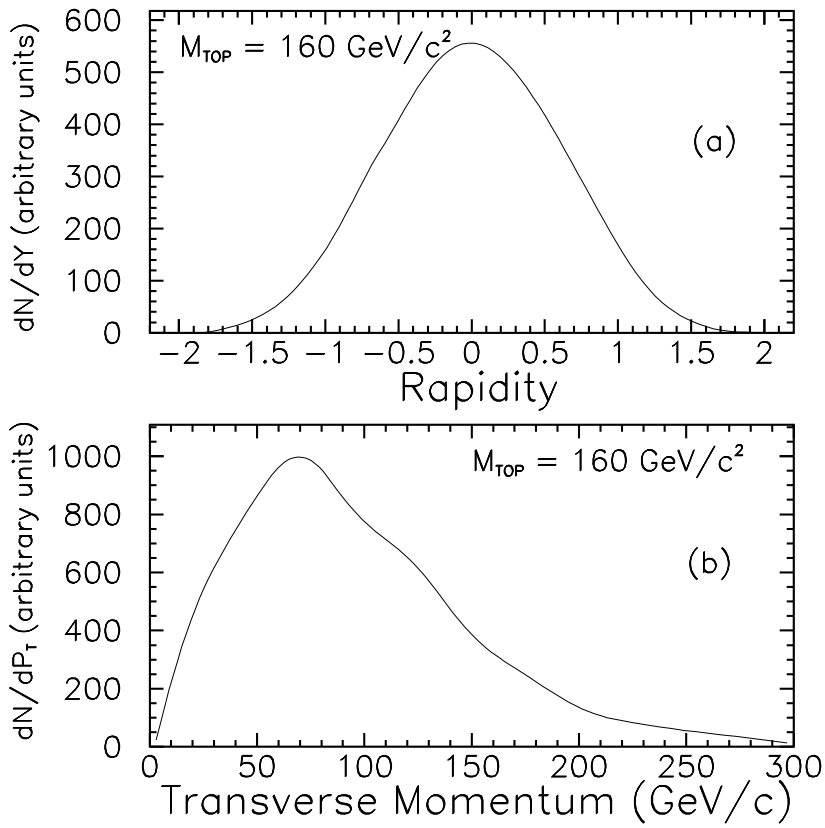

FIG. 25. The expected rapidity (y) and transverse momentum (P_T) distributions for top quarks at the Tevatron. The predictions are form the ISAJET Monte Carlo program.

detector. The charged particle multiplicity in the central region per unit pseudo-rapidity ($dN^{ch}/d\eta$) grows approximately logarithmically with the center-of-mass energy, and at $\sqrt{s} =$ 1.8 TeV is $dN^{ch}/d\eta \approx 4$ (F. Abe *et al.*, 1990e). (NB: the rapidity y of a particle is defined in terms of the longitudinal Lorentz boost, with $\beta = \tanh y$, to the frame in which the particle's momentum is purely transverse. Rapidity can be written as

$$y \;= \frac{1}{2}\,\ln\frac{E+P_z}{E-P_z} \;=\; \frac{1}{2}\,\ln\frac{(E+P_z)^2}{M^2+P_T^2}$$

where E is the energy of the particle, M is its mass, and P_z and P_T are the components of momenta parallel and transverse to the beam direction. Pseudo-rapidity (η) is the rapidity calculated neglecting the particle's mass, $\eta = -\ln\tan(\theta/2)$, where θ is the polar angle with respect to the proton direction. Zero rapidity or pseudorapidity corresponds to particles moving at 90° from the beamline; high values of $|y|$ or $|\eta|$ implies very forward or backward going particles).

D. Modelling of top quark production

The reliability of the modeling of $t\bar{t}$ production in is an important issue. Top production is usually modelled using a QCD shower Monte Carlo program, such as ISAJET (Paige

and Protopopescu, 1986), HERWIG (Marchesini and Webber, 1984 and 1988) or PYTHIA (Sjöstrand and Bengtsson, 1987). These Monte Carlos are used by the experimental groups to calculate the $t\bar{t}$ acceptance and kinematics, and to model the resolution of the top quark mass measurement, see Section IX.

In all these Monte Carlo programs, the initial hard scatter is generated from tree-level matrix elements convoluted with parametrizations of the parton distribution functions. Initial and final state partons are then developed into a gluon and $q\bar{q}$ radiation cascade, with angular and energy spectra based on the QCD Altarelli-Parisi splitting function. The QCD shower is terminated when the virtual invariant mass of the parton in the cascade becomes smaller than a minimum value which is of order 1 GeV for HERWIG and PYTHIA and 6 GeV for ISAJET, at which point perturbative QCD is expected to break down. Phenomenological models are then employed to combine the remaining partons into hadrons. The underlying event is also modelled in a phenomenological way, with a number of parameters tuned to reproduce the hadron multiplicities and transverse momentum spectra measured in soft $p\bar{p}$ collisions (minimum bias events). Short lived particles are made to decay, with branching ratios and decay models based on the compilation from the Particle Data Group (Montanet *et al.*, 1994).

The main differences between these Monte Carlo event generators reside in the modeling of the radiation processes. ISAJET employs an independent fragmentation model, i.e. radiation from each parton occurs independently from the structure of the rest of the event, whereas in both HERWIG and PYTHIA radiation is more realistically emitted taking into account color-correlations between all partons in the initial and final state. The output of these Monte Carlo event generators consists of a list of stable particles, which can then be fed to a detector simulation for detailed studies of the expected signature of a top event.

In the pair production process, the t and $\bar{t}$ quarks are produced in the central rapidity region, with P_T of order $\mathrm{M}_{top}/2$, (see Fig. 25). These features of $t\bar{t}$ production can be simply understood from the properties of the $i + j \rightarrow t\bar{t}$ process. The cross-section for the $q\bar{q} \rightarrow t\bar{t}$ subprocess, which dominates at high top mass, is given at lowest order by (see for example Nason, Dawson, and Ellis, 1988) :

$$\hat{\sigma} \quad = \frac{8\pi\alpha_s^2}{27\hat{s}}\sqrt{1 - \frac{4M_{top}^2}{\hat{s}}} \;\; (1 + \frac{2M_{top}^2}{\hat{s}})$$

The parton-parton cross-section as a function of $\hat{s}$ rises from zero at threshold ($\hat{s} = 4\mathrm{M}_{top}^2$), reaches a maximum at $\hat{s} = 5.6\mathrm{M}_{top}^2$, and then falls off asymptotically as $1/\hat{s}$. When convoluted with the falling $q\bar{q}$ luminosity, (see Fig. 20), the maximum of the $q\bar{q} \rightarrow t\bar{t}$ cross-section is shifted down to $\hat{s} \approx 4.5\mathrm{M}_{top}^2$. Therefore, the most probable energy for a top quark is E $\approx \sqrt{4.5}\mathrm{M}_{top}/2 \approx 1.1\mathrm{M}_{top}$, and the most probable momentum is P $\approx 0.4\mathrm{M}_{top}$.

From the definition of rapidity, it is clear that the maximum of $|y|$ occurs as $P_T \rightarrow 0$ and at maximum E, which for pair-produced objects is $E = 0.5\sqrt{s} = 900$ GeV at the Tevatron. For $\mathrm{M}_{top} = 160$ GeV/c^2, the kinematic limit is then $|y| < 2.4$; however, as can be seen from Fig. 25, most top quarks have $|y| < 1.5$. High values of $|y|$ are suppressed because they require $P_T \rightarrow 0$, where the phase space factor also $\rightarrow 0$, and they require high values of E, i.e. high values of $\hat{s}$. Both the parton-parton luminosities and parton-parton cross-section fall off with increasing $\hat{s}$.

The lowest order diagrams (Fig. 16) lead to a back-to-back topology for the t and the $\bar{t}$ in the transverse plane, which is slightly modified by higher order corrections. Because the top quark momentum is not large compared to M_{top}, the decay products are not significantly boosted along the original top quark flight path, leading to nearly spherical events. In the next Section we will turn to the discussion of top decays and signatures.

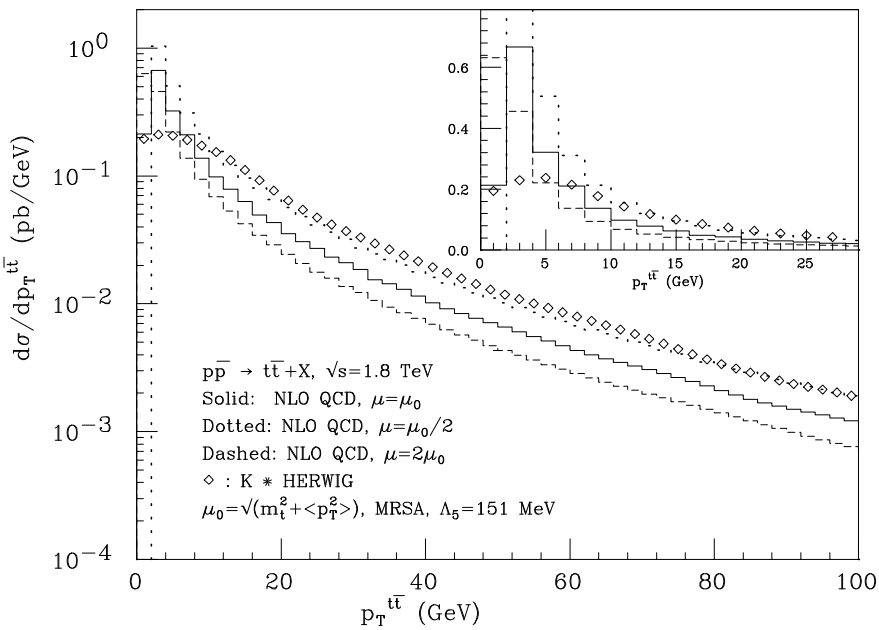

FIG. 26. Comparison of the transverse momentum distributions of the $t\bar{t}$ pair as predicted from the Herwig Monte Carlo and next-to-leading order (NLO) QCD. At Tevatron energies, and for M_{top} = 176 GeV/c^2. From Frixione *et al.*, 1995.

As was mentioned above, shower Monte Carlos are based on the LO matrix element for $t\bar{t}$ production and models of initial and final state radiation. It is interesting to compare these models with higher order QCD calculations. The earlier NLO order calculations of $t\bar{t}$ production (Nason, Dawson, and Ellis, 1988; Beenaker *et al.*, 1991) are not sufficient, since these are calculations of single quark kinematic distributions such as P_T and rapidity, integrated over the whole phase-space for the other quark. More recently, a NLO calculation of the doubly-inclusive cross-section for heavy quark production has become available (Mangano, Nason and Ridolfi, 1992). This calculation allows for comparisons not only of single t or $\bar{t}$ distributions, but also of correlated distributions, e.g. the $t\bar{t}$ invariant mass ($M(t\bar{t})$), the $t\bar{t}$ transverse momentum ($P_T(t\bar{t})$), and the azimuthal separation between t and $\bar{t}$ ($\Delta\phi$). Detailed comparisons between the Herwig model and NLO-QCD have been performed (Frixione *et al.*, 1995). Excellent agreement is found in the shapes of distributions of quark rapidity, P_T, and $M(t\bar{t})$, except for very large values of the latter two quantities. In this kinematic regime, multiple gluon emission from the final state top quarks becomes

important, and this process is not modelled by the NLO QCD calculation. Disagreement between NLO QCD and HERWIG is also observed in distributions of $P_T(t\bar{t})$ and $\Delta\phi$, (see Fig. 26). Note that at LO these distributions are delta-functions, with $P_T(t\bar{t}) = 0$ and $\Delta\phi = 180^o$, and deviations from the delta-function behavior are due entirely to higher order corrections. For small $P_T(t\bar{t})$, multiple gluon emission is expected to dominate, and the HERWIG model is expected to be more realistic.

Studies of the expected single top quark P_T and rapidity distributions, calculated in NLO QCD and including the resummation of the leading soft gluon corrections, have also been performed (Kidonakis and Smith, 1995). The shapes of these distributions are found to be essentially identical to those calculated at NLO, which were shown to agree with the Herwig model. Comparisons of gluon emission in $t\bar{t}$ events from HERWIG and from a $O(\alpha_s^3)$ matrix element calculation, including initial and final state gluon radiation have also been made (Orr, Stelzer, and Stirling, 1995). These authors find larger contributions of gluon radiation in HERWIG than in the matrix element calculation. This effect may also be due to the absence of multi-gluon emission in the calculation.

As we will discuss in Section IX, understanding gluon radiation in $t\bar{t}$ events is crucial for a precise determination of the top mass. We expect that this subject will attract more and more attention in the next few years.

V. TOP QUARK SIGNATURES

Since the top quark decays with a very short lifetime, only its decay products can be detected. Therefore, to understand the experimental signature for a top event, we first discuss the decay modes of the top quark. In this Section we review the top quark decay properties and we present a general discussion of how the top quark can be observed, paying particular attention to the background sources. We will concentrate on the signature for $p\bar{p} \to t\bar{t}$, since this is the most important production mechanism at Tevatron Collider energies.

A. Standard Model top quark decay modes

As mentioned in the previous Section, according to the Standard Model the top quark decays as $t \to Wb$, where the W boson is real or virtual depending on the top mass. (Non-Standard Model decay modes of the top quark will be reviewed in Section VI.C). The W will subsequently decay into fermion pairs, either $W \to l\nu$ or $W \to q\bar{q}$, where l denotes a charged lepton, and $q\bar{q}$ denotes a light-quark pair, $u\bar{d}$ or $c\bar{s}$. At tree level, the W couples with equal strength to leptons and quarks, so each W decay mode occurs with equal probability. There are three leptonic channels ($e\nu$, $\mu\nu$, and $\tau\nu$), and six hadronic channels ($u\bar{d}$ and $c\bar{s}$, with three possible color assignments), hence each decay mode has a branching ratio of 1/9. QCD corrections enhance the branching ratios of the hadronic modes by a factor of $(1 + \alpha_s/\pi) \approx 1.05$. Given the W branching fractions, it is a simple matter to list the $t\bar{t}$ decay modes, see Table III.

Decay mode	Branching ratio
$t\bar{t} \to q\bar{q}\ q\bar{q}\ b\bar{b}$	36/81
$t\bar{t} \to q\bar{q}\ e\nu\ b\bar{b}$	12/81
$t\bar{t} \to q\bar{q}\ \mu\nu\ b\bar{b}$	12/81
$t\bar{t} \to q\bar{q}\ \tau\nu\ b\bar{b}$	12/81
$t\bar{t} \to e\nu\ \mu\nu\ b\bar{b}$	2/81
$t\bar{t} \to e\nu\ \tau\nu\ b\bar{b}$	2/81
$t\bar{t} \to \mu\nu\ \tau\nu\ b\bar{b}$	2/81
$t\bar{t} \to e\nu\ e\nu\ b\bar{b}$	1/81
$t\bar{t} \to \mu\nu\ \mu\nu\ b\bar{b}$	1/81
$t\bar{t} \to \tau\nu\ \tau\nu\ b\bar{b}$	1/81

TABLE III. Decay modes for a $t\bar{t}$ pair and their lowest order branching ratios assuming Standard Model decays.

B. Detection of the top decay products

The possible final states contain combinations of electrons, muons, taus, neutrinos, and quarks. Here we briefly illustrate techniques for detection of the top-quark decay products.

General-purpose $p\bar{p}$ collider detectors are needed for top quark physics. These detectors are designed to cover as much as possible of the solid angle around the interaction point, and are composed of a number of sub-detectors optimized for study of different aspects of the event. A number of such detectors have been used (UA1 and UA2 at the CERN S$p\bar{p}$S), are still in operation (CDF and D0 at Fermilab's Tevatron), or are now being designed and constructed (CMS and ATLAS, at the proposed LHC pp collider). While the details of the design of these detectors are different, their overall structure is in general quite similar. The region immediately surrounding the interaction region is instrumented with detectors designed to measure the trajectories of charged particles. Except for UA2 and D0, the tracking volume is immersed in a magnetic field for momentum measurement. The tracking volume is surrounded by calorimeters, where measurements of the energy of electromagnetic and hadronic showers are performed. Calorimeters are segmented both longitudinally and transversely to the direction of flight of particles originating from the interaction point. Transverse segmentation is necessary to measure the position of the showers, while longitudinal information is used to distinguish between electromagnetic (EM) and hadronic (HAD) showers. Calorimeters cover most of the 4π solid angle around the interaction region, however the very forward and backward regions must be left uninstrumented to allow for the passage of the beam pipe. Muon detectors consisting of additional tracking devices, hadron absorbers, and possibly magnets for momentum measurement, are placed outside the calorimeter. Drawings of the two collider detectors at Fermilab's Tevatron are shown in Fig. 27 and Fig. 28.

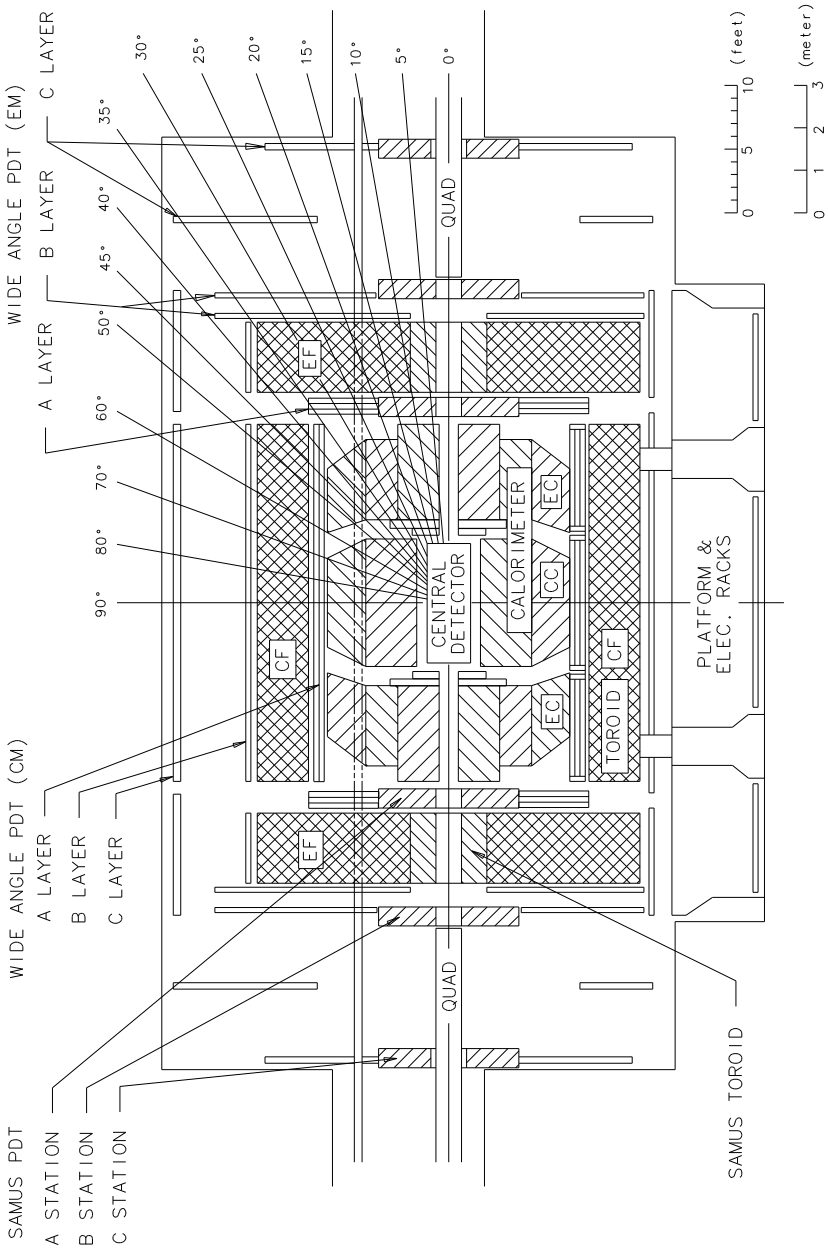

FIG. 27. The D0 detector at the Tevatron. EC and CC are liquid-argon-uranium calorimeters. The central detector provides tracking information. Muons are detected using the five toroids (CF, EF, SAMUS) and the proportional drift tube (PDT) systems, CM and EM. From Snyder, 1995a.

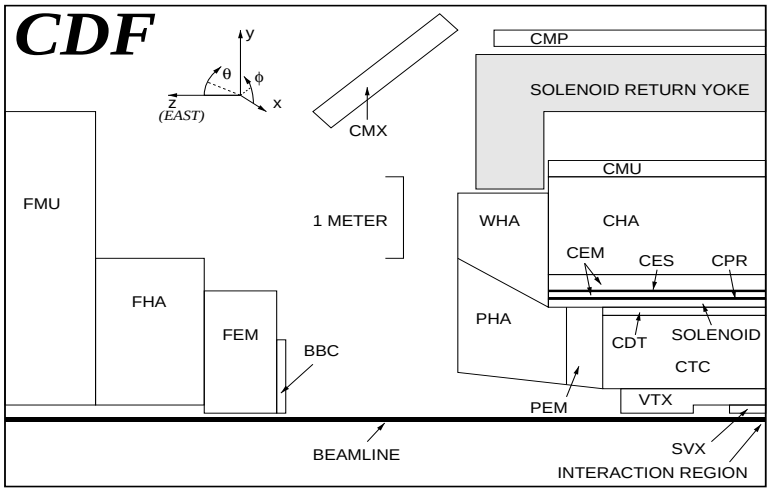

FIG. 28. A side-view cross-section of one quadrant of the CDF detector at the Tevatron. The detector is forward-backward symmetric about the interaction region, which is at the lower-right corner of the figure. SVX, VTX, CTC, and CDT are tracking detectors. CEM, CHA, WHA, PEM, PHA, FEM, and FHA are calorimeters. CMU, CMP, CMX, and FMU are muon detectors. BBC is a bank of scintillators. CPR and CES are multiwire proportional chambers placed in front and in the middle of the central electromagnetic calorimeter (CEM). From F. Abe *et al.*, 1994a.

1. Detection of electrons and muons

Electrons are identified as highly electromagnetic showers in the calorimeters. If momentum information from the tracking system is available, consistency between the measured momentum of the electron candidate and the energy of the corresponding EM-shower provides a powerful handle for rejection of backgrounds from e.g. hadronic shower fluctuations and overlaps between hadron tracks and photons from π^0 decay. Information from the transverse and longitudinal shapes of the shower, from ionization measurements in the tracking chamber (dE/dX), and from the response of transition radiation and preshower detectors, are also used for electron identification.

Electrons from W decays in top events have high transverse momentum, (P_T, see Fig. 29), and are expected to be isolated, i.e. well separated from the other decay products of the two top quarks in a $t\bar{t}$ event. These electrons can be identified with high efficiency, and their energy can be measured very precisely in the calorimeter (see Table IV). On the other hand, identification of electrons from $b \to ce\nu$ in a top event is much more problematic. These electrons have lower transverse momentum than electrons from W decays and, since the b is highly boosted, the nearby hadrons from the b fragmentation and b or c decay may deposit their energy in the same calorimeter cells as these electrons.

Muons can also be reliably identified as charged particles that penetrate the calorimeter and reach the outside muon detectors. Backgrounds to the muon signal arise from decays in flight of pions and kaons, and from hadrons that traverse the calorimeter and hadron absorbers without interacting (*punchthrough*). If there is a magnetic field in the inner tracking system (before the calorimeter), then the muon momentum is precisely measured;

Detector	Electron energy resolution	Muon momentum resolution
UA1	σ(E)/E = (0.15-0.21)/$\sqrt{E}$ $\oplus$ .03	σ(P)/P = 0.005P
UA2	σ(E)/E = 0.17/$\sqrt{E}$ $\oplus$ .02	-
CDF	$\sigma(\mathrm{E}_T)/\mathrm{E}_T = 0.14/\sqrt{E_T}$ $\oplus$ .02	$\sigma(\mathrm{P}_T)/\mathrm{P}_T = 0.0009\mathrm{P}_T$ $\oplus$ 0.0066
D0	σ(E)/E = 0.15/$\sqrt{E}$ $\oplus$ .01	σ(P)/P = 0.01P $\oplus$ .2

TABLE IV. Electron energy (GeV) and muon momentum (GeV/c) resolutions in the central region for the UA1 (Albajar *et al.*, 1989), UA2 (Alitti *et al.*, 1992a), CDF (F. Abe *et al.*, 1994a), and D0 (Abachi *et al.*, 1994) detectors. The UA1 muon momentum resolution is for measurements in the central-detector, for muons at 90° from the direction of the dipole field. The UA1 electron energy resolution changed between 1983 and 1985 due to radiation damage of the scintillator. The symbol $\oplus$ indicates that the two terms are added in quadrature. The subscript T refers to components transverse to the beam direction.

otherwise, (e.g. in the D0 experiment) it is measured, with worse resolution, in the outer muon detector (see Table IV).

2. Detection of quarks

Quarks hadronize and are detected as collimated *jets* of particles, (see Fig. 30). Jets in $p\bar{p}$ collisions are reconstructed by summing up the energy deposited in the calorimeter cells within a fixed cone in $\eta-\phi$ space, where η is the pseudorapidity, and ϕ is the azimuthal angle around the beamline. The fixed cone algorithm is used because jets are are approximately *circular* in $\eta-\phi$ space, because the $\eta-\phi$ size of a jet of a given P_T is independent of the rapidity of a jet, and because this size is only weakly dependent on the transverse momentum of the jet, as we will briefly discuss below.

If the typical longitudinal and transverse momentum components of a fragmentation particle with respect to the jet axis are q_T and q_l, then the typical spread of the jet will be $\Delta\theta \approx q_T/q_l$ and $\Delta\phi \approx q_T/(q_l \sin\theta)$, for $q_T << q_l$. Then, $\Delta\eta = (\mathrm{d}\eta/\mathrm{d}\theta)\ \Delta\theta \approx -q_T/(q_l \sin\theta)$ $= -\Delta\phi$, i.e. jets are approximately circular in $\eta-\phi$ space. Since the rapidity of a massless particle under a longitudinal boost changes as $\mathrm{y} \rightarrow \mathrm{y} + \Delta\mathrm{y}$, where Δy only depends on the boost, in the limit that the mass of the fragmentation hadrons is small, the η size of a jet of a given P_T is invariant under longitudinal boosts, i.e. independent of the η of the jet itself. The size of a jet does vary slightly with its transverse momentum; for example a simple model of jet fragmentation uniform in rapidity along the jet axis predicts that the angular size of the cone containing half of the particles in the jet varies as $1/\sqrt{E}$, where E is the energy of the jet.

The size of the cone used in jet reconstruction must be matched to the size of a jet. On average, of order 70% of the jet energy is contained within a cone of radius $\Delta\mathrm{R} = \sqrt{\Delta\eta^2 + \Delta\phi^2} = 0.4$ (F. Abe *et al.*, 1991c and 1993a; Linneman, 1995.). See also Fig. 31; NB: $\Delta\mathrm{R} < 0.4$ translates into $\Delta\phi < 23^o$ in Fig. 31.

The energy of a jet is defined as the energy of the corresponding calorimeter cluster. The resolution in the measurement is typically only of order $\sigma(\mathrm{E}_T)/\mathrm{E}_T \approx 1.0/\sqrt{E_T}$ (E_T in GeV),

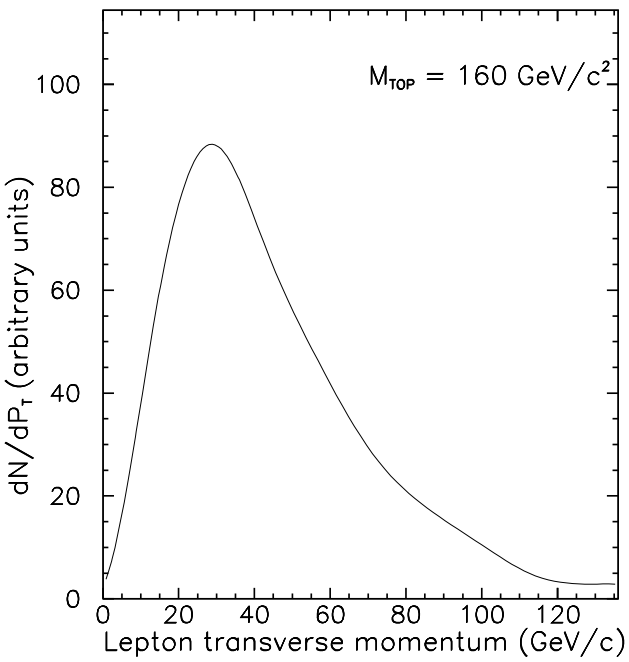

FIG. 29. The expected lepton transverse momentum from $t \to Wb \to l\nu$ from the ISAJET Monte Carlo generator. This is for $p\bar{p} \to t\bar{t}$ at $\sqrt{s} = 1.8$ TeV. Detector effects are not included.

(see Fig. 32). This poor resolution is due to (i) the intrinsic large fluctuations in the response of calorimeters to hadronic showers, (ii) differences in the calorimeter response between charged hadrons and electrons or photons, (iii) energy loss in uninstrumented calorimeter regions, e.g. in the vicinity of boundaries between calorimeter modules, (iv) energy loss due to the use of a finite cone-size in jet reconstruction, and (v) overlaps between the jet and hadrons from the underlying event. The direction of a jet is measured by linking the position of the energy cluster in the calorimeter with the position of the interaction point. The resolution on the angular measurement is a few degrees.

The number of detected jets for a given decay mode in a $t\bar{t}$ event is not expected to correspond to the number of quarks in the final states listed in Table III. There are a number of reasons for this. First, as the P_T of the parton becomes small, identification of the corresponding jet becomes more and more problematic, as it tends to blend with the underlying event. In practice, one imposes a minimum cutoff on the jet transverse momentum which is set to a value at least of order 10 GeV/c. Furthermore, as will be discussed further in this Section, backgrounds to the top signal consist mainly of events with low P_T jets. Therefore, to achieve the needed background rejection, the minimum jet P_T requirement is often chosen to be higher than 10 GeV/c. A second source of jet reconstruction inefficiency is jet merging. Nearby jets can be resolved only if their separation in $\eta - \phi$ space is larger than a minimum distance of the order of the clustering radius used in jet reconstruction. Top events have a large number of partons in the final state, and the probability that at least two of them will be too close to be separately identified is substantial. In those cases, the two nearby jets are merged and are reconstructed as a single jet.

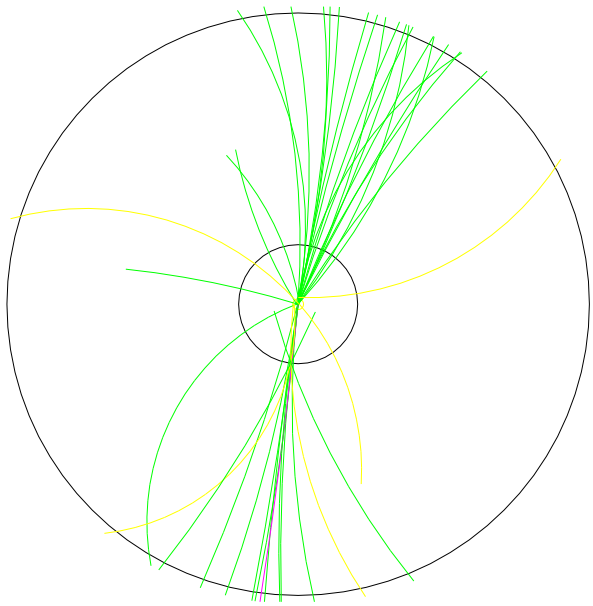

FIG. 30. A $p\bar{p} \rightarrow$ jet-jet event in CDF. Here we show the reconstructed tracks in the transverse plane. The *two-jet* structure is apparent.

To illustrate some of these effects, we show in Fig. 33 the expected transverse momenta and separation (ΔR) in $\eta - \phi$ space for quarks in $t\bar{t} \rightarrow q\bar{q}\ l\nu\ b\bar{b}$ events for $M_{top} = 170$ GeV/c^2. Different experiments and different analyses use different cone clustering radii, typically between 0.3 and 1.0. In a significant fraction of events, the minimum ΔR between quarks is small enough that at least two of the quark-jets are expected to be merged. Even for a high top mass, the fraction of events with at least one relatively soft jet is substantial (again, see Fig. 33). For lower top masses of course the transverse momenta will be even lower. The situation for M_{top} close to M_W is particularly difficult. In that case the kinetic energy liberated in the $t \rightarrow Wb$ decay is low and the b momentum in the top rest frame is small. Even after boosting to the laboratory frame, the b momentum remains soft, (see Fig. 34).

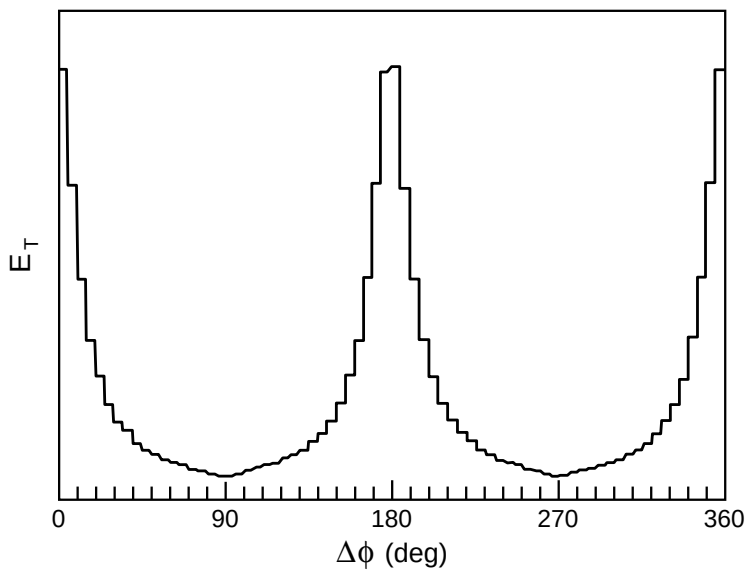

FIG. 31. The relative E_T distribution in calorimeter cells at an angle ϕ with respect to the transverse jet thrust axis for CDF di-jet data with a 30 GeV E_T jet trigger threshold. Note that in these di-jet events one jet is at $\phi = 0^o$, and the other jet is at $\phi = 180^o$. From F. Abe *et. al*, 1991c.

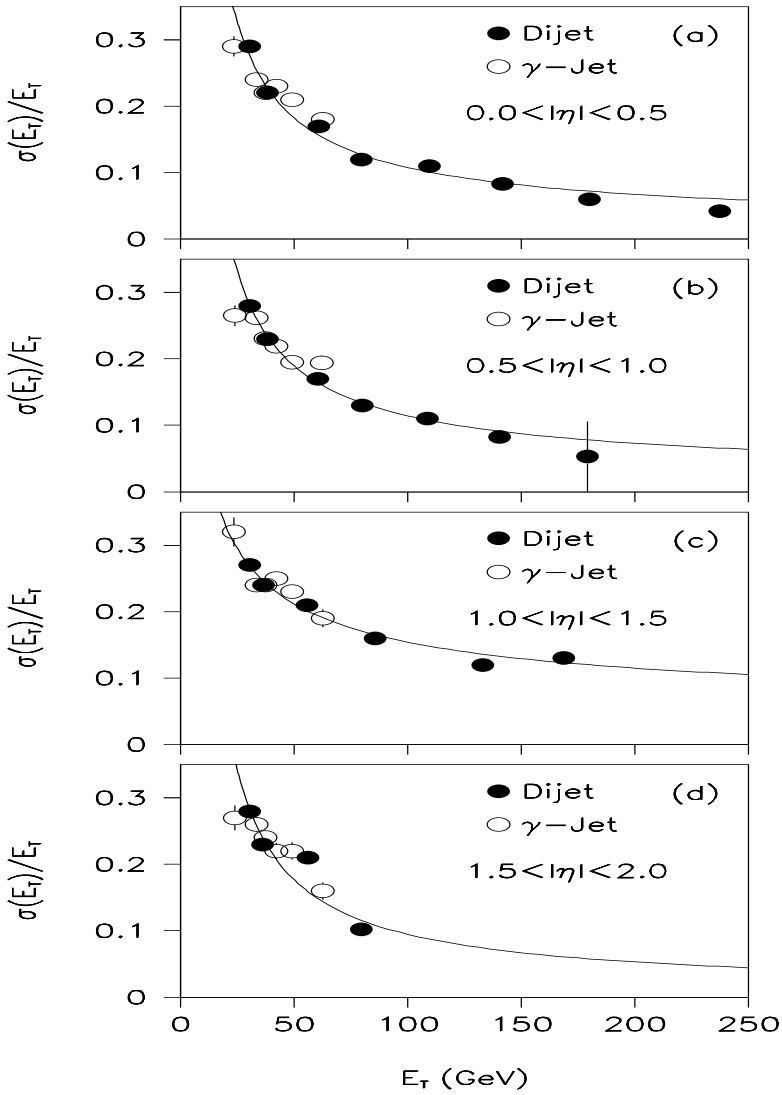

FIG. 32. From the D0 experiment, Abachi 1995d; jet energy resolution as a function of jet transverse energy (E_T) as computed from di-jet and photon-jet events in four pseudo-rapidity regions. The fits are of the form $(\sigma_E/E)^2 = (N/E)^2 + (S/\sqrt{E})^2 + C^2$. The fitted values of N, S, and C are : (a) $N = 7.07$, $S = 0.81$, $C = 0.0$; (b) $N = 6.92$, $S = 0.91$, $C = 0.0$; (c) $N = 0.0$, $S = 1.45$, $C = 0.052$; (d) $N = 8.15$, $S = 0.48$, $C = 0.0$. Jets are reconstructed using a cone-size of 0.5.

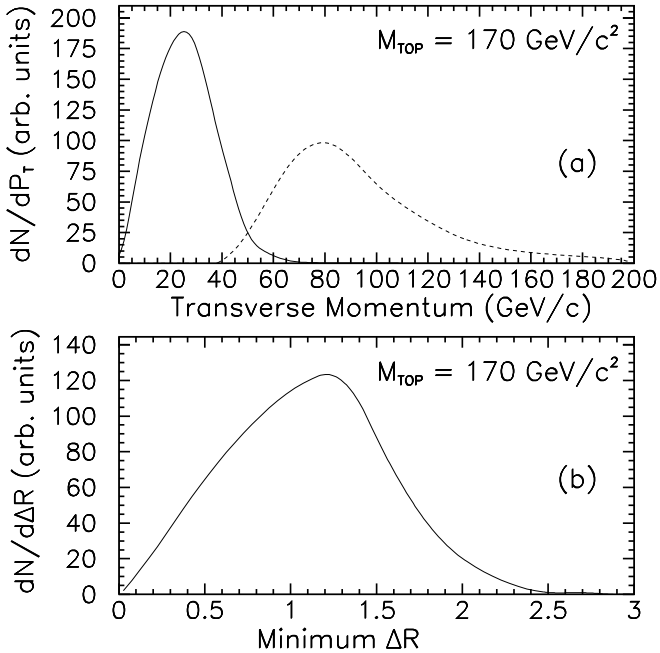

FIG. 33. (a) The expected transverse momentum of the lowest (solid) and highest (dashed) P_T quark in lepton + jets events; (b) ΔR between the closest two quarks in $p\bar{p} \to t\bar{t} \to q\bar{q}\ l\nu\ b\bar{b}$. Results are from the ISAJET Monte Carlo event generator at $\sqrt{s} = 1.8$ TeV. Detector effects are not included.

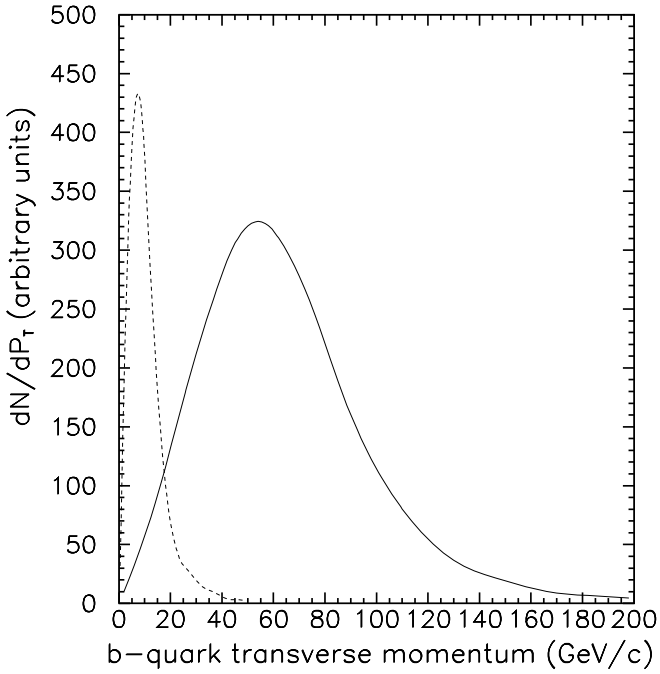

FIG. 34. The expected transverse momentum distribution of b-quarks from top decay for M_{top} = 170 GeV/c^2 (solid) and M_{top} = 90 GeV/c^2 (dashed). Results are from the ISAJET Monte Carlo event generator for the process $p\bar{p} \to t\bar{t}$ at $\sqrt{s} = 1.8$ TeV. Detector effects are not included.

The situation gets even more complicated when initial and final state radiation are taken into account. Initial state gluon radiations gives a net P_T to the $t\bar{t}$ system, and therefore alters the jet P_T spectrum calculated at tree-level; the radiated gluons can be detected as additional jets in the final state; large angle radiation from the final state quarks softens the spectrum of reconstructed jets, and can also result in additional jets.

All of these jet reconstruction effects are important, and must be studied using QCD-inspired Monte Carlo event generators, in conjunction with a simulation of the detector response, see for example Fig. 35. They constitute one of the major systematic uncertainties in the calculation of the $t\bar{t}$ acceptance and, more importantly, in the determination of the top mass, see Section IX.

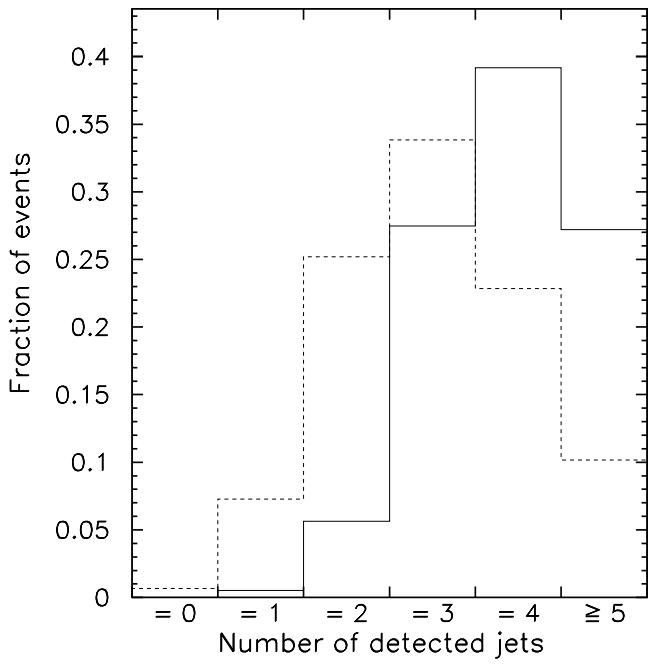

FIG. 35. Jet multiplicity in $t\bar{t} \to l\nu bq\bar{q}b$ (lepton + jets) events from the ISAJET Monte Carlo and the CDF detector simulation. Solid line : M_{top} = 200 GeV/c^2; dashed line : M_{top} = 120 GeV/c^2. Jets are reconstructed using a cone-size ΔR=0.4, and must have $|\eta| < 2$. The jet transverse energy threshold is 15 GeV, without application of jet energy corrections. (The jet energy corrections will be described in Section IX.A.3; a 15 GeV jet in CDF is corrected on average to $\approx$ 23 GeV). Note that in the absence of gluon radiation these events should have $N_{jets} \leq 4$; the significant fraction of events with additional jets in the final state is an indication of the importance of gluon radiation.

3. Detection of neutrinos

Neutrinos are detected by missing momentum techniques: since the initial center-of-mass momentum is zero, the vector sum of the momenta of all of the neutrinos in the event is inferred as the negative of the vector sum of the momenta of all the detected particles. However, because the very forward and backward detector regions are uninstrumented, longitudinal information is lost, and only the transverse components of the momenta of neutrinos

Detector	$\sigma(\not{E}_{\rm T})$	Reference
UA1	$0.7\ \sqrt{\Sigma E_T}$ (in GeV)	Albajar *et al.*, 1989
UA2	$0.8\ (\Sigma E_T)^{0.4}$ (in GeV)	Alitti *et al.*, 1990b
CDF	$0.7\ \sqrt{\Sigma E_T}$ (in GeV)	F. Abe *et al.*, 1994a
D0	1.08 GeV + $0.019\ \Sigma E_T$	Abachi *et al.*, 1995d

TABLE V. Missing transverse energy resolution for minimum bias events.

can be measured. In practice, what is measured is not the momentum of all of the particles, but rather the energy deposited in the calorimeter. The missing transverse energy vector ($\vec{\not{E}}_{\rm T}$) is defined as $\vec{\not{E}}_{\rm T} \equiv -\Sigma_i \vec{E_T^i}$, where the sum is over all calorimeter cellss, and $\vec{E_T^i}$ is a vector whose direction points to the *ith* cell and whose magnitude is equal to the transverse energy deposited in the *ith* tower. The missing transverse energy vector must be corrected for detected muons which only loose a minimal amount of energy in the calorimeter, and is then associated with the neutrino transverse momentum.

The resolution on the neutrino energy measurement is very much dependent on the event topology, since it depends directly on the resolution in the measurements of all the leptons and jets in the event. Since leptons are in general well measured, the uncertainty in the measurement of $\not{E}_{\rm T}$ arises mostly from errors in the measurements of jet energies. It is customary to parametrize the resolution in $\not{E}_{\rm T}$, $\sigma(\not{E}_{\rm T})$, as a function of the total transverse energy in the event, ΣE_T, see Table V.

4. Detection of tau leptons

Taus are very hard to identify. Approximately 36% of the time, a tau lepton will decay into a muon or an electron. The signature for an event with a $t \to W \to \tau\nu \to l\nu\nu$, where $l = e$ or μ, is very similar to that of an event with a $t \to W \to l\nu$ decay, except that the final state lepton will in general have lower momentum. Taus that decay hadronically are detected as jets. Separation between jets from hadronic decays of taus and quarks or gluon jets in $p\bar{p}$ collisions has been achieved in e.g. measurements of the $p\bar{p} \to W \to \tau\nu$ cross-section (Albajar *et al.*, 1989; Alitti *et al.*, 1991b; F. Abe *et al.*, 1992b), and in searches for non Standard-Model top quark decays, see Section VI.C. The separation is based on the distinctive narrowness of a jet from the hadronic decay of a high $\rm P_T$ tau-lepton, and/or the characteristic one- and three-prong track multiplicities. However, the efficiency for detecting hadronic taus is so low, and the backgrounds from jet fluctuations are so high, that these techniques are only now just beginning to be applied successfully in the context of a Standard Model top search.

For the remainder of this article, we will refer to $t\bar{t}$ final states with zero, one, or two leptons (e or μ) from W decay as *all hadronic, lepton + jets*, and *dilepton* respectively. Signatures that include the explicit identification of hadronic tau-decays will not be considered in this review. We now turn to a discussion of the $t\bar{t}$ signatures in these three channels.

C. All hadronic mode

The all hadronic final state, ($t\bar{t} \rightarrow q\bar{q}\ q\bar{q}\ b\bar{b}$, see Table III) is the most common, but it competes with very high backgrounds from $p\bar{p} \rightarrow 6$ jets (see for example Benlloch, Wainer, and Giele, 1993). The cross-sections for this QCD process at the Tevatron is higher than the top cross-section by approximately three orders of magnitude. Despite the extremely high background levels, it may be possible, with sufficient statistics, to isolate a top signal in this mode by applying further kinematic cuts, and by identifying the b-quark(s) in the final state. These issues are being carefully studied by the experimenters (Castro, 1994; Tartarelli, 1996; Narain 1996). In this review we will concentrate on the dilepton and lepton + jets modes.

D. Dilepton mode

The signature for the dilepton final state ($t\bar{t} \rightarrow l\nu\ l\nu\ b\bar{b}$, see Table III) consists of two leptons, two b-jets, and $\not{E}_{\rm T}$ from the two neutrinos. Since the leptons originate from W decay, they tend to be isolated and to have high transverse momenta. The $\not{E}_{\rm T}$ is also expected to be high, (see Fig. 36). Typical minimum lepton transverse momentum or $\not{E}_{\rm T}$ requirements are set around 20 GeV/c. Despite the low branching ratio, this mode turns out to be very important because background levels are very low.

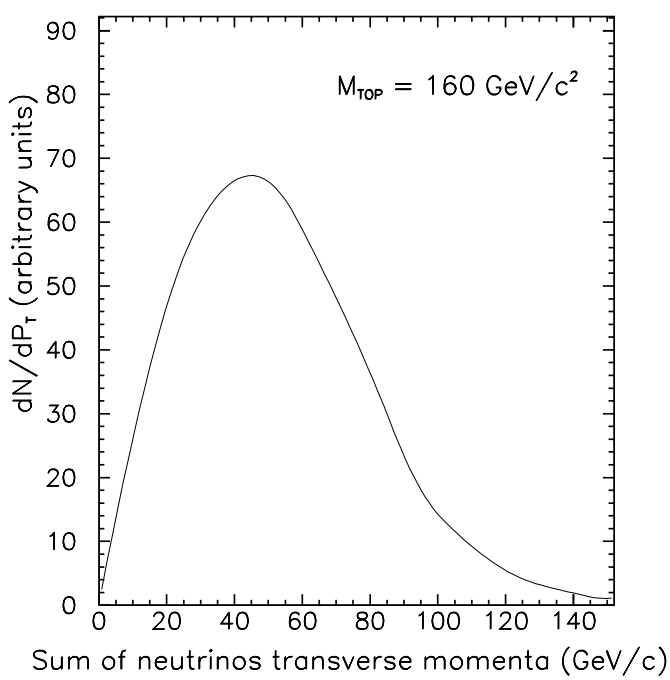

FIG. 36. Expected sum of neutrinos' transverse momenta in the dilepton channel ($p\bar{p} \rightarrow t\bar{t} \rightarrow l\nu b l\nu \bar{b}$) at $\sqrt{s} = 1.8$ TeV. From the ISAJET Monte Carlo event generator, for $M_{top} = 160$ GeV/c^2.

The most probable way to obtain two isolated leptons in $p\bar{p}$ collisions is through the Drell-Yan process, see Fig. 37. This mechanism yields e^+e^- and $\mu^+\mu^-$ pairs, but not $e\mu$

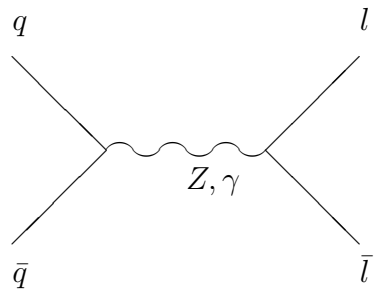

FIG. 37. Lowest order Feynman diagram for Drell-Yan production of lepton pairs.

pairs, except through $\tau\tau$ production, with both taus decaying leptonically. Here we begin by addressing backgrounds from direct Drell-Yan production of ee and $\mu\mu$ pairs.

The dominant Drell-Yan $p\bar{p} \to Z \to l^+l^-$ resonance can be easily eliminated by a l^+l^- invariant mass cut, with a modest ($\approx$ 25 %) loss in top acceptance. After the Z removal, the rate of high transverse momentum Drell-Yan pairs is still approximately two orders of magnitude higher than the $t\bar{t}$ dilepton rate (for $M_{top} \approx 150$ GeV/c^2). Additional background rejection can be obtained because (i) in Drell-Yan events there are no additional emitted jets at lowest order, and (ii) there are no neutrinos, and hence zero $\not{E}_T$ except for resolution effects. Higher order QCD corrections to the diagram shown in Fig. 37 give rise to final state jets, for example from gluons radiated off the q and $\bar{q}$ lines. For each additional jet, the rate is reduced by a factor of $O(\alpha_s) \approx 0.15$. Since there are two b-quark jets in $t\bar{t}$ dilepton events, one can achieve a significant background rejection factor, while maintaining efficiency for top, by demanding that at least two jets be detected in addition to the l^+l^- pair. In conjunction with a $\not{E}_T$ requirement, the Drell-Yan background can then be reduced to a tenth or less of the expected top signal for top masses as high as 200 GeV.

As was mentioned above, Drell-Yan $\tau\tau$ production, followed by leptonic decays of both taus ($\tau \to l\nu\nu$), constitutes an additional source of lepton pairs. Events from the $Z \to \tau\tau$ resonance cannot be easily removed because the invariant mass information is lost due to the presence of four neutrinos in the final state. However, the transverse momenta of the leptons and the $\not{E}_T$ for these events are significantly lower than in $t\bar{t}$ dilepton events, (see Figs. 38, 29, and 36). By requiring high transverse momentum leptons, high $\not{E}_T$, and two jets, this background can be reduced to approximately the same level as the ee and $\mu\mu$ Drell-Yan background. We note here that, unlike in the case of direct Drell-Yan production of ee and $\mu\mu$ pairs, this process can result in $e\mu$ final states.

Diboson production, (see Fig. 39), constitutes an additional source of high P_T dileptons and $\not{E}_T$. These are exceedingly rare processes, which are extremely interesting in their own right. The cross-section for WW production has been calculated to next-to-leading order, and at $\sqrt{s} = 1.8$ TeV it is estimated to be $\sigma(WW) \approx 10$ pb (Ohnemus, 1991a). This is the same as $\sigma(t\bar{t})$, for $M_{top} \approx 160$ GeV/c^2. When both W-bosons decay leptonically, the kinematics for the leptons and the neutrinos are very similar as those expected from $t\bar{t}$, which also results in a WW pair in the final state. The most efficient method that can be used suppress this background is to require that there be jets in the event. Just as in the Drell-Yan process, there are no jets at leading order in WW events. By demanding that there be two jets, the background is reduced by a factor of order $\alpha_s^2 \approx 0.02$. Backgrounds from WZ and ZZ production are smaller by over one order of magnitude because (i) the

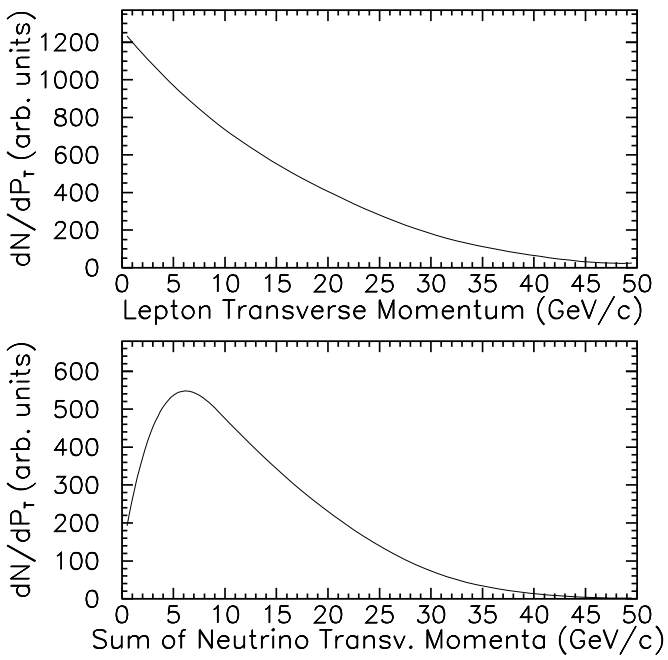

FIG. 38. The expected lepton and neutrino transverse momenta in $p\bar{p} \to Z \to \tau^+\tau^-$, $\tau^+ \to l^+\nu\nu$, $\tau^- \to l^-\nu\nu$ at $\sqrt{s} = 1.8$ TeV. From the ISAJET Monte Carlo generator.

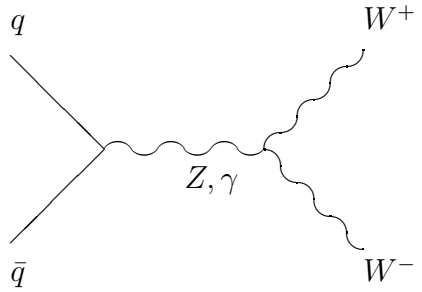

FIG. 39. Lowest order Feynman diagram for production of WW pairs in $p\bar{p}$ collisions; similar diagrams lead to WZ and ZZ production.

WZ and ZZ production cross-sections are significantly lower than that of WW (Ohnemus, 1991b; Ohnemus and Owens, 1991), (ii) the leptonic branching ratios of the Z are a factor of three smaller than those of the W, and (iii) l^+l^- pairs from Z decays can be eliminated with an invariant mass cut.

Additional backgrounds to the dilepton signal from fake leptons as well as doubly-semileptonic decays of $b\bar{b}$ pairs also have to be considered, but are generally found to be small. In a given analysis the signal-to-background level can be tuned by the choice of requirements. In general, raising the minimum P_T cut on the jets eliminates more background events than signal events. The reason for this is that for sufficiently high M_{top} the P_T spectrum of b-jets in dilepton top events is harder than the brehmstrahlung-like spectrum of jets in all the processes listed above. Higher $\not{E}_{\mathrm{T}}$ or lepton P_T requirements would considerably lower all backgrounds except the diboson background; the $Z \to \tau\tau$ background could be entirely eliminated by requiring the invariant mass of the l^+l^- pair to be higher than the Z

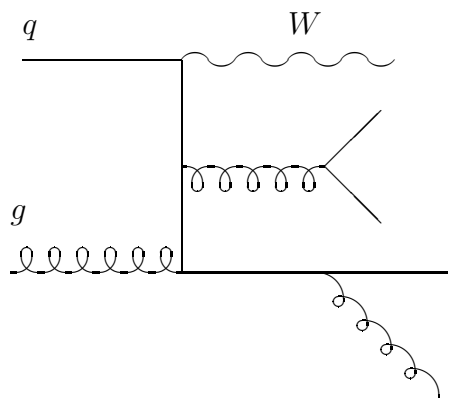

FIG. 40. Feynman diagram for $W+$ 4 jet production in $p\bar{p}$ collisions. Many other diagrams also contribute.

mass; requiring that jets be b-tagged would reduce all backgrounds by about two orders of magnitude. With sufficient luminosity, it should be possible to obtain very pure $t\bar{t}$ samples in the dilepton mode.

E. Lepton + jets mode

The branching ratio for this mode ($t\bar{t} \to q\bar{q}l\nu b\bar{b}$) is quite large, 24/81, see Table III. The signature consists of one isolated, high P_T lepton (e or μ), $\not{E}_T$ from the neutrino, two light quark jets (u, d, c, or s), and two b-quark jets.

As was discussed in Section V.B.2, in practice the number of detected jets is not expected to be always four. In order to maintain high efficiency, in most analyses the number of jets requirement is usually relaxed to ≥ 2 or ≥ 3, except for very high top mass, or where detection of a fourth jet is essential, e.g. for the determination of the top mass, see Section IX.

1. $W+$ jets background

For sufficiently high top mass, the dominant background to $t\bar{t}$ in the lepton + jets channels is due to W + multijets production, (see Fig. 40). The inclusive W production cross-section at the Tevatron is $\sigma(p\bar{p} \to W) \approx 20$ nb, over three orders of magnitude higher than the $t\bar{t}$ cross-section for $M_{top} > 150$ GeV/c^2. The cross-section for $W+$ N jets is suppressed by factors of order α_s^N.

Other backgrounds, such as $p\bar{p} \to b\bar{b}$ + jets followed by $b \to cl\nu$, and backgrounds from fake leptons also need to be carefully evaluated. For top masses above ≈ 40 GeV/c^2, where an efficient lepton + jets top selection can be devised based on **both** a high P_T lepton and high missing transverse energy, these backgrounds are in general found to be much smaller.

The importance of the W + multijets process as a background to top production, as well as to more exotic phenomena (e.g. supersymmetry), was noted soon after the first results from the S$p\bar{p}$S collider became available. As a result, a large theoretical effort was directed towards the calculation of the cross-sections and kinematic properties for $p\bar{p} \to W$ (or Z) + N jets. The first calculations, for N=1 or 2, were performed in the mid-eighties (Ellis and Gonsalves, 1985; Ellis, Kleiss, and Stirling, 1985; Kleiss and Stirling, 1985; Gunion and

Kunstz, 1985). These were then extended to final states with 3 (Berends, Giele, and Kuijf, 1989; Hagiwara and Zeppenfeld, 1989) and 4 jets (Berends *et al.*, 1991).

These calculations are performed at tree-level, and therefore they diverge as the angular separation between outgoing partons becomes very small or as their transverse momenta tend to zero (*collinear* and *infrared* divergences). However, far enough away from the regions of divergence, calculations are expected to be quite reliable, within the estimated theoretical uncertainties due to the missing higher order terms. Agreement is found between the measured W + jets cross-section and the theoretical prediction, (see Fig. 41). The degree of confidence in these LO calculations is such that the theoretical predictions have been used to extract the value of α_s from the W+ jet data (Lindgren, 1992; Alitti *et al.*, 1991c). More recent measurements of α_s (Abachi *et al.*, 1995c) have been based on the full NLO (order α_s) calculation for $p\bar{p} \to W$ (Giele, Glover, and Kosower, 1993).

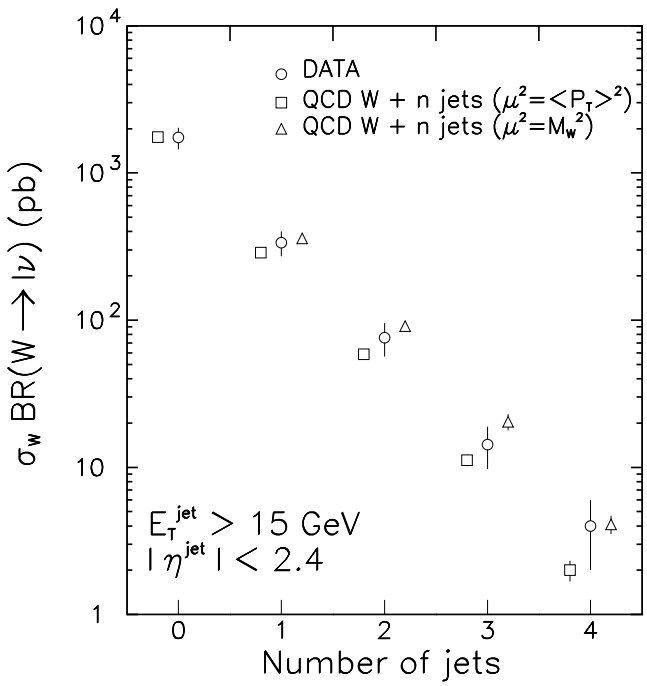

FIG. 41. Product of W cross-section (σ_W) times leptonic branching ratio as a function of jet multiplicity in $p\bar{p}$ collisions at $\sqrt{s} = 1.8$ TeV. The LO QCD predictions are shown for two different choices of the renormalization and factorization scale μ. The jet E_T threshold was set at 15 GeV. From F. Abe *et al.*, 1993b.

The LO theoretical calculation for $p\bar{p} \to W$ (or Z) + N jets, for N up to 4, is implemented in the VECBOS Monte Carlo event generator (Berends *et al.*, 1991), which is extensively used by the experimenters to model the W + jets background. VECBOS is a parton-level Monte Carlo generator, i.e. its output consists of parton four-vectors only. In order to properly simulate the response of the detector, hadronization effects are included by interfacing the VECBOS event generator with hadronization models based e.g., on independent parton-fragmentation (Field and Feynman, 1978), or the HERWIG model (Marchesini and Webber, 1984 and 1988). A model of the underlying event also needs to be included.

In what follows we will show several comparisons of theoretical expectations for $t\bar{t}$ and

$W+$ jets at Tevatron energies. These comparisons are performed at the parton-level only, i.e. hadronization, as well as detector effects, such as resolution smearing, efficiencies etc., are not included. Therefore, the discussion presented here is intended only as a general illustration of the issues involved.

The two processes are modeled with the ISAJET (for $t\bar{t}$) and VECBOS (for $W+$ jets) event generators. The ISAJET model employed here does not include initial and final state gluon radiation effects; the $t\bar{t}$ rates are normalized to a recent $p\bar{p} \rightarrow t\bar{t}$ cross-section calculation (Laenen, Smith, and van Neerven, 1994). In order to mimic actual experimental conditions, and to avoid the infrared and collinear divergencies in the $W+$ jets calculation, we impose the following requirements :

- P_T of partons (quarks or gluons) > 15 GeV/c
- $|\eta|$ of jets < 2
- P_T of leptons (electrons, muons and neutrinos) > 20 GeV/c
- $|\eta|$ of electron or muon < 1
- ΔR between jets > 0.5

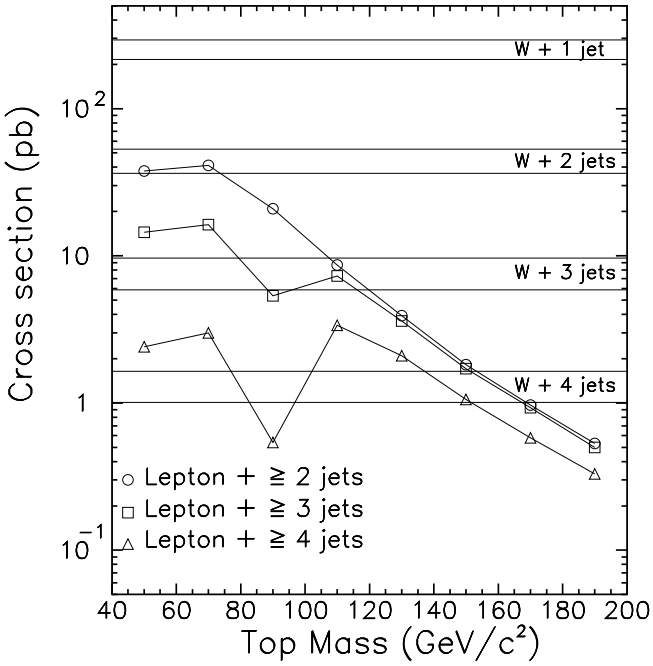

FIG. 42. Comparison of expected lepton + jets rates at the Tevatron for $t\bar{t}$ and $W+$ jets as a function of jet multiplicity and top mass. Detector and $t\bar{t}$ gluon radiation effects are not included. The $W+$ jets theoretical predictions are given as bands which reflect the effects of reasonable variations in the μ^2 scale. See text for details.

In Fig. 42 we show the expected rates of lepton + jets events from $t\bar{t}$ and $W+$ jets. (To get a feeling for the effects of gluon radiation, which are not included here, see for example

Fig. 35). Note the drop in efficiency for detecting a fourth jet in $t\bar{t}$ events, even at top masses of 200 GeV. As discussed in Section V.B.2, this is due to (i) final state quarks having P_T below the threshold (15 GeV/c in this case), and (ii) to the effect of jet merging. The expected signal-to-background, for a lepton + $\geq$ 3 jets selection, with a 15 GeV jet P_T threshold, varies between about 1/1 at M_{top} = 100 GeV/c^2 and 1/10 at M_{top} = 200 GeV/c^2. By requiring $\geq$ 4 jets, the signal-to-background for high top quark mass is significantly improved (by approximately a factor of 3 for M_{top} = 200 GeV/c^2). As we will show, further improvements in signal-to-background can be achieved by raising the P_T threshold on the jets. For top masses in the neighborhood of the W-mass, b-quarks are expected to have a soft transverse momentum spectrum, (see Fig. 34). As a result, the probability of detecting more than two jets in this mass region is particularly low. The required number of detected jets in a lepton + jets top search is therefore in general dependent on the top mass region that is being explored.

The cross-section for $W+$ N jets is proportional to α_s^N, therefore for each additional jet the W cross-section drops by a factor of order α_s. The $W+$ jets predictions in Fig. 42 are derived from VECBOS, which is based on a tree-level calculation with significant uncertainties. These uncertainties can be partially quantified by the stability of the calculation under changes in the factorization and renormalization scale μ. Here we present these predictions as bands that reflect the variation between the choices $\mu^2 = M_W^2$ and $\mu^2 =< P_T >^2$, where $< P_T >$ is the average transverse momentum of the partons in the event.

The relative uncertainty on the $W+$ N jets cross-section due to the choice of μ grows with the number of jets. This is because $\sigma(W+$ N jets) is proportional to $\alpha_s^N(\mu^2)$, so that when choosing a different μ^2, $\delta\sigma/\sigma$ becomes proportional to N $\delta\alpha_s/\alpha_s$ (where we have ignored the μ^2 dependence of the parton distribution functions that need to be convoluted with the partonic cross-section).

Because of these theoretical uncertainties, the existence of the top quark cannot be firmly established based on just the observation of an excess of $W+$ jets events. Additional information need to be employed to isolate a potential top signal. A number of possibilities will be discussed next.

2. Separation of $W+$ jets and $t\bar{t}$ for $M_{top} < M_W + M_b$

As discussed previously, if $M_{top} < M_W + M_b$, the W from the decay $t \to Wb$ will be virtual (W^*). In this case, the invariant mass of the $l\nu$ pair in $t\bar{t}$ events from $W^* \to l\nu$ will be smaller than both M_W and M_{top}. In contrast, the $l\nu$ pair in $W+$ jets events, which originates from real W decays, has invariant mass equal to the W mass. However, as was mentioned in Section V.B.3, the longitudinal component of the neutrino momentum cannot be measured, so the $l\nu$ invariant mass cannot be calculated. Fortunately, the *transverse mass* (M_T) of the $l\nu$ pair still provides significant discrimination between real and virtual W-decays (Rosner, 1989). The transverse mass is defined as the pseudo-invariant mass of the lepton and the neutrino constructed from the transverse components only :

$$M_T^2 \equiv (P_{T\nu} + P_{Tl})^2 - (\vec{P}_{T\nu} + \vec{P}_{Tl})^2 = 2P_{T\nu}P_{Tl}(1 - \cos\Delta\phi)$$

where $P_{T\nu}$ and P_{Tl} are the neutrino and lepton transverse momenta respectively, $\Delta\phi$ is the

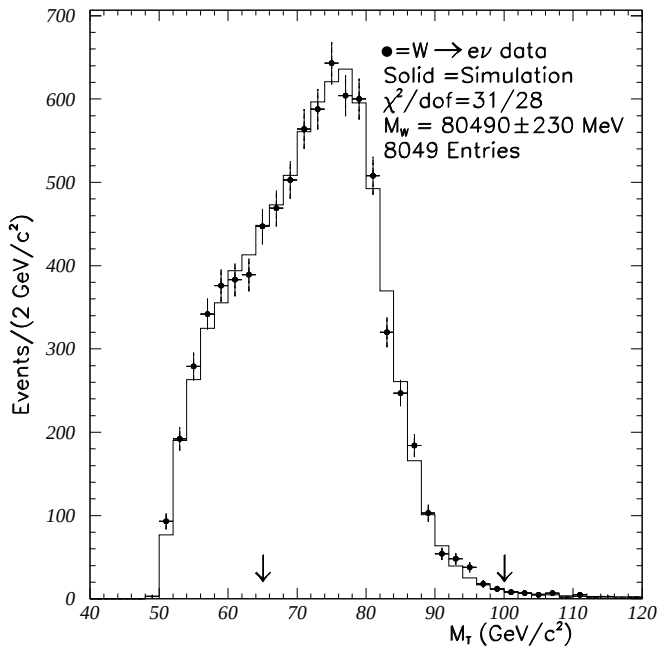

FIG. 43. Transverse mass distribution in $W \to e\nu$ decays. From the CDF collaboration, Frisch, 1995. This distribution is used to measure the W mass by fitting to Monte Carlo expectations; the arrows delimit the range of the fit.

angle between the two transverse momentum vectors, and where we have ignored the mass of the lepton compared to its momentum. Transverse mass distributions, (see Fig. 43), have the following properties : (i) M_T is less than or equal the invariant mass of the lepton-neutrino pair; (ii) M_T distributions are invariant under longitudinal boosts, hence they are independent of the longitudinal momentum of the pair; (iii) they result in Jacobian peaks at the original $l\nu$ invariant mass; (iv) they are fairly insensitive to the total transverse momentum of the pair. (The transverse mass distribution of a pair of invariant mass M and transverse momentum P_T differs from that of a $\mathrm{P}_T = 0$ pair by corrections of order $\approx (\mathrm{P}_T/\mathrm{M})^2$, see for example Barger and Phillips, 1987).

In Fig. 44 we show expected transverse mass distributions for $W+$ jets and $t\bar{t}$, with $\mathrm{M}_{top} = 70$ GeV/c^2. A top signal would result in a significant distortion of the transverse mass spectrum of $W+$ 2 jets events, even after accounting for smearing due to resolution effects (see Section VI). By concentrating on just the shape of the transverse mass distribution, uncertainties due to the theoretical expectation of the $W+$ jets rate do not enter in the analysis. Furthermore, the shape of the transverse mass distribution for the $W+$ jets background is dominated by the kinematics of the $W \to l\nu$ decay, and depends only weakly on the modeling of the W production properties. We note that the transverse mass method can be used to separate a top signal from the $W+$ jets background for both the $t\bar{t}$ and $W \to t\bar{b}$ production mechanisms.

For higher top masses, the $l\nu$ transverse mass distributions in $t\bar{t}$ and $W+$ jets events become indistinguishable, since top quarks will decay into real W bosons. In order to separate signal from background in the lepton + jets mode, one then has to rely on the

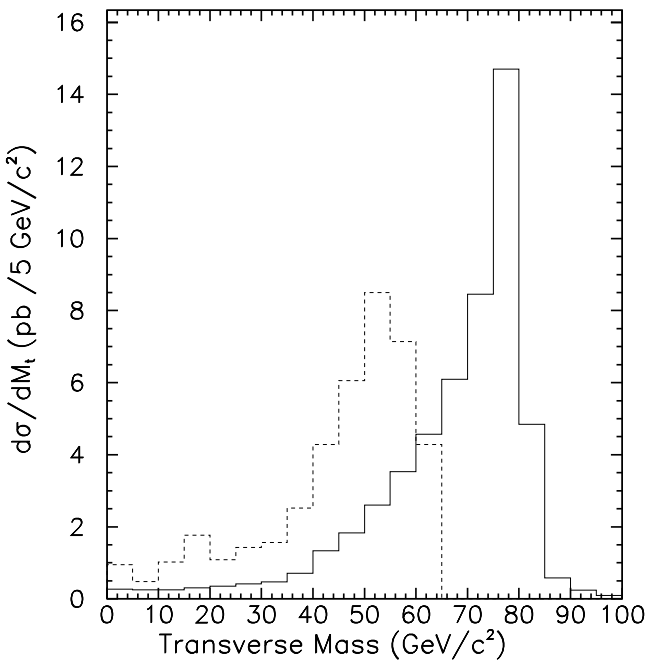

FIG. 44. Expected transverse mass distributions for $W+$ 2 jets (solid) and $p\bar{p} \to t\bar{t} \to$ lepton + 2 jets, for M_{top} = 70 GeV/c^2 (dashed). This is at Tevatron energies (1.8 TeV). The $W+$ 2 jets calculation has been performed with a scale $\mu^2 =< P_T >^2$. Detector and $t\bar{t}$ gluon radiation effects are not included. Relative normalizations are from Monte Carlo. See text for details.

kinematic differences between the two processes, and/or the fact that $t\bar{t}$ events always contain two b-quarks in the final state.

3. Kinematic differences between $t\bar{t}$ and $W+$ jets

Several possible ways of extracting a top signal from the $W+$ jets background using kinematic signatures have been suggested in the literature (Berends *et al.*, 1989; Baer, Barger and Phillips, 1989; Agrawal and Ellis, 1989; Giele and Stirling, 1990; Berends, Tausk, and Giele, 1993; Barger, Ohnemus, and Phillips, 1993; Benlloch, Sumorok, and Giele, 1994; Cobal, Grassmann, and Leone, 1994; Barger *et al.*, 1995). Briefly, the differences between the two processes are the following :

- In $t\bar{t}$ events, the invariant mass of three of the jets should reconstruct to the top mass, and two out of these three jets should have invariant mass equal to the W mass. This is the consequence of the decay chain $t \to Wb$ followed by $W \to q\bar{q}$. Of course no such invariant mass enhancements occurs for the $W+$ jets background.

- Jets in $W+$ jets events tend to have lower transverse momentum than jets in $t\bar{t}$ events. This is due to the fact that jets in W events arise from a brehmstrahlung-like process. For the same reason, these jets also tend to be emitted more in the forward direction than jets from the decay of centrally produced top quarks.

- Top events tend to be more spherical and aplanar than $W+$ jets events. The reason for this is that the QCD $W+$ jets matrix element introduces significant spatial correlations between the jets, e.g. gluon brehmstrahlung ($q \to qg$) and gluon splitting ($g \to q\bar{q}$) favor small opening angles between partons in the final state.

At first glance two-jet and three-jet invariant masses appear to be the most attractive discriminators. Unfortunately, because of the poor jet energy resolution and the number of possible jet combinations that may be present in a given event, this method turns out to be useful only if very large statistics data sets are available. We will not further discuss jet invariant masses in this Section. We will however revisit the issue in Section IX, where the measurements of the top mass will be reviewed.

As an illustration of the kinematic differences between W and top events at the Tevatron, we show the Monte Carlo transverse momentum and pseudorapidity distributions of jets in lepton + 4 jets events for $W+$ 4 jets and $t\bar{t}$ (see Figs. 45, 46, and 47). As anticipated, jets in top events tend to be more central and to have higher transverse momenta. The scalar sum of the transverse momenta of all of the jets in the event is a simple global variable that is expected to provide good discrimination between signal and background, (see Fig. 46).

Note that the choice of scale in the $W+$ jets calculation affects not only the expected rate, but also the shape of kinematic distributions, particularly the jet transverse momentum spectrum. Comparing the distributions for the two equally arbitrary, and a-priori equally reasonable choices, $\mu^2 =< P_T >^2$ and $\mu^2 = \mathrm{M}_W^2$, it is found that the $\mu^2 = \mathrm{M}_W^2$ choice results in a harder jet P_T spectrum, see Figs. 45 and 46. This can simply be understood as follows. The cross-section for a $W+$ N jets event is just given by the convolution of the relevant matrix element with the parton distribution functions. Neglecting the μ^2-dependence of the parton distribution functions, the only scale dependence is due to the factor $\alpha_s^N(\mu^2)$ which appears in the $W+$ N jets matrix element. Because of the running of the strong coupling constant, the choice of an event-by-event scale such as $\mu^2 = < P_T >^2$ results in a higher probability for events with low P_T jets as compared to what one would obtain by choosing a global scale like $\mu^2 = \mathrm{M}_W^2$.

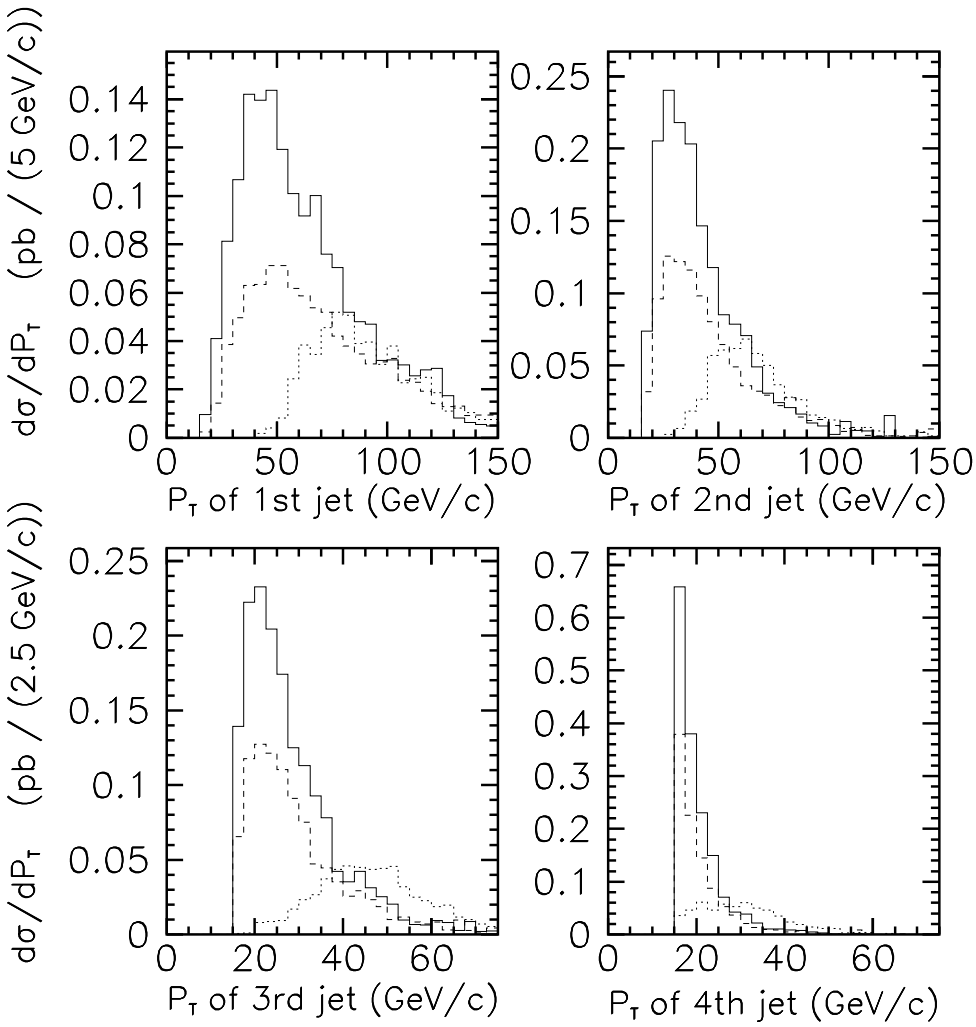

FIG. 45. Expected transverse momentum (P_T) distributions of the first, second, third, and fourth highest P_T jet in $W+$ 4 jets and $t\bar{t}$ events. For $p\bar{p}$ collisions at $\sqrt{s} = 1.8$ TeV. Solid line : $W+$ 4 jets, scale $\mu^2 =< P_T >^2$; dashed line : $W+$ 4 jets, scale $\mu^2 = M_W^2$; dots : $t\bar{t}$, $M_{top} = 170$ GeV/c^2. Note the expanded horizontal scale for the third and fourth jets and that all jets have been required to have $E_T > 15$ GeV. Detector and $t\bar{t}$ gluon radiation effects are not included. See text for details.

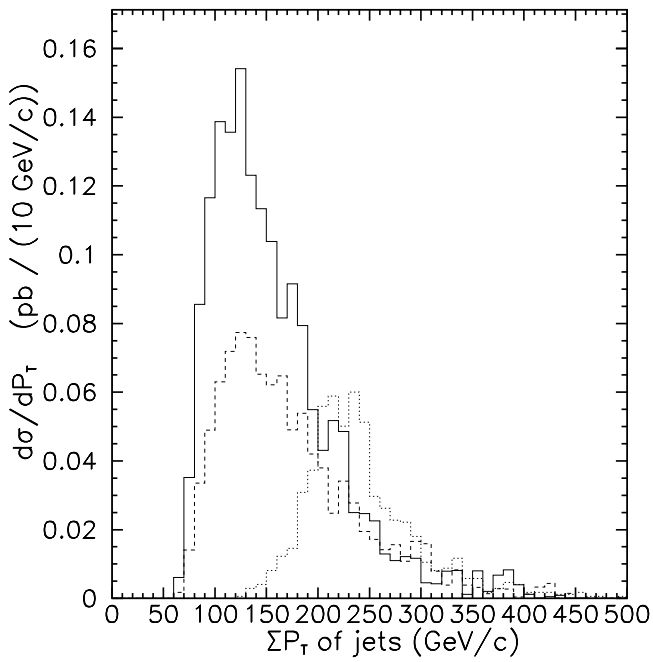

FIG. 46. Expected scalar sum of transverse momenta of 4 jets in $W+$ 4 jets and $t\bar{t}$ events. For $p\bar{p}$ collisions at $\sqrt{s} = 1.8$ TeV. Solid line : $W+$ 4 jets, scale $\mu^2 =< P_T >^2$; dashed line : $W+$ 4 jets, scale $\mu^2 = \mathrm{M}_W^2$; dots : $t\bar{t}$, $\mathrm{M}_{top} = 170$ GeV/c^2. Detector and $t\bar{t}$ gluon radiation effects are not included. See text for details.

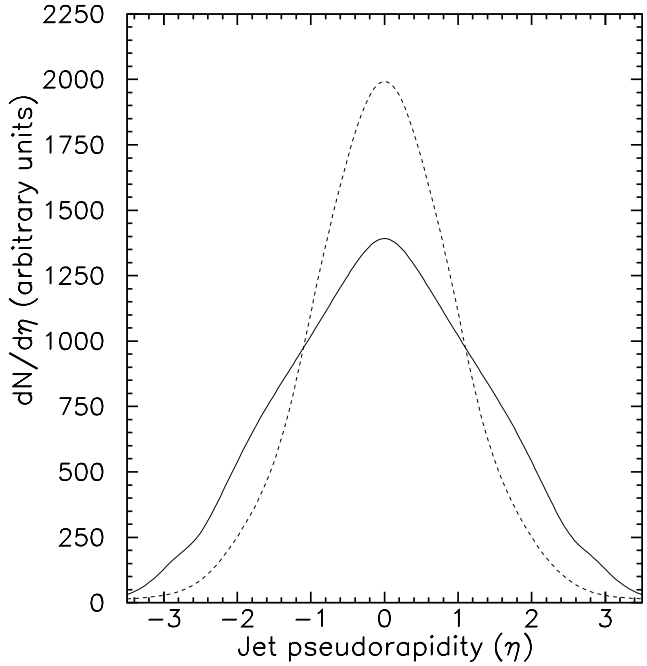

FIG. 47. Pseudorapidity distribution of jets in $W+$ 4 jets and $t\bar{t}$ events. For $p\bar{p}$ collisions at $\sqrt{s} =$ 1.8 TeV. Solid line : $W+$ 4 jets, scale $\mu^2 =< P_T >^2$; dashed line : $t\bar{t}$, $\mathrm{M}_{top} = 170$ GeV/c^2.

Another discriminant that can be employed is *aplanarity*. Aplanarity is defined as $\mathcal{A} \equiv 3/2\lambda_1$, where λ_1 is the smallest eigenvalue of the matrix $M_{ab} = \sum P_a P_b / \sum P^2$, where P_i are the cartesian components of momentum of the parton, P is the magnitude of the three-momentum, and the sum is over all final state objects: jets, electrons, muons, and neutrinos. Zero aplanarity corresponds to planar events. $W+$ jets events are expected to be more planar than $t\bar{t}$ events, (see Fig. 48).

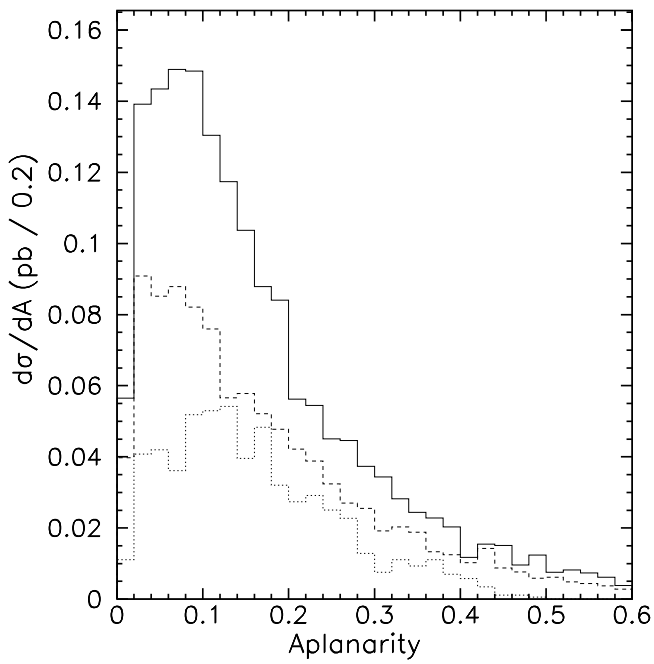

FIG. 48. Expected aplanarity for $W+$ 4 jets and $t\bar{t}$ events. For $p\bar{p}$ collisions at $\sqrt{s} = 1.8$ TeV. Solid line : $W+$ 4 jets, scale $\mu^2 =< P_T >^2$; dashed line : $W+$ 4 jets, scale $\mu^2 = \mathrm{M}_W^2$; dots : $t\bar{t}$, $\mathrm{M}_{top} = 170$ GeV/c^2. Aplanarity here is calculated in the laboratory frame from the four jets, the lepton, and the neutrino. Detector and $t\bar{t}$ gluon radiation effects are not included. See text for details.

It is clear from this discussion that in order to extract a top signal from kinematic distributions, special attention must be payed to the systematic uncertainties associated with the theoretical modeling of the $W+$ jets backgrounds. The theoretical uncertainties can be bounded by comparing the data with theoretical predictions in kinematic regions where the top signal is small, e.g. in samples of events with low jet multiplicity and/or low transverse momentum jets. Deviations from the $W+$ jets expectations in kinematic regions where the top quark is expected to contribute would then signal the presence of $t\bar{t}$ events in the sample (or possibly of some other source of $W+$ jets events beyond standard QCD production).

Samples of $Z+$ jets events in principle provide the ideal testing ground for the $W+$ jets calculation. Unfortunately, at $\sqrt{s} = 1.8$ TeV the cross-section for $p\bar{p} \to Z$ is a factor of 3.3 smaller than that for $p\bar{p} \to W$. Furthermore, the leptonic branching ratio of the Z is also a factor of three smaller than that of the W. As a result, the number of reconstructed Z events is approximately one order of magnitude smaller than that of W events. Because

of the limited statistics, Z events, although useful as a first order check, do not provide stringent bounds on the modeling of vector boson + ≥ 3 jets production. We will discuss these issues in more detail in Section VIII, where the experimental results will be reviewed.

4. b-quark tagging

An alternative method that can be employed to separate the $t\bar{t}$ signal from the $W+$ jets background is to *tag* the b-quarks in top events. Each $t\bar{t}$ event contains one b- and one $\bar{b}$-quark from the decays $t \to Wb$ and $\bar{t} \to W\bar{b}$, whereas the jets in W events arise mostly from the fragmentation of gluons and light quarks.

There are two ways to detect the presence of b-quarks. The first method is based on the detection of additional leptons from the semileptonic decays $b \to cl\nu$ or $b \to c \to sl\nu$. The semileptonic branching ratios of bottom and charm quarks are approximately 10% per lepton species (Montanet *et al.*, 1994). There is on average about one lepton (electron + muon) from b or c decay in each top event, where we have also included the contributions from c-quarks from $W \to c\bar{s}$, which occurs in one half of all hadronic W decays. From an experimental point of view, detection of these leptons is more difficult than detection of leptons from W decays, because these leptons tend to have a much lower transverse momentum (compare Figs. 49 and 29). Furthermore, these leptons are not isolated but are accompanied by nearby hadrons from the b-quark fragmentation and the b-hadron decay. This makes efficient detection of electrons particularly challenging.

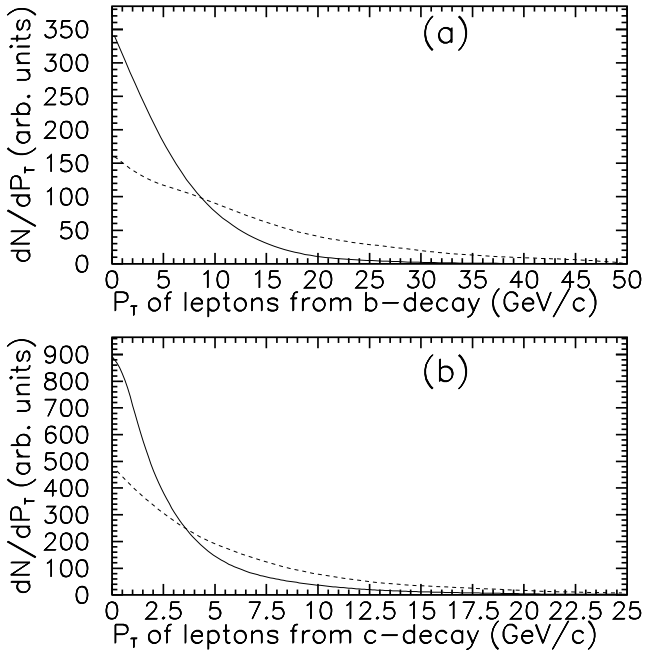

FIG. 49. (a) Expected transverse momentum of leptons from $t \to b \to cl\nu$ Solid line : $M_{top} = 110$ GeV/c^2; dashed line : $M_{top} = 170$ GeV/c^2. (b) Same as (a), but for $t \to b \to c \to sl\nu$. For $p\bar{p} \to t\bar{t}$ at $\sqrt{s} = 1.8$ TeV, from the ISAJET Monte Carlo generator. Note the different horizontal scales in (a) and (b).

Bottom and charm quarks can also be tagged by exploiting the long lifetime of b- and c-hadrons. The recent compilation from the Particle Data Group (Montanet *et al.*) reports a lifetime of 1.537 ± 0.021 ps for b-hadrons, and 0.415 ± 0.004 ps and 1.057 ± 0.015 ps for neutral and charged D mesons respectively. As a consequence of the long lifetime, b-hadrons in a top event are expected to travel several mm before decaying, (see Fig. 50). With the advent of silicon microstrip-vertex detectors, the position of decay vertices can be measured with resolutions of order 100-150 μm. It then becomes possible to separate with good efficiency the secondary vertex where the b-decay occurs from the primary $p\bar{p}$ interaction point.

There are two main sources of background to the lepton- or vertex-tagged $t\bar{t}$ signal. The first one is instrumental. Hadrons originating from the fragmentation of gluons and light quarks in $W+$ jets events can be misidentified as muons or electrons. This happens for example when hadronic showers in the calorimeter fluctuate to mimic the electron signature, or when kaons and pions decay to muons. Also, track mismeasurements or decays of other long-lived particles such as Λ and K_s can result in the reconstruction of spurious detached vertices. Needless to say, these effects have to be considered very carefully. As we will discuss in Section VIII, sufficiently good instrumental background rejection has been achieved, and methods to precisely estimate the remaining background have been developed.

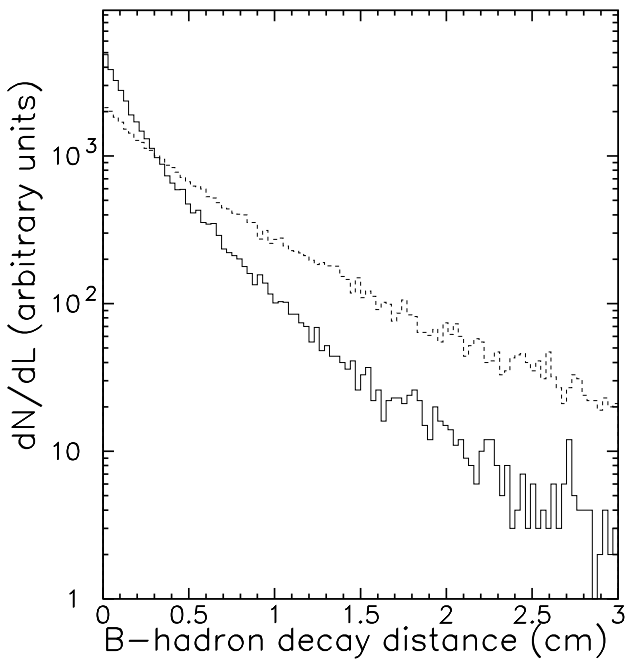

FIG. 50. Distance travelled by b-hadrons in top events before decaying. Solid line : M_{top} = 110 GeV/c^2; dashed line : M_{top} = 170 GeV/c^2. This distance is calculated by convoluting the momentum spectrum of b-hadrons from the ISAJET $p\bar{p} \to t\bar{t}$ ($\sqrt{s}$ = 1.8 TeV) Monte Carlo with their lifetime.

The second background source stems from the fact that a small fraction of jets in $W+$ jets events will contain heavy-quarks (b or c). In the absence of additional kinematic information, these events constitute an irreducible physical background to the lepton + jets + b-tag

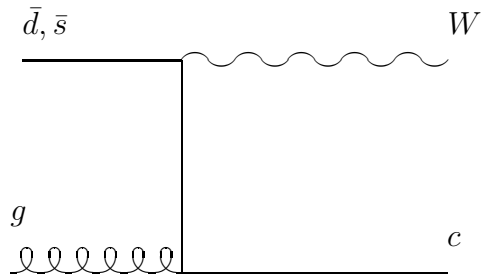

FIG. 51. Lowest order Feynman diagram for production of $W+$ charm in $p\bar{p}$ collisions. At higher order, $gg \to Wc\bar{s}$ diagrams also contribute.

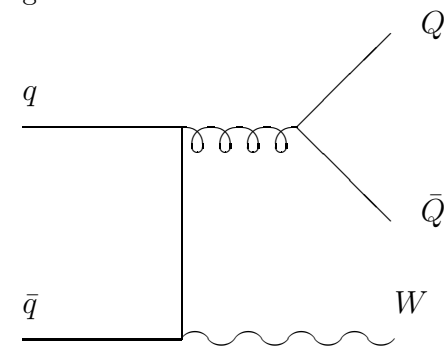

FIG. 52. Lowest order Feynman diagram for production of $WQ\bar{Q}$ in $p\bar{p}$ collisions. $Q = c$ or b.

$t\bar{t}$ signature which needs to be carefully evaluated. A comprehensive discussion of these backgrounds, in the context of the CDF experiment, is given by F. Abe *et al.*, 1994a, and will be summarized below. The discussion here applies equally well to lepton or vertex b-tagging methods.

Heavy-quarks in $W+$ jets event can be produced singly, in the process $\bar{s}g \to Wc$ or $\bar{d}g \to Wc$, (see Fig. 51), or in pairs, when a gluon in a $W+$ jets event *splits* into a $c\bar{c}$ or $b\bar{b}$ pair, (see Fig. 52). The gluon splitting probability, $g \to Q\bar{Q}$, $Q = c$ or b, is estimated to be of order a few percent, with significant theoretical uncertainties (Mangano and Nason, 1992; Müller and Nason, 1985 and 1986). Experimental extractions of the $g \to c\bar{c}$ probability in both $p\bar{p}$ (Ikeda, 1990, F. Abe *et al.*, 1990d) and e^+e^- collisions (Akers, 1995) are found to be in agreement with the results of the theoretical calculations, within the large experimental and theoretical uncertainties. In what follows we will refer to these two processes as Wc and $WQ\bar{Q}$ respectively.

The Wc background estimation begins by computing the fraction of $W+$ jets events that contain a single c-quark, from diagrams like the one shown in Fig. 51, using the VECBOS and HERWIG event generators. This fraction is found to be of order 8%, with small variations depending on the jet multiplicity and the choice of the input parton distribution function for strange quarks in the proton. To obtain an absolute background prediction, this fraction is then multiplied by the number of observed $W+$ jets event and the tagging efficiency for c-quarks. The tagging efficiency for these events clearly depends on the details of the tagging algorithm. However, it is in general much smaller (typically by a factor of order 5) than the tagging efficiency for $t\bar{t}$ since (i) the tagging efficiency for c-quarks is lower than that of b-quarks because e.g. there are fewer tracks in a c decay than in a b decay, and (ii) there are multiple b- and c-quarks in a top event that can potentially be tagged. Therefore, as a result

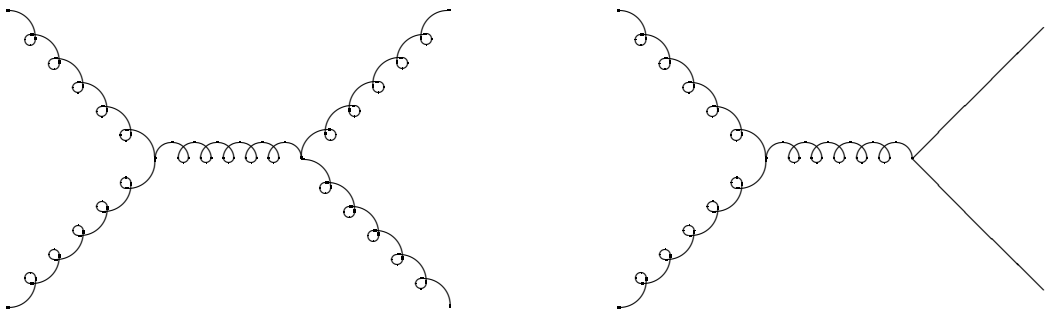

FIG. 53. Two of the possible LO Feynman diagrams for jet production in $p\bar{p}$ collisions: $gg \to gg$ and $gg \to q\bar{q}$.

of the small probability for a Wc event and its small tagging efficiency, the Wc background is much smaller than the expected tagged $t\bar{t}$ rate. The highly uncertain overall normalization of the $W+$ jets theoretical calculation does not enter in the background estimate, since only the **fraction** of Wc events is taken from theory.

The $WQ\bar{Q}$ background is more important because the tagging efficiency for $Wb\bar{b}$ is comparable to that of $t\bar{t}$. This background can be estimated in two ways. The first method (*Method I*) requires a minimum of theoretical input, and is expected to yield an overestimate of the $WQ\bar{Q}$ background. The alternative method, (*Method II*), is based on the state-of-the-art theoretical understanding of heavy quark production,

At the heart of the Method I background calculation is the assumption that the heavy flavor content (b or c) of jets in $p\bar{p} \to$ jets (*generic-jets*, see Fig. 53) is the same or larger than the heavy flavor content of jets in $W+$ jets events. Accepting this assumption for now, we proceed to describe the Method I background calculation.

The generic-jet sample includes gluon and light-quark jets, as well as a small fraction of heavy-quark jets. A generic-jet can be tagged due to instrumental effects resulting in a false tag of a light-quark or gluon jet, or due to the b- or c-quark contribution. Operationally, a *tag-rate* is measured for generic-jets as the probability of tagging a generic-jet as a function of several relevant variables (e.g. jet P_T, track multiplicity). The generic-jet tag-rate is then applied to the sample of jets in $W+$ jets events, to predict an upper limit for the sum of the instrumental and $WQ\bar{Q}$ backgrounds to the $t\bar{t} \to W+$ jets + b-tag signature. From an experimental point of view this has the advantage that both the instrumental and $WQ\bar{Q}$ backgrounds are estimated simultaneously directly from the data. No a-priori knowledge of the tagging efficiency, or the $WQ\bar{Q}$ content of the sample, is needed.

We now turn to a discussion of the theoretical assumption on which the Method I $WQ\bar{Q}$ background calculation is based. At Tevatron energies, generic-jets in the relevant P_T range (20-150 GeV/c) consist predominantly of gluon-jets. There will also of course be a contribution from light-quark jets as well as $p\bar{p} \to Q\bar{Q}$. The lowest order Feynman diagrams for direct production of $b\bar{b}$ and $c\bar{c}$ pairs in $p\bar{p}$ collisions are identical to the ones for $t\bar{t}$ production shown in Fig. 16. For the b- and c-quarks however, it is found that higher order diagrams such as the ones displayed in Fig. 54 contribute a very significant amount to the $p\bar{p} \to Q\bar{Q} + X$ cross-section. For instance, the gluon splitting diagram is believed to account

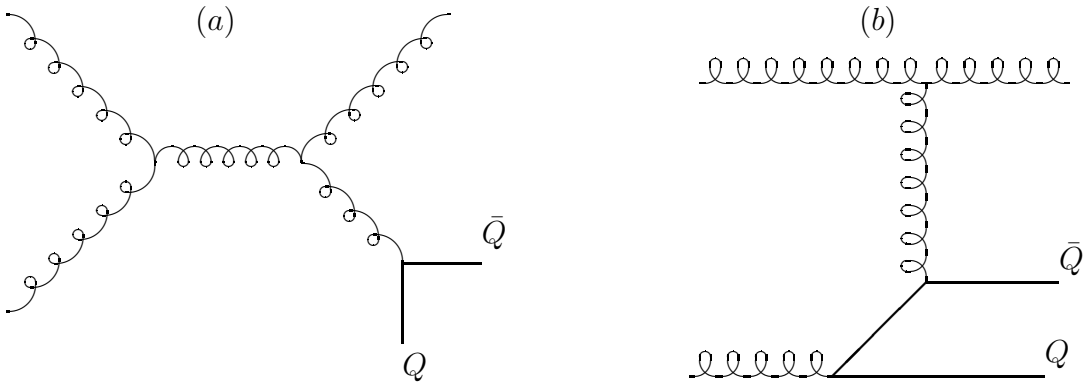

FIG. 54. Higher order Feynman diagrams for $Q\bar{Q}$ production in $p\bar{p}$ collisions: (a) gluon splitting; (b) flavor excitation.

for of order 70% of the $b\bar{b}$ and $c\bar{c}$ production rate (Mangano, Nason, and Ridolfi, 1992).

The heavy-flavor content of generic-jets is expected to be higher than that of jets in $W+$ jets events for two reasons : (i) in $W+$ jets events there are no contributions from lowest order, direct, $Q\bar{Q}$ production (Fig. 16) and next-to-leading order flavor excitation (Fig. 54b), and (ii) generic-jets consist mostly of gluon jets which can result in $Q\bar{Q}$ pairs via gluon splitting, whereas the jets in $W+$ jets events consist of an approximately equal mixture of gluon and light-quark jets. These very simple qualitative arguments are borne out by a more quantitative calculation, as we will illustrate below.

The second way of estimating the $WQ\bar{Q}$ background (Method II) is based on an explicit calculation of the $WQ\bar{Q}$ process. Just as in the Wc case, uncertainties on the overall normalization of the $W+$ jets calculation are minimized by using as the theoretical input the fraction of $W+$ jets events that contain a $Q\bar{Q}$ pair, rather than the absolute rate prediction. The absolute background level is then estimated by multiplying this fraction by the number of observed $W+$ jets events and the tagging efficiencies for $Wc\bar{c}$ and $Wb\bar{b}$.

The $WQ\bar{Q}$ fraction is estimated using a combination of the HERWIG Monte Carlo event generator and the lowest order $WQ\bar{Q}$ matrix element (Fig. 52) calculation (Mangano, 1993). This calculation differs from the $W+$ jets calculation in that it includes all mass effects and is therefore free from collinear and infrared divergencies. Since the calculation does not include higher order terms, it cannot be used directly to estimate the $WQ\bar{Q}$ rate in events with more than two jets, which are the most relevant for the top search. Instead, the results of the exact calculation are compared to those of HERWIG, where the $Q\bar{Q}$ pairs are produced by gluon splitting from initial- and final-state parton evolution. The HERWIG results are found to be in good agreement with those of the $WQ\bar{Q}$ matrix element calculation. The gluon splitting process in HERWIG also provides a good description of the measured tagging rate in generic-jet events, giving further evidence for the validity of the HERWIG model. Thus, this model is used to predict the fraction of $WQ\bar{Q}$ events as a function of jet multiplicity. For the sample of $W+ \geq 3$ jets, it is estimated that the fractions of W events containing a $b\bar{b}$ or $c\bar{c}$ pair are approximately 3% and 5% respectively. The systematic uncertainties associated with these predictions are clearly significant and are estimated to be at the level

of 80%. The $WQ\bar{Q}$ background estimated with this method turns out to be approximately a factor of three lower than the conservative estimate made under the assumption that the heavy flavor content of jets in $W+$ jets events is the same as that of generic-jets.

To assess the impact of the $WQ\bar{Q}$ background on the top search, we re-examine the predicted rates of lepton + jets from $t\bar{t}$ and $W+$ jets. For example, from Fig. 42, the signal-to-background for a $W+$ 4 jets selection, with jet P_T threshold set at 15 GeV/c, is expected to vary from approximately 3/1 at M_{top} = 120 GeV/c^2 to approximately 1/3 at M_{top} = 200 GeV/c^2. With the fraction of $W+$ jets events containing a $Q\bar{Q}$ pair given above, the signal-to-background, ($t\bar{t}$ vs. $WQ\bar{Q}$) will be at least of the order of 7/1. Thus, provided the instrumental backgrounds can be adequately controlled, and enough luminosity is available to the experimenters, the top signal can be separated from the $W+$ jets background with b-tagging methods.

VI. EARLY SEARCHES FOR THE TOP QUARK

Experimental searches for the top quark began immediately following the discovery of the b-quark. In this Section we will review these searches up to approximately 1990.

A. Searches in e^+e^- collisions

In e^+e^- collisions, top quarks would be produced in pairs through e^+e^- annihilation into a photon or a Z. Since at leading order this is a purely electroweak process, the production cross-section can be accurately calculated. At center-of-mass energies well below the Z mass, where annihilation of the e^+e^- pair into a photon dominates, $t\bar{t}$ production would manifest itself as an increase by an amount $\delta R \approx 3Q_{top}^2 = 4/3$ in the ratio $R = \sigma(e^+e^- \to \text{hadrons}) / \sigma(e^+e^- \to \mu^+\mu^-)$ well above the energy threshold for the production of a $t\bar{t}$ pair. This expected increase in R is largely independent of the top quark decay mode, as long as the top-quark decays into final states containing hadrons.

Between 1979 and 1984, measurements of R were performed at the PETRA e^+e^- collider in the center-of-mass energy range between 12 and 46.8 GeV (Barber *et al.*, 1979 and 1980; Berger *et al.*, 1979 and 1980; Bartel *et al.*, 1979a, 1979b, and 1981; Brandelik *et al.*, 1982; Adeva *et al.*, 1983a, 1983b, 1985, and 1986; Behrend *et al.*, 1984; Althoff *et al.*, 1984a and 1984b). The value of R was found to be consistent with Standard Model expectations without a top-quark contribution. Event topology studies gave no evidence for excesses of spherical, aplanar, or low thrust events that could be attributed to $t\bar{t}$ production. The measured rate of prompt muons was also found to be in agreement with expectations from models of c- and b-quark production and decay, and could not accommodate a contribution from semileptonic decays of top quarks. Existence of the top quark with mass below 23.3 GeV/c^2 was ruled out at the 95% confidence level (C.L.).

Similar searches were later performed at the TRISTAN collider, which reached a center-of-mass energy of 61.4 GeV (Yoshida *et al.*, 1987; Sagawa *et al.*, 1988; Adachi *et al.*, 1988; Igarashi *et al.*, 1988; K. Abe *et al.*, 1990). No evidence for top quark production was reported, resulting in a lower limit on the top mass of 30.2 GeV/c^2.

In 1989-90, the SLC and LEP e^+e^- colliders, with $\sqrt{s} \approx \mathrm{M}_z$ became operational. Studies of event topologies and measurements of the Z width were found to be inconsistent with a $Z \to t\bar{t}$ contribution, and resulted in lower limits on the top quark mass as high as 45.8 GeV/c^2 (Abrams *et al.*, 1989; Akrawi *et al.*, 1990a; Decamp *et al.*, 1990; Abreu *et al.*, 1990b and 1991; Adriani *et al.*, 1993).

B. Early searches in $p\bar{p}$ collisions assuming Standard Model top-quark decay

With the emergence in the 1980's of $p\bar{p}$ colliders, first at CERN and then at Fermilab, and with evidence from e^+e^- experiments pointing towards a very high mass for the top quark, focus in the search for top rapidly shifted to hadron colliders. The obvious advantage of hadron colliders for top physics is the high center of mass energy, which enables the exploration of higher mass regions. However, unlike in e^+e^- collisions, the large backgrounds make it impossible to directly search for the top quark in a model-independent way. It is necessary to concentrate on particular signatures, based for example on the Standard Model decay modes of the top quark discussed in the previous Section.

In this Section we will discuss searches for the top quark in $p\bar{p}$ collisions, assuming Standard Model top-quark decay, that were carried out in the mid to late 1980's at CERN and Fermilab. No evidence for top quark production was uncovered, leading to lower limits on the top quark mass as high as 91 GeV/c^2, at the 95% C.L.. These searches do not result directly in limits on the top mass, but rather in upper limits on the product of top production cross-section and branching ratio for top quark decay. To turn these limits into mass limits for the top quark, it is necessary to (i) assume that the top quark decays as $t \to Wb$, as prescribed by the Standard Model, and (ii) use theoretical expectations for the production cross-section. As discussed in Section IV, the main production mechanisms are $W \to t\bar{b}$ decays at S$p\bar{p}$S energies, and $t\bar{t}$ pair production at Tevatron energies. The expected cross-section for $p\bar{p} \to W \to t\bar{b}$ can be reliably predicted from direct measurements of $p\bar{p} \to W \to l\nu$; on the other hand, there are significant theoretical uncertainties on the predicted top-pair production cross-section as a function of the top mass, see Section IV, Figs. 21 and 22. Since these theoretical uncertainties are difficult to quantify, limits on M_{top} in the absence of a top signal in the data are placed based on the lower range of the calculation of the top production cross-section. This results in conservative 95% C.L. lower limits on M_{top}.

Initial results reported by the UA1 collaboration (Arnison *et al.*, 1984; Revol, 1985) at the CERN S$p\bar{p}$S collider ($\sqrt{s}$ = 630 GeV/c), seemed to be consistent with production of a top quark of mass 40 ± 10 GeV/c^2. These results were based on the observation of 12 isolated lepton + 2 jets events, with an expected background of approximately 3.5 events in an exposure with an integrated luminosity of 200 nb^{-1} (Revol, 1985). In these events, the invariant mass of the lepton, neutrino and one of the jets was found to cluster around a common value of approximately 40 GeV/c^2, while the invariant mass of the two jets, the lepton, and the neutrino was found to be consistent with the W mass. This is the expected signature for the process $p\bar{p} \to W \to t\bar{b}$, followed by $t \to bl\nu$. The excess of events over the background prediction was also consistent with the expected top production cross-section, providing further evidence for a top quark with $\mathrm{M}_{top} \approx 40$ GeV/c^2.

These first results were however not supported by a subsequent UA1 analysis (Albajar *et al.*, 1988), with a higher statistics data sample, as well as a more complete evaluation of the backgrounds. This analysis was based on samples of events with one isolated muon + ≥ 2 jets or one isolated electron + ≥ 1 jet. The integrated luminosity was 700 nb^{-1}. Given this integrated luminosity, and the expected top production rate, this search was sensitive to a top quark with $M_{top} < 55$ GeV/c^2. A maximum lepton-neutrino transverse mass requirement of 40 (45) GeV/c^2 was imposed in the muon (electron) sample to substantially reduce the $W \rightarrow l\nu$ background, while maintaining good efficiency for top quarks in the relevant mass range. No missing transverse energy ($\not\!\!E_T$) requirement was imposed, since for low top mass the probability for **both** the lepton and the neutrino in $t \rightarrow bl\nu$ to have high transverse momentum is low.

With no $\not\!\!E_T$ requirement, the backgrounds from fake leptons, Drell-Yan l^+l^- pairs, as well as $b\bar{b}$ and $c\bar{c}$ production are significant. The number of observed events was found to be fully consistent with the non-top background contribution only. Furthermore, it was shown that the event selection requirements resulted in background invariant mass distributions that were similar to those expected from top-quark production and decay (for $M_{top} \approx 40$ GeV/c^2). Thus, this property of the background accounted for the features of the invariant mass distributions observed in the previous analysis. Dilepton events were also studied, and their properties were found to be in agreement with expectations from semileptonic decays in $b\bar{b}$ and $c\bar{c}$ events.

An upper limit on the combined $W \rightarrow t\bar{b}$ and $t\bar{t}$ cross-sections was extracted from the background-subtracted lepton + jets event rates, as well as kinematic distributions such as those of jet E_T, $\not\!\!E_T$, and lepton isolation. At the time that these results were obtained, only a LO calculation for $p\bar{p} \rightarrow t\bar{t}$ was available. Using a conservative value for this cross-section the limit was inferred to be $M_{top} > 44$ GeV/c^2 at the 95% confidence level. A subsequent re-evaluation (Altarelli *et al.*, 1988), based on the NLO calculation of heavy-quark pair-production (Nason, Dawson, and Ellis, 1988) resulted in a slightly modified lower limit $M_{top} > 41$ GeV/c^2. This limit is obtained from the $t\bar{t}$ cross-section corresponding to the lower range of the theoretical prediction.

The lesson to be learned from the UA1 experience is that the reliability of background estimates is of paramount importance. Their first analysis did not include the J/Ψ, Υ, and Drell-Yan backgrounds, and the $b\bar{b}+c\bar{c}$ backgrounds were underestimated by a factor of four. The top signature at hadron colliders is complicated, and involves comparing the number of observed events and/or kinematic distributions with background expectations. If at all possible, dependences on uncertain theoretical models of background processes should be minimized.

More sensitive searches for the top quark were performed in the period 1988-89. At CERN, the new Antiproton Accumulator Complex (AAC) was commissioned, resulting in luminosities as high as 3 x 10^{30} cm^{-2} s^{-1} for the S$p\bar{p}$S. The UA1 electromagnetic calorimeter was removed to allow for a replacement based on Uranium-TMP (tetramethylpentane) technology. This new calorimeter was unfortunately not ready to be installed, resulting in the loss of electron identification in UA1. The UA2 detector at the CERN S$p\bar{p}$S was significantly upgraded, with improved calorimeter coverage, and enhanced electron detection capabilities. In the US, the first high-luminosity (up to 2 x 10^{30} cm^{-2} s^{-1}) run of the Tevatron Collider also started in 1988, with the CDF detector ready for data-taking.

The 1988-89 UA1 top search (Albajar *et al.*, 1990) was based on an integrated luminosity of 4.7 pb^{-1}, a factor of seven higher than had been previously available. Because of the missing EM calorimeter, only $\mu + \geq 2$ jets and $\mu\mu$ final states were considered. The $\mu +$ jets analysis was essentially an extension of the previous UA1 search (Albajar *et al.*, 1988), with the maximum transverse mass requirement raised to 60 GeV/c^2. For each event, a likelihood-like variable ($\mathcal{L}_1$) was defined to discriminate between top and background on an average basis. This likelihood was based on the $\not{E}_T$, the isolation of the muon, and the opening angle between the muon and the highest E_T jet in the event.

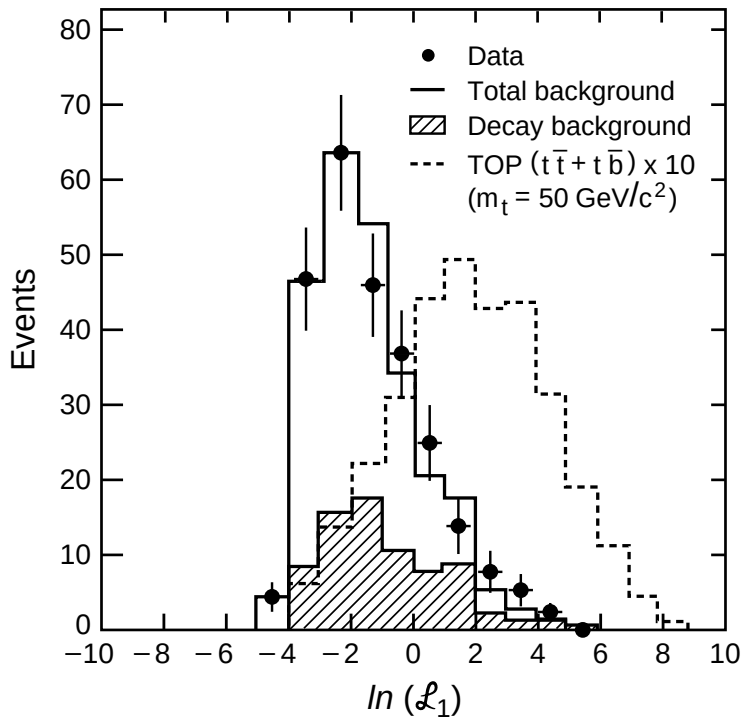

FIG. 55. The $\ln(\mathcal{L}_1)$ distribution compared with the expected background and top contributions. The shaded histogram is for the K and $\pi \to \mu\nu$ background. The other major background contribution is from $b\bar{b}$ and $c\bar{c}$ events. The expected top contribution, scaled up by a factor of 10, is shown in the dashed histogram. From the UA1 collaboration, Albajar *et al.*, 1990.

The $\mathcal{L}_1$ distributions of data, expected background, and expected signal, are shown in Fig. 55. The data are well-described by the background contribution only. Based on the number of observed events with $\ln(\mathcal{L}_1) > 4$, and the expected top production cross-section, the $\mu+$ jets data from UA1 results in a lower limit on the mass of the top quark of 52 GeV/c^2 at the 95% confidence level.

A similar likelihood variable was defined for $\mu\mu$ events, based on the transverse momentum and isolation of the highest P_T muon, and the azimuthal opening angle between the two muons. Recall that at $\sqrt{s} = 0.63$ TeV for $M_{top} > 40$ GeV/c^2 the major source of top events is W decays, $W \to t\bar{b}$, see Section IV. Hence, the dilepton final state arises from semileptonic decays of both the t- and b-quarks, and the muon from $b \to c\mu\nu$ is not expected to be isolated. Studies of the likelihood distribution for $\mu\mu$ events also gave a null result.

Results from the $\mu+$ jets and the $\mu\mu$ data were combined with the lower statistics earlier UA1 results, yielding a lower limit on the top mass of 60 GeV/c^2 (95% C.L.).

A better limit on the top-quark mass was also obtained at the same time by the UA2 collaboration, based on an integrated luminosity of 7.5 pb^{-1} at the S$p\bar{p}$S (Akesson *et al.*, 1990). Without muon detection capabilities, the UA2 results were based entirely on the electron + ≥ 1 jet channel. The UA2 search strategy differed considerably from that of UA1, with a $\not{E}_T > 15$ GeV and an electron isolation requirement imposed in the event selection. As a result, backgrounds from $b\bar{b}$, $c\bar{c}$, and fake electrons were highly suppressed, and contributed only of order 10% to the data sample. The bulk of the background was due to $W \to e\nu+$ jets events. As was discussed in Section V.E.2, for $M_{top} < M_W + M_b$, the W in the decay $t \to Wb$ is virtual. The differences between the lepton-neutrino transverse mass distributions of real and virtual $W \to l\nu$ can then be exploited to separate a top signal from the background.

In Fig. 56 we show the transverse mass distribution for electron + jet + $\not{E}_T$ events in UA2. No evidence for an excess of low transverse mass events was found, resulting in a lower limit of $M_{top} > 69$ GeV/c^2.

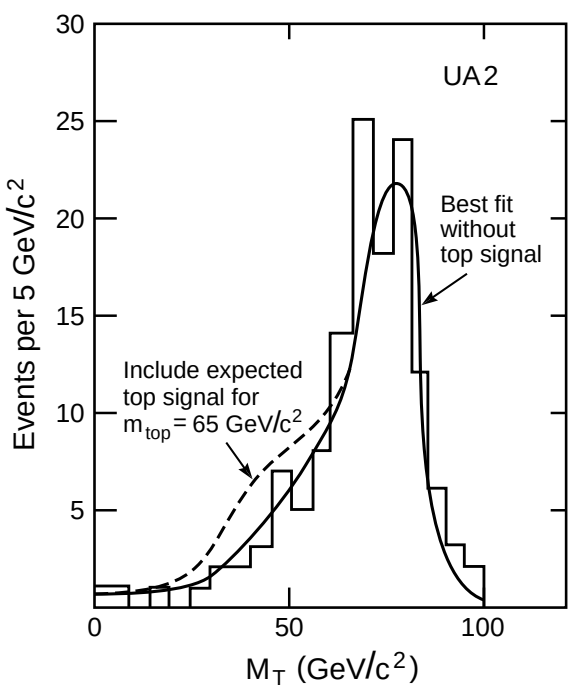

FIG. 56. The electron-neutrino transverse mass distribution in electron + jet + $\not{E}_T$ events. The data are inconsistent with a top contribution. From the UA2 collaboration, Akesson *et al.*, 1990.

The first high statistics run of the Tevatron Collider also took place in 1988-89, with an integrated luminosity of 4 pb^{-1} recorded by the CDF collaboration. As was discussed in Section IV, at the center-of-mass energy of the Tevatron ($\sqrt{s} = 1800$ GeV), top production in the relevant M_{top} range is dominated by the $p\bar{p} \to t\bar{t}$ process. The CDF collaboration searched for top in both the lepton + jets (see Section V.E) and dilepton (see Section V.D) modes.

The CDF top search in the isolated electron + ≥ 2 jets channel (F. Abe *et al.*, 1990a and 1991a) was qualitatively similar to the UA2 search. An explicit $\not\!\!E_T$ requirement was imposed, yielding a data sample containing $W \to e\nu + 2$ jets events, with a small contamination from semileptonic b- and c-quark decays, as well as fake electrons. The resulting transverse mass distribution was found to be consistent with no top contribution, (see Fig. 57). The existence of a Standard Model top quark with 40 GeV/c^2 $< M_{top} <$ 77 GeV/c^2 was ruled out. (The limit was not extended below 40 GeV/c^2 because of poor acceptance at low top quark mass). Consistent results were also found in a subsequent study of $\mu+$ jets events (Demortier, 1991).

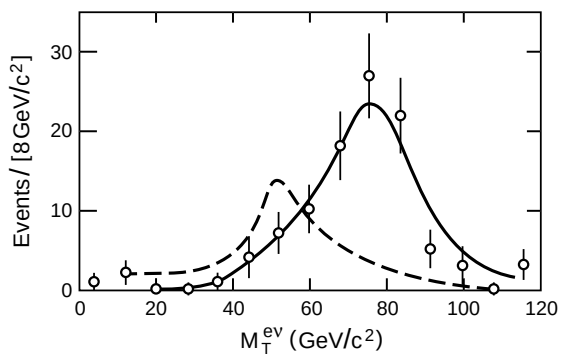

FIG. 57. The transverse mass distribution of electron + two or more jets + $\not\!\!E_T$ events. From the CDF collaboration, (F. Abe *et al.*, 1990a). The solid and dashed lines represent expectations from the $W + 2$ jets and $t\bar{t}$ ($M_{top} = 70$ GeV/c^2) Monte Carlo calculations.

Both the UA2 and CDF results were based on studies of the shape of the transverse mass distribution in lepton + jets events and were therefore independent of uncertainties in the theoretical predictions for the $p\bar{p} \to W+$ jets cross-section. Furthermore, the shape of the transverse mass distribution depends only weakly on the details of $W+$ jets production. It is sensitive mostly to the kinematics of the W decay, and the $\not\!\!E_T$ resolution in the detector, and it is fairly insensitive to the transverse momentum of the W, see the discussion in Section V.E.2. Therefore, the influence of the theoretical modelling of the background was minimized in the CDF and UA2 lepton + jets top searches.

The CDF collaboration also searched for $t\bar{t}$ production in the dilepton channel. Initially, only the $e\mu$ channel was considered (F. Abe *et al.*, 1990b). As discussed in Section V.D, the $t\bar{t}$ dilepton signature consists in principle of two isolated high P_T leptons, $\not\!\!E_T$ and two jets. Since the backgrounds in this channel are small, in order to maximize the top acceptance, no $\not\!\!E_T$, isolation, or jet requirements were imposed. One event was observed, with an expected background of 1.4 events, mostly from $Z \to \tau\tau$ followed by leptonic decays of both taus. An upper limit on the $t\bar{t}$ production cross-sections was then obtained based on the observation of one event, under the conservative assumption that this one event was due to $t\bar{t}$ production and decay. The mass region $28 < M_{top} < 72$ GeV/c^2 was excluded at the 95% C.L.

A subsequent CDF search (F. Abe *et al.*, 1992a) in the dilepton channel, based on the same integrated luminosity of 4 pb^{-1}, also included the ee and $\mu\mu$ channels, resulting in an increase in the top acceptance by a factor of two. As discussed in Section V.D, backgrounds in the ee and $\mu\mu$ channels are in general higher than in the $e\mu$ channel. $Z \to ee$ and

Experiment	Integ. luminosity	Mode	Mass limit (95% C.L.)	Ref.
UA1	5.4 pb^{-1}	μ + jets,	> 52 GeV/c^2	Albajar *et al.*, 1988
UA1	5.4 pb^{-1}	μ + jets, $\mu\mu$	> 60 GeV/c^2	Albajar *et al.*, 1988
UA2	7.5 pb^{-1}	e + jets	> 69 GeV/c^2	Akesson *et al.*, 1990
CDF	4 pb^{-1}	$e\mu$	> 72 GeV/c^2	F. Abe *et al.*, 1990b
CDF	4 pb^{-1}	$e+$ jets	> 77 GeV/c^2	F. Abe *et al.*, 1990a
CDF	4 pb^{-1}	dileptons ($ee, \mu\mu, e\mu$)	> 85 GeV/c^2	F. Abe *et al.*, 1992a
CDF	4 pb^{-1}	dileptons and l + jets $+b-$tag	> 91 GeV/c^2	F. Abe *et al.*, 1992a

TABLE VI. Summary of lower limits on the top quark mass from $p\bar{p}$ collisions, circa 1992. See text for details.

$Z \to \mu\mu$ decays were eliminated by an invariant mass cut, leaving a large number of events from off-shell Drell-Yan production of ee and $\mu\mu$ pairs. In order to control this background, additional requirements were imposed on the $\not{E}_T$ and the azimuthal opening angle between the two leptons.

No events consistent with $t\bar{t}$ were found in the ee and $\mu\mu$ channels. The resulting limit from the dilepton ($ee + \mu\mu + e\mu$) channel was $M_{top} > 85$ GeV/c^2, at the 95% confidence level.

The CDF experiment also searched for top-quarks in the electron or muon + ≥ 2 jets channel, where the dominant $W+$ jets background was reduced by attempting to tag b-quarks through their semileptonic decay into muons, $b \to \mu$ or $b \to c \to \mu$ (F. Abe *et al.*, 1992a). No events consistent with the top hypothesis were found. Despite the high branching ratio for the lepton + jets mode, the acceptance in this search was approximately a factor of 3 smaller than that of the search in the dilepton channel for $M_{top} \sim 90$ GeV/c^2. The low acceptance was the consequence of the low ($\approx 4.5\%$) muon tagging efficiency for lepton + jets top events. This low tagging efficiency was due to (i) the semileptonic b-quark branching ratio, (ii) the limited ($|\eta| < 0.6$) muon coverage of the CDF detector as configured for the 1988-89 run, and (iii) the low transverse momentum of b-quarks in top decays for $M_{top} \sim 90$ GeV/c^2. Combining results from this search and the dilepton search, resulted in a 95% C.L. lower limit on the top quark of 91 GeV/c^2, (see Fig. 58). This limit was extracted using the NLO calculation of the $t\bar{t}$ cross-section (Ellis, 1991). The 91 GeV/c^2 limit corresponds to the point where the cross-section limit curve crosses the lower (i.e. more pessimistic) bound of the theoretical prediction. Using a more up-to-date calculation of $\sigma(t\bar{t})$ (Laenen, Smith, and van Neerven, 1994), would result in a limit of 95 GeV/c^2.

The lower limits on the top mass from the UA1, UA2, and CDF experiments are summarized in Table VI. With the top quark being so massive, hopes to observe the top quark at the CERN S$p\bar{p}$S were abandoned, because of the small top production cross-section at $\sqrt{s} = 630$, (see Fig. 22). In Section VIII we will discuss the most recent, higher statistics, searches for the top quark at the Tevatron Collider, which finally resulted in the discovery of the top quark.

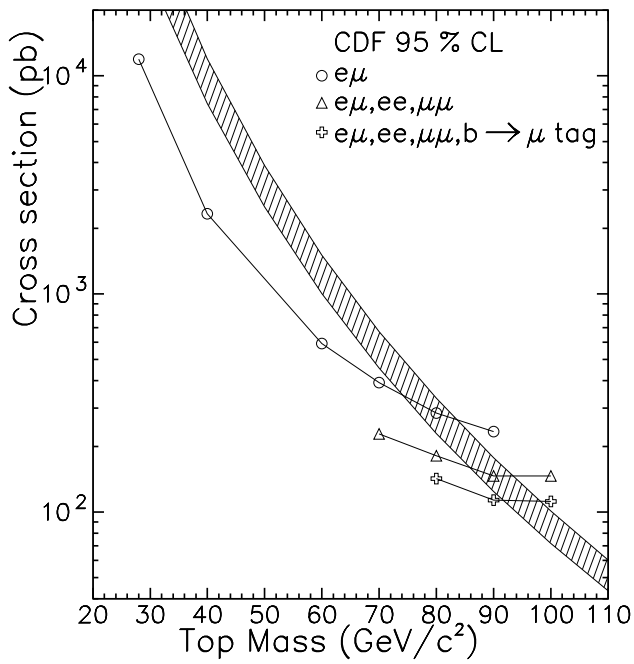

FIG. 58. The 95% C.L. upper limits on the $t\bar{t}$ cross-section from F. Abe *et al.*, 1992a. Circles : $e\mu$ channel only. Triangles : dilepton channel ($e\mu$, ee, and $\mu\mu$). Crosses : dilepton channel + lepton + jets with a $b \to \mu$ tag. The band represents the NLO theoretical prediction for the $t\bar{t}$ cross-section from Ellis, 1991. The integrated luminosity was 4 pb^{-1}. The cross-section limits are a function of the top mass because the $t\bar{t}$ acceptance depends on the top mass.

C. Searches for non-Standard Model top quark decay modes

The lower limits on M_{top} from $p\bar{p}$ collisions discussed in Section VI.B are not valid if the top quark does not decay as $t \to Wb$. If $\mathrm{M}_{top}+\mathrm{M}_b < \mathrm{M}_W$, the decay $W \to t\bar{b}$ is possible and contributes to the width of the W boson, $\Gamma(W)$.

The width of the W is difficult to measure directly since the mass signature of the W is a Jacobian and not a Breit-Wigner (see Fig. 43), and because the $\not{E}_{\mathrm{T}}$ resolution is much larger than the natural width of the W. However, constraints on the top quark mass independent of decay mode can be obtained from measurements of the leptonic W branching ratio $Br(W \to l\nu) = \Gamma(W \to l\nu)/\Gamma(W)$, based on theoretical expectations for $\Gamma(W \to l\nu)$. At lowest order the branching ratio varies between $Br(W \to l\nu) = 1/9$ for $\mathrm{M}_W < \mathrm{M}_{top}+\mathrm{M}_b$ and $Br(W \to l\nu) = 1/12$ for for very light M_{top}. Experimentally, a value for this branching ratio can be extracted from measurements of the ratio

$$R = \frac{\sigma(p\bar{p} \to W) \;\; Br(W \to l\nu)}{\sigma(p\bar{p} \to Z) \;\; Br(Z \to l^+l^-)}$$

(Cabibbo, 1983; Halzen and Marsula, 1983; Hikasa, 1984; Deshpande *et al.*, 1985; Martin, Roberts, and Stirling, 1987; Berger *et al.*, 1989). The value of the Z leptonic branching ratio is taken from the very precise measurements in e^+e^- annhilations at LEP and SLC (Montanet *et al.*, 1994). The values of $\sigma(p\bar{p} \to W)$ and $\sigma(p\bar{p} \to Z)$ can be calculated in QCD; note that theoretical uncertainties in these calculations largely cancel in the ratio,

and the uncertainty in $\sigma(p\bar{p} \to W)/\sigma(p\bar{p} \to Z)$ is only of order 1%. (Martin, Roberts, and Stirling, 1989; Hamberg, van Neerven and Matsuura, 1991; van Neerven and Zijlstra, 1992).

Early measurements of this ratio from the $Sp\bar{p}S$ were found to be more consistent with a small top quark mass (Albajar *et al.*, 1987; Ansari *et al.*, 1987). These results were used by several authors to set upper limits on the top quark mass, e.g. $M_{top} < 63$ GeV/c^2 at 90% C.L. (Martin, Roberts, and Stirling, 1987); $M_{top} < 60$ GeV/c^2 at 95% C.L. (Halzen, Kim and Willenbrock, 1988); $M_{top} < 70 \pm 5$ GeV/c^2 at 90% C.L. (Colas, Denegri and Stubenrauch, 1988). However, subsequent higher statistics studies at both the $Sp\bar{p}S$ (Albajar *et al.*, 1991a; Alitti *et al.*, 1992b) and the Tevatron (F. Abe *et al.*, 1990c, 1992c, 1994d; Abachi *et al.*, 1995e), found results consistent with expectations for a high top quark mass. A lower limit $M_{top} > 65$ GeV/c^2 at 95% C.L. can be extracted from the world average value of $Br(W \to l\nu)$, (see Fig. 59).

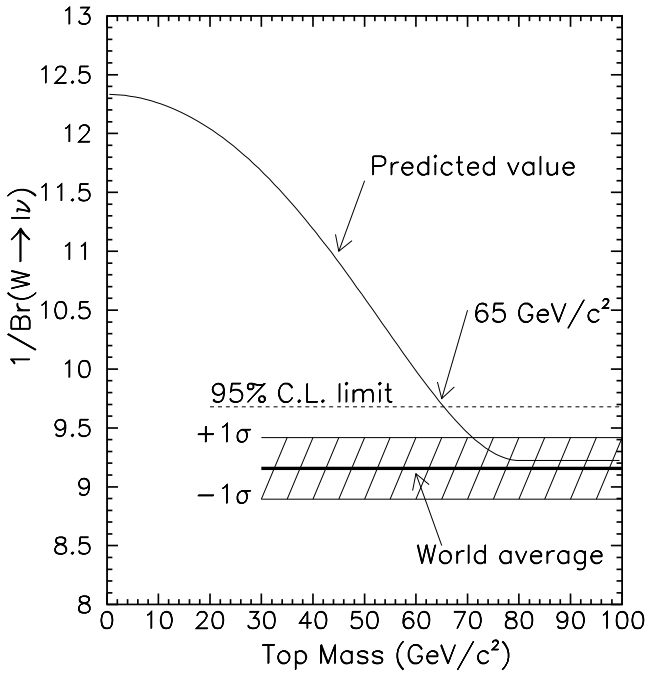

FIG. 59. World average value for the inverse $W \to l\nu$ branching ratio (Abachi *et al.*, 1995e), compared with Standard Model expectations as a function of the top quark mass. Also shown is the 95% lower limit on M_{top}, independent of top quark decay mode, which can be extracted from the measurement.

Direct searches for top quarks decaying into final states different from Wb have also been carried out at $p\bar{p}$ colliders. The decay $t \to H^+b$ is allowed in several models in which the Higgs sector is extended to include charged Higgs scalars (H^+). This includes non-minimal Standard Models, such as supersymmetry (Gunion *et al.*, 1990). In the simplest version of these models, there are two Higgs doublets, and the decay $t \to H^+b$ dominates for $M_{top} < M_W + M_b$. At higher top masses, both $t \to H^+b$ and $t \to Wb$ are allowed. The branching ratios for the two modes are functions of M_{top}, M_{H^+}, and a theoretically unconstrained parameter $\tan\beta$, which is the ratio of vacuum expectation values for the two Higgs doublets. The charged Higgs scalar from top decay would then decay into the heaviest lepton or quark

pair ($\tau\nu$ or $c\bar{s}$), with branching fractions which also depend on the value of tanβ (Glashow and Jenkins, 1987; Barger, Hewett, and Phillips, 1990; Dress and Roy, 1991).

Searches for $t \to H^+b$, $H^+ \to \tau\nu$ based on the identification of hadronic tau decays have been carried out by the UA1 (Albajar *et al.*, 1991b), UA2 (Alitti *et al.*, 1992c), and CDF (F. Abe *et al.*, 1994c) collaborations. No evidence for this process was found, and limits were placed as a function of M_{top}, M_{H^+}, and the $H^+ \to \tau\nu$ branching ratio. The most stringent limits are the result of a higher statistics analysis from the CDF collaboration (F. Abe *et al.*, 1994e) based on the $\tau \to e$ or μ signature, (see Fig. 60).

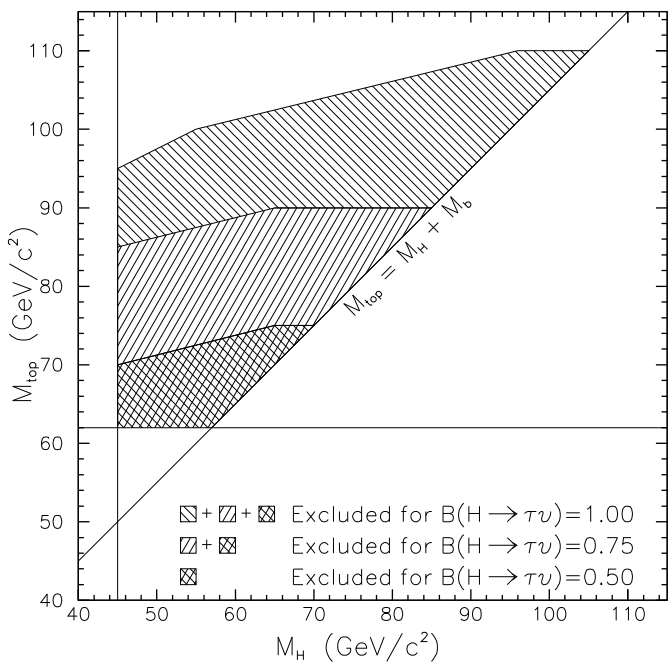

FIG. 60. Regions of the (M_{top} $-M_{H^+}$) plane excluded at 95% C.L. for different values of the branching ratio for $H^+ \to \tau\nu$. From the CDF collaboration, F. Abe *et al.*, 1994e. The vertical line reflects the lower limit $M_{H^+} > 45$ GeV/c^2 from the LEP experiments, (Buskulic *et al.*, 1992; Abreu *et al.*, 1990a; Adriani *et al.*, 1992; Akrawi *et al.*, 1990b). The horizontal line reflects the lower limit $M_{top} > 62$ GeV/c^2 from F. Abe *et al.*, 1994d, based on $Br(W \to l\nu)$. The integrated luminosity is 19 pb^{-1}.

VII. THE FERMILAB PROTON ANTI-PROTON COLLIDER

The Fermilab $p\bar{p}$ Collider in Batavia, Illinois consists of seven accelerating structures, see Fig. 61. It is the highest energy particle accelerator in the world, with a center-of-mass energy of 1800 GeV (Fermilab, 1984).

A. Linear accelerators and synchrotrons

Negatively charged hydrogen ions (H^-) are initially accelerated by a Cockroft-Walton pre-accelerator to 750 keV. These ions are then accelerated in a 145 meter linear accelerator to 400 MeV. They are stripped of their two electrons as they are injected into the first proton synchrotron called the *Booster*. The Booster is a ring of 150 meter diameter, where 18 accelerating cavities are used to accelerate the protons to 8 GeV. The protons are then extracted and injected into the *Main Ring*, which is the original 2 kilometer diameter Fermilab proton synchrotron comissioned in 1972.

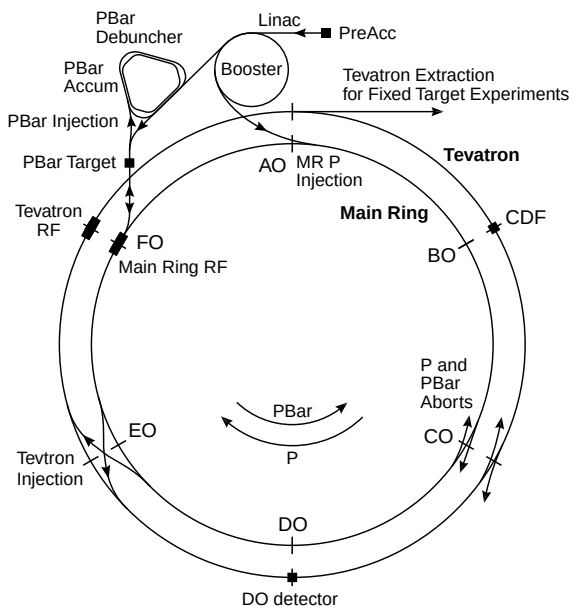

FIG. 61. The Fermilab accelerator complex. From Thompson, 1994.

The Main Ring was built with conventional electromagnets with a maximum dipole bending field of .65 Tesla, with 18 accelerating cavities operating at about 53 MHz, giving a boost of 2.5 MeV per turn. The Main Ring has accelerated protons up to 500 GeV. It is now routinely used to accelerate protons to 120-150 GeV which are then injected into the final synchrotron, the *Tevatron*, or into the anti-proton cooling ring. The Tevatron built in 1983 uses superconducting magnets to bend and focus the beams, and is situated a meter below the Main Ring. The dipoles have a maximum dipole bending field of 4.4 Tesla and the focussing quadrupoles have a maximum field gradient of 67 Tesla/m. With 8 RF accelerating

cavities the Tevatron gives the protons a boost of 1 MeV per turn and can accelerate the protons up to 900 GeV with an energy resolution of $\pm$ 0.9 GeV.

B. Anti-proton source

As was mentioned above, the Main Ring also acts as an injector to the $\bar{p}$ source (Church and Marriner, 1993). The protons are extracted from the Main Ring at 120 Gev and delivered to a target where anti-protons are produced with peak momentum of 8 GeV. The $\bar{p}$'s are then focussed in a lithium lens and fed into the *Debuncher*, which is a ring with a circumference of 500 meters. The $\bar{p}$ bunches are debunched, by turning the narrow time spread of the bunch and large momentum spread into a large time spread and a narrow momentum spread. After this bunch rotation, the $\bar{p}$'s are stochastically cooled (van der Meer, 1972), further reducing the phase space of the beam. The beam is then transferred to the *Accumulator*, added to the anti-protons already stored there using a process called stochastic stacking. When enough $\bar{p}$'s have been accumulated to make an intense beam, the beam is extracted and injected back into the Main Ring, where it is then accelerated and injected into the Tevatron.

During the period when the top data was collected, the accelerator operated with 6 bunches of protons and 6 bunches of anti-protons circulating in the machine. It takes approximately 2.5 hours of shining protons on the $\bar{p}$ source target every 2.4 seconds in order to accumulate enough $\bar{p}$'s to ensure a reasonable luminosity for $p\bar{p}$ collision. To optimize collider livetime, this process of creating and stacking the anti-protons took place during collider operation. This meant that there was often beam in the Main Ring while the collider experiments (CDF and D0) were taking data. The halo from this beam interacted with the walls of the accelerator and sprayed particles into the two collider detectors, depositing large amounts of energy in the calorimeters. In the case of CDF, the Main Ring was diverted via a dogleg up above the detector and shielded by a steel structure approximately one meter thick. Nevertheless, occasionally extra energy was deposited in the calorimeters. These events were rejected offline. The D0 experiment had no such dogleg or beam diversion and consequently the Main Ring ran straight through the D0 detector, approximately 2.5 meters above the Tevatron beampipe. The D0 collaboration was forced to turn off data acquisition while the Main Ring beam was passing through their detector, resulting in a 15% livetime loss.

C. Collider

The p and $\bar{p}$ bunches are approximately 50 cm in length due to the RF frequency of the accelerator. This bunch length determines the long luminous region at the interaction points, which is roughly Gaussian and has a sigma of approximately 30 cm. The length of the luminous region has many limiting features in terms of triggering and solid angle coverage by the detectors. For instance, as will be discussed later in this review, the silicon vertex detector in the CDF experiment was 50 cm long and thus, due to the size of the luminous region, had a limited acceptance of roughly 60% for bottom quarks from top quark decays. Furthermore, the measurements of transverse energies at the trigger level was smeared by the lack of knowledge of the event-by-event interaction position.

Accelerator radius	1000 m
Maximum beam energy	900 GeV
Injection energy	150 GeV
Peak luminosity	2 x 10^{31} cm^{-2} s^{-1}
Number of bunches	$6p, 6\bar{p}$
Intensity per bunch	$\approx 10^{11}p$, 5 x $10^{10}\bar{p}$
Crossing angle	0°
Bunch length (1 σ)	50 cm
Transverse beam radius (1 σ)	$\approx$ 25 μm
Energy spread	0.15 x 10^{-3} GeV
RF frequency	53 MHz
$\bar{p}$ stacking rate	$\approx$3.5 x 10^{10}/hour
Beam crossing frequency	290 kHz
Period between crossings	3.5 μs

TABLE VII. Parameters of the Fermilab Tevatron Collider.

The Tevatron Collider complex was first commissioned with a short run in 1985. The first high-luminosity run took place in 1988-89, at which time only the CDF detector was ready for data-taking. The peak luminosity for that run was approximately 2 x 10^{30} cm^{-2}sec^{-1}, a factor of two higher than the initial design. The second set of high luminosity collider runs, Run Ia and Run Ib, begun in 1992 with data taken by both the D0 and CDF detectors. During these runs, the peak luminosity was 2 x 10^{31} cm^{-2}sec^{-1}, while the average luminosity was about 1.4 x 10^{31} cm^{-2}sec^{-1}. The lifetime of the beams in the Collider and the $\bar{p}$ stacking rate was such that new protons and anti-protons were injected into the Collider once a day. Table VII lists the relevant parameters of the Collider.

VIII. DISCOVERY OF THE TOP QUARK

In this Section we review the recent results that finally led to the establishment of the existence of the top quark. The discovery of the top quark was made possible by the remarkable success of the Tevatron Collider project, see Section VII. These results come from the two collider experiments (CDF and D0) at Fermilab's Tevatron. They are based on data from the 1992-93 (Run Ia) and 1994-1995 (Run Ib) runs of the collider. Analysis of data from the remainder of Run Ib was in progress at the time that this review was being written. Preliminary results from both CDF and D0 are fully consistent with those from the earlier data sets.

The data sets that were used to discover the top quark were collected during Run Ia and the first half of Run Ib. The total integrated luminosities were 67 pb^{-1} for CDF, and between 44 and 56 pb^{-1}, depending on top decay mode, for D0. The difference in integrated luminosities between the two experiments is due mostly to the fact that the Main Ring accelerator at Fermilab which operates asynchronously from the Tevatron, runs through

the D0 calorimeter, see Section VII. Data taking in the D0 experiment must be disabled whenever a Main Ring proton bunch crosses the detector.

Given the $t\bar{t}$ production cross-section at the Tevatron (see Section IV), the number of $t\bar{t}$ pairs produced in an exposure of 67 pb^{-1} is expected to be between approximately 6800 (for M_{top} = 100 GeV/c^2) and 150 (for M_{top} = 200 GeV/c^2). This is a small number of events, especially in light of the fact that not all the the possible $t\bar{t}$ decay channels can be exploited, see the discussion in Section V. Thus, the high luminosity delivered by the Tevatron was crucial in enabling the experimenters to isolate the very rare top signal.

Both the CDF and D0 top searches assumed Standard Model decay ($t \to Wb$) of the top quark, and were based on the $t\bar{t}$ dilepton and lepton + jets signatures discussed in Section V. In all cases, the number of observed events, after a selection procedure designed to maximize the acceptance to top quarks, was compared with the number of expected events from non-$t\bar{t}$ sources. An excess of events over the background prediction then constitutes evidence for the top quark.

At the beginning of Run Ia, the best lower limit on the mass of the top quark was 91 GeV/c^2, from the 1989 CDF top search, see Section VI. The initial top selection criteria for both CDF and D0 were optimized for detection of a low mass ($M_{top} \approx 120$ GeV/c^2) top quark. A lower limit of $M_{top} > 131$ GeV/c^2 at the 95 % C.L. was established by D0 from the Run Ia data with an integrated luminosity of 13.5 pb^{-1} (Abachi *et al.*, 1994).

Initial evidence for the top quark was reported by the CDF collaboration (F. Abe *et al.*, 1994a) based on analysis of the Run Ia data set only, which had an integrated luminosity of 19.3 pb^{-1}. The excess in the number of top candidate events over the background prediction was 2.8 standard deviations. Additional kinematic features of the data, such as a reconstructed mass peak, also supported the $t\bar{t}$ hypothesis. However, these results were not deemed sufficient to unambiguously establish the existence of the top quark. Following the publication of a lower limit on M_{top}, the D0 requirements were reoptimized, i.e. tightened, for higher top masses. With the optimized requirements, a statistically not very significant excess of events (1.9 standard deviations) was also found in the Run Ia D0 data (Abachi *et al.*, 1995a and 1995d). With the addition of the data from the first half of Run Ib, a statistically convincing excess of events emerged from the analyses of the data sets from both collaborations (F. Abe *et al.*, 1995a; Abachi *et al.*, 1995b).

The CDF and D0 searches for $t\bar{t}$ in the dilepton channel were similar and are discussed in Section VIII.A. On the other hand, the search strategies in the lepton + jets channel were quite different. At the beginning of Run Ia, a silicon vertex detector was installed at CDF (Amidei *et al.*, 1994). Given the excellent b-tagging capabilities of this device (see Section V.E.4), b-tagging was used to separate the top signal in the lepton + jets channel from the $W+$ jets background. Both vertex tagging and lepton tagging ($b \to e$ as well as $b \to \mu$) were used in CDF. In contrast, a large fraction of the top sensitivity in this channel for the D0 experiment came from kinematic separation of $t\bar{t}$ and $W+$ jets, although lepton tagging ($b \to \mu$ only) was also employed. Analyses of the kinematic properties of lepton + jets events were also performed on the CDF data (F. Abe *et al.*, 1994a, 1995b, and 1995c). Excesses of top-like events were also seen in these CDF studies, and were used to confirm the results of the b-tagging observations.

In the remainder of this Section, we will describe in some detail the results from the CDF and D0 top searches. Dilepton searches will be reviewed in Section VIII.A, followed

by a summary of the searches in the lepton + jets + b-tag channel in Section VIII.B, and of kinematic separation of $t\bar{t}$ and $W+$ jets in Section VIII.C. The results from the two experiments will then be summarized in Section VIII.D, and their measurements of the $p\bar{p} \to t\bar{t}$ cross-section will be presented in Section VIII.E.

Before beginning the discussion of the CDF and D0 results, we wish to point out a difference in when the measured jet energies are corrected back to the parent parton momenta in CDF and D0. In all D0 analyses, correction to the measured jet energies are made prior to the selection of the sample. (The jet energy correction procedure will be discussed extensively in Section IX.A.3). For most CDF analyses, the measured jet energies are not corrected at the event sample selection stage, or in the following analysis. Corrections are only applied when the measurement of the quark or gluon energy is needed, for example in the measurement of the top mass, see Section IX. Unfortunately, this makes it somewhat difficult to compare results from the two experiments. For the jet energies relevant to the top search (15 GeV $\lesssim$ E_T $\lesssim$ 150 GeV) the multiplicative correction factor for a CDF jet energy cluster is of order 1.5.

A. Dilepton analysis results from CDF and D0

The searches for top quarks performed in the dilepton channel by D0 and CDF are similar. We have discussed the dilepton analysis approach at a general level in Section V.D. What follows are the results of these two analyses. The main difference in analysis strategy between the two experiments is due to the fact that CDF has momentum determination from charged particle tracking in the central region whereas D0 does not, and that D0 imposes more stringent requirements on the transverse energies of the jets.

Channel	Leptons		Jets		$\not\!\!E_T$	H_T
	E_T(e)	$P_T(\mu)$	$N_{\rm jet}$	E_T		
$e\mu$ + jets	$\geq$ 15 GeV	$\geq$ 12 GeV/c	≥ 2	$\geq$ 15 GeV	$\geq$ 20 GeV	$\geq$ 120 GeV
ee + jets	$\geq$ 20 GeV	-	≥ 2	$\geq$ 15 GeV	$\geq$ 25 GeV	$\geq$ 120 GeV
$\mu\mu$ + jets	-	$\geq$ 15 GeV/c	≥ 2	$\geq$ 15 GeV	-	$\geq$ 100 GeV

TABLE VIII. A partial summary of selection criteria for $t\bar{t} \to$ dileptons in D0. Jets must have $|\eta| < 2.5$ and their energies are corrected. The lepton pseudorapidity coverages are $|\eta| < 2.5$ for electrons, $|\eta| < 1.7$ for muons in Run Ia, and $|\eta| < 1.0$ for muons in Run Ib. The loss of muon coverage is due to ageing of the forward muon chambers. The H_T requirement is discussed in the text.

Both analyses require two high P_T leptons, at least two jets and in most cases, high $\not\!\!E_T$. The exceptional case is the D0 search for decays in the $\mu\mu$ channel, where the $\not\!\!E_T$ requirement is removed. The resolution of the D0 muon momentum measurement is limited to of order 20% by multiple scattering in the toroids (see Table IV), and therefore in the $\mu\mu$ channel the measurement of the $\not\!\!E_T$ is poor and is not used in the D0 analysis. The major backgrounds to the top quark signature in the dilepton channel are due to events in which jets fake leptons, $Z \to ee/\mu\mu/\tau\tau$, Drell-Yan lepton pair production, WW and $b\bar{b}$ production. These backgrounds are reduced dramatically by the requirements listed in Table VIII and Table IX.

Channel	Leptons		Jets		$\not\!\!E_T$	$\Delta\phi(\not\!\!E_T$,lepton or jet)$> 20^o$
	E_T(e)	$P_T(\mu)$	N_{jet}	E_T		
$e\mu$ + jets	$\geq$ 20 GeV	$\geq$ 20 GeV/c	≥ 2	$\geq$ 10 GeV	$\geq$ 25 GeV	$\rightarrow \not\!\!E_T \geq 50$
ee + jets	$\geq$ 20 GeV	-	≥ 2	$\geq$ 10 GeV	$\geq$ 25 GeV	$\rightarrow \not\!\!E_T \geq 50$
$\mu\mu$ + jets	-	$\geq$ 20 GeV/c	≥ 2	$\geq$ 10 GeV	$\geq$ 25 GeV	$\rightarrow \not\!\!E_T \geq 50$

TABLE IX. A partial summary of selection criteria for $t\bar{t} \rightarrow$ dileptons in CDF. Jets must have $|\eta| < 2.5$ and their energies are not corrected. The lepton pseudorapidity coverage is $|\eta| < 1.0$. The $\not\!\!E_T$ requirement is tightened when the missing transverse energy vector is collinear with either a lepton or a jet. See the discussion in the text.

In particular, as discussed in Section V.D, asking for the presence of two jets in the event is a very powerful discriminator between signal and all sources of background.

There are two other differences in the kinematic requirements applied by CDF and D0. In the D0 analysis, there is a requirement on H_T, defined as $H_T \equiv \Sigma_{jets}(E_T) + E_T^e$ which is the scalar sum of all jet transverse energies plus the highest transverse energy electron in the event, if there is one. This is a kinematic variable that attempts to discriminate between the top signal and background, by exploiting the difference between the total transverse energy of the jets in top and background events. In Fig. 62 we show Monte Carlo predictions of H_T for the principal backgrounds and for $t\bar{t}$ events with $M_{top} = 200$ GeV/c^2.

For the CDF analysis, in events where the $\not\!\!E_T$ is nearly collinear with the P_T of the leptons or jets, the $\not\!\!E_T$ requirement is tightened. As we will show below, this procedure is somewhat effective at suppressing a number of background sources. We will now discuss the dilepton CDF and D0 results, starting with the background sources, and the specific CDF and D0 selection requirements designed to discriminate against them.

1. $Z \rightarrow ee/\mu\mu$ background

Z decays constitute an important background to the $t\bar{t}$ signal in the dilepton channel. Following the $E_T(e)$, $P_T(\mu)$ and N_{jet} requirements listed in Table VIII and Table IX there is still a substantial background from $Z + \geq 2$ jets, in which the Z decays to e^+e^- or $\mu^+\mu^-$. Since Z decays to charged leptons do not produce any neutrinos, no $\not\!\!E_T$ is expected in these events. Therefore, requiring large $\not\!\!E_T$ eliminates these backgrounds completely, except for the effects of mismeasurements of the missing transverse energy in the detector.

To eliminate the $Z \rightarrow ll$ background, e^+e^- and $\mu^+\mu^-$ events with dilepton invariant mass between 75 GeV/c^2 and 105 GeV/c^2 are rejected in the CDF top search. This requirement is expected to be approximately 75% efficient, roughly independent of top mass, for dileptons (e^+e^- and $\mu^+\mu^-$) from $t\bar{t}$ decays. In the D0 analysis, the requirements used to discriminate against the Z background differ in the e^+e^- and $\mu^+\mu^-$ channels because the resolution on the lepton energy/momentum measurement is so much better for electrons than it is for muons. In the e^+e^- channel, if the invariant mass (M_{ee}) of the pair is consistent with the Z mass (79 GeV/c$^2 \leq M_{ee} \leq$ 103 GeV/c^2), the missing transverse energy requirement is tightened to $\not\!\!E_T \geq 40$ GeV. Note that this is in contrast to the CDF approach of rejecting any event that may be consistent with Z decays, regardless of the size of the missing transverse energy in

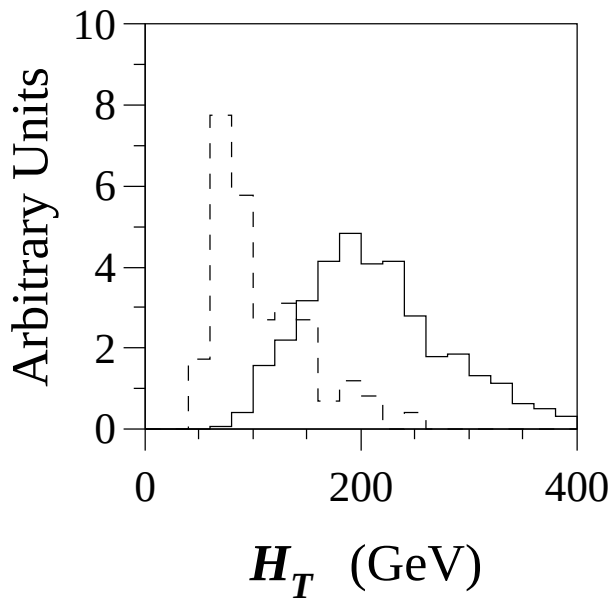

FIG. 62. D0 Monte Carlo predictions of the variable H_T for dilepton decays of a 200 GeV/c^2 top quark (solid) and principal dilepton backgrounds (dashed). From Abachi *et al.*, 1995b.

the event. As was discussed earlier, no $\not\!\!E_T$ information is used by D0 in the $\mu^+\mu^-$ channel. Z decays into muons are then rejected on the basis of an overall kinematic likelihood fit to the $Z \to \mu^+\mu^-$ hypothesis.

Since the Monte Carlo simulation is unlikely to correctly model the tails of the $\not\!\!E_T$ resolution, the D0 collaboration relies on multijet data to estimate the remaining $Z \to ee+$ jets background after the $\not\!\!E_T$ requirement. As a result of $\not\!\!E_T$ studies in the multijet sample, the fraction of $Z \to ee$ events with $\not\!\!E_T > 40$ GeV is estimated to be less than 2 x 10^{-4} (Abachi *et al.*, 1995d). The CDF requirement is more conservative and loses acceptance in return for certainty that there will be no Z decays in the top candidate sample. In Fig. 63 we show the distribution of the invariant mass of the electron-positron pair versus the $\not\!\!E_T$ for D0 events. Expectations for $t\bar{t}$ are displayed in Fig. 64.

It is difficult to compare directly the $\not\!\!E_T$ resolutions of CDF and D0. The parametrizations of the $\not\!\!E_T$ resolutions in the two experiments do not have the same functional form. The CDF resolution grows linearly with $\sqrt{\Sigma E_T}$ whereas the D0 resolution appears to grow linearly with ΣE_T, see Table V. The tails of the distribution in CDF are dominated by cracks in the calorimeter while the D0 detector design minimized cracks. The radioactive noise from the uranium plates in the D0 calorimeter adds of order 25 GeV per event to the total energy making difficult a direct comparison of the resolution at a particular ΣE_T.

2. $Z \to \tau\tau$ background

$Z \to \tau\tau$, followed by leptonic decays of both taus, is a very important background source. These events cannot be eliminated by an invariant mass cut, due to the presence of

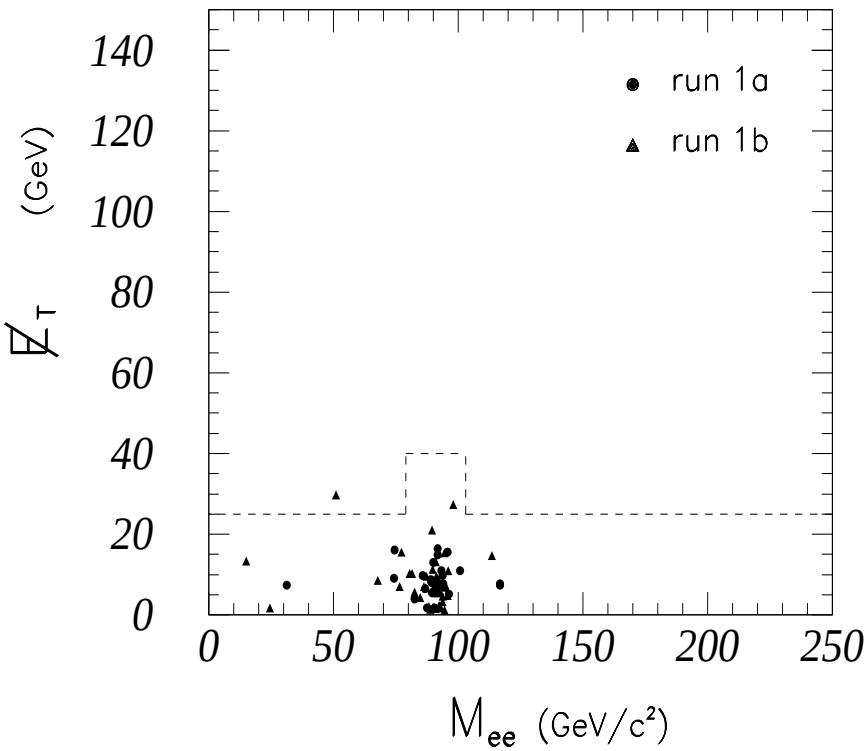

FIG. 63. Dielectron mass versus missing transverse energy in $ee+$ 2 jet events from D0 (Grannis, 1995). The integrated luminosity is 55.7 pb^{-1}. Also shown is the D0 $\not\!\!E_T$ requirement in the dielectron channel.

unmeasured neutrinos from $\tau \to l\nu\nu$. Furthermore, these neutrinos can give rise to $\not\!\!E_T$ in the event. The requirements on jet multiplicity, high E_T or P_T leptons, and high $\not\!\!E_T$ are all effective at reducing the background, see the discussion in Section V.D, and also Fig. 38. In Fig. 65 we show the $\not\!\!E_T$ versus dilepton mass for leptons from $Z \to \tau\tau$ decays from the ISAJET Monte Carlo. This clearly indicates that the background is not eradicated by the $\not\!\!E_T$ requirement alone.

In the decay of a high momentum τ, the decay products are highly collimated, due to the small mass of the τ lepton. As a result, in these events the $\not\!\!E_T$ will often point in the direction of one of the two leptons in the transverse plane. Therefore, in the CDF analysis the $\not\!\!E_T$ requirement is tightened to $\not\!\!E_T \geq 50$ GeV for events in which the azimuthal angle ($\phi_{\not\!\!E_T}$) of the $\not\!\!E_T$ vector is within 20° of the azimuthal angle (ϕ_{lepton}) of either of the two leptons, (see Fig. 66).

There is no such $\Delta\phi$ requirement for D0, see Table VIII. However the requirement made on H_T, see Table VIII, has a rejection power of approximately 2.5 for $Z \to \tau\tau+$ two or more jets.

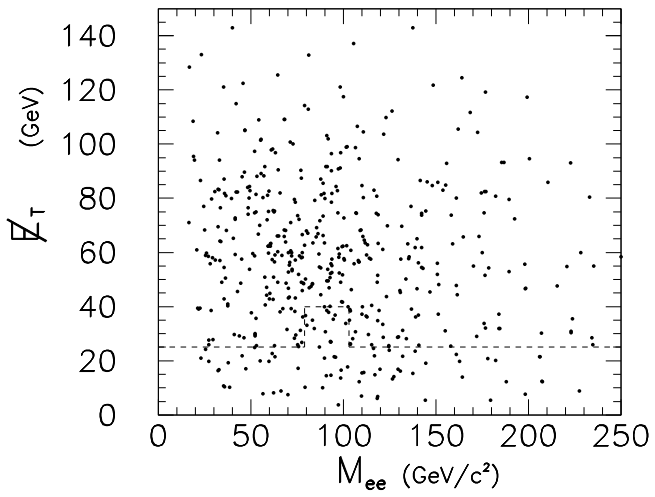

FIG. 64. Dielectron mass versus missing transverse energy in $t\bar{t} \to ee+$ 2 jets events from the D0 Monte Carlo (Grannis, 1995). Also shown is the D0 $\not{E}_T$ requirement in the dielectron channel.

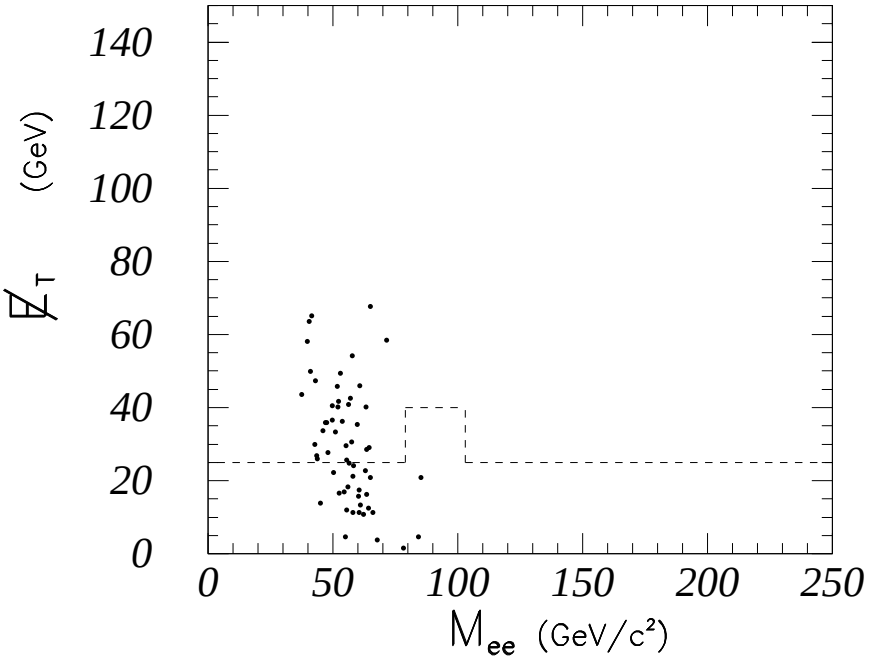

FIG. 65. Missing transverse energy versus dilepton mass for $Z \to \tau\tau + 2$ jets Monte Carlo events. From the D0 collaboration, Grannis, 1995. Also shown is the D0 $\not{E}_T$ requirement in the dielectron channel.

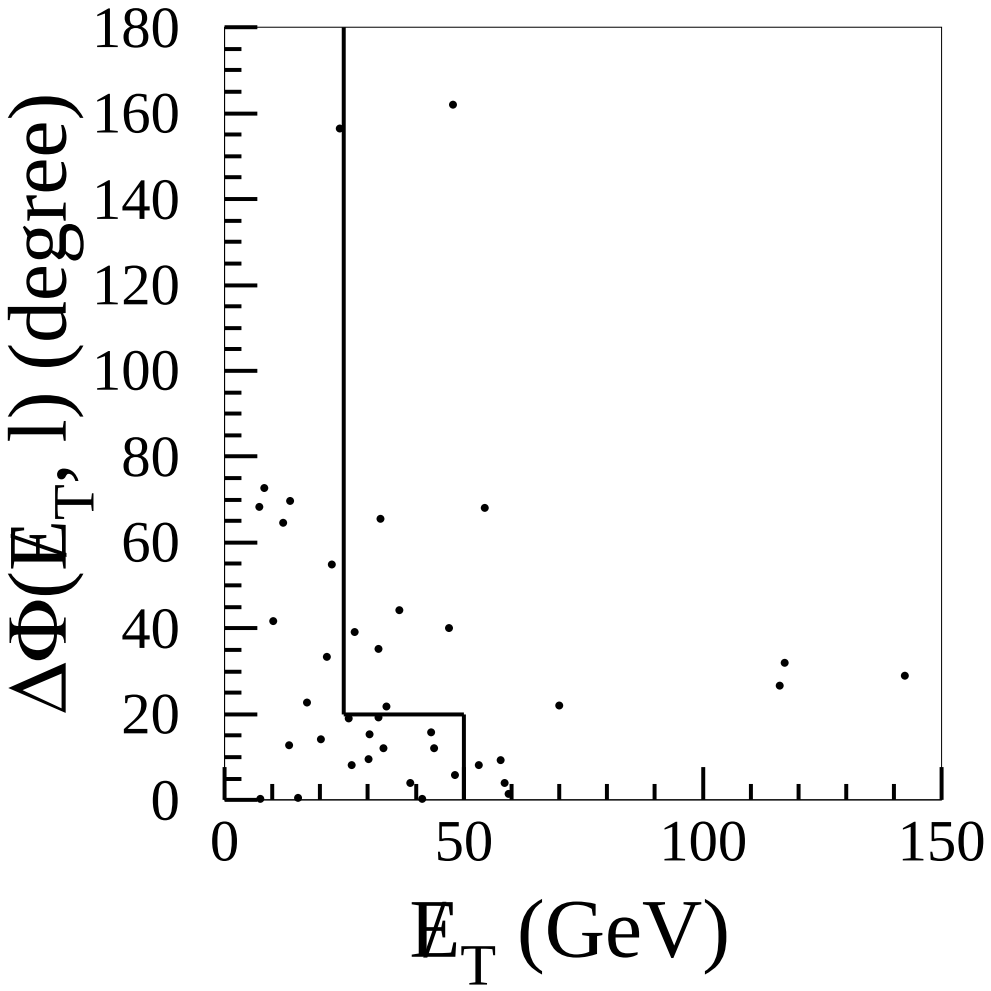

FIG. 66. CDF Monte Carlo distribution of the azimuthal angle between the $\not{E}_T$ and the closest lepton as a function of $\not{E}_T$ in $Z \to \tau\tau$ events with two jets. Also shown is the boundary of the CDF $\not{E}_T$ requirement. From the CDF collaboration, F. Abe *et al.*, 1994a.

3. Drell-Yan Background

Continuum Drell-Yan production of lepton pairs accompanied by two jets is a background not addressed by the Z mass requirement. In the CDF analysis, the $\Delta\phi$ requirement between the $\not\!\!E_T$ and the closest jet (see Table IX) is designed to reduce this background. There is no intrinsic $\not\!\!E_T$ in these events, however jet energy can be lost in cracks, and the measurement of the jet energy can fluctuate, faking a $\not\!\!E_T$ signal. In these cases, the $\not\!\!E_T$ tends to point towards one of the two jets in the event. In order to reduce this background, the $\not\!\!E_T$ requirement in CDF is raised to 50 GeV when the azimuthal angle between the $\not\!\!E_T$ direction and a jet is less than 20°, see Fig. 67.

D0's approach is different. First of all, the H_T requirement is more effective than a minimum number of jets requirement because the jets in Drell-Yan + jets events are in general softer than the jets in $t\bar{t}$ events, for sufficiently high top mass. Furthermore, to reduce the Drell-Yan background, the $\not\!\!E_T$ requirement is raised to 25 GeV for dielectron events. Recall that in the $\mu\mu$ channel, no cut is made on $\not\!\!E_T$ because the muon energy measurement is poor.

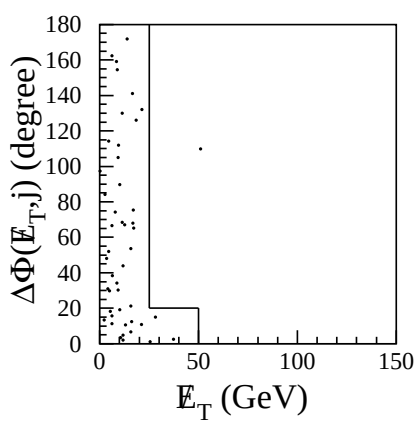

FIG. 67. Distribution of the azimuthal angle between the $\not\!\!E_T$ and the closest jet as a function $\not\!\!E_T$ for $Z \to ll$ events with two jets. The $\not\!\!E_T$ characteristics of these events should closely resemble those of Drell-Yan events. This is CDF data with an integrated luminosity of 19 pb^{-1}. Also shown is the boundary of the CDF $\not\!\!E_T$ requirement. From the CDF collaboration, F. Abe *et al.*, 1994a.

4. WW background

The expected background from diboson production, WW, WZ, and ZZ, is small but not at all negligible. The WW process is the dominant diboson background to the $t\bar{t}$ dilepton signature. The WZ and ZZ production cross-sections are expected to be lower and are further suppressed by the small $Z \to ll$ branching ratio, see the discussion in Section V.D. Neither collaboration has published evidence for the process $p\overline{p} \to W^+W^-$, however the

cross-section expected from theory is slightly higher, of order 10 pb, than the equivalent $t\bar{t}$ cross-section, which is expected to be $\sigma(t\bar{t}) \approx 5$ pb for $M_{top} = 175$ GeV/c^2, (see Fig. 21).

WW events include large transverse momentum leptons and $\not\!\!E_T$. In Fig. 68 we show the expected distributions of $\not\!\!E_T$ and $\Delta\phi$ for $t\bar{t}$ and WW events. The kinematic properties of the two processes are very similar. The most effective way to reduce these backgrounds is to require the presence of high transverse momentum jets. The H_T requirement imposed by D0 is more effective in discriminating against WW than the simple minimum-number-of-jets requirement employed by CDF. The remaining background is estimated entirely from Monte Carlo, using the theoretical expectations for the WW cross-section.

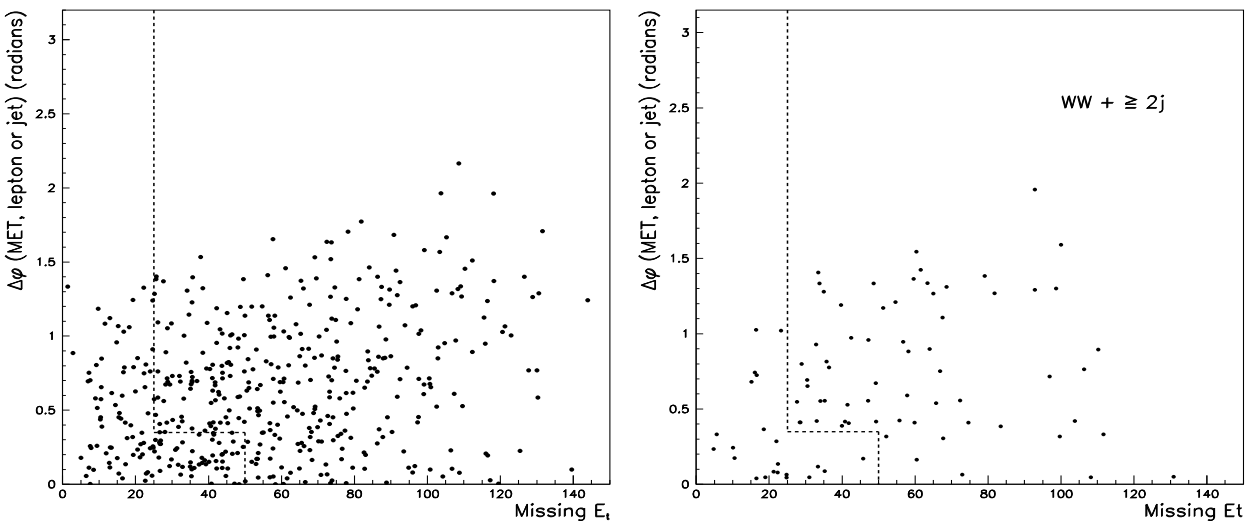

FIG. 68. CDF Monte Carlo expectations for $\Delta\phi$ versus $\not\!\!E_T$ for (a) $t\bar{t}$ with $M_{top} = 180$ Gev/c^2, and (b) WW + $\geq$ + 2 jet production. The vertical axis is the smallest of the azimuthal angles between the $\not\!\!E_T$ vector and the leptons or jets. The symbol MET in the vertical-axis label refers to the $\not\!\!E_T$.

5. $b\bar{b}$ and fake lepton backgrounds

Doubly semileptonic decays in $b\bar{b}$ events and events with fake leptons constitute another important background to the dilepton signature. These backgrounds are considerably reduced by requiring two isolated high transverse momentum leptons, and high $\not\!\!E_T$. The $b\bar{b}$ background is calculated from Monte Carlo, normalized to the rate of lower momentum $b\bar{b} \rightarrow$ dileptons events. The probability of finding two high momentum isolated fake leptons in an event is exceedingly small. The main fake dilepton background is due to $W+$ jets events, where one of the leptons is from the $W \rightarrow l\nu$ decay, and one of the jets is misidentified as a lepton. The background is then estimated by multiplying the number of observed $W+$ jets events by the probability for a jet to fake the isolated electron or muon signature as determined from samples of jet events. This probability is typically of order 10^{-4}.

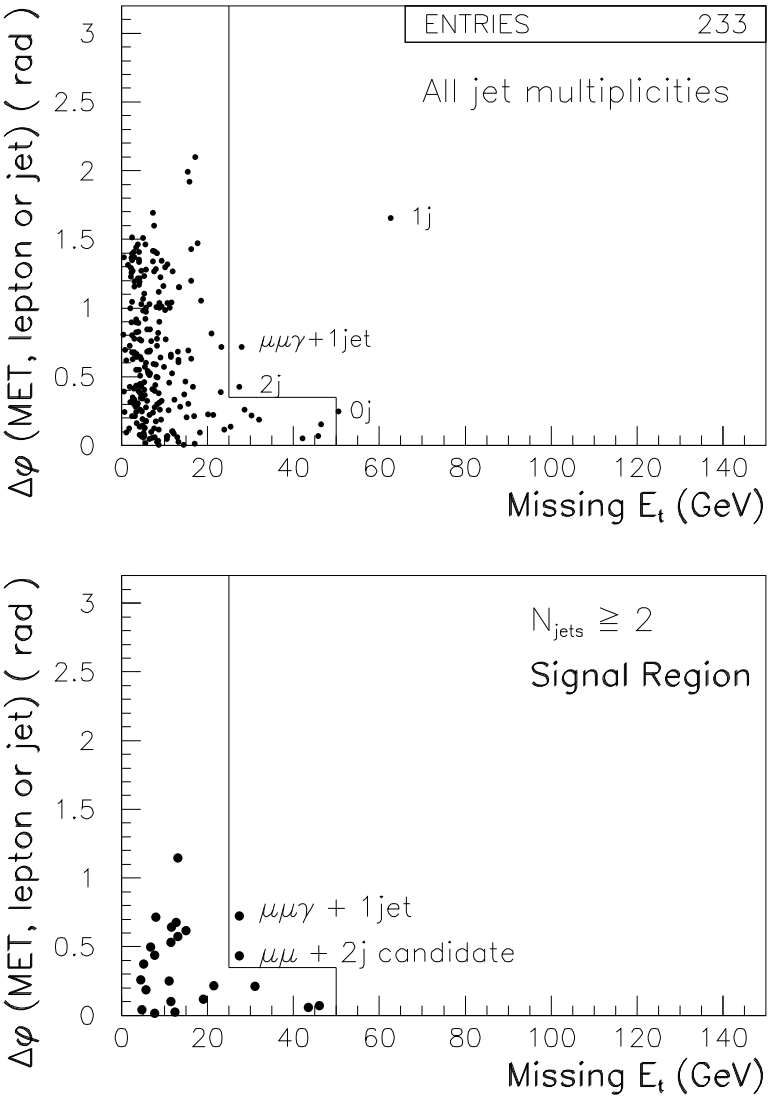

FIG. 69. CDF dilepton results in the $\mu\mu$ channel. The integrated luminosity is 67 pb^{-1}. From Roser, 1995. The vertical axis is the smallest of the azimuthal angles between the $\not\!\!E_T$ vector and the leptons or jets. The symbol MET in the vertical-axis label refers to the $\not\!\!E_T$.

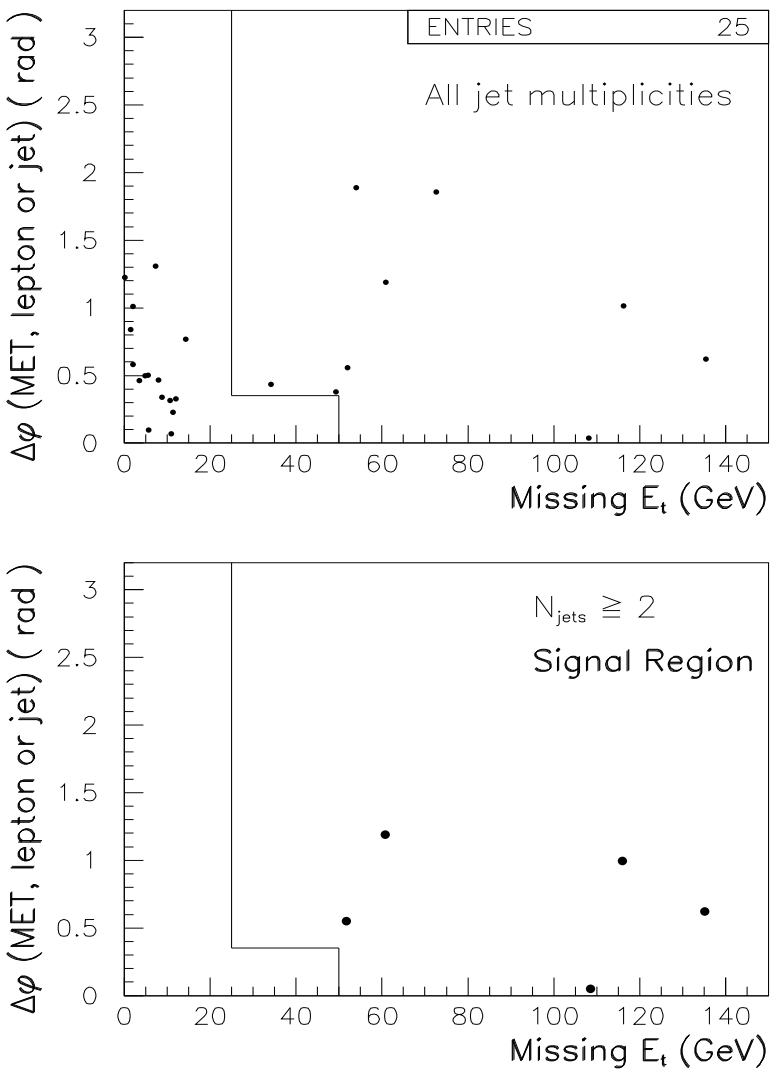

FIG. 70. CDF dilepton results in the $e\mu$ channel. The integrated luminosity is 67 pb^{-1}. From Roser, 1995. The vertical axis is the smallest of the azimuthal angles between the $\not\!\!E_T$ vector and the leptons or jets. The symbol MET in the vertical-axis label refers to the $\not\!\!E_T$.

	CDF	D0
Background Source		
$Z \to \tau\tau$	0.38 ± 0.07	0.24 ± 0.07
WW	0.21 ± 0.07	0.06 ± 0.03
Fakes, $b\bar{b}$	0.26 ± 0.16	0.12 ± 0.04
$Z \to ee$ or $\mu\mu$	-	0.24 ± 0.03
Drell Yan	0.44 ± 0.28	-
Total background	1.3 ± 0.3	0.65 ± 0.15
$t\bar{t}$ expectation, M_{top} = 180 GeV/c^2	2.4	1.2
Data	5 $e\mu$ 1$\mu\mu$	2 $e\mu$ 1 $\mu\mu$

TABLE X. Background sources, $t\bar{t}$ expectations, and event yields in the CDF (Roser, 1995) and D0 (Narain, 1995) dilepton analyses. One additional CDF candidate event, consistent with the $Z \to \mu\mu\gamma$ hypothesis, is not included in this table, see the discussion in the text. The integrated luminosity for the CDF data is 67 pb^{-1}. For the D0 data, the integrated luminosity is 55.7 pb^{-1} for ee, 44.2 pb^{-1} for $\mu\mu$, and 47.9 pb^{-1} for $e\mu$. The $t\bar{t}$ expectations are obtained using the calculation of $\sigma(t\bar{t})$ from Laenen, Smith, and van Neerven, 1994.

6. Results

The acceptance for the CDF analysis for M_{top} = 180 GeV is $\epsilon = (0.87 \pm 0.10)\%$, where this acceptance includes the branching ratio for the dilepton mode (4/81, see Table III). The equivalent acceptance for D0 is $(0.55 \pm 0.04)\%$. With these acceptances, and given the integrated luminosities and the theoretical expectations for $\sigma(t\bar{t})$, both experiments are sensitive to $t\bar{t}$ production for top masses up to $M_{top} \approx 200$ GeV/c^2. The results of the CDF and D0 $t\bar{t}$ searches in the dilepton channel are summarized in Table X.

CDF finds 7 dilepton candidates in 67 pb^{-1} with 1.3 ± 0.3 expected background events. Of these 7 candidate events, five are $e\mu+$ jets events and two are $\mu\mu+$ jets events. One of the two $\mu\mu$ events looks very much like a radiative Z decay, $Z \to \mu\mu\gamma$, since the invariant mass of the $\mu\mu\gamma$ is 86 ± 7 GeV/c^2. Although the background from radiative Z decays was estimated to be less than .04 events, CDF conservatively a-posteriori removes this event from the top candidate sample and is left with 6 events (5 $e\mu$ and one $\mu\mu$). Acceptances for top are such that 60% of $t\bar{t}$ are expected in $e\mu$ and 40% in $ee/\mu\mu$. Figs. 69 and 70 show the CDF data in the $\Delta\phi - \not{E}_T$ plane. As can be seen from these figures, the $e\mu$ channel is much cleaner due to the absence of the Drell-Yan contribution.

D0 finds 3 candidates in approximately 50 pb^{-1} with $.65 \pm 0.15$ expected background events. Of these three events, two are $e\mu+$ jets and one is $\mu\mu+$jets. This is consistent with the ratio of expected number of events, $e\mu : ee : \mu\mu = .34 : .25 : .11$ for a 200 GeV top quark.

Thus, both experiments see an excess of dilepton events over the total background prediction. The size of this excess is loosely consistent with expectations for $t\bar{t}$. It is interesting to notice that there are some significant differences in the CDF and D0 background sources,

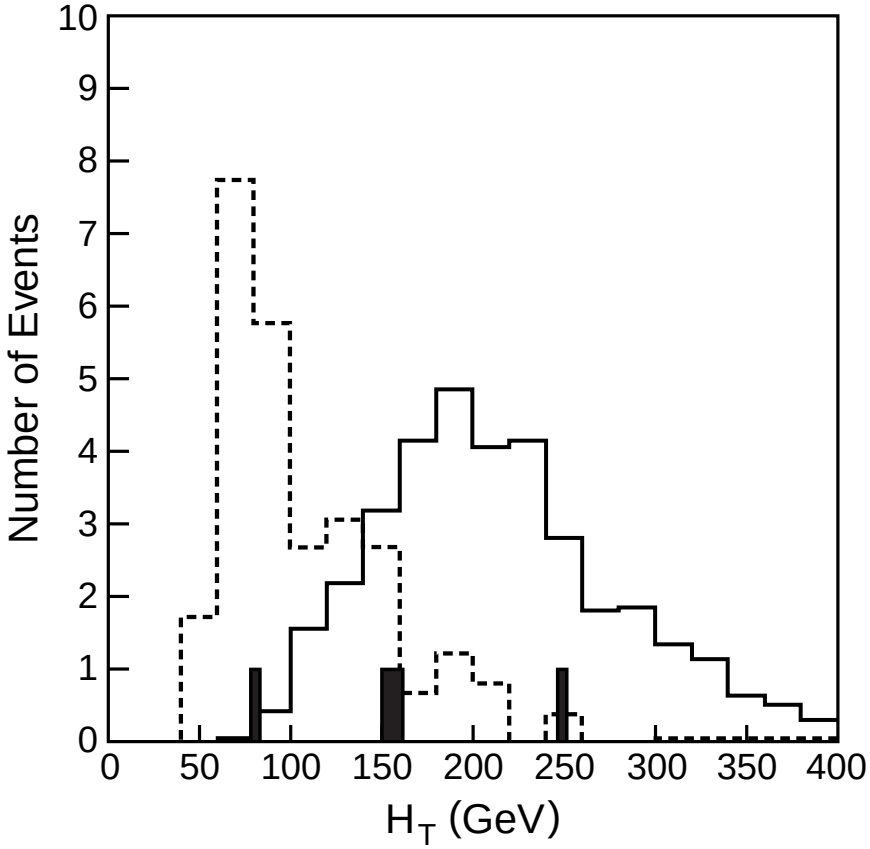

FIG. 71. Distributions of H_T for dilepton data for D0 (Grannis, 1995) The integrated luminosity is ≈ 50 pb^{-1}. The solid line is the expected H_T distribution for top events in the dilepton channel. The dashed line is the expected backgrounds and the solid histogram is the data. See text for details.

see Table X. The highest background source in the CDF analysis is due to Drell-Yan events. This background is negligible in D0, probably due to the D0 H_T requirements, the stricter $\not\!\!E_T$ requirement in the ee channel, and the hermeticity of the D0 detector. Also, $Z \to ee$ and $\mu\mu$ are totally eliminated by the CDF invariant mass requirement, while they make up a substantial fraction of the total background in D0.

As partial evidence that the excess of events is not due to a background fluctuation or to underestimation of the backgrounds, we present in Fig. 71 the H_T distribution of dilepton events from D0. As was discussed earlier, in D0 H_T is defined as the scalar sum of the transverse energy of all of the jets in the event + the E_T of the highest E_T electron (for the ee and $e\mu$ channels). As we argued throughout this Section, and as shown in Fig. 62, H_T is a powerful discriminant between signal and background. The D0 candidate events are distributed in H_T in a manner more consistent with $t\bar{t}$ than background.

In addition, in the six CDF dilepton candidate events, there are five jets (in three events) that are tagged as b-jets by the algorithms which will be described in Section VIII.B. This is to be compared with the expectation of approximately 0.5 b-tagged jets if all six events were background, and approximately 3.6 b-tagged jets if all six events were $t\bar{t}$. This suggests that the excess of dilepton + jets events over the background prediction is correlated with the presence of b-quarks in the event, as expected if the excess were due to $t\bar{t}$.

B. Lepton + jets + b-tag

As was discussed in Section V.E.4, one of the most effective ways of isolating a top signal in the lepton + jets mode ($t\bar{t} \rightarrow q\bar{q}\ l\nu\ b\bar{b}$) is to tag the b-quarks in $t\bar{t}$ events. This can be achieved by searching for leptons from the semileptonic decay of b-quarks (lepton tagging), or by exploiting the long lifetime of b-hadrons (vertex tagging). Lepton tagging has been used by both CDF and D0 to extract a top signal; vertex tagging, which requires momentum analysis, as well as precise vertex detection capabilities, has been performed by CDF only. In Section VIII.B.1 we will review the CDF and D0 selections of lepton + jets data, before the b-tag requirement. The results of the b-tag analyses on these data are then discussed in Sections VIII.B.2 and VIII.B.3 for lepton and vertex tagging respectively. A brief summary of the tagging searches, as well as results of cross-checks performed on samples of $Z+$ jets, are presented in Section VIII.B.4.

1. Selection of lepton + jets data before b-tagging

The CDF and D0 selections of the isolated e or μ + jets data for the b-tagging analyses are summarized in Table XI. The event selection employed by the two collaborations are similar. In principle, one would expect to detect four jets in a $t\bar{t} \rightarrow$ lepton + jets event; however, as discussed in Section V.B.2, the detected number of jets can be smaller (see for example Fig. 35). This is because jets from top decay sometime have E_T below threshold, or two or more of these jets can be close enough to each other that they are reconstructed as a single jet. Therefore, in order to maintain high efficiency, the minimum number of jets required by both CDF and D0 is three rather than four. The one significant difference in the selection requirements between the two experiments is that D0 imposes a further requirement on the minimum scalar sum of the transverse energy of all jets in the event (H_T, see Table XI). This requirement is expected to improve the rejection against the dominant W + jets background, especially for high top quark masses (see Fig. 46). No such requirement is imposed on the CDF data in order to maintain high $t\bar{t}$ detection efficiency for M_{top} as low as 100 GeV/c^2, and because of the superior background rejection capabilities of the CDF vertex tagging analysis.

The selections summarized in Table XI yield data samples consisting mostly of $W+$ jets events, as well as a contamination from QCD events, and hopefully also a $t\bar{t}$ component. The QCD contamination is due to events with fake leptons, as well as semileptonic decays of b-quarks in $p\bar{p} \rightarrow b\bar{b}$ events. In almost all of the channels, these events are estimated to contribute approximately 10% to the event sample; the exception is the D0 $\mu+$ jets channel, where this background is a factor of 2-2.5 larger, due to the poor resolution of the D0 muon momentum measurement. These data samples also include small contributions from Z and diboson events.

The numbers of expected $t\bar{t}$ events in the data samples (see Table XI) depend on M_{top}, since both the $t\bar{t}$ production cross-section and acceptance depend on M_{top}. Given the theoretical expectations for the $t\bar{t}$ production cross-section, the expected signal-to-background in these data samples before applying b-tagging (*pre-tag* samples) varies between approximately 1/16 and 1/3, depending on top mass, and selection details.

	CDF	D0
Lepton E_T or P_T	$\geq$ 20 GeV	$\geq$ 20 Gev (e); $\geq$ 15 GeV (μ)
Lepton rapidity coverage	$\lvert\eta\rvert \leq 1^{(a)}$	$\lvert\eta\rvert \leq 2$ (e); $\lvert\eta\rvert \leq 1.7$ $(\mu)^{(b)}$
$\not{E}_T$	$\geq$ 20 GeV	$\geq$ 20 GeV
Number of jets	≥ 3	≥ 3
Jet E_T	$\geq$ 15 GeV (uncorrected)	$\geq$ 20 GeV (corrected)
Jet rapidity coverage	$\lvert\eta\rvert \leq 2$	$\lvert\eta\rvert \leq 2$
Jet cone clustering radius	0.4	0.5
H_T	-	$\geq$ 140 GeV
Integrated luminosity	67 pb^{-1}	48 pb^{-1} (e); 44 pb^{-1} (μ)
No. of events in data sample	203	66
No. of expected $t\bar{t}$ events, M_{top} = 140 GeV/c^2	$\approx$ 95	$\approx$ 22
No. of expected $t\bar{t}$ events, M_{top} = 200 GeV/c^2	$\approx$ 13	$\approx$ 6

TABLE XI. CDF and D0 lepton + jets requirements for the b-tag analysis. The variable H_T in D0 is defined as the scalar sum of the E_T of all the jets. The expected number of top events are derived from the theoretical estimate of the $t\bar{t}$ cross-section (Laenen, Smith, and van Neerven, 1994) and the calculated acceptances. Notes : $^{(a)}$ the CDF muon chambers only cover $\approx 2/3$ of the solid angle for $0.6 < |\eta| < 1$; $^{(b)}$ Muons in D0 are restricted to $|\eta| < 1$ for the last $\approx 70\%$ of data, due to ageing of the forward muon chambers.

The dominant physics background in the lepton + jet + b-tag channel is due to the associated production of a W boson and a pair of heavy quarks ($WQ\bar{Q}$, $Q = b$ or c, see Section V.E.4, Fig. 52). As discussed in Section V.E.4, the fraction of $W+ \geq 3$ jets events containing a $Q\bar{Q}$ pair is expected to be of order 3% for $Wb\bar{b}$ and 5% for $Wc\bar{c}$. Therefore, given the signal-to-background levels in the lepton + ≥ 3 jets samples before demanding a b-tag, a $t\bar{t}$ signal is expected to stand out after application of a b-tag requirement, provided that instrumental backgrounds can be kept under control.

2. Lepton tagging in CDF and D0

Leptons from b-quarks in $t\bar{t}$ arise from direct ($b \to cl\nu$) or cascade ($b \to c \to sl\nu$) decays. Given the b- and c-quark semileptonic branching ratios, and including the contribution from semileptonic decays of c-quarks from $W \to c\bar{s}$, there is on average approximately one lepton (e or μ) from b or c decay in each $t\bar{t} \to$ lepton + jets event in addition to the lepton from W decay. These additional leptons tend to have low transverse momentum, see Fig. 49, and to be non-isolated because of the presence of nearby hadrons from the b-quark fragmentation and the b-hadron decay, (see Fig. 72). Detection of these leptons is therefore more difficult than detection of the isolated high P_T leptons from W decays.

There are two main differences in the lepton-tagging algorithms developed by the two collaborations. The first difference is that the D0 analysis only tags muons, whereas CDF tags both muons and electrons. This is because detection of non-isolated electrons in D0 is not as effective as in CDF, mostly due to the absence of a magnet for momentum measure-

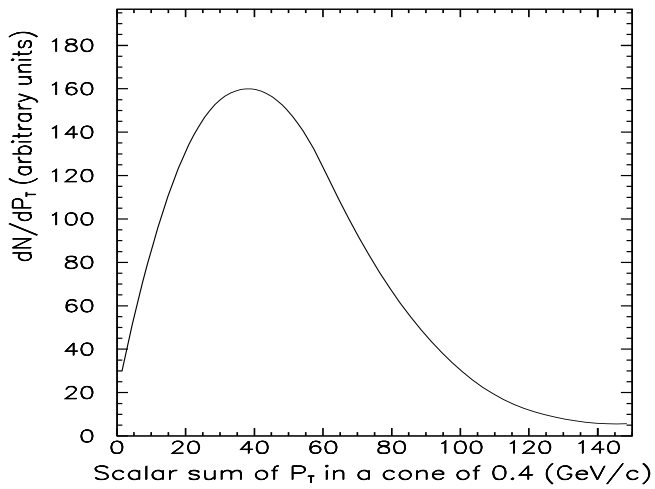

FIG. 72. The expected scalar sum of the transverse momenta of all particles in the $t\bar{t}$ final state within a cone of radius 0.4 of the lepton from $b \to cl\nu$ or $b \to c \to sl\nu$. From the ISAJET Monte Carlo, for M_{top} = 175 GeV/c^2. The momenta of the lepton and the neutrino are not included in the sum.

ment. In CDF electrons from b-decays can be identified with sufficient background rejection. However, the efficiency for detecting these electrons is lower than the efficiency for detecting muons, and only of order 30% of the lepton tagging efficiency in CDF is due to electron tags. The second difference between the two experiments resides in the minimum P_T requirement for these tagging leptons. In D0, this requirement is set at 4 GeV/c, which corresponds to the minimum P_T for a muon to penetrate the D0 muon detectors; in CDF this minimum P_T requirement is set at 2 GeV/c. The lower P_T requirement improves the efficiency for detecting muons from cascade decays, especially for low top quark masses, (see Fig. 49), however it also results in higher background levels.

Additional requirements are imposed in the D0 analysis to reject events with tagging muons collinear or back-to-back with the direction of the $\not\!\!E_T$ vector. These requirements are designed to reject QCD events. The rapidity coverages for tagging leptons in the two experiments are the same as those for the high P_T leptons from W decays, see Table XI. For $M_{top} > 140$ GeV/c^2, the $t\bar{t}$ lepton-tagging efficiency is 20% for both experiments. The greater muon coverage of the D0 detector makes up for the higher P_T threshold and the absence of electron-tags.

Backgrounds to b-tagging were discussed extensively in Section V.E.4. The $WQ\bar{Q}$ backgrounds in both CDF and D0 are calculated by assuming that the heavy flavor content of jets in W + jets events is the same as that of generic jets. This corresponds to the Method I background estimate of Section V.E.4, and is expected to yield an over-estimate of the background. In D0, a tagging rate per jet as a function of jet E_T is defined as the ratio of the number of tagged jets divided by the total number of jets as a function of E_T, (see Fig. 73). The background to the lepton tagged signal is then calculated by convoluting this tagging rate with the E_T spectrum of jets in the $W+ \geq 3$ jets sample. As discussed in Section V.E.4, this procedure yields simultaneously an estimate of the instrumental and $WQ\bar{Q}$ backgrounds.

A similar procedure is used in CDF, with the difference that track-tag rates instead of

jet-tag rates are used. The track-tag rate is defined as the ratio of the number of tracks in jet events that are tagged as leptons divided by the total number of tracks. To calculate the background, electron and muon track-tag rates as a function of P_T are convoluted with the P_T spectrum of tracks in the $W+ \geq 3$ jets sample. The CDF muon track-tag rate is displayed in Fig. 74; the analogous electron track-tag rate is considerably smaller, see F. Abe *et al.*, 1994a.

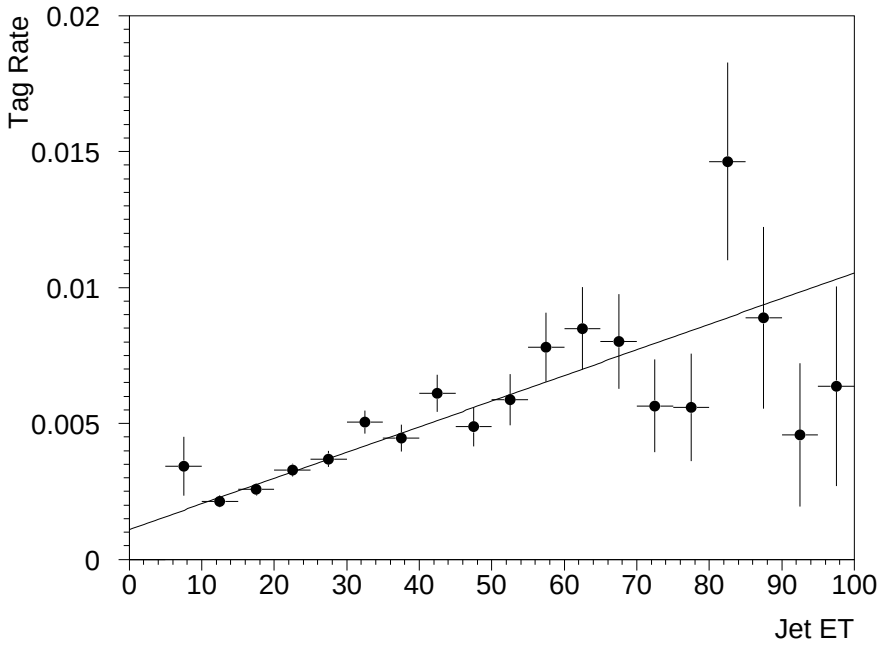

FIG. 73. Tagging rate for jets as a function of E_T in the D0 detector as measured from a sample of fake electron + jets events. From Snyder, 1995a.

An additional physical background to the tagged $W+$ jets search is due to production of a W and a single c-quark, $W+$ charm, (see Fig. 51). In the D0 analysis it is assumed that this background is automatically included when the jet-tag rate is convoluted with the jet E_T spectrum. On the other hand, this background is calculated explicitly by CDF and is added in separately.

A background contribution from $Z \to \mu\mu$ events is also present in D0. The two muons can result in misinterpreting such an event as $W \to \mu\nu$ event with a μ tag. The poor muon momentum resolution does not allow for a clean removal of these events via an invariant mass cut, as is done in CDF. Just as in the D0 dilepton analysis (see Section VIII.A), these events are identified using a global event χ^2-test for consistency with the Z hypothesis. Since the Z removal procedure is not 100% efficient, the D0 background estimate in the lepton + jets + b-tag search also includes a contribution from residual $Z \to \mu\mu$ events in the sample. Additional small backgrounds are due to all sources of dileptons discussed in Section VIII.A (e.g. $Z \to \tau\tau$, dibosons, $b\bar{b}$). These backgrounds are expected to be small. They are included in the CDF background estimate, and taken as negligible by D0.

Both CDF and D0 see an excess of tags in the $W+ \geq 3$ jets samples over their respective background estimates. The D0 collaboration finds 6 events on an expected background of

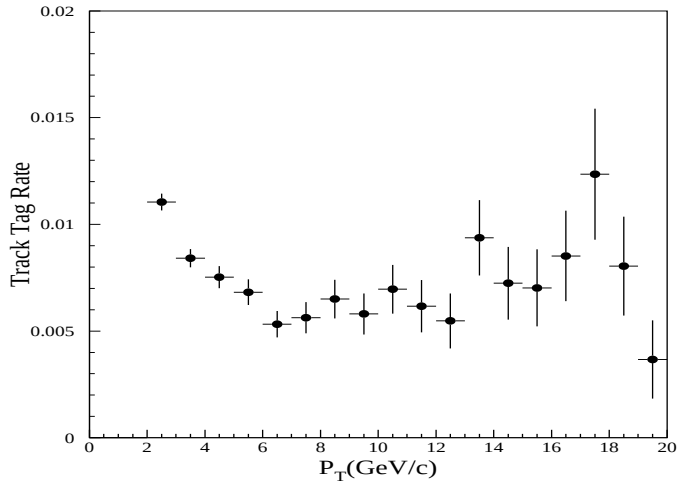

FIG. 74. Muon track tagging rate as a function of P_T in the CDF detector as measured from a sample of jet events. From F. Abe *et al.*, 1994a.

1.2 ± 0.2; the CDF collaboration finds 23 tags in 22 events, with an expected background of 15.4 ± 2.0 tags. The most powerful check of the background calculation procedure is to repeat the exercise for W events with only one or two jets, where the $t\bar{t}$ content of the data sample is expected to be very small. This is summarized in Fig. 75 for D0 and Fig. 76 for CDF. The background calculations reproduce the expected tagging rates in W events with low jet multiplicity.

In this Section and in Section V.E.4, we have argued that the $WQ\bar{Q}$ background is overestimated in both the CDF and D0 analyses, yet the background predictions in the $W+$ 1 and $W+$ 2 jets samples are in good agreement with the data. The reason for this is that the dominant background in these analyses is due to fake leptons, not $WQ\bar{Q}$. For example, if the CDF backgrounds were to be calculated using the best theoretical input for $WQ\bar{Q}$, the background estimate would have been reduced by only about 10%, independently of jet multiplicity (F. Abe *et al.*, 1994a). This is well within the 20% systematic uncertainty assigned to the background calculation.

The sizes of the excesses of events seen by the two collaborations are loosely consistent with expectations for $t\bar{t}$. The D0 collaboration sees an excess of 4.8 events; the number of expected tagged $t\bar{t}$ events varies between 4.4 and 1.2 for M_{top} between 140 and 200 GeV/c^2. The CDF excess is 7.6 tags, to be compared with a $t\bar{t}$ expectations of between 19 tags (M_{top} = 140 GeV/c^2) and 2.6 tags (M_{top} = 200 GeV/c^2).

Despite the fact that the lepton tagging efficiencies are comparable in the two experiments, the signal-to-background is better for the D0 analysis. This is mostly because backgrounds to the detection of low P_T muons are lower in D0 than in CDF. This fact is best illustrated by comparing Fig. 73 with Fig. 74. The muon tagging rate in D0 is a fraction of 1% per jet; in CDF it is a fraction of 1% per track. There are three main reasons for the lower muon background in D0 : (i) muons in D0 have to traverse more steel than in CDF, so that background from hadronic punch-through is lower in D0 than CDF; (ii) the D0 detector is more compact, resulting in a lower probability for decays in flight of pions

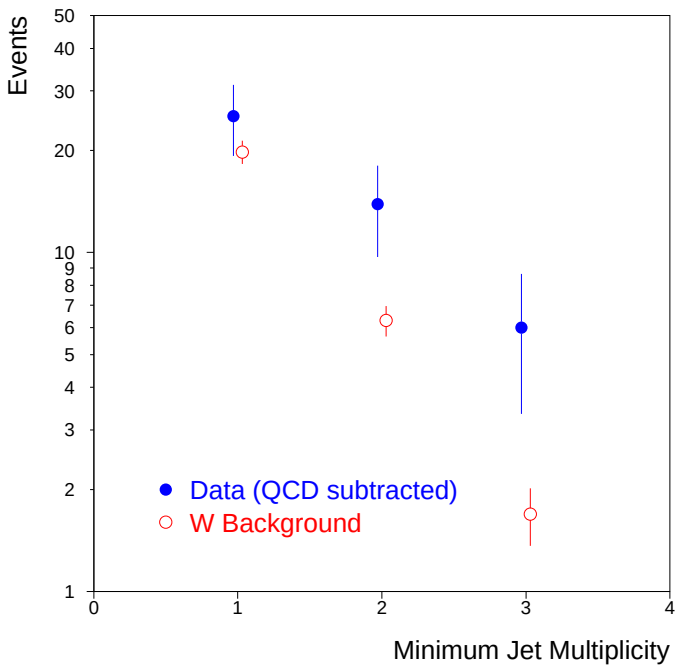

FIG. 75. Comparison between the observed number of muon tags and the background expectation in $W+$ jets event as a function of jet multiplicity for D0 data. The H_T requirement (see Table XI) has been removed for these data. Note that the horizontal axis is in terms of *minimum jet multiplicity*, e.g. the 2-jet bin includes all events with 2 or more jets. From Snyder, 1995a.

and kaons; (iii) the momentum of the muon is measured after the decay-in-flight in D0, whereas in CDF, some average of the momentum of the parent pion and daughter muon is often measured in the drift chamber. The background rate per event, dominated by decays in flight and punch-through, is 1.8% in D0 and 7.6% in CDF.

In addition to these instrumental effects, the different choice of requirements between CDF and D0 contribute to differences in signal-to-background. The D0 pre-tag event sample with the H_T requirement is expected to contain a higher fraction of $t\bar{t}$ events, for sufficiently high top mass. On the other hand, there is no requirement on H_T in CDF, in order to maintain good efficiency for low top masses ($M_{top} < 120$ GeV/c^2). For example, for M_{top} = 200 GeV/c^2, the $t\bar{t}$ contents of the D0 and CDF pre-tag samples are expected to be approximately 9% and 6% respectively, see Table XI.

Furthermore, the minimum P_T requirement for lepton tags is lower in the CDF analysis than in the D0 analysis (2 GeV/c vs. 4 GeV/c). Again, the CDF requirement was chosen to maintain efficiency for low top mass, where leptons from cascade decays have very low transverse momenta, (see Fig. 49). If the CDF requirement were to be raised to 4 GeV/c, the background would be reduced by a factor of ≈ 1.8, while the tagging efficiency for $M_{top} > 130$ GeV/c^2 would be lowered by approximately 20% only (F. Abe *et al.*, 1994a). An excess of events in the CDF lepton tag analysis is also present when the minimum P_T

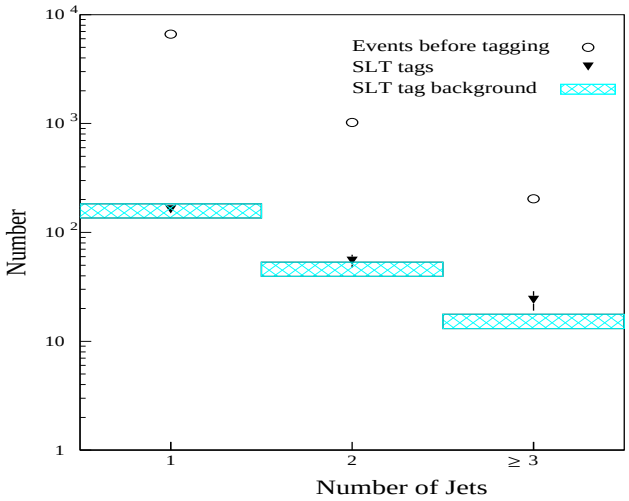

FIG. 76. Comparison between the observed number of lepton tags and the background expectation in $W+$ jets event as a function of jet multiplicity for CDF data (Kestenbaum, 1996).

requirement is raised to 4 GeV/c. In this case, 15 tags in 14 events are observed, with a background of 8.7 ± 1.8 tags (Kestenbaum, 1996).

3. Displaced-vertex tagging in CDF

The most powerful method employed by the CDF collaboration to extract a top signal in the lepton + jet channel is to search for secondary vertices from b-quark decay (vertex tagging). This is made possible with the precise tracking information obtained from a silicon vertex detector.

CDF is the first, and so far the only, experiment to operate such a detector in a hadron collider. The first silicon vertex detector (SVX) at CDF was installed in 1992 prior to the beginning of Run Ia. The SVX (Amidei *et al.*, 1994) is a four-layer cylindrical detector which is 51 cm long. The four layers are at distances of 3.0, 4.2, 5.7, and 7.9 cm from the beamline. Axial microstrips with 60 μm pitch on the three innermost layers and 55 μm pitch on the outermost layer provide precision track reconstruction in the plane transverse to the beam. The single hit resolution is 13 μm, and the impact parameter resolution, for high momentum tracks is 17 μm. The SVX detector suffered significant radiation damage, and was replaced in 1993, during the accelerator shutdown period between Runs Ia and Ib, by a very similar detector (SVX′, Azzi, 1994) equipped with radiation-hard electronics.

The vertex tagging algorithm used by CDF is based on reconstruction of displaced vertices using information from both the central tracking chamber and the SVX (or SVX′). At the Tevatron, $p\bar{p}$ interactions are spread along the beamline with standard deviation $\sigma \approx 30$ cm, so that the geometrical acceptance of the vertex detector is about 60% for $p\bar{p}$ interactions. This geometrical effect turns out to be the largest source of efficiency loss in tagging $t\bar{t}$ events.

The position of the primary vertex is needed before searching for a possible secondary vertex. The transverse spreads of the colliding p and $\bar{p}$ beams result in a luminous region in the transverse plane which is Gaussian in shape with $\sigma \approx 36$ μm. The position and size of this region varies somewhat from store to store, and is monitored with an accuracy of order 10 μm. On an event-by-event basis, knowledge about the position of the primary vertex is improved by performing a fit using information from tracks consistent with originating from the primary vertex. The accuracy of the event-by-event determination of the position of the primary vertex in the transverse plane depends on the number of tracks available to the fit, and varies between 6 and 36 μm.

The vertex tagging algorithm operates on combinations of at least two tracks with impact parameter at least three standard deviations different from zero. Constrained vertex fits are performed on these track combinations in an attempt to find one or more sets of tracks which are consistent with originating from a secondary vertex. Selection criteria are applied to reject tracks from decays of Λ and K^0_s. Results of the vertex fit include the distance in the transverse plane of the secondary vertex from the primary vertex (L_{xy}) and its uncertainty (σ_{lxy}). For a good secondary vertex which results in a b-tag, L_{xy}/σ_{lxy} is required to be > 3. The typical accuracy on the determination of the position of a secondary vertex is $\sigma_{lxy} \approx 130$ μm. This is much smaller than the distance travelled by a b-hadron in a top event (typically a few mm, see Fig. 50), thereby allowing for efficient identification of secondary vertices from b-hadron decay. There are two possible kind of vertex tags, *positive tags* and *negative tags*, (see Fig. 77). Only positive tags are consistent with originating from the decay of a long-lived particle produced at the primary vertex. Negative tags, however, provide useful information on the performance of the b-tagging algorithm, as we will discuss below.

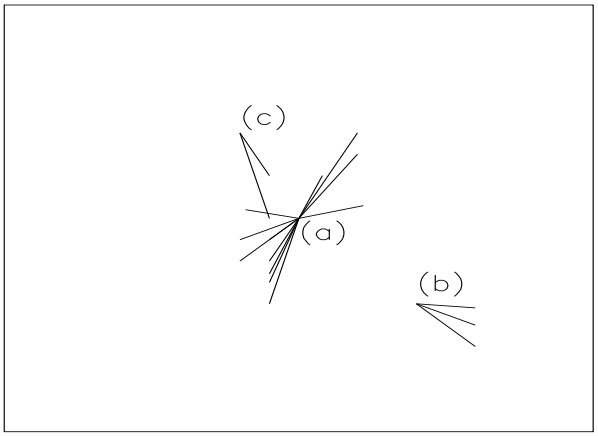

FIG. 77. An idealized sketch of vertex tagging in the transverse plane. The tracks from the primary vertex (a) are used to improve on the accuracy of the determination of the position of the primary vertex. Vertex (b) is a secondary vertex which is consistent with the hypothesis that it originates from the decay of a long-lived particle produced at the primary. This is a *positive tag*. On the other hand, vertex (c), although detached from the primary, is not consistent with the decay of a long-lived particle from the primary. Vertex (c) is an example of a *negative tag*, which is due to track mismeasurements. In a $t\bar{t} \rightarrow$ lepton + jets event, the tracks from vertex (a) in general originate from the underlying event or from the hadronization of the q or $\bar{q}$ from the decay of the W in $t \rightarrow Wb, W \rightarrow q\bar{q}$.

The capabilities of the CDF silicon vertex detector for detection of secondary b-vertices are best illustrated in Fig. 78, which summarizes the CDF measurement of the lifetime of b-hadrons from the decay $B \rightarrow J/\Psi + X; J/\Psi \rightarrow \mu\mu$. The proper decay length (λ) of the b-hadron is reconstructed from the position of the $\mu\mu$ vertex as

$$\lambda = L_{xy} \quad \frac{M_{J/\Psi}}{P_T^{J/\Psi} F(P_T^{J/\Psi})}$$

where $M_{J/\Psi}$ is the J/Ψ mass, $P_T^{J/\Psi}$ is the J/Ψ transverse momentum, and F is a Monte-Carlo determined correction factor which accounts for the undetected particles in the $B \rightarrow J/\Psi + X$ decay. The result of the lifetime fit, $\tau_B = 1.46 \pm 0.06 \pm 0.06$ ps, is one of the world's most precise measurements of this quantity, and is consistent with the results from LEP.

The CDF vertex tag efficiency in top events is $\epsilon_{tag} = (42 \pm 5)\%$. This efficiency is defined as the probability of finding at least one (positive) displaced vertex within one of the jets in a $t\bar{t}$ event with ≥ 3 jets. The vertex tag efficiency is a factor of two larger than the analogous efficiency of the CDF and D0 lepton tag algorithms discussed in the previous Section.

The value of ϵ_{tag} is determined from a Monte Carlo simulation of the response of the detector to $t\bar{t}$ events. In order to verify the reliability of the detector simulation, a number of studies of b-tagging are performed in samples of $b \rightarrow l$ events. The results of these studies are compared with expectations from a Monte Carlo simulation of this process, and the

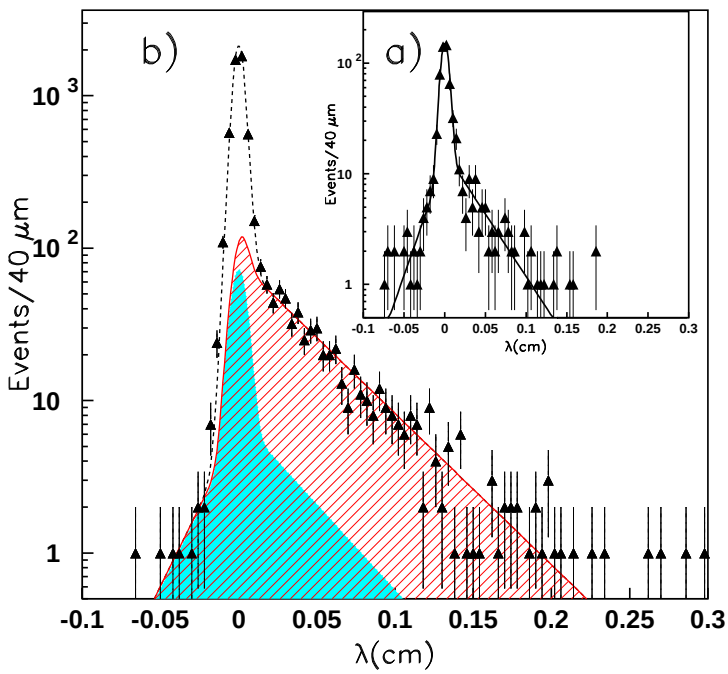

FIG. 78. CDF measurement of the b-hadron lifetime from $B \to J/\Psi + X$ decays. (a) The distribution in λ, the proper decay length, of data in the J/Ψ sideband regions. The solid line shows the result of the fit. (b) The distribution in λ, of data in the J/Ψ region. The curves are the result of the fit. The lightly shaded area is for $B \to J/\Psi + X$ events. The darkly shaded area is for the non-J/Ψ background. The large J/Ψ component at $\lambda \approx 0$ is due to prompt J/Ψ production and to $\chi \to J/\Psi$ decays. From F. Abe *et al.*, 1993d.

level of agreement found between the data and Monte Carlo is used to set the systematic uncertainty on ϵ_{tag}. The largest source of inefficiency is due to the long luminous region of the Tevatron ($\sigma = 30$ cm). Since the vertex detector is only 51 cm long, approximately 40% of the interactions occur outside its geometrical coverage.

Note that the tagging efficiency reported in the first CDF publications on vertex tagging in top events (F. Abe *et al.*, 1994a) was considerably smaller, $\epsilon_{tag} = (22 \pm 6)\%$. This value of the tagging efficiency was underestimated by 15%, due to a mistake in the Monte Carlo simulation. In addition, the tagging algorithm used in the earlier analysis has been substantially improved, and the performance of the SVX′ in terms of efficiency and signal-to-background is somewhat better than that of SVX.

In the lepton tag analyses described in the previous Section, the instrumental and $WQ\bar{Q}$ backgrounds were estimated simultaneously under the assumption that the heavy flavor content of generic jets is the same as the heavy flavor content of jets in W events (Method I, see Section V.E.4). As has been argued before, this method overestimated the size of the $WQ\bar{Q}$ background. On the other hand, the Method II background calculation, which was also discussed at length in Section V.E.4, relies on a theoretical estimation of $WQ\bar{Q}$. To the extent that the instrumental background in the lepton tag analysis is larger than the $WQ\bar{Q}$ background, numerically the Method I and Method II backgrounds are not very different. For the vertex tag analysis, however, this is not the case. Therefore, the CDF collaboration has chosen to calculate the background in this channel using Method II.

The instrumental background, i.e. the background due to false tags in light quarks or gluon jets, is estimated from the negative tagging rate as measured in a sample of generic jets. Since negative tags are almost exclusively due to tracking mismeasurements, and since these mismeasurements are equally likely to produce a positive or a negative tag, the negative tagging rate in generic jet is a measure of the mistag probability. This mistag probability is parametrized as a function of jet E_T, jet pseudo-rapidity, and track multiplicity, (see Fig 79). Based on this probability, the number of expected mistagged jets in the $W+$ jets samples is calculated by summing the mistag probabilities for all the jets in the sample.

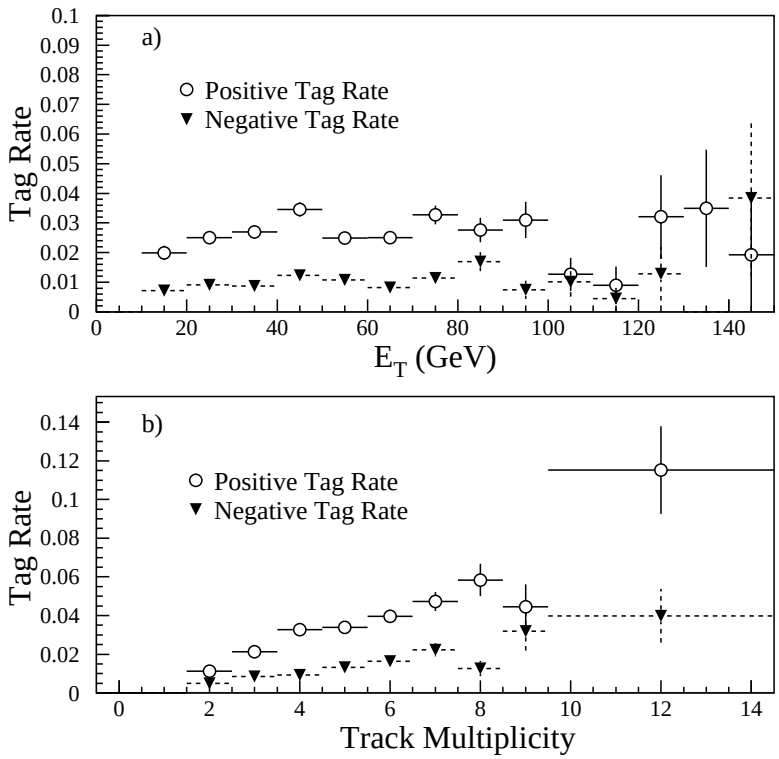

FIG. 79. The tagging rate, defined to be the number of tagged jets divided by the number of jets having two or more tracks with $P_T > 2$ GeV/c reconstructed in the SVX, as a function of (a) the jet E_T, and (b) the number of tracks associated with the jet. Shown are the rates for positive tags (circles) and negative tags (triangles) as measured in a sample of $p\bar{p} \rightarrow$ jets events. The positive tag rate is higher due to the fact that these jets contain a small fraction of heavy quarks (b and c). The positive tag rate is used to calculate the sum of backgrounds due to mistags and $WQ\bar{Q}$ in the Method I background calculation. The negative track rate is used to calculate the mistag background separately in the Method II version of the background calculation. From the CDF collaboration, F. Abe *et al.*, 1994a. Note that these tag rates are not for the final version of the vertex tagging algorithm used by CDF.

The Method II $WQ\bar{Q}$ backgrounds is calculated using theoretical expectations for the rates of $WQ\bar{Q}$. The fraction of W events containing a $Q\bar{Q}$ pair is taken from theory, and multiplied by the number of observed W events to estimate the number of $WQ\bar{Q}$ in the pre-tag samples. The product of this number with the expected $WQ\bar{Q}$ tagging efficiency yields the expected tagged $WQ\bar{Q}$ background. Note that the theoretical input is the fraction of W

Source	$W+$ 1 jet	$W+$ 2 jets	$W+$ 3 jets	$W+ \geq 4$ jets
$WQ\bar{Q}$	13.8 ± 11.1	7.8 ± 6.2	2.0 ± 1.6	0.5 ± 0.4
Mistags	14.8 ± 3.0	5.3 ± 1.1	1.4 ± 0.3	0.5 ± 0.1
$W + c$	15.3 ± 4.6	4.2 ± 1.3	0.9 ± 0.4	0.2 ± 0.1
$Z \rightarrow \tau\tau$, Dibosons	0.8 ± 0.3	0.8 ± 0.3	0.2 ± 0.1	0.04 ± 0.2
$b\bar{b}$	5.7 ± 1.4	3.0 ± 0.8	0.8 ± 0.2	0.18 ± 0.04
Total	50 ± 12	21.1 ± 6.5	5.2 ± 1.7	1.45 ± 0.43
Tagged jets	40	34	17	10

TABLE XII. Summary of Method II backgrounds and tags in the CDF vertex tag analysis (Carithers, 1995). The 27 tags in the $\geq$ 3 jets sample occurr in 21 events. Assuming Standard Model top production, one would expect between approximately 40 (M_{top} = 140 GeV/c^2) and 5 (M_{top} = 200 GeV/c^2) tagged $t\bar{t}$ events in the $\geq$ 3 jets sample.

events that include a $Q\bar{Q}$ pair rather than the much more uncertain absolute rate prediction, see the discussion in Section V.E.4. The $W + c$ background (see Fig. 51) is calculated in a similar manner, i.e. by multiplying the number of $W+$ jets events by the fraction of W events which are expected to contain a single c-quark, and by the tagging efficiency for these events. Other backgrounds, such as $Z \rightarrow \tau\tau$, dibosons, and $b\bar{b}$ are computed mostly from Monte Carlo. The background expectations and event yields are summarized in Table XII, and displayed in Fig. 80

In the $W+ \geq 3$ jets sample, CDF finds 27 tagged jets in 21 events, with a background expectation of 6.7 ± 2.1 tags. The power of the vertex tag algorithm is such that only 1.9 ± 0.4 of these tags can be attributed to mistags, see Table XII. The six events with two tagged jets can be compared with four expected for the top + background hypothesis, and ≤ 1 for background alone. Furthermore, six of the vertex tagged events also include a lepton tag. This is in much better agreement with expectations for top + background (about four events) than with background alone (about one event). As further evidence of a b-contribution to this sample, the proper time distribution for tagged jets is also found to be consistent with expectations from b-jets, see the inset of Fig. 80. As we will show in Section VIII.E, the size of the excess is consistent with expectations from $t\bar{t}$ for a top mass in the neighborhood of 160 GeV/c^2.

The Method II background calculation in the $W+$ 1 jet sample is in good agreement with the data, providing a very important check of the reliability of the background estimation. We note that the Method I background estimate in the $W+$ 1 jet sample yields 80 ± 10 tags, in clear disagreement with the observed 40 tags. In the $W+$ 2 jets sample, the Method II background calculation is lower than the number of tags observed in the data. However, approximately 5 tags from $t\bar{t}$ are expected in this sample based on the excess of tags seen in the higher jet multiplicity samples. After accounting for these events, the background calculation in the $W+$ 2 jet sample is then found to be in satisfactory agreement with the data.

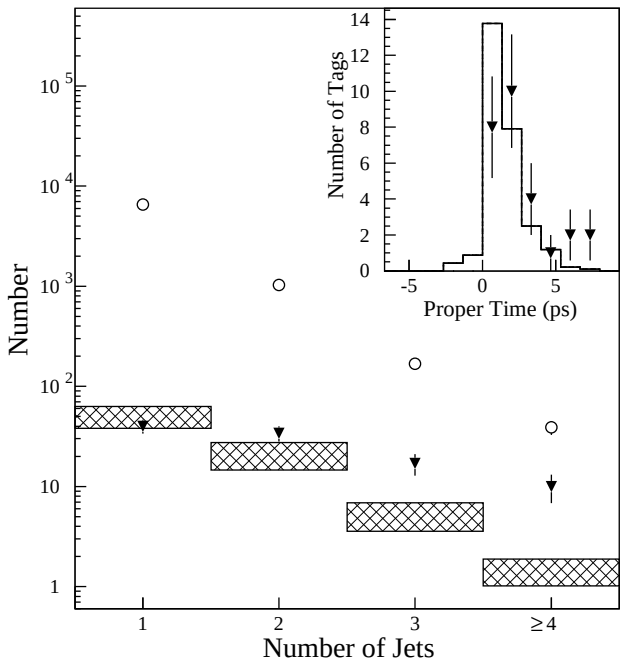

FIG. 80. Number of events before vertex tagging (circles), number of tags observed (triangles), and expected number of background tags (hatched) as a function of jet multiplicity. The inset shows the secondary vertex proper time distribution for the 27 tagged jets in the $W+ \geq 3$ jets data (triangles) compared to the expectation for b-quark jets from $t\bar{t}$ decays. From the CDF collaboration, F. Abe *et al.*, 1995a.

4. Summary and cross checks of the tagging background calculation on $Z+$ jets

Samples of $Z+$ jets in principle provide an ideal testing ground for the calculation of tagging backgrounds in the $W+$ jets sample. The properties of jets in W and Z events are very similar, due to the similarities in the W and Z production mechanism. One exception is that whereas in W events $Q\bar{Q}$ pairs can be produced only through gluon splitting, see Fig. 52, in Z events additional mechanisms are also expected to contribute (e.g. $gg \to Zb\bar{b}$, see Fig. 81). A study of expected tagging rates in W or Z + 4 jets, including a model that approximates experimental efficiencies and backgrounds, indicates that the probabilities of tagging a W or a Z event are expected to be the same within 10-15% (Barger *et al.*, 1994).

Unfortunately, the combined cross-section times branching ratio for $p\bar{p} \to Z \to ll$ is

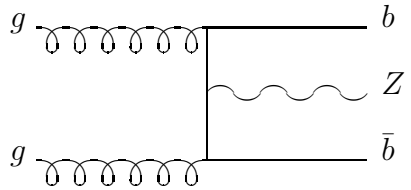

FIG. 81. Feynman diagram for $gg \to Zb\bar{b}$.

	$Z+$ 1 jet	$Z+$ 2 jets	$Z+ \geq 3$ jets
CDF lepton and vertex tag background expectation	17.5	4.2	1.5
CDF lepton and vertex tag data	15	3	2
DO muon tag background expectation	0.97 ± 0.08	0.35 ± 0.05	0.09 ± 0.03
D0 muon tag data	0	0	0

TABLE XIII. Comparison between the number of observed tags in $Z+$ jets data and the background expectations. The CDF results are from Gerdes, 1995, and correspond to an integrated luminosity of 67 pb^{-1}. The D0 results are from Abachi *et al.*, 1995d, and are based on the Run Ia data set only, with an integrated luminosity of 13.5 pb^{-1}.

an order of magnitude lower than the cross-section for $p\bar{p} \to W \to l\nu$, giving only limited statistics in the Z channel. Nevertheless, it is still instructive to compare the yield of tags in the Z sample with the results of the background calculations. This is especially true in light of the fact that two out of the three $Z+ \geq 3$ jets events collected by CDF during run Ia contained one vertex-tagged jet (F. Abe *et al.*, 1994a).

The results of the tagging algorithms on $Z+$ jets events are displayed in Table XIII. With the higher luminosity data sample, the number of tags in the $Z+$ jets data is fully consistent with the background expectations, within the limited statistics. There is no evidence for an anomalously high tagging rate in Z events.

To summarize, the CDF and D0 background calculations have been proved to be reliable and, within the statistical and systematic uncertainties, they have been shown to be able to account for the rate of tagged jets in both $Z+$ jets and $W+$ 1 and 2 jets. There is significant evidence for the presence of an excess of b-jets in the $W+ \geq 3$ jets sample. The largest excess is seen in the CDF vertex tag analysis, which has the highest efficiency and the best signal-to-background. The statistical significances of these excesses, which are consistent in size with the expected $t\bar{t}$ contribution, will be discussed in Section VIII.D.

It is very natural to attribute these excesses to a $t\bar{t}$ component in the data, although they could also be due to some source of $W+$ heavy flavor production beyond standard QCD processes. As we will show in Section VIII.C, additional evidence for the existence of the top quark can be obtained by kinematic studies of lepton + jets events. Furthermore, studies of invariant masses in lepton + jets events show evidence for both $t \to Wb; W \to l\nu$ and $t \to Wb; W \to q\bar{q}$, see Section IX.

Channel	Leptons		Jets				
	$E_T(e)$	$P_T(\mu)$	N_{jet}	E_T	$\not{E}_T$	H_T	$\mathcal{A}$
$e+$jets	≥ 20		≥ 4	≥ 15	≥ 25	≥ 200	≥ 0.05
$\mu+$jets		≥ 15	≥ 4	≥ 15	≥ 20	≥ 200	≥ 0.05

TABLE XIV. D0 kinematic requirements for the standard event selection (energies in GeV, momenta in GeV/c). From Abachi *et al.*, 1995b.

C. Lepton + jets

Both CDF and D0 have performed analyses based on event shapes or kinematic variables rather than b-quark identification in order to increase their $t\bar{t}$ acceptance. They have both used some form of a powerful discriminator between $W+$ jets background and top signal, which is the scalar sum of the transverse energies of the jets and in some cases leptons. D0 has performed an analysis on a data set complementary to the lepton + jet + b-tag data set. That is, it starts with the sample of lepton + jet events in which a b-tag is not found. The results from this counting experiment are used in calculating the significance of the top signal. CDF on the other hand, performs two separate kinematic analyses on the complete lepton+jet data sample which includes b-tagged events. These analyses are however not used in calculating the significance of the top signal both because their results are correlated with the b-tag result, and because kinematic analyses depend to a greater extent on Monte Carlo generation details and theoretical assumptions.

In comparing the data with the theoretical expectations for $W+$ jets, the CDF and D0 analyses use the VECBOS Monte Carlo. As discussed in Section V.E.1, VECBOS is a leading order QCD parton Monte Carlo. Models of the underlying event and of jet fragmentations have been added to VECBOS by both collaborations to allow for comparisons with experimental data.

1. D0 lepton + jet kinematic analysis

The requirements for this analysis are given in Table XIV. This analysis requires that there be at least four jets in the event, in contrast to the b-tag analysis which includes events with three jets. The two main kinematic requirements are that the scalar sum of the transverse energies of the jets, H_T, be > 200 GeV and that the event be aplanar such that, $\mathcal{A} > 0.05$. Aplanarity, $\mathcal{A}$, was defined in Section V.E.3 as $\mathcal{A} \equiv 3/2\lambda_1$, where λ_1 is the smallest eigenvalue of the matrix $M_{ab} = \sum P_a P_b / \sum P^2$, where P_i are the cartesian components of momentum of the parton, P is the magnitude of the three-momentum, and the sum is over all partons. In the D0 analysis, $\mathcal{A}$ is calculated from the jets in the event. Note that the definition of H_T in the D0 lepton + jets analysis is different than the definition of H_T in the dilepton analysis, where the E_T of the highest transverse energy electron was also included, see Section VIII.A. Fig. 82 shows the distribution H_T for top quarks produced by Monte Carlo and expectations for principal backgrounds. There is expected to be a clear separation between signal and background.

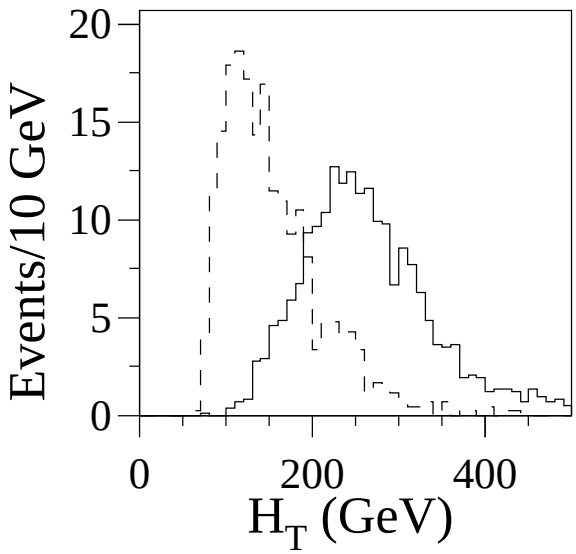

FIG. 82. Expected H_T distributions in D0 for top Monte Carlo events with $M_{top} = 200$ GeV/c^2 in the lepton + jets + no b-tag sample (solid) and the principal backgrounds to this channel (dashed). From Abachi *et al.*, 1995b.

This analysis must rely on the correctness of both the Monte Carlo kinematics and the energy scale of the calorimeters. To check the combined effect, comparisons are performed between data and Monte Carlo distributions of H_T for two samples dominated by background, $W+ \geq 2$ jets and $W+ \geq 3$ jets. Fig. 83 shows the data and VECBOS Monte Carlo prediction for these two samples. These samples may contain some top events, but are dominated by $W+$ jets background if the theoretical expectations for the $t\bar{t}$ production cross-section are correct. The agreement between the data and the Monte Carlo prediction is quite good.

The acceptance, including branching ratio (24/81, see Table III), for the D0 $t\bar{t}$ kinematic search ranges from 0.50% for $M_{top} = 140$ GeV/c^2 to 1.70% for $M_{top} = 200$ GeV/c^2. The expected background, the expected signal and the data are shown in Table XV, and Fig. 84.

The two main sources of background in this analysis are QCD events in which one jet fakes the lepton signature and, especially, $W+ \geq 4$ jet events. The QCD background is calculated by studying a sample of events containing electromagnetic clusters that fail the lepton selection requirements. The estimation of the $W+$ jets background is clearly a crucial issue. This background is estimated in two ways (Abachi *et al.*, 1995d; Grannis, 1995). In the first method, the number of $W+ \geq 4$ jets events in the data is estimated by extrapolating from the number of $W+ \geq 2$ and 3 jets events assuming a scaling law, i.e. assuming that the ratio N_n/N_{n-1} is independent of n, where N_n is the number of QCD $W+ \geq n$ jets events, (see Fig. 85 and Fig. 86). Then, the number of $W+ \geq 4$ jets events expected to satisfy the aplanarity and H_T requirement is obtained from N_4 and the shape of the VECBOS Monte Carlo distribution for $W+ \geq 4$ jets in the $\mathcal{A}$ vs. H_T plane, (see Fig. 84). An alternative estimate is obtained by fitting the number of events in the four regions of the $\mathcal{A}$ vs. H_T plane indicated in Fig. 84 to contributions from $t\bar{t}$, $W+ \geq 4$ jets and QCD events, where the shapes of the $t\bar{t}$ and $W+ \geq 4$ jets components are taken from Monte Carlo. The two methods are in reasonable agreement. The total expected background is 1.9 ± 0.5 events

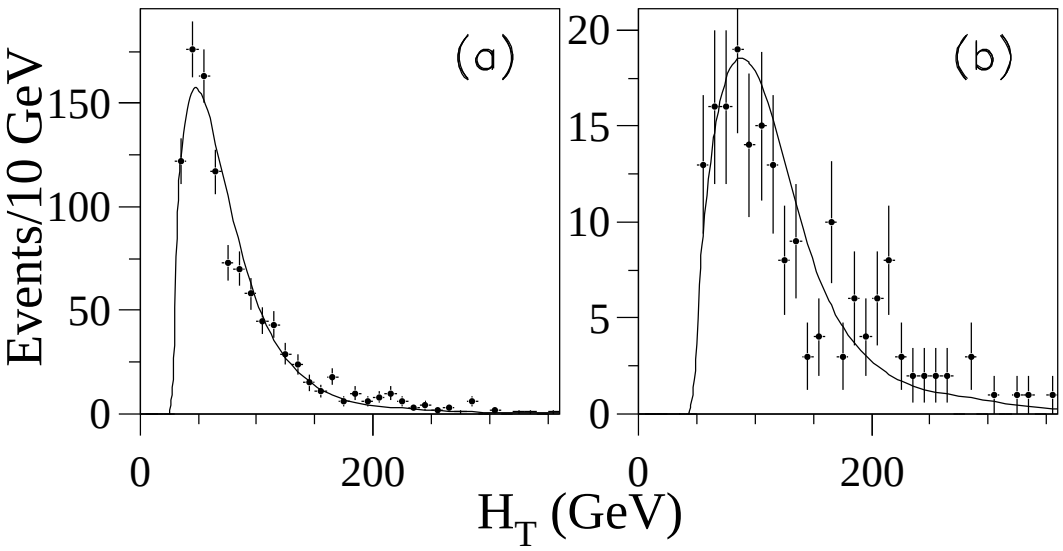

FIG. 83. D0 H_T distributions for (a) e + $\geq$ 2 jets, and (b) e + $\geq$ 3 jets The curves are expectations from the VECBOS Monte Carlo normalized to the data. From Snyder, 1995a, for an integrated luminosity of 48 pb^{-1}.

for the scaling method, and $2.6^{+0.5}_{-0.8} \pm 0.5$ events for the fit in the $\mathcal{A}$ vs. H_T plane (Grannis, 1995).

		Events
e + jets	Expected background	1.22 ± 0.42
	Expected for M_{top} = 140 GeV/c^2	4.05 ± 0.94
	Expected for M_{top} = 200 GeV/c^2	1.8 ± 0.31
	D0 data	5
μ + jets	Expected backgrounds	0.71 ± 0.28
	Expected for M_{top} = 140 GeV/c^2	2.47 ± 0.68
	Expected for M_{top} = 200 GeV/c^2	0.95 ± 0.24
	D0 data	3

TABLE XV. D0 Lepton + jets results. From Abachi *et al.*, 1995b. The integrated luminosities are 48 pb^{-1} for e + jets and 44 pb^{-1} for μ+ jets. The $t\bar{t}$ expectations are normalized to the $\sigma(t\bar{t})$ calculation of Laenen, Smith, and van Neerven, 1994.

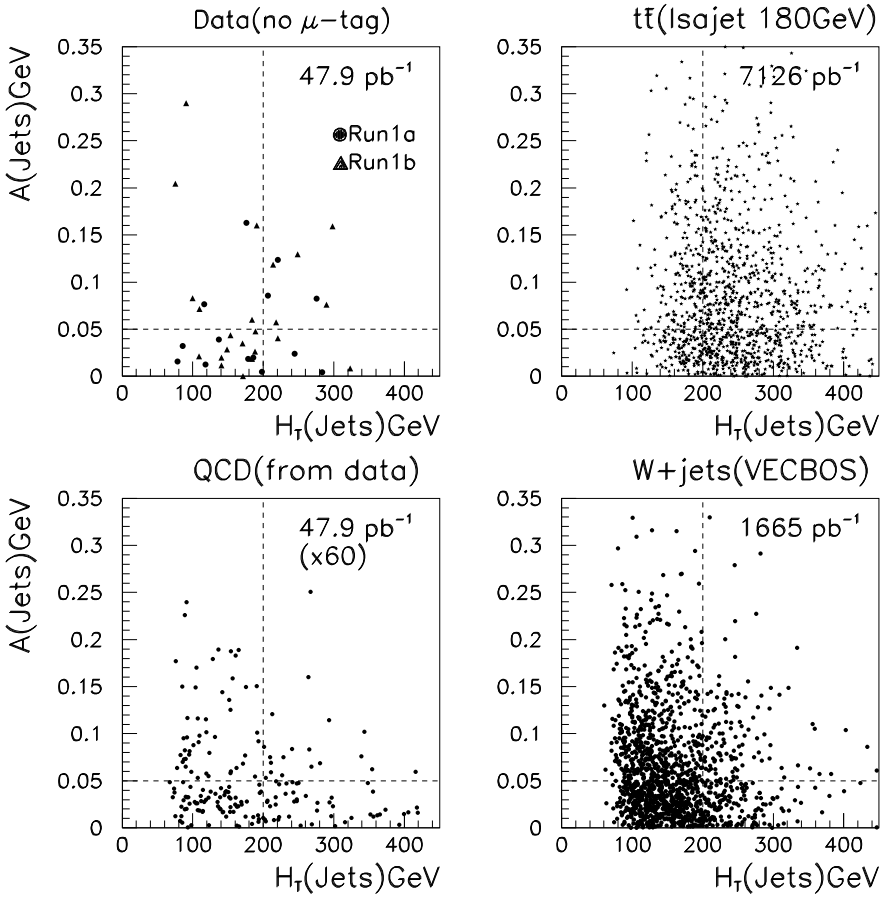

FIG. 84. Aplanarity ($\mathcal{A}$) versus H_T for single-lepton events for data, $t\bar{t}$ Monte Carlo, multijet background from data (with an effective luminosity = 60 x data luminosity), and background from W+ jets VECBOS Monte Carlo. From the D0 collaboration, Abachi *et al.*, 1995f.

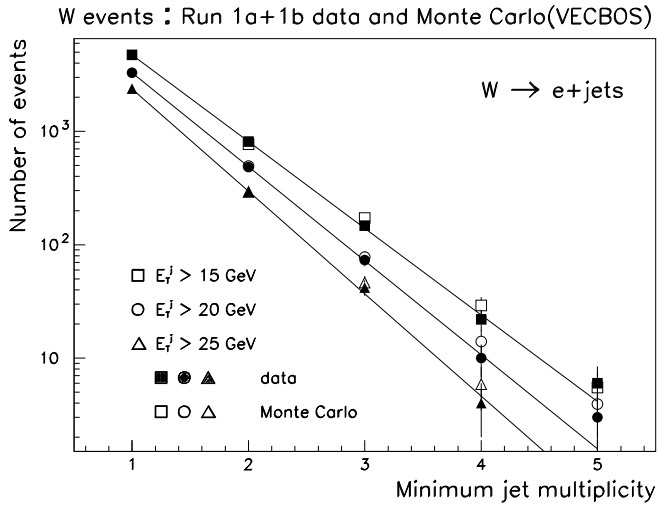

FIG. 85. Inclusive jet multiplicity spectrum for $W \to e\nu$ + jets events for several jet energy thresholds. Data are shown by the solid symbols. Monte Carlo predictions are shown by the open symbols. From the D0 collaboration, Abachi *et al.*, 1995f. The integrated luminosity is 48 pb^{-1}.

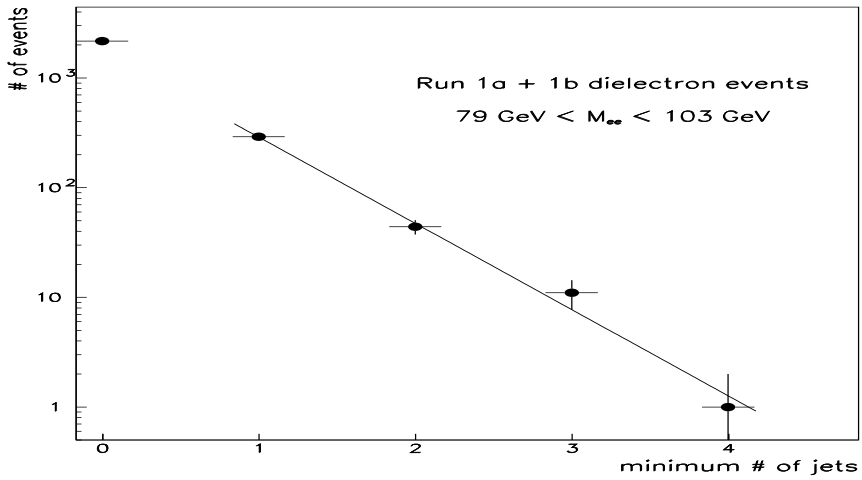

FIG. 86. Inclusive jet multiplicity spectrum for $Z \to ee+$ jets events. From the D0 collaboration, Snyder, 1995a. The integrated luminosity is 56 pb^{-1}.

Sample	Threshold	N_{jets}	E_T (GeV)	$\|\eta_{jet}\|$	Events
Control	low	=3	≥ 8	≤ 2.4	814
		Veto jet 4	≥ 8	≤ 2.4	
Control	high	=3	≥ 15	≤ 2.0	104
		Veto jet 4	≥ 8	≤ 2.4	
Signal	low	≥ 4	≥ 8	≤ 2.4	267
Signal	high	≥ 3	≥ 15	≤ 2.0	99
		≥ 1	≥ 8	≤ 2.4	

TABLE XVI. CDF definition of the two control and two signal samples in the H analysis. The third, fourth and fifth columns list the criteria placed on the jets in each event. The integrated luminosity is 67 pb^{-1}.

2. CDF lepton + jets kinematic analysis

Two kinematic analyses of lepton + jets data have been published by the CDF collaboration. The first analysis (*H analysis*, F. Abe *et al.*, 1995c) is similar to the D0 analysis. The second analysis (*cosθ^* analysis*, F. Abe *et al.*, 1995b) relies on the fact that jets in $t\bar{t}$ events are more central than jets in $W+$ jets.

The variable H in CDF is defined as the scalar sum of the lepton transverse momentum, the $\not\!\!E_T$ (i.e. the P_T of the ν) and the E_T's of all jets with $E_T \geq 8$ Gev and pseudo-rapidity $|\eta| \leq 2.4$. Note that while the event selection uses uncorrected jet transverse energies, H is calculated using corrected energies. The difference between the variables H used by CDF and H_T used by D0 is the inclusion of the measurements of $\not\!\!E_T$ and lepton momentum in H.

The H analysis is performed by comparing the observed H distribution in the data with prediction from the $W+$ jets and $t\bar{t}$ Monte Carlos. A deviation from the $W+$ jets expectation would then signal the presence of $t\bar{t}$ in the data. Note that this approach is totally independent of theoretical expectations for the $W+$ jets cross-section since it relies only on the predicted shape of the H distribution. In order to check the reliability of the theoretical prediction, the data H distribution is compared with theoretical predictions in four different samples, two control samples and two signal samples, see Table XVI.

The two control samples reject events with a fourth jet. These samples are designed to be dominated by background, and are a good testing ground for the VECBOS $W+$ jets calculation. There are less than 10 $t\bar{t}$ expected in each sample. The first control sample has a low requirement on the transverse energy of the jets, to further increase the proportion of $W+$ jet background relative to top events. The two signal samples require the presence of a fourth jet. The first signal sample is obtained with a low transverse energy threshold on the jets (8 GeV); in the second signal samples, which is expected to be enriched in $t\bar{t}$ events, at least three of the four jets must have transverse energies greater than 15 GeV.

Data-Monte Carlo comparisons for the control samples and the signal samples are displayed in Fig. 87 and Fig. 88. The shape of the H distribution in the control samples agrees with the $W+$ jets VECBOS Monte Carlo, while the two signal samples are not consistent

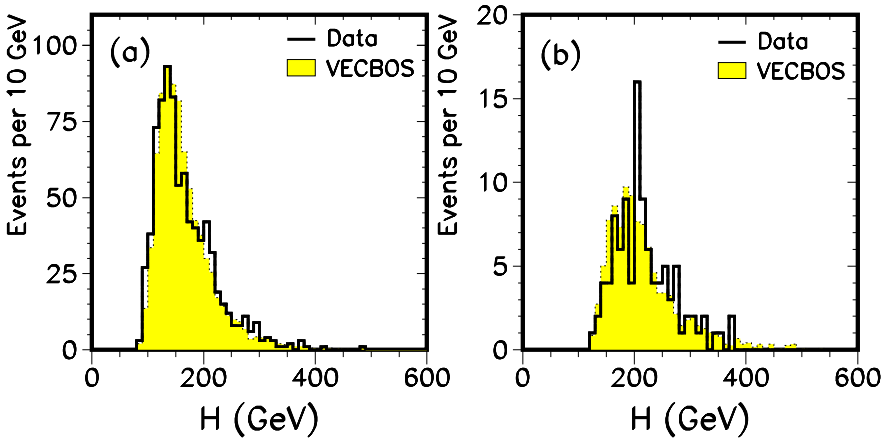

FIG. 87. Comparison of the H distribution for the control data samples and the VECBOS Monte Carlo prediction. (a) $W + 3$ jets events passing the low E_T threshold requirements; (b) $W + 3$ jets events passing the high E_T threshold requirements. The VECBOS prediction, including a 1% $t\bar{t}$ contribution for (a) and 10% $t\bar{t}$ contribution for (b), has been normalized to the data. From the CDF collaboration, F. Abe *et al.*, 1995c. The integrated luminosity is 67 pb^{-1}.

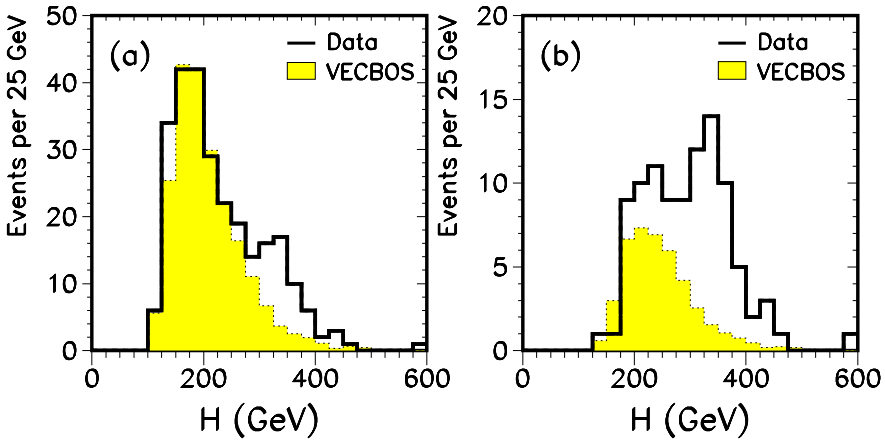

FIG. 88. Comparison of the H distribution for the signal data samples and the VECBOS Monte Carlo prediction. (a) $W+ \geq 4$ jets events passing the low E_T threshold requirements; (b) $W+ \geq 4$ jets events passing the high E_T threshold requirements. The VECBOS prediction is normalized to a fit to the sum of $t\bar{t}$ and $W + 4$ jets Monte Carlo predictions. From the CDF collaboration, F. Abe *et al.*, 1995c. The integrated luminosity is 67 pb^{-1}.

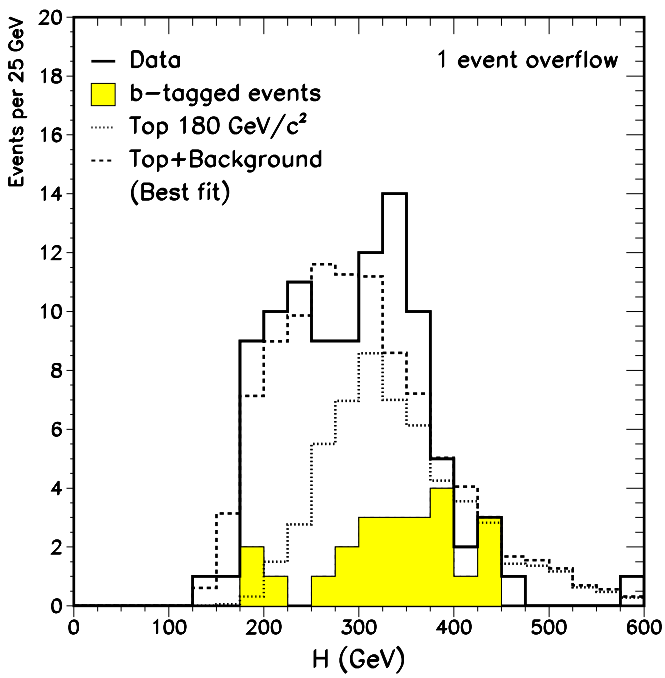

FIG. 89. The binned likelihood fit of the high E_T threshold signal sample (solid line) to a linear combination of the VECBOS $W + 4$ jets and HERWIG $t\bar{t}$ Monte Carlo prediction. The H distribution of b-tagged events is shown in the shaded histogram. From the CDF collaboration, F. Abe *et al.*, 1995c. The integrated luminosity is 67 pb^{-1}.

with $W+$ jets production alone. The differences between the high threshold signal sample and the VECBOS Monte Carlo is too large to be explained entirely by a systematic error in the experimental energy scale.

The shape of the H distribution for $t\bar{t}$ events is expected to be a function of M_{top}. Fitting the data to a linear combination of $W+$ 4 jets and $t\bar{t}$ Monte Carlo prediction yields $M_{top} = 180 \pm 12(\text{stat.})^{+19}_{-15}(\text{syst.})$ GeV/c^2. This value for M_{top} is in good agreement with both the expected value from the Standard Model and with the directly measured value, see Section IX. Furthermore, the $t\bar{t}$ cross-section extracted from this measurement is also in good agreement with the cross-section extracted from studies of dilepton and b-tagged events, see Section VIII.E.

As a further evidence for $t\bar{t}$, the events containing b-tags are highlighted in Fig. 89. These events are concentrated at high values of H, as would be expected for $t\bar{t}$. Note that in background events there is a small dependence on the b-tag probability as a function of jet E_T, and hence as a function of H, which biases the tagged events to high H. However, if one assumes that there are no $t\bar{t}$ events in the sample, this bias is not sufficient to account for the concentration of tagged events at high values of H.

The second CDF kinematic analysis of lepton + jets data, ($\cos\theta^*$ analysis, F. Abe *et al.*, 1995b), is based on the fact that jets in top events are expected to be more central than in $W+$ jets events (Cobal, Grassman, and Leone, 1994). This analysis is also based on control and signal samples, see Table XVII. The only difference in the two samples is in the requirement on the cosine of the polar angle (θ^*) of the jets in the center of mass frame

Channel	Leptons		Jets			$\not\!\!E_T$	$l\nu$ transverse mass
	E_T(e)	$P_T(\mu)$	$N_{\rm jet}$	E_T	$\lvert\cos\theta^*\rvert$		
Signal $e+$jets	≥ 20		≥ 3	≥ 20	≤ 0.7	≥ 25	≥ 40
Signal $\mu+$jets		≥ 20	≥ 3	≥ 20	≤ 0.7	≥ 25	≥ 40
Control $e+$jets	≥ 20		≥ 3	≥ 20	≥ 0.7	≥ 25	≥ 40
Control $\mu+$jets		≥ 20	≥ 3	≥ 20	≥ 0.7	≥ 25	≥ 40

TABLE XVII. CDF kinematic requirements for the $\cos\theta^*$ kinematic analysis. $\cos\theta^*$ is the cosine of the polar angle of the jet in the center of mass frame of the lepton + neutrino + jets system. The $\cos\theta^*$ requirement applies to the three highest E_T jets only. Unlike all other CDF analyses, in this analysis jet energies are corrected at the event selection stage. Energies are in GeV, momenta are in GeV/c. From F. Abe *et al.*, 1995b. The integrated luminosity is 67 pb^{-1}.

of the two incoming partons. Events in the signal sample have three high E_T central jets, events in the control sample have at least one jet that is emitted in the forward or backward region. Monte Carlo studies indicate that top events should be approximately equally split between signal and control samples, whereas of order 75% of $W+$ jets events should be in the control sample. Thus, the signal sample should be enriched in top quarks with respect to the control sample.

An event-by-event Monte Carlo-based relative likelihood for the $t\bar{t}$ versus the $W+$ jets hypothesis is constructed for all events based on the E_T of the second and third highest E_T jets in the event. Distributions of log-likelihood for data and Monte Carlo, for both signal and control sample, are displayed in Fig. 90 and Fig. 91. There is a clear excess of events at high log-likelihood in the signal sample. The probability that the shape of the data log-likelihood distribution can be explained by $W+$ jets alone is $< 0.26\%$, assuming the VECBOS model of $W+$ jets production. Furthermore, the b-tagged events are concentrated in the high log-likelihood region, as one would expect for $t\bar{t}$.

3. Summary of lepton + jets kinematic analyses

The CDF and D0 collaborations have performed extensive studies of the kinematic properties of lepton + jet events. The $W+$ jets data are inconsistent with the expectations from leading order QCD as implemented in the VECBOS Monte Carlo program, for high jet multiplicities and high jet transverse energies. On the other hand, there seems to be satisfactory agreement between data and theory in regions of low jet multiplicity and/or low jet transverse energies. The conclusion that can be drawn is that either the available QCD calculation is incorrect or incomplete, or that there is a source of events beyond standard QCD production of $W+$ jets. The most natural interpretation of the data is to ascribe this discrepancy to a $t\bar{t}$ component in the data. The correlation between high jet transverse energies and b-tags reported by the CDF collaboration strengthens this conclusion.

As was mentioned in Section V.E.3, samples of $Z+$ jets events are ideal to test the predictive power of the vector-boson + jets QCD calculation. A number of such tests have been performed, and they seem to yield results consistent with the QCD calculation. However, the statistics in the Z samples are not sufficient to decisively validate the QCD

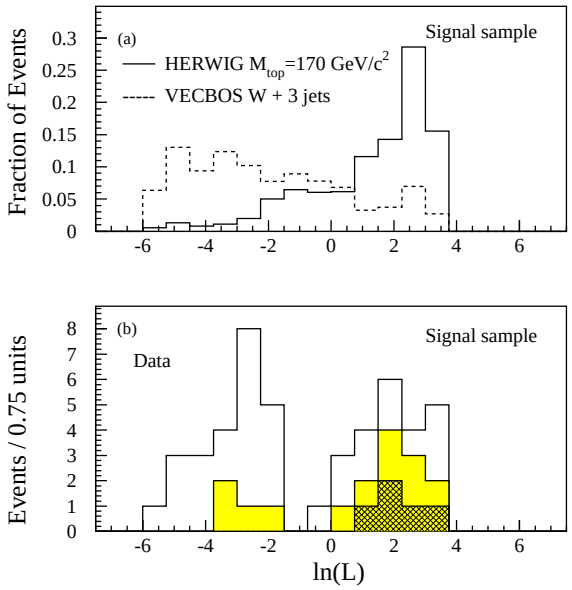

FIG. 90. The distribution in natural log-likelihood for events in the signal sample. (a) Monte Carlo expectations for $W+$ jets (VECBOS) and $t\bar{t}$ (HERWIG); (b) Data. The lightly shaded histogram shows the b-tagged events. The darkly shaded histogram shows events with two b-tags. From the CDF collaboration, F. Abe *et al.*, 1995b. The integrated luminosity is 67 pb^{-1}.

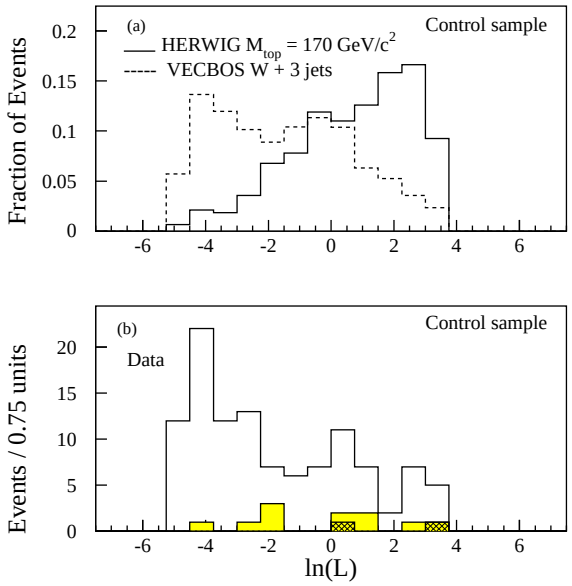

FIG. 91. The distribution in natural log-likelihood for events in the control sample. (a) Monte Carlo expectations for $W+$ jets (VECBOS) and $t\bar{t}$ (HERWIG); (b) Data. The lightly shaded histogram shows the b-tagged events. The darkly shaded histogram shows events with two b-tags. From the CDF collaboration, F. Abe *et al.*, 1995b. The integrated luminosity is 67 pb^{-1}.

calculation in the kinematic region most relevant for the top search.

D. Significance of the top signal

As discussed in Sections VIII.A, VIII.B, and VIII.C, the CDF and D0 top searches in a number of different channels find excesses of top-like events over the background predictions. The significance of the excess for a given channel is defined as the probability that a background fluctuation would yield a number of events equal to or larger than the number of observed events. This probability is calculated by convoluting the Poisson probability for the fluctuation of the mean expected number of background events with its uncertainty, which is assumed to be Gaussian.

When combining results from more than one channel, D0 and CDF use different procedures. In the D0 case, events from all channels as well as backgrounds from all channels are added, and the combined significance is defined as the probability that the sum of all the backgrounds fluctuates to give a total number of events greater than or equal the number of observed events. On the other hand, the CDF combined significance is defined as the probability that the product of the significances for the different channels be less than or equal to the measured value for this product. This is necessary since the CDF vertex-tag channel has so much better efficiency and signal to noise than the dilepton and (especially) the lepton-tag channels. In fact, if the D0 prescription were to be applied to compute the total significance of the CDF excesses in the three channels, the combined excess would appear less significant than the excess seen in the vertex-tag channel alone, despite the fact that excesses are seen in the other two channels as well. When combining different channels, correlations are accounted for. For example, both the CDF lepton and vertex tag searches are sensitive to the size of the $\mathrm{W}Q\bar{Q}$ background, resulting in a correlation between significances in the two channels. These effects are taken into account using Monte Carlo simulations.

The significances for the CDF and D0 results are displayed in Table XVIII. These significances, which as discussed above are just probabilities, are also expressed in number of standard deviations (No. of σ). The number of σ corresponds to the point in a Gaussian probability function of mean zero and unit standard deviation where the integral of the probability function between that point and infinity is equal to the significance.

The results from both experiments are such that the probability that the data can be explained as background fluctuations is exceedingly small. We note that, in the calculation of the combined significance of their top observation, the CDF collaboration very conservatively does not include the excess of top-like events seen in their purely kinematic analyses of lepton + jets data (see Section VIII.C.2). Furthermore, as will be discussed in Section IX, both CDF and D0 find additional evidence for a $t\bar{t}$ contribution to their lepton + jet data samples in the top mass reconstruction analyses. To summarize, the data from the counting experiments at the Tevatron provide overwhelmingly convincing evidence for the existence of new physics. We shall show in the following section that the invariant mass and kinematics of this new physics are consistent with a top quark of $\mathrm{M}_{top} \approx 175$ GeV/c^2.

Experiment	Channel	Events observed	Expected background	Significance	No. of σ
D0	Muon b-tag	6	1.2±0.2	2 x 10^{-3}	2.9σ
D0	Lepton + jets	8	1.9±0.5	2 x 10^{-3}	2.9σ
D0	Dileptons	3	0.7±0.2	3 x 10^{-2}	1.9σ
D0	All combined	17	3.8±0.6	2 x 10^{-6}	4.6σ
CDF	Vertex b-tag	21 (27)	6.7±2.1	2 x 10^{-5}	4.2σ
CDF	Lepton b-tag	22 (23)	15.4±2.0	6 x 10^{-2}	1.5σ
CDF	Dileptons	6	1.3±0.3	3 x 10^{-3}	2.7σ
CDF	All combined	43 (56)	23.4±2.9	1 x 10^{-6}	4.8σ

TABLE XVIII. CDF (F. Abe *et al.*, 1995a) and D0 (Abachi *et al.*, 1995b) event yields, background expectations, and significances of the observed excesses of top-like events in different channels. In the CDF b-tagging channels, we show both the number of events and, in brackets, the number of tags. There are 6 events which are tagged with both a vertex b-tag and a lepton b-tag in CDF. The two *all combined* entries for CDF data refer to 43 events and 56 *objects*, where an object is defined as either a dilepton event or a tag in a lepton + jets event. The CDF b-tag backgrounds are expressed in number of tags; the CDF all combined background is expressed in number of objects. Tags in CDF dilepton events are not included anywhere in this table.

E. Measurement of the $p\bar{p} \to t\bar{t}$ cross-section

The $t\bar{t}$ production cross-section is calculated from the luminosity, the background-subtracted event yields, the acceptances, and the $t\bar{t}$ decay branching fractions for the various channels. The calculated cross-section depends on the top mass, since the acceptances are in general also a function of the top mass.

The measurement is complicated by the fact that in some cases the expected number of background events depends on the cross-section itself. For example, in the CDF b-tag analysis the background due to $WQ\overline{Q}$, which is quoted in computing the significance of the $t\bar{t}$ observation, is calculated under the assumption that the pre-tag $W+ \geq 3$ jets sample does not contain any top events. Having established the existence of the top quark, this background estimate needs to be revised, since the untagged sample does indeed include a $t\bar{t}$ component. This is accomplished by first calculating the cross-section using the overestimated background contribution, then recalculating the background based on the value of the cross-section, and iterating until the result becomes stable.

The CDF and D0 $t\bar{t}$ production cross-sections, are listed in Table XIX, and displayed in Fig. 92. As discussed at the beginning of this Section, the cross-section calculation depends on the assumed value of M_{top}. Here we report $\sigma(p\bar{p} \to t\bar{t})$ computed at the values of M_{top} measured by the two collaborations, see Section IX. The CDF and D0 cross-sections reported here are obtained from data sets of 110 pb^{-1} and 100 pb^{-1} respectively.

The top mass dependence of the cross-section measurement is $\delta\sigma/\delta\mathrm{M}_{top} \approx -0.05$ pb/GeV/c^2 (D0) and -0.04 pb/GeV/c^2 (CDF). For both experiments the dominant uncertainty on $\sigma(p\bar{p} \to t\bar{t})$ is due to the limited statistics of the data samples. Also, for both experiments the separate cross-section measurements in the different channels are nicely consistent with each other. The CDF measurement is lower than, although still consistent

Experiment	Top mass	Channel	Measured cross-section
D0	180 GeV/c^2	Muon tag	6.8 ± 3.2 pb
D0	180 GeV/c^2	Lepton + jets	3.9 ± 1.9 pb
D0	180 GeV/c^2	Dileptons	4.6 ± 3.1 pb
D0	180 GeV/c^2	All combined	4.7 ± 1.6 pb
D0	170 GeV/c^2	All combined	5.2 ± 1.8 pb
CDF	176 GeV/c^2	Vertex tag	$6.8^{+2.3}_{-1.8}$ pb
CDF	176 GeV/c^2	Lepton tag	$8.0^{+4.4}_{-3.6}$ pb
CDF	176 GeV/c^2	Dileptons	$9.3^{+4.4}_{-3.4}$ pb
CDF	176 GeV/c^2	All combined	$7.5^{+1.9}_{-1.6}$ pb

TABLE XIX. CDF (Tartarelli, 1996) and D0 (Narain, 1996; Klima, 1996) measurements of $\sigma(p\bar{p} \to t\bar{t})$ at a center-of-mass energy of 1.8 TeV. The integrated luminosities for these measurements are 110 pb^{-1} for CDF and 100 pb^{-1} for D0. Note that the most recent D0 top mass value is $M_{top} = 170 \pm 18$ GeV/c^2, see Section IX.A.4. Cross section values for this value of M_{top} for the individual channels have not been released by the D0 collaboration. Here we list these cross-sections at $M_{top} = 180$ GeV/c^2 to demonstrate the consistency between the measurements in the different channels.

with, the cross-section value of $13.9^{+6.1}_{-4.8}$ pb obtained from the analysis of the first 19 pb^{-1} of CDF data (F. Abe *et al.*, 1994a).

Both the CDF and D0 $t\bar{t}$ cross-section measurements are in agreement with the theoretical prediction. To summarize, both collaborations have not only reported excesses of top-like events in several different channels, but the sizes of these excesses are also consistent with each other. From these measurements, they have extracted values of $\sigma(p\bar{p} \to t\bar{t})$ which are consistent, within the quoted uncertainties, with Standard Model expectations.

IX. MEASUREMENT OF THE TOP QUARK MASS

The CDF and D0 top quark searches described in Section VIII yield an excess of top-like events over the background expectations. In this Section we will present measurements of the top mass performed on a sub-set of these events. As was discussed in Section III, the mass of the top quark is one of the free parameters of the Standard Model, and its value enters in the calculation of radiative corrections to a large number of electroweak observables. Comparison of the measurement of M_{top} with indirect determinations from electroweak measurements at LEP and SLC, as well as measurements of the W mass at the Tevatron and LEP200, and analysis of neutral current neutrino data, allow for rather stringent tests of the Standard Model.

There are a number of possible ways to extract the top mass from the CDF and D0 data. An indirect method is to simply compare the cross-section for the observed $t\bar{t}$ signal with its theoretical expectation, since the latter depends very strongly on the top mass, (see Fig. 92). However, it is more informative to *measure* both the top mass and the $t\bar{t}$ cross-section, and

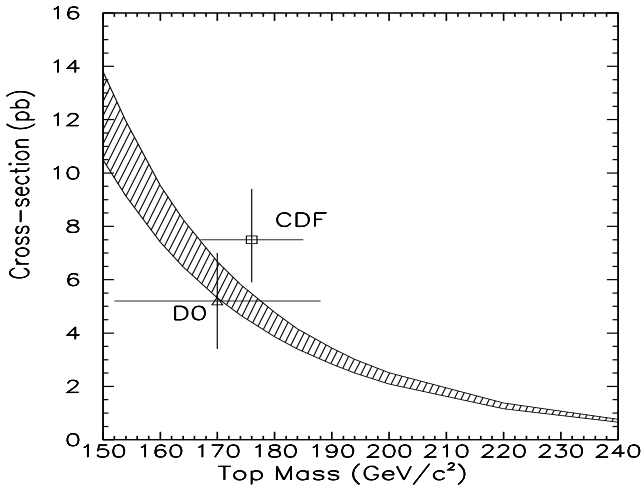

FIG. 92. Combined CDF and D0 top cross-section and mass measurements. (The mass measurements will be summarized in Section IX). Also shown, as a band, is the theoretical expectation for $\sigma(p\bar{p} \to t\bar{t})$ as a function of M_{top} with its uncertainty (Laenen, Smith, and van Neerven, 1994).

then compare with the theoretical prediction for $\sigma(t\bar{t})$. This approach results in a test of the QCD calculation of top production, and is sensitive to possible non-Standard Model production mechanisms for top quarks, see the discussion in Section X.

Both CDF (F. Abe *et al.*, 1994a and 1995a) and D0 (Abachi *et al.*, 1995b) have reported direct measurements of the top mass from lepton + jets data and these will be reviewed in Section IX.A. Other less direct methods to extract the value of M_{top} from both the lepton + jets data and the dilepton data will be summarized in Section IX.B. Finally, in Section IX.C, we will present results of attempts to reconstruct the W mass from $W \to q\bar{q}$ in lepton + jets events.

A. Direct measurements of the top quark mass from lepton + jets events

The method used by both CDF and D0 to measure the top quark mass is the standard method used in particle physics to measure particle masses, namely one measures the momenta of all the decay products, assigns masses to them, and then reconstructs the invariant mass of the original particle. In the case of top quarks, the decay products include neutrinos and hadron jets. The first example of the reconstruction of resonances using jets was UA2's observation of a bump consistent with the W and Z in the jet-jet invariant mass distribution (Alitti *et al.*, 1991a). In this case there was an an enormous background from QCD production of jets not involving a vector boson. The field of jet-spectroscopy is still in its infancy, although much progress has been made in the past year.

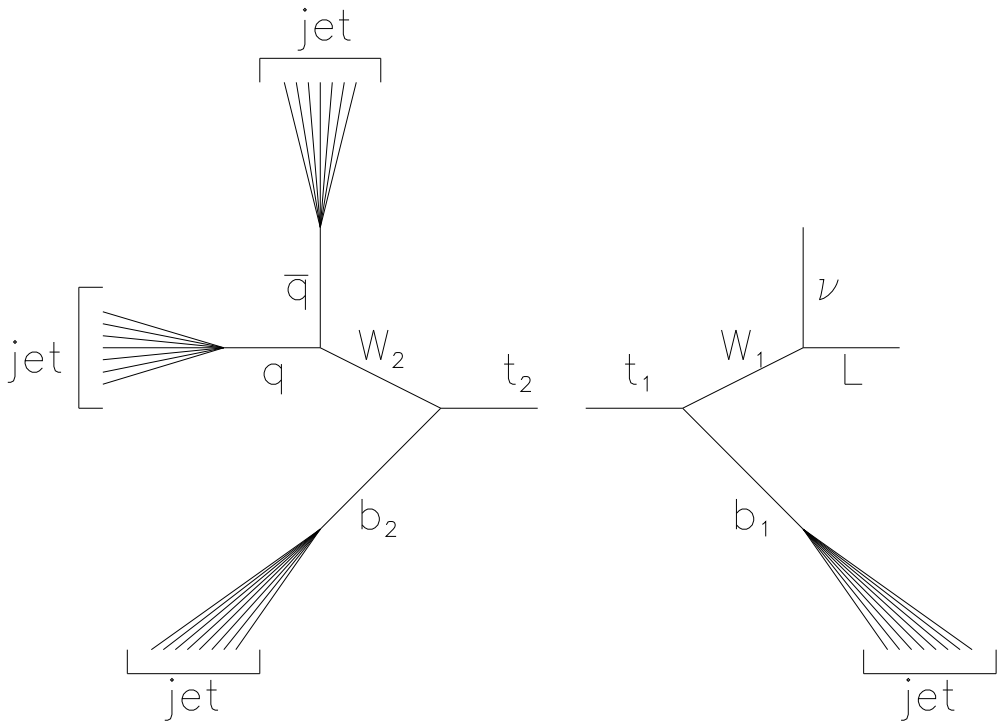

FIG. 93. Sketch of the $t\bar{t}$ decay chain in the lepton + jets channel.

1. Constrained fits, combinatorics, and top mass resolution

In the $t\bar{t} \rightarrow$ lepton + jets mode, one of the two top quarks (t_1) decays semi-leptonicaly and the other one (t_2) decays hadronicaly, (see Fig. 93) :

$$t_1 \rightarrow W_1 b_1 \quad ; \quad W_1 \rightarrow l\nu$$

$$t_2 \rightarrow W_2 b_2 \quad ; \quad W_2 \rightarrow q\bar{q}$$

The mass measurement is performed on the sample of events with a lepton, $\not{E}_{\mathrm{T}}$ and four jets. The four jets are identified with the four quarks in the final state (b_1, b_2, q and $\bar{q}$). Without further information there is no way of knowing which jet originates from which quark. All possible combinations must be considered. A constrained fit to the $t\bar{t}$ hypothesis is then performed for each jet-quark assignment in a given event, assuming energy-momentum conservation at each vertex in the $t\bar{t}$ decay chain. The fit uses the following constraints :

- The invariant mass of the jets assigned to the q and $\bar{q}$ is constrained to the W mass.
- The $\not{E}_{\mathrm{T}}$ gives the transverse momentum of the neutrino. The longitudinal momentum of the neutrino, $\mathrm{P}_{L\nu}$, is obtained by requiring the mass of the lepton and the neutrino to equal the W mass. This condition results in a quadratic equation for $\mathrm{P}_{L\nu}$, which has in general two distinct solutions.

- The invariant masses of the decay products of t_1 and t_2 must be equal, i.e. the invariant mass of the three jets assigned to b_2, q, and $\bar{q}$ (M_2) must be equal to the invariant mass (M_1) of the lepton, neutrino and fourth jet (b_1, see Fig. 93). The top mass for the jet-quark assignment under consideration is then $M_{top} = M_1 = M_2$.

All of the components of momentum for the final state particles are measured, except $P_{L\nu}$. With one unmeasured quantity and three constraints, the fit is a two-constraint (2C) fit. The constrained fit also yields a χ^2 for each combination which is a measure of the goodness-of-fit to the $t\bar{t}$ hypothesis. The fitted value of the top quark mass for a given combination is given by $M_{top} = M_1 = M_2$ at the point where χ^2 is minimized.

There are 4! = 24 possible ways of assigning the four jets to the four final-state quarks. Since there are two solutions for $P_{L\nu}$, this would result in 24 x 2 = 48 configurations. However, the interchange of jet assignments between the q and $\bar{q}$ from the W has no effect (see Fig. 93), so that the number of truly distinct configurations is 48/2 = 24. If one or more of the jets is b-tagged, the number of configurations can be reduced by allowing only configurations where b-tagged jets are associated with the b-quarks in the event. With one b-tagged jet, the number of combinations is twelve; with two b-tagged jets, this number is reduced to four.

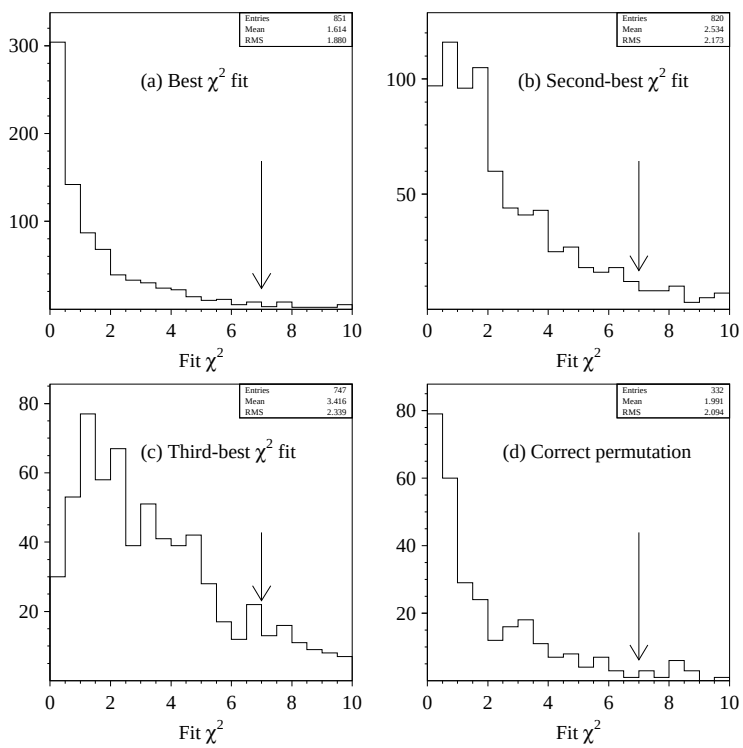

FIG. 94. Fit χ^2 distributions for (a) best, (b) second-best, (c) third-best, and (d) the correct jet permutation. For e+jets events, from the ISAJET Monte Carlo, M_{top}=180 GeV/c^2. The arrow shows the cut value. Note that the plot of correct permutations has less than half as many entries because only the cases in which a correct permutation could be found unambiguously from the Monte Carlo are included. From the D0 collaboration, Snyder, 1995a.

The large number of possible jet-quark assignments, the poor jet energy resolution (see Section V.B.2 and Fig. 32), and the effects of initial and final state gluon radiation, greatly complicate the top quark mass measurement. Monte Carlo studies indicate that there is often at least one combination with incorrect quark-jet assignments which yields a better fit to the $t\bar{t}$ hypothesis than the combination with the correct assignment, (see Fig. 94). Gluon radiation presents a problem because it can give rise to additional jets in the event. Both CDF and D0 consider only the four highest E_T jets in the event, since inclusion of a fifth jet would increase the number of possible combinations by a factor of five. However, if one of these four jets is from gluon radiation, the constrained fit will be operating on the wrong objects. Because of the poor energy resolution, the goodness-of-fit variable is not very effective at eliminating this kind of event from the data sample. An additional effect of gluon radiation is that the lepton + 4 jets sample also includes $t\bar{t}$ events from the *wrong* decay mode, for instance events of the type $t\bar{t} \rightarrow l\nu b\ \tau\nu\bar{b}$ can pass a lepton + 4 jets selection if both b-jets are found, the tau decays hadronically and is reconstructed as a jet, and an additional gluon jet is present.

The size of these effects depends somewhat on the details of the event selection. In the CDF analysis, Monte Carlo studies indicate that approximately 7% of $t\bar{t}$ lepton + 4 jets events are from the wrong decay mode, and of order 50% of the events have at least one of the four highest P_T jets from gluon radiation. In the remaining events, the combination with the lowest χ^2 corresponds to the correct parton-jet assignments only about one half of the times.

Constrained fits to incorrect parton-jet assignments or to $t\bar{t}$ events from the wrong decay mode, in general yield incorrect values of M_{top}. The CDF and D0 groups have chosen to deal with the problem of combinatorics in slightly different ways. In the CDF analysis, only the lowest χ^2 combination in a given event is considered. In the D0 analysis, the top quark mass for a given event is taken as the χ^2-weighted average of all combinations (up to three) that have acceptable values of χ^2. The advantage of the D0 approach is that the M_{top} value for a given event is more stable under small changes in the measurements or the fitting procedure. These changes can cause the fit to converge to a different jet-parton configuration, and result in a value of M_{top} which can be considerably different from the original.

Wrong combinations result in a significant broadening of the expected mass resolution, see Fig. 95. In CDF, the mass resolution for the correct jet assignment is expected to be 12 GeV/c^2. As a result of gluon radiation and wrong parton-jet assignments, the mass resolution is a factor of two worse, with significant non-Gaussian tails. Very similar results have also been reported by the D0 collaboration.

Despite the effects of gluon radiation and the high probability to choose a wrong combination, the peak in the mass distribution of Monte Carlo events is not shifted significantly, (see Fig. 95). This is partly because of order one-half of the wrong combinations involve interchange of one of the quarks from W decay (q or $\bar{q}$) with the b from the hadronic top decay (b_1, see Fig. 93). For this class of events, the reconstructed top mass distribution is broader but still peaks at the correct value.

It may be possible to reduce the effect of wrong combinations by including more information in the event fitting procedure. Examples of additional pieces of information that could be included are the expected angular distributions derived from the V-A structure of the top quark decay or the rapidity distributions of top quarks predicted by the $t\bar{t}$ cross-section

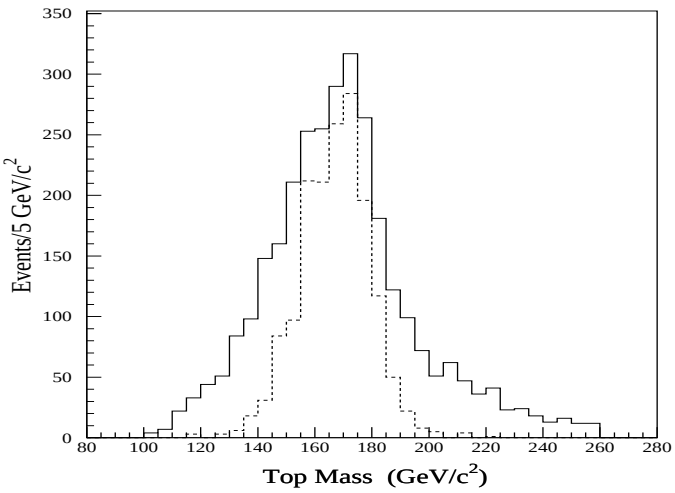

FIG. 95. Reconstructed top mass distribution for Monte Carlo events generated with the HERWIG Monte Carlo program, and simulated with the CDF detector simulation. The input value of the top mass in the Monte Carlo is $M_{top} = 170$ GeV/c^2. The solid line corresponds to the result of the constrained fit when requiring that one of the b-jets is a b in the fit. The dashed histogram refers to the fit with the correct assignment for each of the jets. The width of the top quark, which for this top mass is $\Gamma(t) \approx 1$ GeV/c^2 see Fig. 24, is negligible compared to the experimental resolution. From the CDF collaboration, F. Abe *et al.*, 1994a.

calculation (Kondo, 1991; Goldstein, Sliwa, and Dalitz, 1993).

Another effect of the large number of combinations and the poor jet energy resolution is that the χ^2 goodness-of-fit variable does not provide significant background rejection. (If it did, this variable would have been used to separate the top signal from the background). As discussed in Sections V.E.1, VIII.B, and VIII.C, the main background to the lepton + jets top signal is due to $W+$ jets production. In a $W+$ 4 jets event, it is almost always possible to find one jet-quark assignment with χ^2 low enough to be consistent with the $t\bar{t}$ hypothesis. Therefore, in order to perform the top mass measurement, both the background contamination of the event sample, and the mass distribution of the background events, need to be understood.

2. CDF and D0 top mass measurements

The CDF and D0 top mass measurements are based on the constrained fit procedure described in the previous Section. What is measured in these detectors is the energy and direction of the jets. In order to measure the top mass, the jet energies must be corrected to infer the original momentum of the partons. The correction procedure takes into account effects of non-linearities in the hadron energy response of the calorimeters, underlying event contributions to the energy of the calorimeter cluster, and gluon radiation outside the clustering cone. Special corrections are applied to lepton-tagged b-jets, since additional energy is carried away by the neutrino emitted in the semileptonic b-decay (typically a few GeV).

A value of M_{top} is calculated for each event using the constrained-fit procedure described

above. Events are rejected if the fit χ^2 is inconsistent with the $t\bar{t} \rightarrow$ lepton + jets hypothesis. The top quark mass is extracted by performing a likelihood fit to the M_{top} distribution for the remaining events. This M_{top} distribution is fit to the sum of background and $t\bar{t}$ components, with the value of the top quark mass allowed to vary. The M_{top} distribution for the dominant background, ($W+$ 4 jets events), is obtained by performing the same constrained fit procedure on a sample of events obtained from the VECBOS Monte Carlo and the detector simulation. The shape of the expected M_{top} distribution, as a function of the mass of the top quark, is also taken from Monte Carlo event generators (ISAJET, HERWIG, or PYTHIA) and the detector simulation. In the fit, the size of the background contribution can be constrained, within errors, to its calculated value, or can be left free to float. In the latter case, the size of the background contribution returned by the fit serves as a consistency check of the procedure.

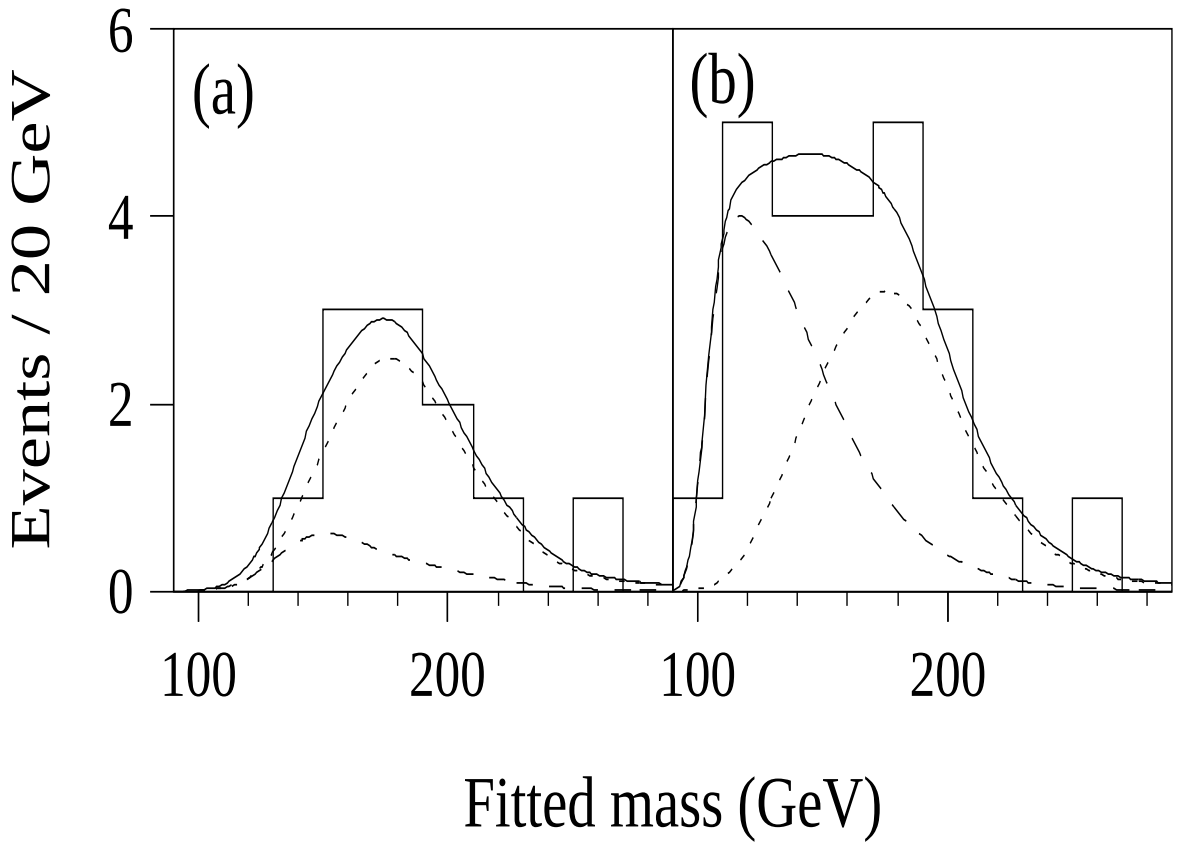

FIG. 96. Mass distribution for D0 top candidate events (histogram) compared with the expected mass distribution for 199 GeV/c^2 top quark events (dotted curve), background (dashed curve), and the sum of top + background (solid curve) for (a) standard and (b) loose event selection. *b*-tagging information is used when available. From Abachi *et al.*, 1995b. The integrated luminosity is ≈ 45 pb^{-1}.

The results of the likelihood fit from the D0 collaboration are shown in Fig. 96(a) and 96(b) for two different event selections, *tight* and *loose*. In both cases the four jets

are required to have $E_T > 15$ GeV. The tight selection includes requirements on H_T and aplanarity. The tight sample includes the eight lepton + four jets events from the analysis described in Section VIII.C, as well as the 6 b-tagged events from Section VIII.B. Only 11 out of these 14 events yield an acceptable fit to the $t\bar{t}$ hypothesis. For the loose selection, the H_T requirement is removed and the aplanarity requirement is loosened. The H_T requirement selects events with high E_T jets, and introduces a bias that favors events with high reconstructed top mass. By removing this requirement, however, the background contribution is enhanced. The number of events increases from 14 to 27; 24 of these have at least one combination with good χ^2 (Snyder, 1995a). As discussed in Section V.B and illustrated in Fig. 33, in $t\bar{t} \rightarrow$ lepton + jets events there is a significant probability for two quarks in the final state to merge into a single jet. To minimize this effect, the jet-cone clustering radius (ΔR, see Section V.B) in the D0 mass reconstruction is changed from the 0.5 used in the selection of the top signal to 0.3. Likelihood fits to the two distributions result in top mass values of $M_{top} = 199^{+31}_{-25}$ GeV/c^2 and $M_{top} = 199^{+19}_{-21}$ GeV/c^2 for the tight and loose selections respectively (statistical errors only). The M_{top} data distributions are not well described by the background hypothesis alone. This provides further kinematic evidence for the existence of the top quark.

The CDF top observation in the lepton + jets channel was based on a sample of b-tagged events with at least three jets of uncorrected $E_T > 15$ GeV, clustered with a cone of radius $\Delta R = 0.4$. As it is clear from Fig. 93, the constrained fit can only be applied to events with at least four jets. Therefore, the CDF mass measurement is performed on the sub-sample of events with a fourth jet. To maintain high efficiency, the E_T threshold on the fourth jet is lowered from 15 to 8 GeV (uncorrected). We stress that uncorrected jet energies are used at the event-selection stage only; for fitting purposes, all jet energies are corrected, see the discussion in Section IX.A.3. In Fig. 97 we show the M_{top} distribution of the pre-tag CDF lepton + 4 jets sample. Based on the CDF $t\bar{t}$ cross-section measurement, this sample is expected to be a mixture of approximately 30% $t\bar{t}$ and 70% $W+$ jets. The probability for the shape of the data M_{top} distribution to be consistent with background only is approximately 2%. Hence, just as in the D0 case, this distribution provides additional evidence for the top quark. By demanding a b-tag, the bulk of events at low M_{top} is removed, leaving a cluster of events between $M_{top} = 150$ and 210 GeV/c^2, see Fig. 98. The result of the likelihood fit to these events is $M_{top} = 176 \pm 8$ GeV/c^2 (statistical error only).

When including systematic effects, the mass values reported by the two collaborations are $M_{top} = 199^{+19}_{-21}$(stat.)$\pm$22(syst.) GeV/c^2 (D0) and $M_{top} = 176 \pm 8$(stat.)$\pm$10(syst.) GeV/c^2 (CDF). The results are consistent with each other. In the following Section we will discuss the important issue of systematic uncertainties.

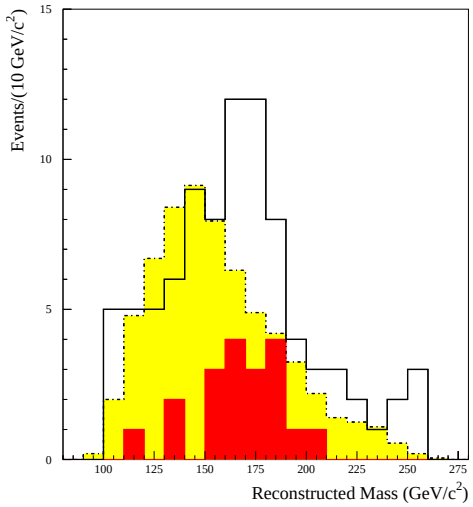

FIG. 97. Mass distribution for the 88 CDF lepton + $\geq$ 4 jets events with a good χ^2 fit to the $t\bar{t}$ hypothesis, before the b-tag requirement (solid line). The darkly shaded histogram is for the 19 events with a b-tag. The expected $W+$ 4 jets contribution to the pre-tag sample is shown in the lightly shaded histogram. From F. Abe *et al.*, 1995a. The integrated luminosity is 67 pb^{-1}.

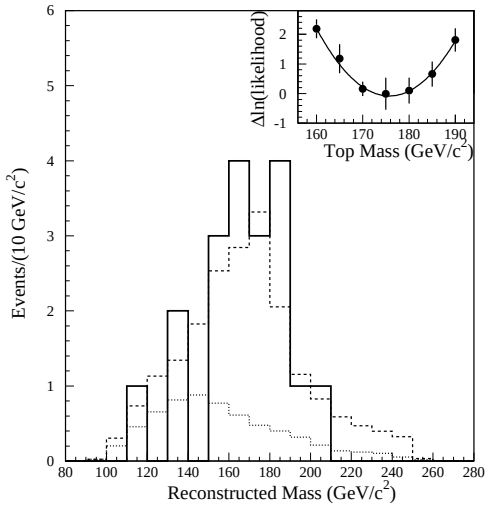

FIG. 98. Mass distribution for the 19 CDF b-tagged lepton + $\geq$ 4 jets events with a good χ^2 fit to the $t\bar{t}$ hypothesis (solid). Also shown are the background shape (dotted), and the sum of background and $t\bar{t}$ Monte Carlo (dashed) for M_{top} = 175 GeV/c^2. The inset shows the likelihood fit used to determine the top mass. From F. Abe *et al.*, 1995a. The integrated luminosity is 67 pb^{-1}.

Although the data samples of top candidates are rather small, the size of the statistical error on the top quark mass measurement is already comparable to the size of the systematic uncertainties. It is expected that in the next decade much larger $t\bar{t}$ samples will be available, see Section X. The systematic uncertainties will then be the limiting factor in the precision of the top mass measurement.

The dominant uncertainty in the top mass measurement is due to the uncertainty in the jet energy scale, i.e. to the transfer function (*correction factor*) that relates the measured jet energies to the energies of the original quarks from top decay. This uncertainty has two components, (i) an instrumental uncertainty related to the response of the calorimeter to hadrons, and (ii) an uncertainty in the understanding of the fragmentation and gluon radiation processes. In order to discuss these systematic uncertainties, we begin by describing the many steps in the jet energy correction procedure (F. Abe *et al.*, 1992d and 1993c; Abachi *et al.*, 1995d).

The jet energy response is in general not uniform across the detector because, for example, of cracks at the boundaries between calorimeter modules. The first task of the correction procedure is to equalize response across the calorimeter. The size of the effect is measured *in-situ* by di-jet or photon balancing techniques. Di-jet balancing is performed on a sample of $p\bar{p} \rightarrow 2$ jets events, with one jet restricted to a well-understood region of the calorimeter. Since the transverse energies of the two jets are expected to be equal, any inbalance as a function of the position of the second jet is a measure of the position-dependent non-uniformity of the calorimeter response. A similar study can be performed using $p\bar{p} \rightarrow \gamma+$ jet events. In these events the accurate measurement of the E_T of the photon can be compared to the measurement of the jet E_T. These effects can be measured, and hence corrected for, with high precision, because of the very large number of di-jet and photon-jet events that can be used for this study.

The jet cluster will in general include energy deposited from particles unrelated to the parent parton, for example particles from the underlying event. The jet energy is therefore corrected by subtracting off the average underlying event deposition as measured in minimum bias events. For jets clustered with a cone radius $\Delta R = 0.4$, this correction amounts to approximately 600 MeV for the CDF detector. Note that in $t\bar{t}$ events the amount of extra energy can be higher, because of cross-talk between the many jets in the final state. An additional, Monte Carlo based, correction for this effect has been developed by the CDF collaboration. A further correction needs to be applied in D0 due to noise from radioactivity of the uranium plates used in the calorimeter.

The next ingredient in the jet energy correction procedure involves understanding the absolute energy response of the calorimeter. The response to individual hadrons is measured in test-beams. In CDF the hadron response of the calorimeter as a function of momentum is also obtained from samples of isolated particles from $p\bar{p}$ collisions. The detector simulation is adjusted to incorporate information from these measurements. Finally, the jet energy scale is measured by simulating the calorimeter response to jets generated using a QCD-based model of jet fragmentation.

The absolute energy scale can also be derived from photon balancing, since the energy of the photon is precisely measured in the electromagnetic calorimeter. The electromagnetic

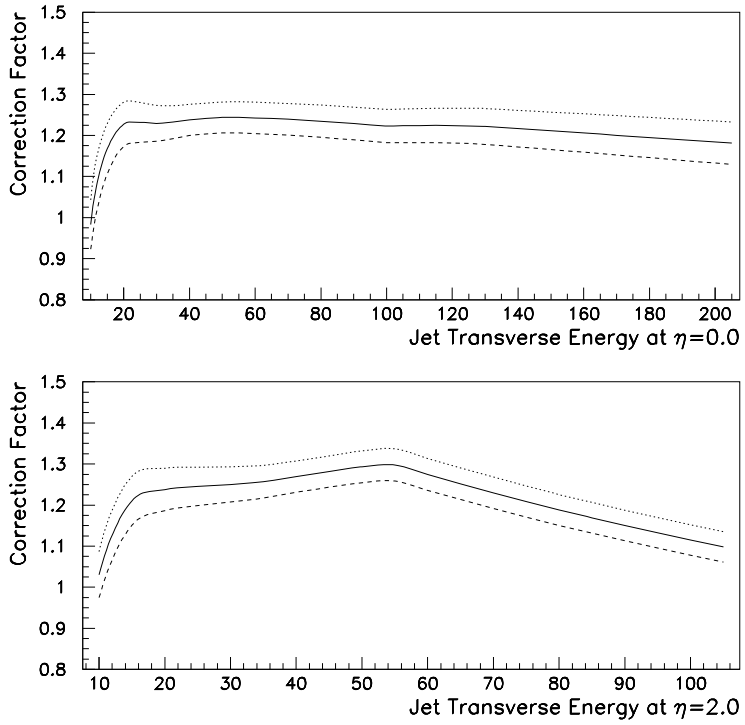

FIG. 99. D0 energy scale correction for jets as a function of jet transverse energy in the central and forward regions. Results are for jets reconstructed using a cone-size ΔR= 0.5. The dashed curves represent the error bands. From Abachi *et al.*, 1995d.

calorimeter is precisely calibrated by studying the distribution of E/P for electrons (CDF), or from reconstruction of the $Z \to ee$ resonance (D0). As we will discuss shortly, the photon balancing technique simultaneously tests instrumental as well as gluon radiation effects.

Finally, in order to go back to the original parton energy, an additional correction has to be applied for energy radiated outside the clustering cone, or carried away by low momentum hadrons swept away by the magnetic field (CDF). This correction is based on a Monte Carlo model of the QCD process. The overall jet energy correction factors are displayed in Fig. 99 and Fig. 100 for D0 and CDF respectively. The observed jet energies are to be multiplied by these correction factors to obtain the corrected energy.

Photon-jet balancing provides a powerful probe of the behavior of the overall jet energy correction function, (see Fig. 101). Unfortunately this test is not free from its own systematic uncertainties. Photon samples collected at the collider are contaminated at about the 50% level by two-jet events, with one of the jets fragmenting to a high momentum π^0 or η, which is misidentified as a single photon. In these cases the transverse energy of the photon candidate is not expected to equal the transverse energy of the recoiling jet, because of the presence of additional fragmentation hadrons in the jet that fakes the photon signature. Furthermore the balancing results can be affected by undetected low-energy initial-state gluon radiation. It is estimated that these effects introduce an uncertainty of order 5% on the determination of the absolute energy scale. Similar studies are performed using $Z+$ jet

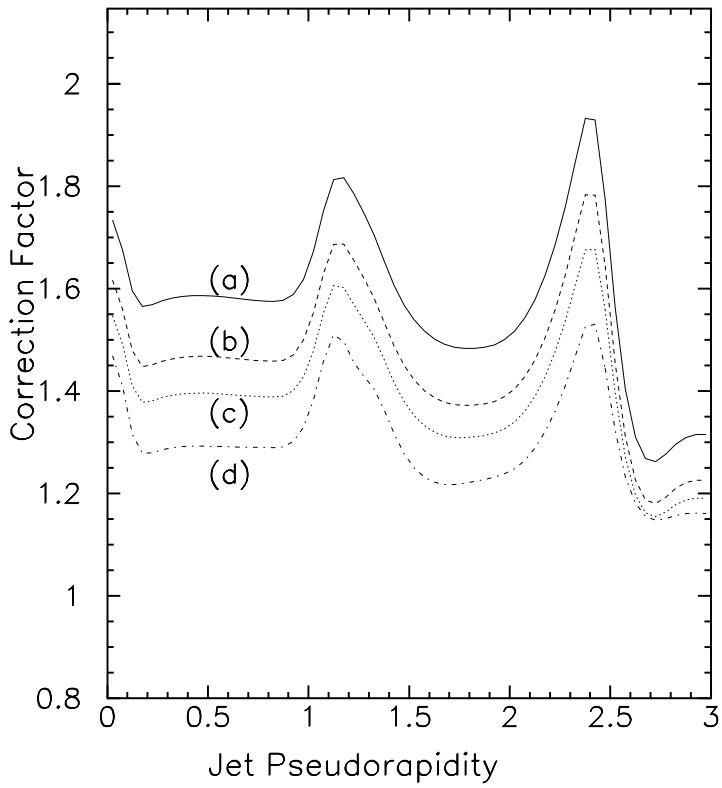

FIG. 100. CDF energy scale correction for jets as a function of jet pseudorapidity. Results are for jets reconstructed using a cone-size $\Delta R = 0.4$. (a) observed $E_T = 15$ GeV; (b) observed $E_T = 30$ GeV; (c) observed $E_T = 50$ GeV; (d) observed $E_T = 100$ GeV. The cracks between calorimeter modules (at $\eta \approx 0., 1.1, 2.4$) are apparent.

events, (see Fig. 102). The background effects which systematically limit the usefulness of photon-jet balancing are not present in this case; however, the available statistics are considerably lower.

The correction procedure described above applies to gluon and light-quark jets. Monte Carlo studies show no significant difference for b-jets, except in the case of semileptonic decays where an additional correction for the undetected neutrino needs to be applied.

The uncertainty in the jet energy scale for both the CDF and D0 mass analyses is estimated to be 10%. This value is somewhat larger than one would infer from photon-jet and Z-jet balancing studies, (see Fig. 101 and Fig. 102). There are however additional questions concerning the applicability of this correction procedure to the hadronic environment in top events which contribute to the 10% uncertainty estimate. The 10% jet energy scale uncertainty translates to a top mass uncertainty of 8 GeV/c^2 and 21 GeV/c^2 for CDF and D0 respectively. The difference between the two experiments in the size of the reported M_{top} uncertainties is not fully understood at this time.

There are additional smaller systematic uncertainties on the top mass measurement. A related uncertainty comes from the Monte Carlo modeling of gluon radiation in $t\bar{t}$ events. As was discussed in the previous Section, gluon radiation broadens the reconstructed M_{top} distribution. Since the top mass is extracted from a fit to the M_{top} data based on the

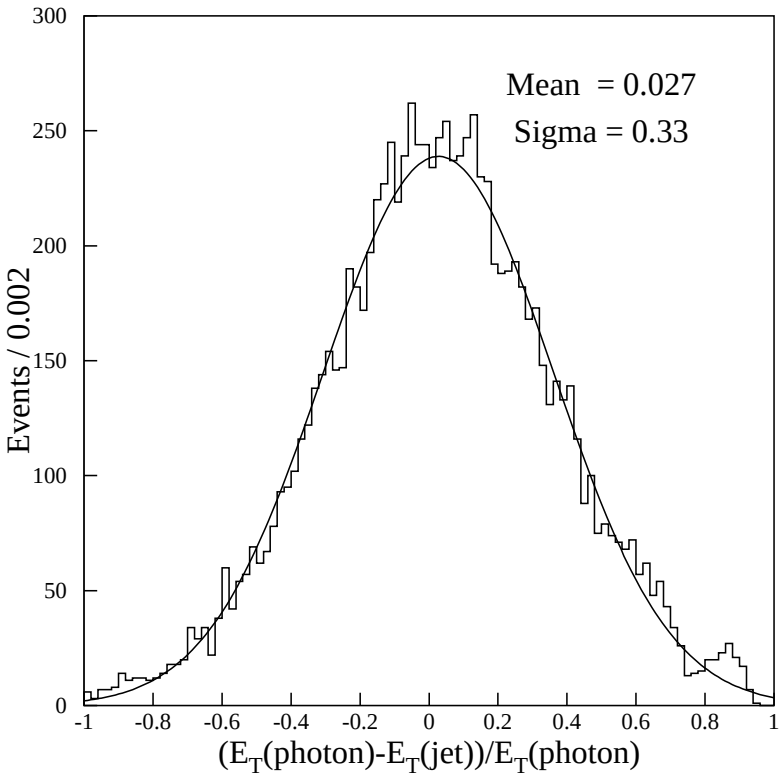

FIG. 101. Δ = (E_T (photon) - E_T (recoiling-jet))/E_T (photon). The jet transverse energy is corrected. Jets are clustered in a cone $\Delta R = 0.4$. From the CDF collaboration, F. Abe *et al.*, 1994a.

expected $t\bar{t}$ M_{top} distribution, different assumptions on its shape can result in shifts of the measured top mass. For example, differences between the ISAJET and HERWIG models result in shifts of 4 and 1 GeV/c^2 for D0 and CDF respectively. Further uncertainties at the 1-2 GeV/c^2 level are present in the CDF measurement from uncertainties in the background shape, which is taken mostly from the VECBOS Monte Carlo, as well as the details of the likelihood fitting technique.

The CDF and D0 M_{top} measurements are the first examples of the application of jet spectroscopy techniques to the determination of the mass of an elementary particle. The understanding and control of the systematic uncertainties due to the jet energy measurements are expected to improve in the future. This will be crucial to allow for more precise measurements of the top mass. We will discuss a number of possible approaches in Section X.

4. Updated CDF and D0 top mass measurements

As this review article was being completed, both the CDF (Tartarelli, 1996) and D0 (Narain, 1996) top mass results have been updated. In both experiments, the statistical

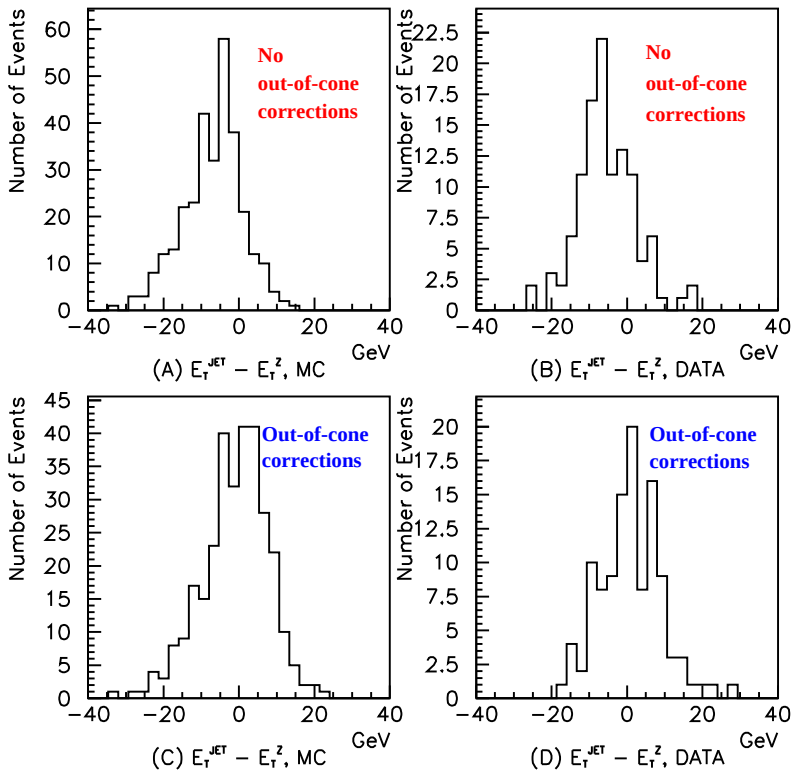

FIG. 102. Difference between the transverse energy of the electron pair and the jet in $(Z \to ee) + 1$ jet events. For Monte Carlo and data, with and without out-of-cone corrections, but including all other corrections. The minimum jet E_T is 10 GeV. Jets are clustered in a cone ΔR =0.3. From the D0 collaboration, Snyder, 1995a.

errors have decreased due to the larger data samples and, more importantly, the systematic uncertainties have been reduced as a result of more detailed studies of the jet energy scales in the two experiments. Since numerically the D0 result is somewhat different than the 1995 result discussed in Section IX.A.2, we briefly include these updated results here.

The new D0 measurement is based on an integrated luminosity of 100 pb^{-1}. Besides the improvement in statistics, there are four differences between the old and new D0 mass measurements: (i) the selection of the sample on which the mass fit is performed has been changed, (ii) an error in the out-of-cone jet energy corrections has been fixed, (iii) the HERWIG Monte Carlo is used instead of ISAJET, and (iv) the jet energy scale has been shifted downwards by 5%.

The new sample is derived from the loose lepton + four jets sample, removing the aplanarity cut. The sample is then split into two pieces, those events with and without a low P_T muon b-tag. The untagged events must satisfy two additional requirements: (i) the transverse energy of the leptonic W must be greater than 60 GeV, and (ii) the pseudorapidity of the W must be in the interval $\pm$ 2. The longitudinal momentum of the neutrino from the W is chosen from two possibilities as the one having the lowest momentum. Furthermore, the events are required to pass a kinematic liklihood test. This was done in order to reduce background for the loose sample, while reducing the mass bias due to the previous H_T

Source	M_{top} uncertainty
Jet energy scale (4% ± 1 GeV)	7 GeV/c^2
Different Monte Carlo $t\bar{t}$ generators	6 GeV/c^2
Fitting	3 GeV/c^2
Background uncertainty	2 GeV/c^2
Total	10 GeV/c^2

TABLE XX. Systematic uncertainties in the updated D0 mass measurement. From Narain, 1996.

Source	M_{top} uncertainty
Jet energy scale (detector effects)	3.1 GeV/c^2
Soft gluon effects	1.9 GeV/c^2
Hard gluon effects	3.6 GeV/c^2
Different Monte Carlo $t\bar{t}$ generators	0.9 GeV/c^2
b-tagging bias	2.3 GeV/c^2
Background spectrum	1.6 GeV/c^2
Fit configuration	2.5 GeV/c^2
Likelihood method	2.0 GeV/c^2
Monte Carlo statistics	2.3 GeV/c^2
Total	7.1 GeV/c^2

TABLE XXI. Systematic uncertainties in the updated CDF mass measurement. From Tartarelli, 1996.

requirement. No further requirements are made on the sample with a b-tag, except for additional improvements to the algorithm for removing $Z \to \mu\mu$, and for the application of a tighter low P_T muon selection.

This analysis results in 30 events which satisfy the fit χ^2, five of which have a b-tagged jet. The background in this sample is estimated to be 17.4 ± 2.2 events; the fit is shown in Fig. 103, and gives $M_{top} = 170 \pm 15(\text{stat.}) \pm 10(\text{syst.})$ GeV/c^2. This is to be compared with the earlier result $M_{top} = 199^{+19}_{-21}(\text{stat.}) \pm 22(\text{syst.})$ GeV/c^2. The systematic uncertainties are summarized in Table XX.

The updated CDF measurement, based on an integrated luminosity of 110 pb^{-1}, is performed in the same manner as described in Section IX.A.2. The result is $M_{top} = 176 \pm 6(\text{stat.}) \pm 7(\text{syst.})$ GeV/c^2; the systematic uncertainties are summarized in Table XXI.

The combined top mass measurement from the two Tevatron collaborations is $M_{top} = 175 \pm 8$ GeV/c^2. Here we have added the errors in quadrature and neglected correlations in the systematic uncertainties. These correlations are due, for example, to the modelling of $t\bar{t}$ production, and to the common assumptions made by the two collaborations in the determination of the jet energy scale.

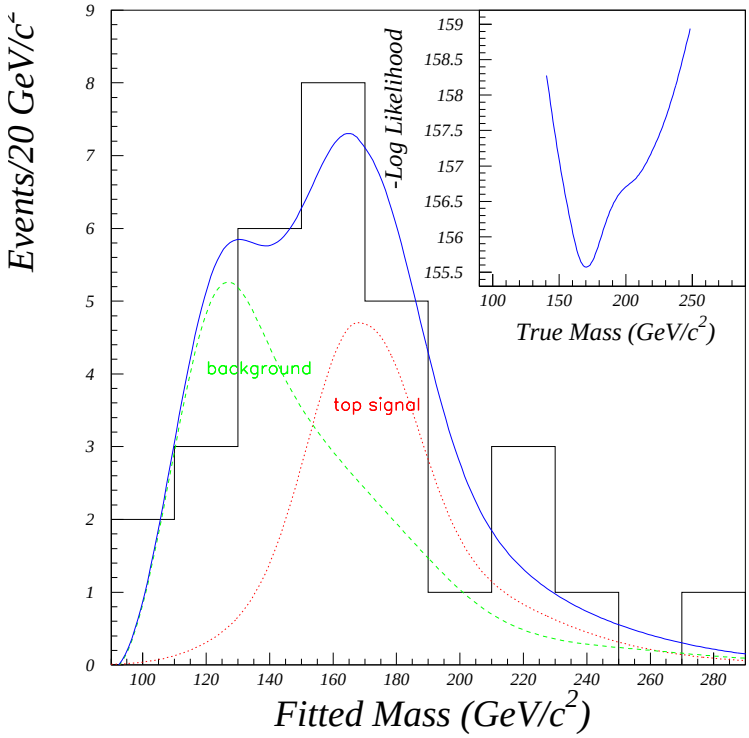

FIG. 103. Mass distribution for the 30 D0 lepton + $\geq$ 4 jets events with a good χ^2 fit to the $t\bar{t}$ hypothesis, from the 100 pb^{-1} data sample. The solid line is a fit to top plus expected background; the dashed line is the expected background from VECBOS (W + jets) and QCD multi-jet background; the dotted line is the fitted top contribution. The inset shows the liklihood distribution. From Narain, 1996.

B. Top mass from dilepton events and kinematic distributions

The top mass can also be reconstructed, in a less direct way, from dilepton events (Dalitz and Goldstein, 1992; Kondo, 1988 and 1991). In a $t\bar{t}$ dilepton event, both top quarks decay semi-leptonicaly :

$$t_1 \rightarrow W_1 b_1 \quad ; \quad W_1 \rightarrow l_1 \nu_1$$

$$t_2 \rightarrow W_2 b_2 \quad ; \quad W_2 \rightarrow l_2 \nu_2$$

Because of the presence of two neutrinos, a direct event-by-event reconstruction of the top mass based only on the measurements of the momenta of the leptons and the jets is not possible. The system is underconstrained, as can be seen from a simple accounting of the degrees of freedom. To fully describe the event, one needs the momenta of all the quarks and leptons in the final state. The momenta of the charged leptons are measured, and those of the quarks are inferred from the jet energies. Six parameters are needed to fully describe the two neutrinos; only two measurements (from the two components of $\not{E}_{\rm T}$), and three constraints are available : $\mathrm{Mass}(l_1\nu_1) = \mathrm{M}_W$; $\mathrm{Mass}(l_2\nu_2) = \mathrm{M}_W$; $\mathrm{Mass}(l_1\nu_1 b_1) = \mathrm{Mass}(l_2\nu_2 b_2)$. This leaves $6-5 = 1$ parameter undetermined. In order to measure the top mass, additional information need to be included. Possibilities include the Standard Model V-A expectations for the angular distributions in the top decay chain, or theoretical expectations for the kinematic properties of the produced t and $\bar{t}$.

The D0 collaboration (Snyder, 1995b) recently reported a preliminary measurement of the top mass from dilepton events. The D0 dilepton mass measurement uses five dilepton events. It is based on a data sample with a higher integrated luminosity than the D0 dilepton top search described in Section VIII.A which yielded three candidate events.

The top quark mass reconstruction for a single event goes as follows. By **assuming** a value of M_{top}, and for a given jet-b-quark assignment, the momenta of ν_1 and ν_2 are determined up to a possible four-fold ambiguity from the two quadratic constraints $\mathrm{M}^2(l_1\nu_1) = \mathrm{M}_W^2$ and $\mathrm{M}^2(l_2\nu_2) = \mathrm{M}_W^2$. For each configuration (two jet-b-quark assignments, and possible four-fold neutrino ambiguity), the event is fully reconstructed. A probability (Prob_{lep}) is assigned to each configuration based on the energy of the leptons in the rest frame of the top quarks. This probability is calculated for the assumed top mass, and is based on the expected structure of the decay. The momentum fractions x_1 and x_2 of the incoming quarks q_1 and $\bar{q}_2$ in the reaction $q_1 + \bar{q}_2 \rightarrow t\bar{t}$ are also reconstructed from the invariant mass ($\mathrm{M}_{t\bar{t}}$) and momentum ($\mathrm{P}_{t\bar{t}}$) of the $t\bar{t}$ system. Modulo the effects of gluon radiation, x_1 and x_2 can be obtained from $\mathrm{M}_{t\bar{t}} = \sqrt{x_1 x_2 s}$ and $\mathrm{P}_{t\bar{t}} = 0.5\sqrt{s}(x_1 - x_2)$, where $\sqrt{s} = 1.8$ TeV is the center-of-mass energy of the $p\bar{p}$ collision. An additional probability (Prob_x) is assigned to the configuration, still as a function of the assumed top mass, based on the parametrization of the parton distribution functions at momentum fractions $x = x_1$ and $x = x_2$, (see Fig. 19). Because the parton distribution functions are decreasing functions of x, Prob_x includes a correction to remove biases towards low values of M_{top}. The total probability for the configuration is given by the product $\mathrm{Prob}_{lep}\mathrm{Prob}_x$. The total probability for the event is the sum of the probabilities for all possible configurations. By varying the value of the assumed top mass, this procedure yields a probability distribution for each event as a

function of top mass. To include resolution effects, the procedure is repeated many times after smearing the measurements of the lepton and jet momenta according to their expected resolutions. The total probability distribution for a single event is then defined as the sum of the probability distributions for the smeared events. An event top mass value is defined as the value of M_{top} at which the probability distribution is maximum (M_{peak}). Finally, the top mass is extracted from likelihood fits of the data M_{peak} distribution to the superposition of the expected $t\bar{t}$ and background contributions, (see Fig 104).

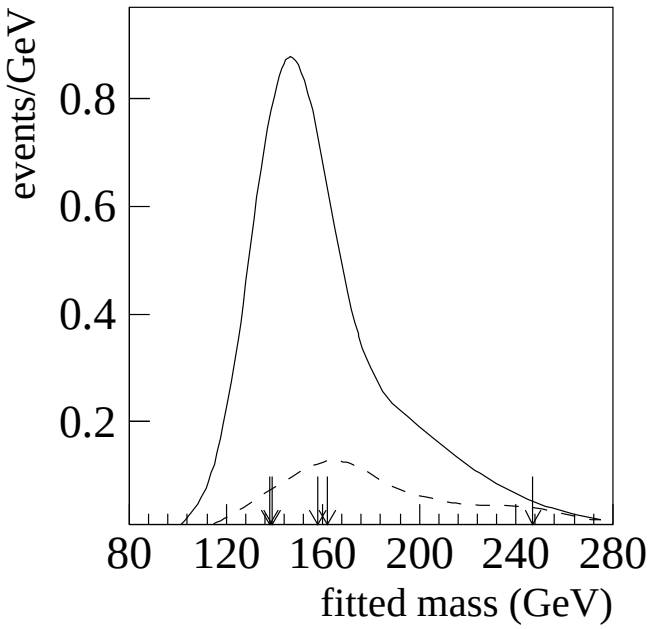

FIG. 104. Dilepton mass measurement from the D0 experiment. The arrows show the M_{peak} values for the five D0 dilepton candidate events. The solid curve is the expected signal distribution for $M_{top} = 145$ GeV/c^2, the dashed curve is the expected background distribution. See text for details. From Snyder, 1995b.

The preliminary D0 result for this procedure is $M_{top} = 145 \pm 25(\text{stat.}) \pm 20(\text{syst.})$ GeV/c^2. The systematic uncertainties include energy scale effects, Monte Carlo modeling, and uncertainties in the background contributions to the fit. Within the large errors, this value is consistent with both the CDF ($M_{top} = 176 \pm 9$ GeV/c^2) and D0 ($M_{top} = 170 \pm 18$ GeV/c^2) measurements in the lepton + jets channel described in Section IX.A.4.

A number of kinematic quantities in both dilepton and lepton + jet events have also been shown to be sensitive to the top mass (see for example Baer *et al.*, 1990). It is then in principle possible to perform a measurement of the top mass by comparing kinematic distributions to expectations for $t\bar{t}$. Some possibilities are the event transverse mass in dilepton events, the mean of the lepton-b mass, the transverse momentum of b-jets, or the total transverse energy, (see Fig. 105).

These more indirect measurements are less statistically powerful than the direct measurement of the top mass described in Section IX.A, since the mass peak used in the direct measurement provides optimal discrimination between different M_{top} hypotheses. However, indirect measurements are sensitive to different systematic effects. For instance, the combi-

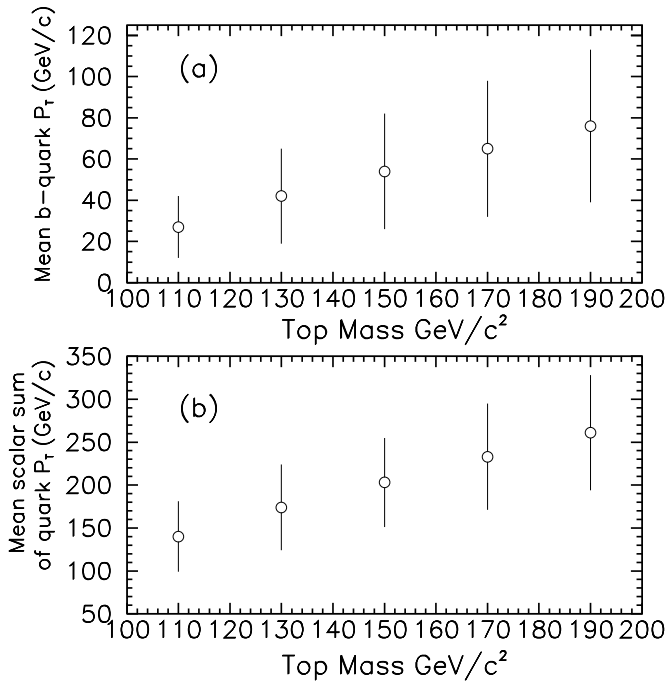

FIG. 105. Predictions from the ISAJET $p\bar{p} \to t\bar{t}$ Monte Carlo at $\sqrt{s} = 1.8$ TeV, as a function of the top mass, for (a) the mean transverse momentum of b-quarks, and (b) the mean of the scalar sum of the transverse momenta of the four quarks in lepton + jets events. The vertical error bars represent the expected RMS for these quantities.

natorics problem which plagues the direct top mass measurement, would not play a role in most of these techniques. A measurement of the top mass based on the b-quark transverse momentum spectrum or the b-lepton invariant mass, is almost entirely independent of initial state radiation in $t\bar{t}$ events.

The CDF collaboration has also reported measurements of the top mass based on kinematic distributions in both dilepton events (Tartarelli, 1996) and lepton + jets events (F. Abe *et al.*, 1995c). The dilepton mass determination is based on a fit to the jet E_T spectrum in these events and yields $M_{top} = 159^{+24}_{-22}(\text{stat.})\pm 17(\text{syst.})$ GeV/c^2. The lepton + jet measurement is based on a fit to the the total transverse energy distribution (see Section VIII.C), and gives $M_{top} = 180 \pm 12(\text{stat.})^{+19}_{-15}(\text{syst.})$ GeV/c^2. Both these results are in agreement with the results derived by direct mass reconstruction techniques.

The direct top mass measurement in b-tagged lepton + jets events is, and is likely to remain, the method of choice for determining the top mass. Nevertheless, alternative methods such as the under-constrained dilepton mass reconstruction or methods based on kinematic distributions, serve as useful consistency checks.

C. Reconstruction of the W mass from hadronic decays in lepton + jets events

In a $t\bar{t} \rightarrow$ lepton + jet event, one of the two W bosons from the top decay chain is expected to decay hadronically ($W \rightarrow q\bar{q}$, see Fig. 93). Both the CDF and D0 collaborations have reported evidence for this decay mode by reconstructing a peak in the invariant mass distribution of two jets in the event. Hadronic W reconstruction is interesting for two reasons. First of all, the presence of such a peak in the data is further strong evidence that the excess of events over the background prediction is indeed due to $t\bar{t}$ production. Furthermore, the hadronic W peaks provide the most ideal calibration for the jet energy scale of the two experiments. Note that it is extremely difficult to get the scale information from inclusive W decays to two jets, because of the very high QCD di-jet background which would both mask the signal and saturate the data acquisition bandwidth.

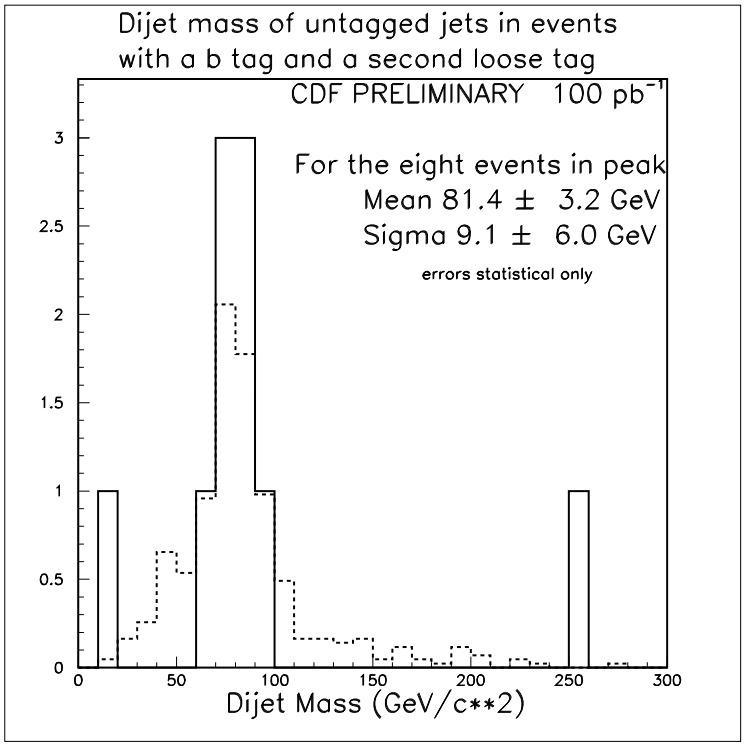

FIG. 106. The di-jet mass of untagged jets in data events with a double b-tag (histogram), compared to the expected signal from the top Monte Carlo (dotted). The integrated luminosity for this data set is 100 pb^{-1}. From the CDF collaboration, Yao, 1995.

The hadronic W has been reconstructed by the CDF collaboration (Yao, 1995). The method uses $W+ \geq 4$ jet events with two b-tagged jets. One of the jets is tagged using either of the standard CDF lepton or vertex tagging algorithms. In order to increase the statistics of the sample, the second jet is tagged using a looser vertex tag algorithm. Such a double-tag requirement considerably reduces many sources of background, and the $t\bar{t}$ purity of the sample is very high. Just as in the constrained fit procedure described in Section IX.A,

only the four highest E_T jets are considered. With this restriction, in a doubly b-tagged $t\bar{t}$ event there is no ambiguity in assigning jets to the hadronic W-decay. The invariant mass distribution of the two untagged jets in this sample is shown in Fig. 106. In eight of the ten events, the invariant masses of the two untagged jets cluster tightly around $M_{jj} \approx 80$ GeV/c^2. This provides overwhelming evidence for the presence of hadronic decays of W bosons in the lepton + jets + b-tag sample. The two outlying events are most likely due to cases where one of the untagged jets considered to be from the W is really a gluon jet from initial or final state radiation.

The D0 hadronic W mass reconstruction procedure (Strovink, 1995) in lepton + jets events is much more complicated, since the b-tag in D0 is not as efficient as in CDF. The analysis uses lepton + ≥ 4 jets data, and considers only the four jets with the highest E_T. Just as in the constrained fit procedure (see Section IX.A), the neutrino longitudinal momentum ($P_{L\nu}$) is obtained by constraining the lepton-neutrino invariant mass to the W-mass, and only the solution with the smallest $|P_{L\nu}|$ is considered. No constraint is placed on the di-jet mass, so that there are four different ways of partitioning the event into $(l\nu j_1)$ and $(j_2 j_3 j_4)$, unless one of the jets is b-tagged, in which case the number of combinations is two. A two-dimensional scatter-plot of di-jet mass versus top mass is filled for each combination with weight proportional to $\exp(-\chi^2/2)$, where $\chi^2 \equiv \ln^2(\text{mass}(l\nu j_1)/\text{mass}(j_2 j_3 j_4))$. The normalization is chosen in such a way that the weights for all combinations in a given event sum to unity. The top mass is defined as the average of mass$(l\nu j_1)$ and mass$(j_2 j_3 j_4)$ for electron + jets events. For muon + jets events, the top mass is calculated by taking a weighted average of the two, with the values of hadronic and leptonic masses weighted in the ratio 60 : 40. The di-jet mass is defined as follows. If one of the jets in $(j_2 j_3 j_4)$ is tagged, the di-jet mass is the invariant mass of the two other jets. Otherwise, the most energetic jet in the top rest frame is used as the b. But if no jets in $(j_2 j_3 j_4)$ are tagged, and their energy in the top rest frame are such that $(E_2 - E_3) < (E_3 - E_4)$, then the permutation is plotted twice, with equal weights, with di-jet mass chosen as mass$(j_3 j_4)$ or mass$(j_2 j_4)$. Studies of $t\bar{t}$ Monte Carlo events, indicate that this procedure results in a peak in the di-jet-mass vs. top-mass scatter plot at di-jet-mass = M_W and top-mass = M_{top}. On the other hand, background events are expected to peak at lower values. Projections from the di-jet-mass vs. top mass scatter plot are shown in Fig. 107. The top mass and di-jet mass distributions are peaked around 180 and 80 GeV/c^2 respectively. The probability for these distributions to be consistent with the background-only hypothesis is 1.3%.

In conclusion, both collaborations have shown evidence for hadronic W decays in their respective top event samples. With the aid of vertex tagging, the CDF $W \to q\bar{q}$ peak is very clean and straightforward to understand. Future higher statistics samples of $W \to q\bar{q}$ in top events will provide a very important calibration to the top mass measurement, see Section X.

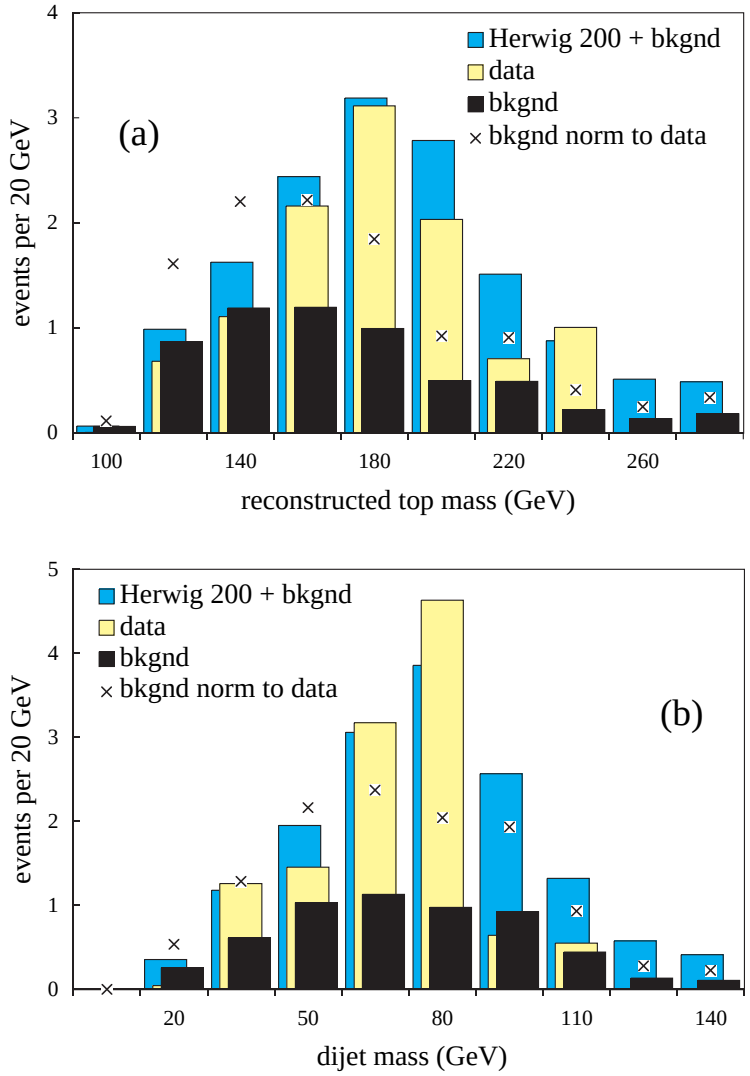

FIG. 107. Distributions of (a) reconstructed top quark mass, and (b) reconstructed di-jet-mass. The reconstructed top-mass is plotted only for di-jet-mass > 58 GeV/c^2. The reconstructed di-jet mass is plotted only for top mass > 150 GeV/c^2. Distributions are shown for data, sum of background and HERWIG $t\bar{t}$ Monte Carlo, background alone, and background normalized to match the area of the data. From the D0 collaboration, Strovink, 1995.

X. FUTURE PROSPECTS

One of the goals of particle physics in the next decade is to perform detailed experimental studies of the properties of the top quark. Since the mass of the top quark is of the same order as the scale for electroweak symmetry breaking, it is possible that new physics effects will manifests themselves in the top sector. While we do not know what these new effects might be, it is clear that top quark physics represents an opportunity to uncover physics beyond the Standard Model.

In this Section we will concentrate on prospects for top physics at the Tevatron. We will begin by briefly summarizing plans for the upgrade of the accelerator and the detectors in Section X.A. Detailed studies of the possibilities for the Tevatron top physics program are well under way (Amidei and Brock, 1996). Prospects for improving the accuracy of the top mass measurement will be discussed in Section X.B; the potential for study of the Wtb vertex will be addressed in Section X.C; finally, additional tests of the Standard Model, as well as searches for new physics involving the top quark will be discussed in Section X.D.

A. Accelerator and detector upgrades

The CDF (CDF collaboration, 1995) and D0 (Tuts, 1996) detectors at the Tevatron will be undergoing major upgrades in the next few years. The most significant improvements for top physics will be the installation of a magnet for charged particle momentum determination in D0 and new 3D silicon vertex detectors in both detectors. Since vertex-tagging of b-quarks in top events has been shown to be such a powerful tool, the capabilities of the upgraded D0 detector for top physics will be considerably enhanced. The new CDF silicon vertex detector will also have a significant impact in the top physics program at CDF. With three dimensional information, the b-tagging efficiency will be improved, and the instrumental background level will be reduced; furthermore, the new vertex detector will be long enough to cover the whole luminous region of the Tevatron, increasing the acceptance for vertex tags (recall that the geometrical coverage of the present CDF vertex detector is only about 60%, see Section VIII.B.3).

At the same time, the Fermilab accelerator complex will be upgraded with the construction of a new high intensity 120 GeV proton accelerator (*The Main Injector*). The Main Injector will replace the Main Ring, whose aperture currently limits the luminosity, as the injector to both the Tevatron and the $\bar{p}$ source. In addition, a new 8 GeV permanent magnet ring (*Recycler*) has been proposed to achieve a more efficient accumulation of antiprotons by recycling (hence the name) the $\bar{p}$ from the previous store, store the anti-protons when the accumulator is full, and protect them from power glitches in the accelerator (Foster, 1995; Jackson, 1995). The number of bunches will also be increased from 6 to 36, allowing higher luminosity without increasing the number of interactions per crossing. This increase shortens the bunch crossing interval from the current value of 3.5 μsec to 396 ns. This requires an upgraded trigger, data acquisition and front-end electronics systems, which must be pipelined to handle the increased rate. After completion of these upgrades in 1998-99, the Tevatron luminosity will be increased by one order of magnitude to 2 x 10^{32} cm^{-2}s^{-1}, with further luminosity improvements likely to occur in the following years. The center-of-mass

energy of the Tevatron is also expected to increase from 1.8 TeV to 2 TeV, resulting in a increase of approximately 30% in the $t\bar{t}$ cross-section.

This series of improvements in the Fermilab collider program will allow for much more detailed studies of the top quark than those that are possible with the low statistics data samples that are available now. The projected sizes of the $t\bar{t}$ samples in each experiment for an integrated luminosity of 1 fb^{-1} will be of order 100 events in the dilepton channel and of order 500 events in the lepton + 4 jets channel with one b-tag, with half of these events having both b-jets tagged (Amidei and Brock, 1996).

In addition, towards the middle of the next decade, the Large Hadron Collider (LHC) at CERN will become operational. The LHC is a very high luminosity ($> 10^{34}$ cm^{-2} s^{-1}) pp machine with $\sqrt{s} = 14$ TeV. At this energy, $\sigma(pp \to t\bar{t}) \approx 700$ pb, a factor of 100 higher than $\sigma(p\bar{p} \to t\bar{t})$ at the Tevatron. With the high luminosity and the high cross-section, the LHC can be considered to be a top-factory. In the even more distant future, top physics will also be pursued at a very high energy electron collider (e.g. *The Next Linear Collider*, NLC), assuming that such a machine will be built.

B. Improving the top mass measurement

As was discussed in Section III, the top quark mass is a fundamental parameter of the Standard Model. Its value enters in the calculation of radiative corrections to a large number of electroweak observables. It is therefore very important to measure the top quark mass as accurately as possible to allow for precise tests of the Standard Model.

The best value of M_{top} as obtained from fits to the LEP and SLC measurements, as well as the measurements of the W mass from $p\bar{p}$ experiments and deep inelastic neutrino scattering, is $M_{top} = 179 \pm 9^{+17}_{-10}$ GeV/c^2 where the second uncertainty comes from varying the Higgs mass between 60 and 1000 GeV/c^2 (see Section III). This is in good agreement with the values reported by the CDF ($M_{top} = 176 \pm 9$ GeV/c^2) and D0 collaborations ($M_{top} = 170 \pm 18$ GeV/c^2), see Section IX.

The accuracies of the neutrino measurements and of the LEP and SLC measurements at the Z are not expected to dramatically improve in the coming years. On the other hand, the accuracy in the determination of the W mass will improve by almost one order of magnitude, from the Tevatron experiments as well as from $e^+e^- \to W^+W^-$ at LEP200. Within the Standard Model, radiative corrections to the W propagator (see Fig. 11) result in definite predictions for the W mass as a function of the top and Higgs mass (see Fig. 12). It is therefore very interesting to measure both the W mass and the top mass as precisely as possible.

How accurately can the top mass be measured? Experience from CDF and D0 indicates that the method of choice for measuring the top mass is to perform constrained fits on the b-tagged lepton + jets data sample, see Section IX.A. We can extrapolate the statistical accuracy of a future top mass measurement from the present CDF measurement. This measurement has a statistical uncertainty of 6 GeV/c^2 for an integrated luminosity of 110 pb^{-1}. After the first Main Injector run of the Tevatron, we can expect the integrated luminosity to be of order 1 fb^{-1} per experiment, with a 30% increase in top cross-section from running at the higher center of mass energy of 2 TeV, and a 40% increase in geometrical acceptance

from the new CDF vertex detector. Since the statistical uncertainty varies inversely as the square root of the number of events, we can expect a statistical uncertainty of order 1.5 GeV/c^2 from CDF. A similar uncertainty can be expected from the upgraded D0 detector. Systematic effects, which at present are at the level of 7 GeV/c^2, will be the limiting factor in the precision of the top mass determination.

The systematic uncertainties in the top mass measurements have been described in Section IX.A.3. The largest uncertainty is due to the understanding of the jet energy scale, as well as the related issue of additional jets from gluon radiation. At this time, it is not entirely clear what the ultimate precision will be. The dominant component of the energy scale uncertainty is related to the reliability of the extrapolation from jet energies to parton energies, and it is the understanding of the QCD process, rather than the understanding of the detector, which limits the measurement. Higher statistics tests of the understanding of the energy scale will be performed in γ + jet and Z + jet events (see Section IX.A.3, Figs. 101, and 102). The Monte Carlo modeling of gluon radiation will be more precisely checked and/or tuned by examining the energy flow within a jet. There will however remain systematic uncertainties related to the transfer of this calibration from the control samples to the hadronic environment in $t\bar{t}$ events. The ultimate size of these uncertainties is at the moment not well understood.

The additional statistics that will become available will be important to reduce the systematic uncertainty. With enough statistics, the number of lepton + jets events with two b-tagged jets will be sizable, and these events will provide a very important tool for understanding systematic uncertainties in the top mass measurement. In these events, there are no ambiguities in assigning the two jets to the hadronic W decay. The invariant mass of these two jets, which ideally should reconstruct to the W mass, provides an in-situ calibration of $W \rightarrow$ jet-jet invariant mass reconstruction. First results from this kind of study are very promising, (see Fig. 106). Besides the energy scale issue, studies of doubly-b-tagged events will provide useful handles on other systematic effects that limit the precision of the top mass measurement. Since mis-tag backgrounds in this data sample are very small, events in the tails of the jet-jet invariant mass distribution will be $t\bar{t}$ events with one jet from gluon radiation and W$Q\bar{Q}$ events. Therefore doubly-b-tagged events will be useful in directly measuring these components of the data set. This will improve the understanding of the top resolution function, which also depends on the number of jets from gluon radiation in the sample. The doubly-b-tagged sample will also allow for a test of the modeling of the $WQ\bar{Q}$ background component, which affects the top mass measurement since the top mass is extracted from a likelihood fit of the data to the sum of $t\bar{t}$ and W background. The number of jet-parton combinations for doubly-b-tagged events is only four, as opposed to twelve combinations that must be considered in the present CDF analysis which only demands one b-tag, see Section IX.A.1. Since statistics are not expected to be the limiting factor, it is possible that a measurement of the top mass using these events will be ultimately more accurate than a measurement based on events with one b-tag. Alternatively, these events can be used to study the effect of wrong combinations. Using these events, it will also become possible to measure the probability for the constrained fit to converge to a combination with a b-tagged jet assigned to a light quark jet.

Further improvements in the understanding of the systematic uncertainties will be possible due to the high statistics $t\bar{t}$ samples that will be available. It will become possible to

better quantify the effects of gluon radiation by measuring the relative rates of $t\bar{t} \rightarrow$ dilepton + 2 vs. 3 jets, and $t\bar{t} \rightarrow l+$ 4 vs. 5 jets. The modeling of the $W+$ jets background, which at present is entirely based on the VECBOS Monte Carlo, will be tested using the large sample of $Z+$ jets.

In summary, while the ultimate precision of the top quark mass measurement is not fully known at this time, it is likely that an accuracy of order of a few GeV/c^2 will be achievable. In conjunction with a W mass measurement with a precision of tens of MeV/c^2, this measurement will be sensitive to physics beyond the Standard Model, and will provide useful information on the value of the Higgs mass. In Fig. 108 we show what the M_{top} vs. M_W measurements might look like by the year 2000. If the experimental point in the M_W vs. M_{top} plane was to fall outside the region allowed by the Standard Model, this kind of measurement would provide indirect evidence for physics beyond the Standard Model.

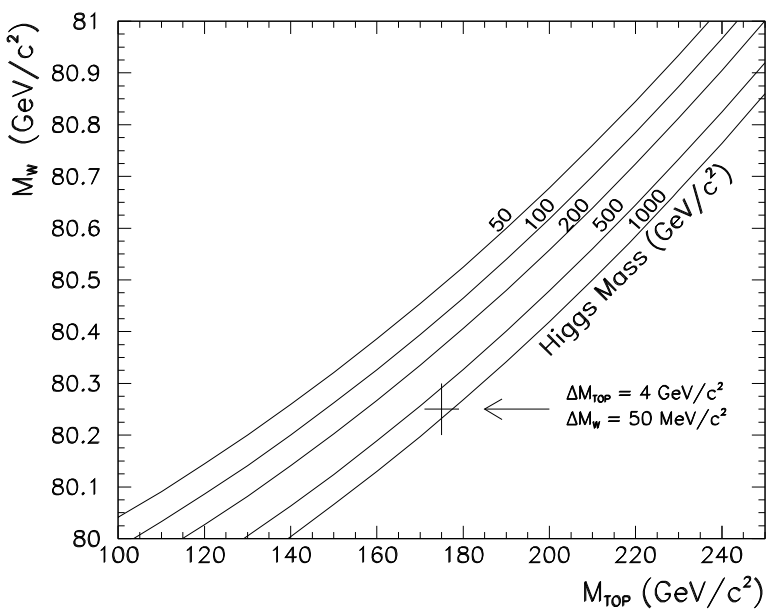

FIG. 108. The expected correlation between the masses of the top, the W and the Higgs. We also show, at an arbitrary point, results of measurements of the W mass to 50 MeV/c^2 and the top mass to 4 GeV/c^2.

C. Probing the Wtb vertex

The structure of the Wtb vertex can be probed by studying top decay and/or production of single top quarks. Up to this point we have mostly discussed $t\bar{t}$ pair production. However, as mentioned in Section IV, top quarks in $p\bar{p}$ collisions can also be produced singly, in the Drell-Yan process $q\bar{q} \rightarrow W^* \rightarrow t\bar{b}$, (see Fig. 17), and in the W-gluon fusion process $qg \rightarrow t\bar{b}q'$,

or $qb \to tq'$, (see Fig. 18). The expected cross-sections for Drell-Yan and W-gluon fusion single top production at the Tevatron are displayed in Fig. 21. These cross-sections are smaller than the strong $p\bar{p} \to t\bar{t}$ production cross-section, but they are sizable enough that single top production is expected to be observable at the Tevatron. Production of tW is also allowed, but its cross-section is much smaller.

The potential for studying single top production has attracted a lot of attention for the future top physics program at the Tevatron. The cross-section is proportional to the top quark width, $\Gamma(t \to Wb)$, and within the context of the Standard Model, proportional to the square of the CKM-matrix element $|V_{tb}|$. Note that the top lifetime is too short to be directly measured, (see Fig. 24); furthermore, the top width is very hard if not impossible to measure from the reconstruction of the Breit-Wigner, since the experimental resolution is one order of magnitude worse than the width itself (see Fig. 95). Hence, only indirect measurements of $\Gamma(t \to Wb)$ and $|V_{tb}|$ can be performed.

Assuming three generations and unitarity of the CKM matrix, the value of $|V_{tb}|$ is expected to be very near unity, in the range $0.9988-0.9995$ (Montanet *et al.*, 1994). It is clearly very interesting to test this result. An additional potentially interesting measurement using the single top sample would be a comparison of the rates for $p\bar{p} \to tX$ and $p\bar{p} \to \bar{t}X$, which can be used to search for CP violating effects in the top sector.

The possibility of extracting a single top-quark signal has been examined by many authors (Yuan, 1990; Cortese and Petronzio, 1991; Jikia and Slabospitsky, 1992; Ellis and Parke, 1992; Carlson and Yuan, 1993; Stelzer and Willenbrock, 1995; Amidei and Brock, 1996). Because of the high multi-jet QCD background, only events with $t \to Wb$ followed by $W \to l\nu$ are useful. The signature then is a lepton, missing energy, and two b-jets for Drell-Yan $q\bar{q} \to W^* \to t\bar{b}$ production, and one or two b-jets + one light quark jet for W-gluon fusion, ($qg \to t\bar{b}q'$ or $qb \to tq'$, see Fig. 18). Just as in the $t\bar{t}$ search, the main background is from $W+$ jets production (see Section V.E.1), and b-tagging must be used to reduce this background to a manageable level. Rejection of the tagged $WQ\bar{Q}$ background can be achieved by requiring the mass of the lepton, neutrino, and b-jet to reconstruct to the known top mass. Pair production of $t\bar{t}$ also constitutes a significant background to observation of single top production. Since the jet multiplicity in $t\bar{t}$ events is higher, the optimal sample in which to isolate the single top signal seems to be that of events with one lepton + $\not{E}_{\rm T}$+ two and only two jets.

A study of the expected signal and background for single top production at the Tevatron shows that a signal-to-background of order 1 to 2 can be achieved. The number of signal events for $|V_{tb}| \approx 1$ would be of order 120 per fb^{-1}, resulting in a statistical uncertainty in the cross-section measurement of order 17% in a 1 fb^{-1} data set (Amidei and Brock, 1996). An additional study, optimized for the detection of the Drell-Yan $q\bar{q} \to W^* \to t\bar{b}$ process, suggests that with the requirement of a double b-tag the signal can be isolated, (see Fig. 109 Stelzer and Willenbrock, 1995). Indications from this study are that, assuming that $|V_{tb}|$ is indeed close to unity, a 3 fb^{-1} exposure would yield a 20% measurement of the cross-section, and therefore a 10% measurement of $|V_{tb}|$. If on the other hand no signal is seen in 3 fb^{-1}, then $|V_{tb}| < 0.60$ at the 95% confidence level. The authors of this study also suggest that the Drell-Yan process may be more useful in extracting $|V_{tb}|$ than the W-gluon fusion process. This is because expectations for the cross-section for $p\bar{p} \to W^* \to t\bar{b}$ are well understood, and can be also normalized to the observed rate of $p\bar{p} \to W^* \to l\nu$. In contrast,

the calculation of W-gluon fusion suffers from uncertainties in the higher order corrections as well as in the input gluon density.

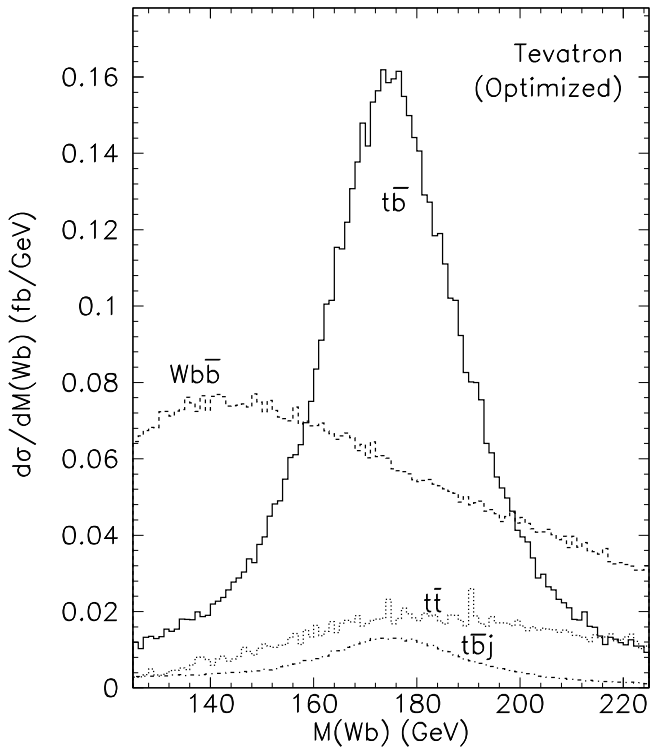

FIG. 109. Expected observed cross-section for $p\bar{p} \to W^* \to t\bar{b}$, $t \to Wb$, $W \to l\nu$ as a function of the invariant mass of the Wb. Also shown are expectations for the most important backgrounds ($t\bar{b}j$ denotes W-gluon fusion). This analysis is based on the $W+$ 2 jets sample. From Stelzer and Willenbrock, 1995.

The CKM matrix element $|V_{tb}|$ can also be measured from the ratio of branching ratios

$$\frac{Br(t \to Wb)}{Br(t \to Wq)} = \frac{|V_{tb}|^2}{|V_{tb}|^2 + |V_{ts}|^2 + |V_{td}|^2}$$

The b-tag can differentiate between $t \to Wb$ and $t \to Wd$ or Ws. Therefore, this ratio can be measured by comparing the number of single- and double-b-tagged $t\bar{t} \to$ lepton + jets events and by measuring the tagging rate in $t\bar{t} \to$ dilepton events. A preliminary analysis by the CDF collaboration finds (Yao, 1995):

$$\frac{Br(t \to Wb)}{Br(t \to Wq)} = 0.94 \pm 0.27 \pm 0.13$$

and sets a (not-yet-very-interesting) limit $|V_{tb}| > 0.022$ at the 95% confidence level. The statistical sensitivity for this branching ratio measurement is projected to be 3% for a 1 fb^{-1} exposure (Amidei and Brock, 1996).

Top decays also provide a unique opportunity to test the the structure of the charged weak current at the $t \to Wb$ vertex. Because the top quark is so heavy, it is possible that new physics may manifest itself at the Wtb vertex. The most general form of the Wtb interaction is (Kane, Ladinsky, and Yuan, 1992) :

$$\begin{aligned} L &= \frac{g}{\sqrt{2}} \left[W_\mu^- \bar{b}\gamma^\mu (f_1^L P_- + f_1^R P_+) t \;-\; \frac{1}{M_W} \partial_\nu W_\mu^- \bar{b}\sigma^{\mu\nu}(f_2^L P_- + f_2^R P_+) t \right] \;+ \\ & \frac{g}{\sqrt{2}} \left[W_\mu^+ \bar{t}\gamma^\mu (f_1^{L*} P_- + f_1^{R*} P_+) b \;-\; \frac{1}{M_W} \partial_\nu W_\mu^+ \bar{t}\sigma^{\mu\nu}(f_2^{R*} P_- + f_2^{L*} P_+) b \right] \end{aligned}$$

where $P_\pm = \frac{1}{2}(1 \pm \gamma_5)$ and $i\sigma^{\mu\nu} = -\frac{1}{2}[\gamma^\mu, \gamma^\nu]$.

The quantities f_1^L and f_1^R parametrize the strength of the left-handed and right-handed weak charged current. The f_2's can be interpreted as giving rise to an anomalous weak magnetic moment. In the Standard Model at tree level $f_1^L = 1$ and $f_1^R = f_2^L = f_2^R = 0$. There is obviously no direct experimental information on these form factors, although consistency with the measured branching ratio for $b \to s\gamma$ constrains f_1^R to be at most a few percent (Fujikawa and Yamada, 1994).

The polarization of the W in the $t \to Wb$ decay probes the values of the form factors. Denoting the left-handed, right-handed, and longitudinal polarization states of the W by λ_-, λ_+, and λ_0 respectively, the expected relative polarizations of the W boson after averaging over the top and bottom polarization states, are (Kane, Ladinsky, and Yuan, 1992) :

$$\begin{aligned} \lambda_- &= |f_1^L + \beta f_2^R|^2 \\ \lambda_+ &= |f_1^R + \beta f_2^L|^2 \\ \lambda_0 &= \frac{1}{2}|f_2^R + \beta f_1^L|^2 \;+\; \frac{1}{2}|f_2^L + \beta f_1^R|^2 \end{aligned}$$

with $\beta = \frac{M_{top}}{M_W}$. Therefore, the Standard Model predicts $\lambda_+ = 0$, and the fraction of longitudinally polarized W-bosons in top decays is $\frac{1}{2}\beta^2$. These polarizations can be measured from the angle of emission of the lepton in W-decays. Studies indicate that the statistical accuracies in the measurements of λ_0 and λ_+ in an exposure of 1 fb^{-1} at the Tevatron should be 5% and 2% respectively (Amidei and Brock, 1996). These form factors can also be probed by measuring the single top production cross-section (Carlson, Malkawi, and Yuan, 1994; Malkawi and Yuan, 1994).

The longitudinal polarization state of the W is directly connected with the breaking of electroweak symmetry, since it arises from the Goldstone boson degree of freedom. This kind of study therefore provides a rather unique and particularly interesting test of the Standard Model.

The $p\bar{p} \to t\bar{t}$ cross-section can be calculated in QCD. Its measurement tests the predictive power of QCD and is sensitive to new physics. Considerable theoretical interest in the subject was triggered by the initial measurement of the $t\bar{t}$ cross-section by the CDF collaboration (F. Abe *et al.*, 1994a). The measured value was higher than expected, although still consistent with the QCD calculation, within the large experimental uncertainties. The more recent higher statistics measurement by both CDF and D0 are in better agreement with the calculation (see Fig. 92).

The precision of the $t\bar{t}$ cross-section measurement depends on the accuracy of the luminosity normalization (3.5%), the background estimate, and the acceptance calculation. The uncertainty in the acceptance calculation is mostly due to the uncertainty in the b-tag efficiency and the uncertainties in the modeling of $t\bar{t}$ production (e.g. the effects of gluon radiation). The high statistics $t\bar{t}$ data samples that will be collected at the Tevatron will provide several handles to reduce this uncertainty. It is not clear what the ultimate systematic uncertainty on the $t\bar{t}$ cross-section will be; our guess is that a precision of 10%, comparable to the uncertainty in the QCD calculation of $t\bar{t}$ production, should be achievable.

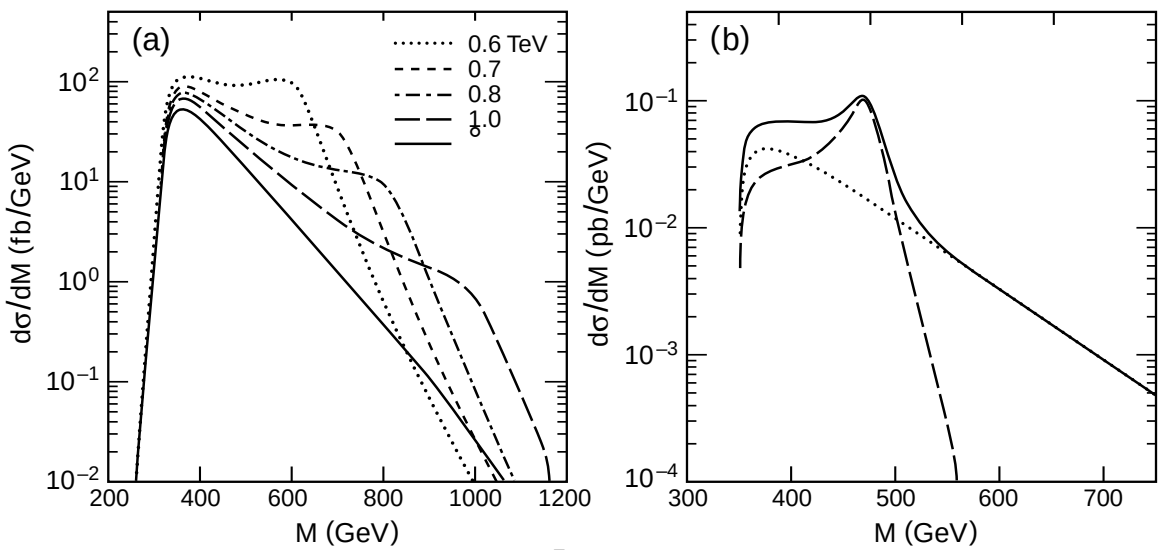

FIG. 110. Expected invariant mass of the $t\bar{t}$ pair : (a) including the contribution of a color octet vector meson in the top color model (from Hill and Parke, 1994). The different curves show the expectation as the vector meson mass varies from 600 GeV/c^2 to infinity. (b) including the effect of a 475 GeV/c^2 color-octet technipion in multiscale walking technicolor (from Lane, 1995). The dotted line is the QCD prediction; the dashed line is the technipion contribution; and the solid line is the sum of the two.

Large enhancements to the $t\bar{t}$ cross-section and, more dramatically, resonances in the $t\bar{t}$ invariant mass spectrum are expected in a number of models, (see Fig. 110). These could be due to color octet vector mesons (Hill and Parke, 1994) in models where the electroweak symmetry breaking is realized via top condensation (Hill, 1991; Martin, 1992a and 1992b), or to technipions (Eichten and Lane, 1994) in multiscale models of walking technicolor (Lane and Eichten, 1989; Lane and Ramana, 1991).

Measurements of the $t\bar{t}$ invariant mass distributions are possible in the lepton + jets

channel. Preliminary CDF (Yao, 1995) and D0 (Narain, 1996) analyses are consistent with QCD expectations, (see Fig. 111). With the high statistics that will become available, these models will be critically tested in the future.

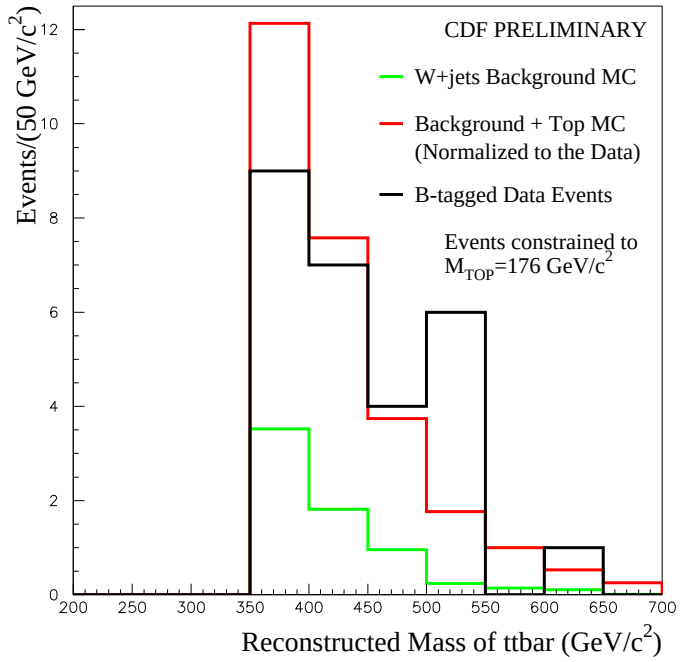

FIG. 111. Reconstructed invariant mass of the $t\bar{t}$ pair compared to the background and $t\bar{t}$ + background expectations. From the CDF collaboration, Yao, 1995. The integrated luminosity is ≈ 100 pb^{-1}.

Chromoelectric and chromomagnetic dipole moments of the top quark affect the structure of the $t\bar{t}$-gluon vertex, and hence affect the $t\bar{t}$ production cross-section and $t\bar{t}$ transverse momentum (Atwood, Kagan, and Rizzo, 1994; Rizzo, 1994; Cheung, 1995; Haberl, Nachtmann, and Wilch, 1995). A top-quark chromomagnetic dipole moment can occur in composite and technicolor models, with magnitude of order M_{top}^2/Λ^2, where Λ is the characteristic scale for new physics. As can be seen from Fig. 112, the present measurement of the $t\bar{t}$ cross-section is already accurate enough to probe the scale $\Lambda \approx 200$ GeV. A chromoelectric dipole moment would be CP-violating, and could arise from large couplings between top quarks and Higgs bosons in the multi-Higgs doublet model (Atwood, Aeppli, and Soni, 1992; Brandenburg and Ma, 1993; Cheung, 1995; Haberl, Nachtman, and Wilch, 1995).

CP violation effects in $t\bar{t}$ production would manifest themselves in different polarizations for the t and the $\bar{t}$ (Kane, Ladinsky, and Yuan, 1992; Schmidt and Peskin, 1992, Kao, Ladinsky, and Yuan, 1994). Because the top quark lifetime is short, the top decays before hadronization and polarization information is preserved in the $t \to Wb$ decay. Assuming Standard Model Wtb couplings, the polarization of the top quark is then analyzed by the polarization of the W from the top decay. Examples of CP violating observables that can be studied are differences in rates between $t_L\bar{t}_L$ and $t_R\bar{t}_R$, or $t_L\bar{t}_R$ and $t_R\bar{t}_L$, where the subscripts L and R denote left- and right-handed polarizations respectively.

In the single top production process, top quarks are almost 100% longitudinally polarized, since they are produced through the weak interaction (Carlson and Yuan, 1993). Searches

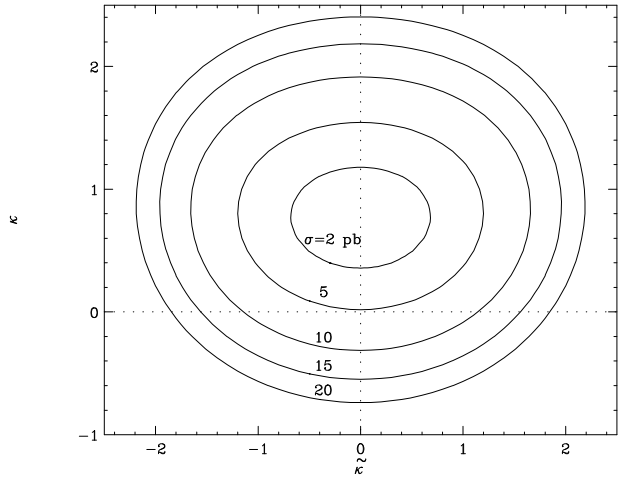

FIG. 112. Contours of $t\bar{t}$ cross-section (M_{top} = 176 GeV/c^2) as a function the chromoelectric ($\tilde{\kappa}$) and chromomagnetic (κ) dipole moments of the top quark.

for CP violation in the top quark decay can then also be carried out in the $t \to W^+b \to l^+\nu b$ decay by studying the quantity $\sigma \cdot (\mathbf{P}_b \times \mathbf{P}_l)$, where σ is the top polarization vector (Kane, Ladinsky, and Yuan, 1992; Grzadowski and Gunion, 1992).

Precise measurements of polarization effects in the top sector will however be rather difficult. These measurements require very high statistics and good control of the systematics. Most likely, only very large asymmetries will be accessible experimentally.

Physics beyond the Standard Model can also give rise to exotic decays of the top quark. The measurement of the ratio of branching ratios

$$R \quad = \quad \frac{Br(t\bar{t} \to l + jets)}{Br(t\bar{t} \to ll + jets)}$$

is quite generally sensitive to decays different from $t \to WX$, provided that the new top quark decay mode includes jets. More model-dependent searches for new top quark decays can also be carried out.

One example of a non-Standard Model decay of the top quark is the decay $t \to H^+b$, which can occur in models with two Higgs doublets, see Sec VI.C. The H$^+$ would then decay into the heaviest fermion pairs, $c\bar{s}$ or $\tau\nu$. The branching ratios depend on the ratio of vacuum expectation values for the two doublets, tanβ, (see Fig. 113). If tanβ is large, the signature for this decay mode would be an excess of lepton + hadronic $\tau + b$-tag events; if tanβ is small, one could search for the $H^+ \to c\bar{s}$ peak in the invariant mass distribution of lepton + jets events. Other possible exotic decays of the top quark which can be searched for include flavor changing neutral current decays such as $t \to Zc$ (Han, Peccei, and Zhuang, 1995) and $t \to \gamma c$, and decays into a supersymmetric top quark (*stop*) and a neutralino (Mrenna and Yuan, 1995). Some preliminary limits on these FCNC have been presented by CDF (LeCompte, 1995).

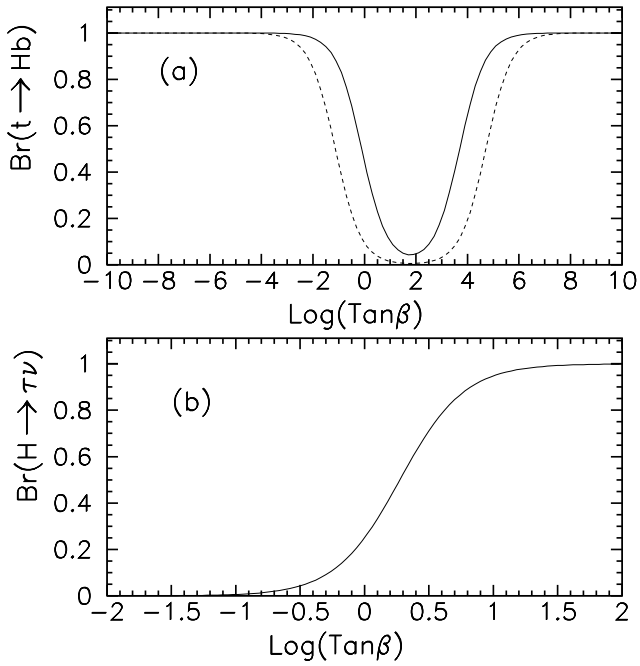

FIG. 113. (a) Expected branching ratios of $t \to H^+b$ in the two Higgs model for $M_{top} = 180$ GeV/c^2 as a function of log(tanβ). Solid line: $M_H = 70$ GeV/c^2; dashed line: $M_H = 150$ GeV/c^2. (b) Expected branching ratio for $H^+ \to \tau\nu$ as a function of log(tanβ).

XI. CONCLUSION

The evidence for the existence of the top quark from the CDF and D0 collaborations at the Tevatron is persuasive. The mass of the top quark is $M_{top} = 175 \pm 8$ GeV/c^2, in agreement with expectations from precision electroweak measurements. This mass is a factor of forty higher than the mass of the second heaviest fundamental fermion, and is of the same order of magnitude as the scale for electroweak symmetry breaking. The high mass of the top quark is a somewhat of a surprise; in Fig. 114 we show the evolution of the top mass limits and measurements since the discovery of the companion b-quark. It is interesting to notice that theoretical arguments based on local supersymmetry from the early eighties, when the experimental lower limit on the top quark mass was only approximately 20 GeV/c^2, favored a rather high top mass, see Section II. It is however still far from clear whether the high value of the top mass is an accident, or a consequence of physics at a higher mass scale.

The properties of the top quark will be studied much more precisely at the upgraded Tevatron starting in 1999. There is a possibility that effects beyond the Standard Model will manifest themselves in the top sector. If that is the case, the CDF and D0 collaborations are well positioned to observe them. In the more distant future, the LHC pp collider at CERN, with the higher energy and luminosity, will serve as a $t\bar{t}$ factory.

ACKNOWLEDGMENTS

First of all, we wish to thank our CDF colleagues with whom we shared the excitement of the hunt for the top quark. A number of people helped us to write this review. N. Hadley,

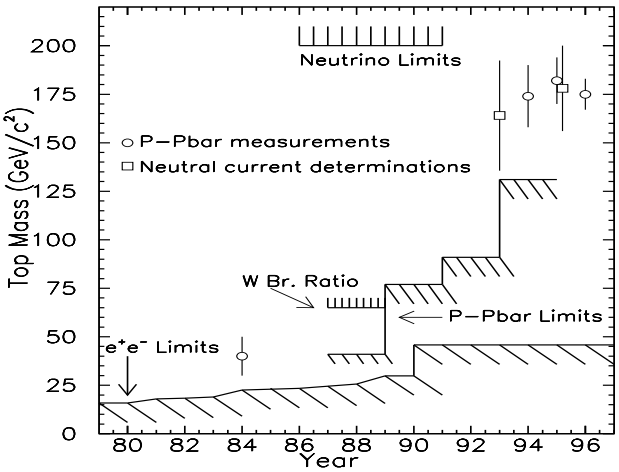

FIG. 114. A brief history of the search for the top quark. Here we show the limits from searches in e^+e^- (Section VI.A) and $p\bar{p}$ (Section VI.B). The square data points are predictions from neutral current studies, mostly at LEP and SLC (Section III). We also show the limit from neutrino experiments that were obtained prior to the commissioning of LEP and SLC (Amaldi *et al.*, 1987). The circular data points show the recent measurements of the top mass (Section IX.A), as well as the UA1 1984 result $M_{top} = 40 \pm 10$ GeV/c^2, which turned out to be wrong (Section VI.B). Just for fun, we also show the **upper** limit on the top mass from early measurements of the W leptonic branching ratio at the S$p\bar{p}$S (Section VI.C). More recent measurements of this quantity at both the Tevatron and the S$p\bar{p}$S are consistent with a high top quark mass.

B. Klima, M. Narain, S. Protopopescu, and S. Snyder explained many aspects of the D0 top analysis. E. Laenen kindly provided us with a modern calculation of the $t\bar{t}$ cross-section at S$p\bar{p}$S energies. A. Blondel helped us understand the implications of the very precise neutral current measurements. We also benefited from discussions with D. Amidei, P. Giromini, A. Heinson, S. Holmes, D. Kestenbaum, Y.K.Kim, J. Konigsberg, J. Kroll, M. Kruse, M. Mangano, M. Mannelli, and J. Polchinski. We also wish to thank D. Ceder and D. McLaren for assistance in the preparation of the manuscript.

REFERENCES

Abachi, S. *et al.*, 1994, Phys. Rev. Lett. **72**, 2138.
Abachi, S. *et al.*, 1995a, Phys. Rev. Lett. **74**, 2422.
Abachi, S. *et al.*, 1995b, Phys. Rev. Lett. **74**, 2632.
Abachi, S. *et al.*, 1995c, Phys. Rev. Lett. **75**, 3226.
Abachi, S. *et al.*, 1995d, Phys. Rev. D **52**, 4877.
Abachi, S. *et al.*, 1995e, Phys. Rev. Lett. **75**, 1456.
Abe, F. *et al.*, 1990a, Phys. Rev. Lett. **64**, 142.
Abe, F. *et al.*, 1990b, Phys. Rev. Lett. **64**, 147.
Abe, F. *et al.*, 1990c, Phys. Rev. Lett. **64**, 152.
Abe, F. *et al.*, 1990d, Phys. Rev. Lett. **64**, 348.
Abe, F. *et al.*, 1990e, Phys. Rev. D **41**, 2330.
Abe, F. *et al.*, 1991a, Phys. Rev. D **43**, 664.
Abe, F. *et al.*, 1991b, Phys. Rev. D **44**, 29.
Abe, F. *et al.*, 1991c, Phys. Rev. D **44**, 601.
Abe, F. *et al.*, 1992a, Phys. Rev. Lett. **68**, 447; Phys. Rev. D **45**, 3921.
Abe, F. *et al.*, 1992b, Phys. Rev. Lett. **68**, 3398.
Abe, F. *et al.*, 1992c, Phys. Rev. Lett. **69**, 28.
Abe, F. *et al.*, 1992d, Phys. Rev. D **45**, 1448.
Abe, F. *et al.*, 1993a, Phys. Rev. Lett. **70**, 713.
Abe, F. *et al.*, 1993b, Phys. Rev. Lett. **70**, 4042.
Abe, F. *et al.*, 1993c, Phys. Rev. D **47**, 4587.
Abe, F. *et al.*, 1993d, Phys. Rev. Lett. **71**, 3421.
Abe, F. *et al.*, 1994a, Phys. Rev. D **50**, 2966; Phys. Rev. Lett. **73**, 225.
Abe, F. *et al.*, 1994b, Phys. Rev. D **50**, 5550.
Abe, F. *et al.*, 1994c, Phys. Rev. Lett. **72**, 1977.
Abe, F. *et al.*, 1994d, Phys. Rev. Lett. **73**, 220.
Abe, F. *et al.*, 1994e, Phys. Rev. Lett. **73**, 2667.
Abe, F. *et al.*, 1995a, Phys. Rev. Lett. **74**, 2662.
Abe, F. *et al.*, 1995b, Phys. Rev. D **51**, 4623; Phys. Rev. Lett. **75**, 1012.
Abe, F. *et al.*, 1995c, Phys. Rev. D **52**, 2605.
Abe, K. *et al.*, 1990, Phys. Lett. B **234**, 382.
Abrams, G.S. *et al.*, 1989, Phys. Rev. Lett. **63**, 2447.
Abramowicz, H. *et al.*, 1986, Phys. Rev. Lett. **57**, 298.
Abreu, P. *et al.*, 1990a, Phys. Lett. B **241**, 449.
Abreu, P. *et al.*, 1990b, Phys. Lett. B **242**, 536.
Abreu, P. *et al.*, 1991, Nucl. Phys. B **2367**, 511.
Adachi, I. *et al.*, 1988, Phys. Rev. Lett. **60**, 97.
Adeva, B. *et al.*, 1983a, Phys. Rev. Lett. **50**, 799.
Adeva, B. *et al.*, 1983b, Phys. Rev. Lett. **51**, 443.
Adeva, B. *et al.*, 1985, Phys. Lett. B **152**, 439.
Adeva, B. *et al.*, 1986, Phys. Rev. D **34**, 681.
Adriani, O. *et al.*, 1992, Phys. Lett. B **294**, 457.
Adriani, O. *et al.*, 1993, Phys. Rep. **236**, 1.

Agrawal, P. and S.D. Ellis, 1989, Phys. Lett. B **221**, 393.
Akers, R. *et al.*, 1995, Phys. Lett. B **353**, 595.
Akesson, T. *et al.*, 1990, Z. Phys. C **46**, 179.
Akrawi, M.Z. *et al.*, 1990a, Phys. Lett. B **236**, 364.
Akrawi, M.Z. *et al.*, 1990b, Phys. Lett. B **242**, 299.
Albajar, C. *et al.*, 1987, Phys. Lett. B **198**, 271.
Albajar, C. *et al.*, 1988, Z. Phys. C **37**, 505.
Albajar, C. *et al.*, 1989, Z. Phys. C **44**, 15.
Albajar, C. *et al.*, 1990, Z. Phys. C **48**, 1.
Albajar, C. *et al.*, 1991a, Phys. Lett. B **253**, 503.
Albajar, C. *et al.*, 1991b, Phys. Lett. B **257**, 459.
Allaby, J.V., *et al.*, 1986, Phys. Lett. B **177**,446.
Allaby, J.V., *et al.*, 1987, Z. Phys. C **36**, 611.
Alitti, J. *et al.*, 1990a, Z. Phys. C **47**, 11.
Alitti, J. *et al.*, 1990b, Phys. Lett. B **235**, 363.
Alitti, J. *et al.*, 1991a, Z. Phys. C **49**, 17.
Alitti, J. *et al.*, 1991b, Z. Phys. C **52**, 209.
Alitti, J. *et al.*, 1991c, Phys. Lett. B **263**, 563.
Alitti, J. *et al.*, 1992a, Phys. Lett. B **276**, 354.
Alitti, J. *et al.*, 1992b, Phys. Lett. B **276**, 365.
Alitti, J. *et al.*, 1992c, Phys. Lett. B **280**, 365.
Altarelli, G. *et al.*, 1988, Nucl. Phys. B **308**, 724.
Altarelli, G., R. Kleiss, and C. Verzegnassi (editors), 1989, *Z Physics at LEP 1, Volume 1*, CERN-89-08.
Altarelli, G., *et al.*, 1996, CERN Preprint CERN-TH-96-20.
Althoff, M. *et al.*, 1984a, Z. Phys. C **22**, 307.
Althoff, M. *et al.*, 1984b, Phys. Lett. B **138**, 441.
Alvarez-Gaume, L., J. Polchinski, and M.B. Wise, 1983, Nucl. Phys. B **221**, 495.
Amaldi, U., *et al.*, 1987, Phys. Rev. D **36**, 1385.
Amidei, D. *et al.*, 1994, Nucl. Inst. and Meth. A **350**, 73.
Amidei, D. and C. Brock (editors), 1996, *Report of the Tev 2000 Working Group*, Fermilab Preprint Fermilab-Pub-96/082.
Ansari, R. *et al.*, 1987, Phys. Lett. B **194**, 158.
Anselmo, F., B. van Eijk, and G. Bordes, 1992, Phys. Rev. D **45**, 2312.
Arnison, G. *et al.*, 1984, Phys. Lett. B **147**, 493.
Arroyo, C.G., *et al.*, 1994, Phys. Rev. Lett. **72**, 3452.
Atwood, D., A. Aeppli, and A. Soni, 1992, Phys. Rev. Lett. **69**, 2754.
Atwood, D., A. Kagan, and T.G. Rizzo, 1995, Phys. Rev. D **52**, 6264.
Azzi, P. *et al.*, 1995, Nucl. Instrum. Meth. A **360**, 137.
Babcock, J., D. Sivers, and S. Wolfram, 1978, Phys. Rev. D **18**, 162.
Baer, H., V. Barger, and R.J.N. Phillips, 1989, Phys. Rev. D **39**, 2809 and 3953.
Baer, H. *et al.*, 1990, Phys. Rev. D **42**, 54.
Barber, D.P. *et al.*, 1979, Phys. Lett. B **85**, 463.
Barber, D.P. *et al.*, 1980, Phys. Rev. Lett. **44**, 1722.
Barger, V., J.L. Hewett, and R.J.N. Phillips, 1990, Phys. Rev. D **41**, 3421.

Barger, V., J. Ohnemus, and R.J.N. Phillips, 1993, Phys. Rev. D **48**, 3953.
Barger, V. *et al.*, 1994, Phys. Lett. B **338**, 336.
Barger, V. *et al.*, 1995, Phys. Lett. B **344**, 329.
Barger, V. and R. Phillips, 1987, in *Collider Physics*, (Addison-Wesley, Redwood City, Ca) p. 259.
Bartel, W. *et al.*, 1979a, Phys. Lett. B **88**, 171.
Bartel, W. *et al.*, 1979b, Phys. Lett. B **89**, 136.
Bartel, W. *et al.*, 1981, Phys. Lett. B **99**, 277.
Bartel, W. *et al.*, 1984, Phys. Lett. B **146**, 437.
Beenaker, W. *et al.*, 1991, Nucl. Phys. B **351**, 507.
Behrend, H.J. *et al.*, 1984, Phys. Lett. B **144**, 297.
Benlloch, J.M., N. Wainer, and W.T. Giele, 1993, Phys. Rev. D **48**, 5226.
Benlloch, J.M., K. Sumorok, and W.T. Giele, 1994, Nucl. Phys. B **425**, 3.
Berends, F.A., W.T. Giele, and H. Kuijf, 1989, Nucl. Phys. B **321**, 39.
Berends, F.A. *et al.*, 1989, Phys. Lett. B **224**, 237.
Berends, F.A. *et al.*, 1991, Nucl. Phys. B **357**, 32.
Berends, F.A., J.B. Tausk, and W.T. Giele, 1993, Phys. Rev. D **47**, 2746.
Berger, Ch. *et al.*, 1978, Phys. Lett. B **76**, 243.
Berger, Ch. *et al.*, 1979, Phys. Lett. B **86**, 413.
Berger, Ch. *et al.*, 1980, Phys. Rev. Lett. **45**, 1533.
Berger, E.L. *et al.*, 1989, Phys. Rev. D **40**, 83.
Berger, E. L. and H. Contopanagos, 1995, Phys. Lett. B **361**, 115.
Bethke, S., 1995, Nucl. Phys. B (Proc. Suppl.), **39B,C** 198.
Bienlein, J.K. *et al.*, 1978, Phys. Lett. B **78**, 360.
Bigi, I. *et al.*, 1986, Phys. Lett. B **181**, 157.
Blondel, A. *et al.*, 1990, Z. Phys. C **45**, 361.
Bordes, G. and B. van Eijk, 1993, Z. Phys. C **57**, 81.
Bordes, G. and B. van Eijk, 1995, Nucl. Phys. B **435**, 23.
Brandelik, R. *et al.*, 1982, Phys. Lett. B **113**, 499.
Brandenburg, A. and J.P. Ma, 1993, Phys. Lett. B **298**, 211.
Büchmuller, W., G. Grunberg, and S.H.H. Tye, 1980, Phys. Rev. Lett. **45**, 103; *Erratum:* ibid. **45**, 587 (1980).
Buskulic, D. *et al.*, 1992, Phys. Rep. **216**, 253.
Cabibbo, N. 1983, in *Proceedings of the 3rd topical workshop on proton-antiproton collider physics, Rome, Italy, 12-14 January 1983*, edited by C. Bacci and G. Salvini (European Organization for Nuclear Research, Geneva) p. 567.
Carithers, W. 1995, Fermilab seminar 3/2/1995.
Carlson, D.O., E. Malkawi, and C.P. Yuan, 1994, Phys. Lett. B **337**, 145.
Carlson, D.O. and C.P. Yuan, 1993, Phys. Lett. B **306**, 386.
Carlson, D.O. and C.P. Yuan, 1995, Michigan State University Preprint MSUHEP-50823.
Castro, A., 1994, Fermilab Preprint Fermilab-CONF-94/152-E.
Catani, S. *et al.*, 1996, CERN Preprint CERN-TH/96-21.
CDF Collaboration, 1995, *The CDF upgrade*, CDF note CDF/DOC/CDF/PUBLIC/3171.
Cheung, K., 1996, Phys. Rev. D **53**, 3604.
Church, M.D. and J. P. Marriner, 1993, Annu. Rev. Nucl. Part. Sci. **43**, 253.

Cobal, M., H. Grassmann, and S. Leone, 1994, Nuovo Cimento A **107**, 75.
Colas, P., D. Denegri, and C. Stubenrauch, 1988, Z. Phys. C **40**, 527.
Collins, J.C., D.E. Soper, and G. Sterman, 1986 Nucl. Phys. B **263**, 37.
Combridge, B.L., 1979, Nucl. Phys. B **151**, 429.
Contopanagos, H. and G. Sterman, 1993, Nucl. Phys. B **400**, 211.
Contopanagos, H. and G. Sterman, 1994, Nucl. Phys. B **419**, 77.
Cortese S. and R. Petronzio, 1991, Phys. Lett. B **253**, 494.
Dalitz, R.K. and G. Goldstein, 1992, Phys. Rev. D **45**, 1531.
Darden, C.W. *et al.*, 1978, Phys. Lett. B **76**, 246.
Decamp, D. *et al.*, 1990, Phys. Lett. B **236**, 511.
Demortier, L., 1991, PhD thesis, Brandeis University.
Deshpande, N.G. *et al.*, 1985, Phys. Rev. Lett. **54**, 1757.
Dress, M. and D.P. Roy, 1991, Phys. Lett. B **269**, 155.
Eichten, E. and K. Gottfried, 1977, Phys. Lett. B **66**, 286.
Eichten, E. and K. Lane, 1994, Phys. Lett. B **327**, 129.
Eichten, E. *et al.*, 1984, Rev. Mod. Phys. **56**, 579; *Erratum:* ibid. **58**, 1065 (1986).
Ellis, J. *et al.*, 1983, Phys. Lett. B **125**, 275.
Ellis, R.K. and R.J. Gonsalves, 1985, in *Supercollider Physics, Proceedings of the Oregon Workshop, Eugene, Oregon, 1985*, edited by D. Soper (World Scientific, Singapore), p. 287.
Ellis, R.K., 1991, Phys. Lett. B **259**, 492.
Ellis, R.K. and S. Parke, 1992, Phys. Rev. D **46**, 3785.
Ellis, S.D., R. Kleiss, and W.J. Stirling, 1985, Phys. Lett. B **154**, 435.
Fermilab, 1984, *Design Report for the Tevatron I Project.*
Field, R. and R. Feynman, 1978, Nucl. Phys. B **136**, 1.
Flattum, E., 1996, to be published in *Proceedings of the 11th Topical Workshop on Proton-Antiproton Collider Physics, Padova, Italy.*
Foster, G.W., 1995, in *10th Topical Workshop on Proton-Antiproton Collider Physics*, edited by R. Raja and J. Yoh (American Institute of Physics, Woodbury, NY) p. 201.
Frisch, H.J., 1995, in *95 Electroweak Interactions and Unified Theories*, edited by J. Tran Thanh Van (Editions Frontieres, Gif-sur-Yvette, Cedex-France) p. 69.
Frixione *et al.*, 1995, Phys. Lett. B **351**, 555.
Fujikawa, K. and A. Yamada, 1994, Phys. Rev. D **49**, 5890.
Georgi, H. *et al.*, 1978, Ann. Phys. **114**, 273.
Gerdes, D., 1995, in *Proceedings of Les Rencontres de Physique de la Vallée d'Aoste*, edited by M. Greco (Frascati Physics Series, Frascati, Italy) p. 713.
Giele, W.T., E.W.N. Glover, and D.A. Kosower, 1993, Nucl. Phys. B **403**, 633.
Giele, W.T. and W.J. Stirling, 1990, Nucl. Phys. B **343**, 14.
Glashow, S.L. and E.E. Jenkins, 1987, Phys. Lett. B **196**, 233.
Gluck, M., J.F. Owens, and E. Reya, 1987, Phys. Rev. D **17**, 2324.
Goldstein, G.R., K. Sliwa, and R.H. Dalitz, 1993, Phys. Rev. D **47**, 967.
Grzadowski, B. and J.F. Gunion, 1992, Phys. Lett. B **287**, 237.
Grannis, P., 1995, Fermilab seminar 3/2/1995
Gunion, J.F. and Z. Kunstz, 1985, Phys. Lett. B **161**, 333.
Gunion, J.F. *et al.*, 1990, *The Higgs Hunter's Guide*, Addisson-Wesley, New York.
Haberl, P., O. Nachtmann, and A. Wilch, 1996, Phys. Rev. D **53** 4875.

Hagiwara, K. and T. Yoshino, 1979, Phys. Lett. B **80**, 282.
Hagiwara, K. and D. Zeppenfeld, 1989, Nucl. Phys. B **313**, 560.
Halzen, F., C.S. Kim, and S. Willenbrock, 1988, Phys. Rev. D **37**, 229.
Halzen, F. and M. Marsula, 1983, Phys. Rev. Lett. **51**, 857.
Hamberg, R., W.L. van Neerven, and T. Matsuura, 1991, Nucl. Phys. B **359**, 343.
Han, T., R.D. Peccei, and X. Zhuang, 1995, Nucl. Phys. B **454**, 527.
Heinson, A.P., A.S. Belyaev, and E.E. Boos, 1995, University of California at Riverside preprint UCR-95-17.
Herb, S.W. *et al.*, 1977, Phys. Rev. Lett. **39**, 252.
Hikasa, K., 1984, Phys, Rev. D **29**, 1939.
Hill, C.T., 1991, Phys. Lett. B **266**, 419.
Hill, C.T. and S. Parke, 1994, Phys. Rev. D **49**, 4454.
Ibanez, L. E. and C. Lopez, 1983, Phys. Lett. B **126**, 54.
Igarashi, S. *et al.*, 1988, Phys. Rev. Lett. **60**, 2359.
Ikeda, M., 1990, in *Proceedings of the 8th Topical Workshop on Proton-Antiproton Physics, Castiglione della Pescaia, Italy*, edited by G. Bellettini and A. Scribano (World Scientific, Singapore) p. 558.
Jackson, G, (editor), 1995, *Recycler Ring Conceptual Design Study*, Fermilab Library FERMILAB-TM-1936.
Jikia, G.V. and S.R. Slabospitski, 1992, Phys. Lett. B **295**, 136.
Jones, L.M. and H. Wyld, 1978, Phys. Rev. D **17**, 782.
Kane, G.L., G.A. Ladinsky, and C.P. Yuan, 1992, Phys. Rev. D **45**, 124.
Kane, G.L., and M.E. Peskin, 1982, Nucl. Phys. B **195**, 29.
Kao, C., G.A. Ladinsky, and C.P. Yuan, 1994, in *The Albuquerque Meeting : Proceedings of the 8th Meeting, Division of Particle and Fields of the American Physical Society*, edited by S. Seidel (World Scientific, Singapore) p. 713.
Kestenbaum, D., 1996, PhD thesis, Harvard University.
Kidionakis N. and J. Smith, 1995, Phys. Rev. D **51**, 6092.
Klima, B., 1996, personal communication.
Kleiss, R. and W.J. Stirling, 1985, Nucl. Phys. B **262**, 235.
Kondo, K., 1988, J. Phys. Soc. Jpn **57**, 4126.
Kondo, K., 1991, J. Phys. Soc. Jpn **60**, 836.
Krasemann, K.H. and S. Ono, 1979, Nucl. Phys. B **154**, 283.
Laenen, E., J. Smith, and W.L. van Neerven, 1992, Nucl. Phys. B **369**, 543.
Laenen, E., J. Smith, and W.L. van Neerven, 1994, Phys. Lett. B **321**, 254.
Lane, K., 1995, Phys. Rev. D **52**, 1546.
Lane, K. and E. Eichten, 1989, Phys. Lett. B **222**, 274.
Lane, K. and M.V. Ramana, 1991, Phys. Rev. D **44**, 2678.
Leader, E. and E. Predazzi, 1982, in *An Introduction To Gauge Theories And The New Physics*, (Cambridge University Press, Cambridge, UK) p.76.
LeCompte, T., 1995, to appear in *Proceedings of the 1995 Recontres de Physique de Vietnam.*
Lindgren, M. *et al.*, 1992, Phys. Rev. D **45**, 3038.
Linneman, J.T., 1995, in *Proceedings of the XXVII International Conference on High Energy Physics, 20-27 July 1994, Glasgow, Scotland, UK*, edited by P.J. Bussey and I.G. Knowles (Institute of Physics, Philadelphia, Pa.), p. 823.

Malkawi, E. and C.P. Yuan, 1994, Phys. Rev. D **50**, 4462.
Mangano, M.L., 1993, Nucl. Phys. B **405**, 536.
Mangano, M.L. and P. Nason, 1992, Phys. Lett. B **285**, 160.
Mangano, M.L., P. Nason, and G. Ridolfi, 1992, Nucl. Phys. B **373**, 295.
Marchesini, G. and B.R. Webber, 1984, Nucl. Phys. B **238**, 1.
Marchesini, G. and B.R. Webber, 1988, Nucl. Phys. B **310**, 461.
Martin, A.D., R.G. Roberts, and W.J. Stirling, 1987, Phys. Lett. B **189**, 220.
Martin, A.D., R.G. Roberts, and W.J. Stirling, 1989, Phys. Lett. B **228**, 149.
Martin, S.P., 1992a, Phys. Rev. D **45**, 4283.
Martin, S.P., 1992b, Phys. Rev. D **46**, 2197.
Matteuzzi, C. *et al.*, 1983, Phys. Lett. B **129**, 141.
Montanet, L. *et al.*, 1994, *Review of Particle Properties*, Phys. Rev. D **50**, 1433.
Morfin, J. and W.K. Tung, 1991, Z. Phys. C **53**, 13.
Mrenna, S. and C.P. Yuan, 1996, Phys. Lett. B **367**, 188.
Müller, A.H. and P. Nason, 1985, Phys. Lett. B **157**, 226.
Müller, A.H. and P. Nason, 1986, Nucl. Phys. B **266**, 265.
Narain, M., 1995, personal communication.
Narain, M., 1996, to be published in *Proceedings of the 1996 Les Rencontres de Physique de la Vallée d'Aoste*, edited by M. Greco.
Nason, P., S. Dawson, and R.K. Ellis, 1988, Nucl. Phys. B **303**, 607.
Ohnemus, J., 1991a, Phys. Rev. D **44**, 1403.
Ohnemus, J., 1991b, Phys. Rev. D **44**, 3477.
Ohnemus, J. and J.F. Owens, 1991, Phys. Rev. D **43**, 3626.
Orr, L.H., , 1991, Phys. Rev. D **44**, 88.
Orr, L.H., T. Stelzer, and W.J. Stirling, 1995, Phys. Rev. D **52**, 124.
Paige, F. and S.D. Protopopescu, 1986, Brookhaven National Laboratory Preprint BNL-38034.
Para, A., 1988, in *7th Topical Workshop on Proton-Antiproton Collider Physics*, edited by R. Raja, A. Tollestrup, and J. Yoh (World Scientific, Singapore), p. 131.
Perl, M.L. *et al.*, 1975, Phys. Rev. Lett. **35**, 1489.
Peterson, C. *et al.*, 1983, Phys. Rev. D **17**, 105.
Quigg, C. and J.L. Rosner, 1977, Phys. Lett. B **71**, 153.
Revol, J.P., 1985, in *Proceedings of the 6th workshop on grand unification*, edited by S. Rudaz and T.F. Walsh (World Scientific, Singapore), p. 275.
Rice, E. *et al.*, 1982, Phys. Rev. Lett. **48**, 906.
Rizzo, T.G., 1994, Phys. Rev. D **50**, 4478.
Roser, R., 1995, *10th Topical Workshop on Proton-Antiproton Collider Physics*, edited by R. Raja and J. Yoh (American Institute of Physics, Woodbury, NY) p. 248.
Rosner, J.L., 1989, Phys. Rev. D **39**, 3297; *Erratum:* Phys. Rev. D **40**, 1701 (1989).
Rosner, J.L., C. Quigg, and H.B. Thacker, 1978, Phys. Lett. B **74**, 350.
Sagawa, H. *et al.*, 1988, Phys. Rev. Lett. **60**, 93.
Schmidt, C.R. and M.E. Peskin, 1992, Phys. Rev. Lett. **69**, 410.
Sjöstrand, T. and M. Bengtsson, 1987, Comp. Phys. Comm. **43**, 367.
Snyder, S.S., 1995a, PhD thesis, SUNY-Stony Brook.
Snyder, S.S., 1995b, to appear in *Proceedings of the 1995 International Europhysics Confer-*

ence on High Energy Physics, Brussels, Belgium. Fermilab Preprint Fermilab-PUB-95/341-E

Stelzer, T. and S. Willenbrock, 1995, Phys. Lett. B **357**, 125.

Strovink, M., 1995 to in *10th Topical Workshop on Proton-Antiproton Collider Physics*, edited by R. Raja and J. Yoh (American Institute of Physics, Woodbury, NY) p. 320.

Tartarelli, G.F., 1996, to be published in *Proceedings of the XXXIst Rencontres de Moriond, Electroweak Interactions and Unified Theories*; Fermilab preprint FERMILAB-CONF-96/099-E.

The LEP Collaborations ALEPH,DELPHI,L3,OPAL and the LEP Electroweak Working Group, 1995, CERN Preprint CERN-PPE/95-172.

Thompson, W.J., 1994, PhD thesis, SUNY-Stony Brook.

Tuts, P.M., 1996, in *Proceedings of the International Europhysics Conference on High-Energy Physics*, edited by J. Lemonne, C. Vander Velde, and F. Verbeure (World Scientific, Singapore), p. 187.

van der Meer, S., 1972, CERN Internal Report, CERN/ISR-PO/72-31.

van Neerven, W.L. and E.B. Zijlstra, 1992, Nucl Phys. B **382**, 11.

Voloshin, M. and V.I. Zakharov, 1980, Phys. Rev. Lett. **45**, 688.

Wells, J.D. and G.L. Kane, 1996, Phys. Rev. Lett. **76**, 869.

Willenbrock, S.S.D. and D. Dicus, 1986, Phys. Rev. D **34**, 155.

Woods, M., 1996, in *Proceedings of the International Europhysics Conference on High-Energy Physics*, edited by J. Lemonne, C. Vander Velde, and F. Verbeure (World Scientific, Singapore), p. 31.

Yao, W., 1995, to be published in *Proceedings of the 17th International Symposium on Lepton-Photon Interactions*, Beijing, China.

Yoshida, H. *et al.*, 1987, Phys. Lett. B **198**, 570.

Yuan, C.P., 1990, Phys. Rev. D **41**, 42.